The drag of a circulation controlled aerofoil

Hustad, C. W.

Award date:
1986

Awarding institution:
University of Bath

THE DRAG OF A CIRCULATION CONTROLLED AEROFOIL

Submitted for the degree of Ph.D
by

C.W.Hustad, BSc. May 1986

Part 1 - Summary
- Acknowledgements
- Contents
- Notation
- Text
- References

ProQuest LLC
789 East Eisenhower Parkway
P.O. Box 1346
Ann Arbor, MI 48106-1346

THE DRAG OF A CIRCULATION - CONTROLLED AEROFOIL

SUMMARY

An experimental and a theoretical investigation has been made of a 20% elliptic circulation-controlled aerofoil with single leading and trailing edge blowing slots.

Experimental Reynolds number based on the chord was 0.9 to 1.3 x 10^6, with typical slot height to chord ratio of .0020. The performance with no leading edge blowing, a trailing edge blowing coefficient from 0 to 0.04, and geometric incidence from -10 to $+10^0$ resulted in lift coefficients from -0.5 to +1.2.

Drag was measured using a rake, and comparison of the momentum deficit downstream with the resulting force on the model due to the pressure distribution and skin friction gave reasonable agreement.

The theoretical work included development of a discrete vortex model used to predict the growth and eventual separation of the trailing edge wall-jet.

Preliminary results show that performance of the theoretical model is comparable with the experimental work.

COPYRIGHT

C W Hurstead

A C K N O W L E D G E M E N T S

This section, though at the beginning is the last to be written and is therefore the most satisfying to complete. It summarises the help and effort which I, as author, have received during the course of this present study. In chronological order I am first of all indebted to Dr. James F. Henderson who as supervisor has provided much support with regards both subjective criticism, academic formalities and financial arrangements. Secondly I would like to thank Dr. Norman J. Wood for his help and recommendations at the start of the present study.

Needless to say, no postgraduate doing wind-tunnel work can avoid being in contact with technicians who build and maintain the experimental facilities. I am therefore very grateful for the assistance from Mr. Tom Keston, Mr. John Butt and Mr. David Tallin who have contributed with everything from technical expertise to moral support and numerous cups of tea.

The instrumentation and data-acquisition equipment was kindly lent by Dr. David A. Cook and Mr. Richard T. Lewis M.Sc. from School of Architecture at Bath University.

I have while writing-up received support and help from Mr. Haldor Hole of Consultas A/S, Horten, Norway and from my present employer, Kongsberg Vaapenfabrikk A/S, Kongsberg, Norway.

I owe an especial gratitude to my immediate superior Mr. Kjell Paulsen, Head of the Aerostructure and Mechanics Group (FP-46) who has provided me with both time and facilities to complete the work.

Finally no thesis is complete without a typist - such work is either done for love or for money. I am wholly indebted to my mother, Mrs. Gine G. Hustad who thankfully offered to do the work for the former and not the latter reason. A final mention is due to her employer, Hesnes Shipping A/S, Tjøme, Norway for use of their word processing facilities.

To all of you very many thanks.

Part 1 C O N T E N T S Page No.

NOTATION

Page No.

Page No.

Part 2 C O N T E N T S Page No.

NOTATION

a	Lift-curve slope for the unblown model.
a	Constant used with subsripts 0 and 1 defined in equation 5.9.
a_e	Aerofoil effective incidence (also used α_e).
a_g	Aerofoil geometric incidence (also used α_g).
a_i	Aerofoil induced incidence ($=\alpha_g - \alpha_e$).
b	Model span (0.689m).
b	Constant used with subsripts 0 and 1 defined in equation 5.9.
b'	Width of wake at the traverse point downstream of the model.
C_{D_b}	Drag coefficient of a cylinder measured directly using a balance.
C_{D_e}	Equivalent drag coefficient (see eqn. 2.18).
C_{D_i}	Induced drag coefficient (see section 2.2.4)
C_{D_j}	Thrust due to jet-blowing momentum.
$C_{D_{ke}}$	Incremental drag coefficient due to the kinetic energy of the jet (see eqn. 2.17).
C_{D_o}	Minimum drag coefficient.
C_{D_p}	Profile drag coefficient.
$C_{D_{pj}}$	Drag coefficient due to blowing slot exit pressure.
C_{D_r}	Rake drag coefficient (see eqn. 2.22).
C_{D_s}	Section drag coefficient (see eqn. 2.14).
C_{D_w}	Wake drag coefficient (see eqn. 2.16).
C_{D_x}	Chordwise force coefficient resolved parallel to the longitudinal tunnel axis.
C_D'	Pressure drag coefficient resolved parallel to free-stream direction.
C_f	Section skin friction coefficient.

C_j	Jet-blowing momentum coefficient (see eqn. 2.7).
C_M	Moment coefficient about the LE.
C_N	Normal force coefficient due to surface static pressure.
C_p	Pressure coefficient.
C_{p_j}	Jet-exit pressure coefficient.
C_X	Chordwise force coefficient due to surface pressure.
C_X'	Chordwise force coefficient corrected for jet-exit pressure.
c	Aerofoil chord (0.593m).
c	Constant used with subsripts 0 and 1 defined in equation 5.9.
c_f'	Local skin friction coefficient.
d	Lip thickness (approx. = 0.25mm).
d	Constant used with subsripts 0, 1, 2 and 3 defined in equation 5.11.
dt	Time-step in seconds (also used Δt).
e_s	Blockage factor (see eqn.2.3).
f	Vortex frequency in Hz.
f	Constant used with subsripts 0, 1 and 2 defined in equation 5.7.
Go	Initial vortex strength.
g	Vortex strength in m^2/s.
H	Total pressure measured in mm of water.
H	Modified boundary-layer shape factor.
H	Angular momentum.
h	Slot height.
h	Height of razor blade above static pressure tapping.
K	Vortex strength decay rate.

k	Starting length ratio (see eqn. 4.9).
k	Constant used to relate induced drag with lift coefficient squared. Defined in equation 5.19.
k_o	Empirical constant used in equation 5.6.
$k_{1,2}$	Empirical constants used in equation 5.19.
$\dot{m}$	Massflow rate in kg/s.
P	Static pressure measured in mm of water.
P	Number of discrete vortex pairings.
p	General term used for pressure.
p_j	Mean jet-exit pressure.
Q	Summation of external vortex strengths.
Q	Dynamic pressure measured in mm of water.
q	General term used for dynamic pressure.
q	Lift augmentation rate dC_N/dC_j.
R	Radius.
R	Gas constant.
R_c	Reynolds number based on chord.
R_{cr}	Critical Reynolds number for boundary-layer transition from laminar to turbulent flow.
R_d	Reynolds number based on diameter.
R_e	Reynolds number based on the boundary-layer energy thickness.
r	Vortex core radius.
s	Distance measured around the surface from the blowing slot.
s	Vortex starting length (see eqn. 4.4).
T	Temperature in ^oK.
t	Maximum aerofoil thickness.
t	Age of vortex in seconds.

U_{fs}	Free-stream velocity (also used U_{∞}).
V_e	Excess jet velocity ($V_j - V_p$).
V_i	Induced velocity.
V_j	Jet exit velocity.
V_{jfs}	Jet velocity following an isentropic expansion from plenum to free-stream pressure.
V_p	Velocity at the lip due to the free-stream.
V_s	Induced slot surface velocity.
x	Distance in chordwise direction.
y	Distance normal to the chord.
Z	Distance along vortex path.

Greek symbols.

α	Incidence.
β	Flow angle with respect to adjacent surface.
η	Angular position of the rear stagnation point on an ellipse.
γ	Vortex strength.
ϑ	Angular position from the blowing slot.
ϑ_o	Angular position of the LE stagnation point.
ϱ	Air density.
τ	Local skin friction in N/m^2.
ψ	Stream function.

Subscripts.

atm	Atmospheric condition.
fs	Free-stream condition (also used $_\infty$).
i	Suffix used for the image vortices.
j	Relates to the blowing jet.
j	Suffix used for the external vortices.
l	Lower-surface condition.
mc	Mid-chordwise condition.
o	Stagnation or initial condition.
p	Relates to potential flow parameters.
r	Relates to razor blade parameters.
tr	Transition from laminar to turbulent boundary-layer
u	Upper-surface condition.
wk	Wake condition.

Abbreviations.

CC	Circulation controlled.
CCA	Circulation-controlled aerofoil.
DVM	Discrete vortex model.
KE	Kinetic energy.
LE	Leading edge.
RMS	Root mean square.
RPD	Tunnel reference pressure difference.
TDC	Top dead centre.
TE	Trailing edge.
VTOL	Vertical take-off and landing.

THE DRAG OF A CIRCULATION-CONTROLLED AEROFOIL

1. INTRODUCTION

A circulation-controlled aerofoil (CCA), shown in Fig.1.1, is distinguished by its blunt trailing edge (TE) around which the separation point is moved in order to develop lift. This is achieved by varying the strength of a wall-jet which emerges from a slot on the upper surface. Lift independent of incidence is possible, but this is accompanied by increased drag due to suction produced by the TE wall-jet.

Application of circulation control to future aircraft design extends from simple lift augmentation (as substitute for flaps or control surfaces) through to reducing the mechanical complexity of rotorcraft hubs by using sequential blowing along the blades to compensate for cyclic variation in lift. Development of dual fixed-rotor/wing aircraft operating with both leading and trailing edge blowing slots has also shown the potential for combining transonic performance with vertical take-off and landing (VTOL) capabilities.

Demand for comprehensive design data has demonstrated the usefulness of theoretical models to predict performance with variations in geometry, free-stream conditions and blowing strength. Early experimental

work showed that performance was also dependent on understanding of the interaction between the wall-jet and the boundary-layers developing along the upper and lower surfaces. Despite extensive theoretical and experimental research with varying degrees of complexity, a comprehensive understanding of the "TE Coanda flow" is still unresolved.

The wall-jet interaction with the upper surface boundary-layer produces a two-phase shear flow, with entrainment and vorticity being dominant features immediately downstream of the lip. Further around, curvature, angular momentum and a radial static pressure gradient define the streamline pattern and separation from the surface.

The present study has involved both experimental and theoretical work on a 20% elliptic CCA. This has provided information about the TE region in addition to overall lift and drag performance data.

1.1 PREVIOUS EXPERIMENTAL WORK

Relevant experimental work can be divided into two categories. The first relates to work on cylinders using either single or multiple tangential blowing slots and the second is an extension of such work to sections with fore and aft symmetry, the simplest being an ellipse.

Lockwood(1), Jones(2) and Cheeseman(3) provided some initial test data which was extended by Dunham(4) who attempted to derive empirical correlations of lift and drag for different CC-cylinder configurations. The work by Levinsky and Yeh(5) performed on a 0.152m diameter cylinder with a maximum slot height to radius ratio of .015 resulted in data for comparison with their theoretical model which was an extension of the work by Dunham discussed in section 1.2. This data has also been used while developing the proposed theoretical model discussed in section 4.2.

Work in the second category was performed at the National Gas Turbine Establishment from 1965 to 1969 on elliptic section CCAs. This included wind-tunnel tests at Mach numbers from 0.1 to 0.6 with blowing coefficients up to 0.2.

A summary of this work is given by Osborne(6) and provides lift and pitching moment data with variations in geometric incidence. Two near-elliptical aerofoil sections with thickness to chord ratio of 10 and 20% were tested by Barbour(7) under similar conditions to the present study. The results included pressure distributions in addition to lift, drag and pitching moment obtained from a three-component mechanical balance, with the compressed air supply fed to the model through a labyrinth seal which removed any mechanical contact which might interfere with the balance reading.

Work in the United States on cambered and uncambered elliptic CCAs was started at the David Taylor Naval Ship Research and Development Center (DTNSRDC) in 1970 and has included work by Williams(8), Englar(9) and Ostensoser(10) to name but a few. An extension of this work, which includes the collection of a database with the specific intention of developing efficient transonic CCAs is also described in a bibliography of the work at DTNSRDC by Englar(11). In addition to performance data, work at NASA-Ames by Bachalo(12) has involved a flow visualisation study of the trailing edge flowfield using holographic interferometry.

The wall-jet, which can be described in terms of velocity profiles, turbulence parameters and shear stress distribution, has been investigated by Kind(13), Jones(14) and Wood(15). Kind's model at Cambridge was probably the closest equivalent to the present study, with a Reynolds number based on chord of 0.8×10^6 and slot height to chord ratio of .0010, as compared with 1.3×10^6 and .0024 for the present study. Jones used a 1.2m chord model to increase the scale of the wall-jet and measured shear stress, as well as velocity profiles, with a single hot-wire probe.

The work by Wood between 1977-80 on the present model at Bath University involved measuring the turbulence parameters in the vicinity of the trailing edge. He also integrated the pressure distribution around the model centre-line to calculate the lift coefficient. However, there were insufficient pressure tappings to give reliable drag data.

1.2 PREVIOUS THEORETICAL WORK

One of the earlier theoretical models, suggested by Dunham(16), contained the major elements of the more complex models which have emerged in the last 15 years. It involved calculation of the appropriate potential flow around the body. Superimposed on this was development of the boundary-layer along the lower surface, starting at the LE stagnation point, moving downstream through transition and separation near the rear of the aerofoil. A similar method was applied along the upper surface upto the blowing slot. This resulted in a wall-jet/boundary-layer interaction and the introduction of correct parameters to get the wall-jet to separate at the same pressure as the lower surface boundary-layer. If the separation pressures were not the same, new wall-jet parameters were inserted until the iteration loop could be satisfied.

Dunham's model was developed further by Levinsky and Yeh(5) who defined a four-layer wall-jet/boundary-layer velocity profile and introduced expressions for the shear stress distribution together with curvature and induced pressure terms. The results were useful but sensitive to the developing wall-jet profile.

Kind(17) extended Dunham's model to predict the performance of an elliptic CCA. He revised the initial wall-jet conditions: entrainment, separation and curvature effects. He included an angular momentum equation and developed an empirical expression for the mean static pressure across the jet. However, insufficient experimental data on the turbulent structure within the wall-jet, and dependence on knowledge of the experimental pressure distribution around the trailing edge, restricted the usefulness of the model.

Ambrosiani(18) continued Kind's analysis and developed a self-contained model which did not require such experimental data. He also revised the previously assumed Thwaite's criterion which imposed a constant pressure within the TE separation bubble. Wall-jet separation was formulated using a concept of conservation of mass. The solution involved an iterative matching of an assumed lift coefficient with that calculated from the actual pressure distribution over the section in the presence of the TE blowing.

The computer program CIRCON was developed by Dvorak and Kind(19) and applied to arbitrary CCAs by using a vortex lattice arrangement to generate the potential flow distribution. This was used as a basis for an

integral method along the boundary-layer. A finite difference technique, which included the effect of surface curvature and a transverse pressure gradient, was used within the wall-jet. The model accounted for viscous effects by including eddy viscosity based on: intermittency, mixing length arguments and Reynolds shear-stress terms. Results were encouraging but sensitive to the wall-jet parameters and required the use of semi-empirical expressions.

Dvorak and Choi(20) extended the above programme with TRACON for application to transonic CCAs, taking account of compressibility within the boundary-layer analysis. Prediction of the pressure distribution concurred with experimental results for both low and transonic speeds at negative angles of attack. However, the model was insensitive to variations of the TE surface and also unable to resolve the flow downstream of a choked blowing slot.

An alternative approach was suggested by Smith(21) using discrete vortices to approximate shear between the boundary-layer and wall-jet emerging tangential to the surface of a cylinder in a free-stream.

Smith's proposal was a theoretical model as shown in Fig.1.2. Discrete point vortices were shed at a regular interval from the lip, and their development was calculated using the potential flow solution and summing the induced velocity due to each vortex. Their position was found after each time-step, and a new vortex introduced at the lip. This led to the convection downstream of a starting vortex at the free end of the vortex sheet, and eventual flow stabilisation as seen in Fig.1.3. Steady-state solution was dependent upon the initial vortex strength, determined by the velocity difference at the slot. To prevent the model going unstable, Smith introduced artificial viscosity, and a vortex decay-rate K, to take account of entrainment.

Continuation of Smith's work by Soliman(22) clarified some original problems and extended the concept for comparison with elliptic sections. A universal constant value for K produced similar experimental and theoretical results, but a physical explanation for the breakdown of the discrete vortex structure was not included.

Experimental justification for such a model has been reported by Wood(15), who proposed that the wall-jet might be considered as a stream of coherent vortices emanating from the lip region as shown in Fig.1.4.

Breakdown of the shear layer between the wall-jet and upper surface boundary-layer leads to the formation of discrete vortices with a frequency dependent on slot geometry and the jet-blowing momentum. Entrainment caused vortex growth and an eventual breakdown of the vortex stream due to pairing when adjacent vortices touched. The exact mechanism for the pairing process was not understood and this aspect has been considered in more detail during the theoretical part of the present study.

1.3 PRESENT INVESTIGATION

1.3.1 Experimental Work

The purpose of the present experimental investigation was to build upon the work by Wood(15) and investigate the drag performance of a 20% elliptic CCA. The work has been performed in three stages between which improvements to the apparatus and experimental procedure were made.

1.3.1.1 Experimental Session 1

Following initial modifications described in section 2.1.1, this session was primarily a repeat of previous work by Wood, but with a larger slot height, additional pressure tappings and a modified boundary-layer control system.

The results, recorded as RUN-1 to RUN-33, confirmed the reliability of the data acquisition system described in section 2.1.5. However some limitations of the apparatus, due to three-dimensional effects, were revealed by flow visualization work.

1.3.1.2 Experimental Session 2

Following improvements to the boundary-layer control system, this session included the use of a fixed rake downstream of the model and provision for the measurement of skin friction. The results were recorded as RUN-34 to RUN-77.

1.3.1.3 Experimental Session 3

Consisting of DRUN-1 to DRUN-44, this session concentrated on the wake region with the rake mounted on a traversing mechanism and connected to a now modified data acquisition system. This gave detailed measurement of the flow angle, in addition to total and static pressure for calculation of the momentum deficit in the wake.

1.3.2 Theoretical Work

The purpose of the theoretical work was to extend the model proposed by Smith(21) by relating both lift and drag performance of the 20% elliptic CCA to the shedding of discrete vortices from the TE blowing lip. The work was performed in two sessions during the final 18 months of the three year study.

1.3.2.1 Theoretical Session 1

This session consisted of reconstructing the model proposed by Smith and implementing some of the modifications which included:

(1) A vortex shedding frequency dependent on vortex core size, blowing strength and slot height.

(2) A pairing process for when adjacent vortices overlap, ensuring a rapid breakdown of the vorticity and resulting in a realistic prediction of the flow in the wake of the model.

(3) Detail of the flow pattern by "seeding" the model with passive points. These are vortices with zero strength which do not disturb the flow but are translated with the streamlines, thus revealing the local velocity and flow direction.

The work, performed using an HP-85 computer, was concerned with developing the correct algorithm, rather than with speed and capacity for large "number crunching" routines.

1.3.2.2 Theoretical Session 2

Consisted of transferring the almost fully developed program on to the mainframe Multics system available at Bath University. This procedure involved a direct line transfer via a serial(RS-232) interface from the HP-85 to Multics, followed by a line-by-line edit to remove certain incompatibilities between the HP-Basic and the Basic compiler available on Multics.

The compiled program used an average CPU time of between one to three hours for the majority of the cases considered. The model was first applied to the experimental results of Levinsky and Yeh(5) about a CC-cylinder before extending it to the elliptic CCA.

Chapter 2 of this dissertation describes the apparatus and method used to record the experimental results which are shown in chapter 3. The theoretical work is presented (with results) in chapter 4 and both experimental and theoretical results are discussed in chapter 5. Finally conclusions and recommendations for further work are given in chapter 6.

2. EXPERIMENTAL METHOD

2.1 DESCRIPTION OF APPARATUS

2.1.1 Modifications to the Original Model

The model used by Wood(15) is shown in Fig.2.1. The 20% elliptic section of 0.59m chord with 0.69m span was mounted vertically between endplates in the 2.1 x 1.5m wind-tunnel at Bath University. Separate supplies to the leading and trailing-edge slots gave a dual-blowing capability and tip-jets inside the TE slot reduced spanwise pressure variations.

The aerofoil section was constructed around a rectangular plenum box divided into two chambers by a main spar as shown in Fig.2.2. Sixteen splitter plates maintained the box geometry and the walls were strengthened by cylindrical spacers. Six ribs, bolted either side of the plenum, supported the skin which maintained the elliptic profile. The upper and lower-surface lips were fixed onto the ends of the plenum wall-plates with the blowing slot between the LE and TE tube and the moveable upper-surface lip as shown in Fig.2.3.

The original tubes, including the TE wall-jet traversing mechanism, were replaced with ground stainless steel tubes to produce a smoother surface finish,

thereby reducing the possibility that separation of the wall-jet from the surface would be caused by excessive roughness or probe interference.

The modifications to the tubes included insertion of pressure tappings near mid-span around the LE and TE extending from 18^{o} inside of the blowing slot to 138^{o} around from the slot onto the lower surface, with 6^{o} angular spacing. The tappings were staggered in two rows up to 20mm either side of mid-span with each consecutive tapping offset 2.5mm spanwise to minimise interference downstream. Table 2.1 summarises the exact location of the tappings giving both chordwise and spanwise position together with the angle from the blowing slot around the circular tubes.

Tip-jets suppressed the root vortex formed by the interaction between the endplates and the adverse pressure gradient over the rear half of the aerofoil. These tip-jets were considered to be insufficient with the higher blowing rates which were developed using an increased slot height. On the recommendation of Englar and Williams(24) endplate blowing through slots adjacent to the trailing edge, as shown in Fig.2.4, was adopted.

2.1.2 Tunnel

The dual-purpose wind-tunnel used for the experimental work is shown in Fig.2.5. The tunnel was powered by a 170hp electric motor driving a four-bladed, 3.05m diameter fan. The maximum velocity was 50m/s in the working section and 12m/s in the industrial return section, both of which could be vented to atmospheric pressure.

The model was stored on a false floor below the working section, and hoisted through the removeable floor panel before connecting the blowing supply pipes and pressure tapping tubes.

Free-stream conditions were determined with a Betz manometer, measuring the pressure difference (RPD) along the contraction upstream of the working section.

Tunnel controls, together with all the instrumentation, were located within the operating area as seen in Fig.2.6.

2.1.3 Blowing Supply

The external supply of compressed air was fed to both ends of the model through the tunnel roof and floor as shown in Fig.2.7. The three supply lines were initially connected to the TE plenum chamber, the tip-jets and the endplate blowing supply.

Following some early experimental work, the internal tip-jet plenum chambers were removed and the redundant supply line connected to the LE plenum chamber to investigate the performance with LE blowing.

The compressed air was delivered direct to a settling tank at 5.5 atms. After the main stop valve, the air was filtered and divided into three channels, each independently controlled by Hale-Hamilton RL6D dome valves operated by separate L-15 controllers. The model's main blowing supply was divided between two 50mm bore reinforced pvc-pipes and the mass flow was measured using orifice plates before entering the plenum chamber. The endplate and tip-jet flows (when connected) were transferred to 9mm-bore nylon tubes before entering their respective plenum chambers. Due to the unequal length of these tubes, restrictor valves were inserted to allow for finer spanwise adjustments using the boundary-layer control blowing supply.

2.1.4 Present Experimental Model

The general layout of the model mounted vertically in the working section is shown in Fig.2.8. which gives a view of the upper and lower surface.

Tappings 91 to 94 and 96 to 99 were connected to a multi-tube manometer to check the spanwise pressure distribution. Tappings T5 to T12 on the TE blowing lip, which were used when adjusting the endplate and tip-jet blowing supplies, were also connected in this way. Tappings S1 to S4 on the upper surface and S5 to S8 on the lower surface were used in conjunction with the skin friction measurements as described in section 2.2.5.

For the first experimental session, pressure tappings 1 to 79 were connected to two scanivalves so that only the mid-span pressure distribution was recorded with various blowing conditions, thereby giving an indication of the model's performance. Flow visualization showed strong three-dimensional interference; the internal tip-jet plenum chambers were therefore removed to obtain a clean blowing slot across the complete span of the model.

The second experimental session concentrated on collecting reliable two-dimensional section data for both the pressure distribution and skin friction drag, together with a preliminary investigation of the wake using the rake described in section 2.2.6.

The final experimental session involved extending the work downstream of the model by mounting the rake on a traversing mechanism, disconnecting the model pressure tappings and using one of the scanivalves connected to the rake pressure probes to measure the momentum deficit and flow angle in the wake of the model.

2.1.5 Data Acquisition and Hardware

A diagram of the data acquisition hardware used during the first two experimental sessions is shown in Fig.2.9. The system was controlled by a Hewlett-Packard HP-85 desk-top computer, using a RS-232 serial interface and a HP-IB (IEEE-488) parallel interface bus. An addressable asynchronous receiver/transmitter (AART) positioned the scanivalves, and a dual channel analogue to digital (A/D) converter monitored the pressure transducer outputs.

The 79 pressure tappings around the model centre-line were distributed between the two 48-port scanivalves. Scanivalve 1 contained a 2.5psi Statham transducer which read tappings 5 to 52. Scanivalve 2 contained a 5psi Setra transducer which read the TE pressure tappings 53 to 79 and 1 to 4. The remaining ports were connected to tappings located inside the TE blowing slot, together with tappings S1 to S8 used for skin friction measurements.

The output from the transducers was converted by the A/D into three bytes of information. The first two bytes contained the eight most significant bits (MSB) of data from each channel respectively. The final byte contained the four least significant bits (LSB) from channel 1 and the four LSB from channel 2. Thus 12 bits were available to cover the 10 volt range of

each A/D converter giving an accuracy of 2.44mV per LSB.

The output from each transducer was calibrated regularly during each experimental session. A typical transducer gain of 1mV per N/m^2 resulted in a resolution of 0.25mm of water per LSB.

The sampling rate could be altered by a variable trigger unit which allowed rates from 25 to 200 samples per second. The majority of the scans consisted of 50 samples recorded at 50Hz. This provided a reasonable indication of the mean pressure and a complete scan could be stored within the available memory.

Before starting a scan, the transducer datum was checked at port 0 which was open to atmosphere on both scanivalves. If the offset was more than $10N/m^2$, a correction to the calibration constant was applied and a new datum reading taken. This reduced drift due to variations in ambient temperatures during long running periods. If the RMS of the datum sample was greater than 3mV, the hardware was not sampling properly and data had been lost while transferring through the serial interface. A simple manual resetting of the AART remedied this.

For the final experimental session which concentrated on measurement in the wake of the model, the 0.38m

span rake shown in Fig.2.10 was connected to one of the scanivalves with a 0.5psi Druck transducer.

The rake was positioned horizontally in the working section at the model's mid-span location and 1.4 chord distance downstream of the trailing edge. The location of the 22 total pressure, 4 static pressure and 3 pairs of yaw-head tubes is given in Table 2.2.

The traversing mechanism was located below the working section with a thin slot in the floor for the rake support rod. Movement was limited to across the wake at a fixed spanwise and chordwise location. The yaw heads gave an indication of flow direction and the rake could be rotated if necessary, to point directly into the wake flow.

2.2 MEASUREMENT PROCEDURE

2.2.1 Free-stream Conditions

Measurements upstream as well as along the length of the working section and across the plane level with the drag rake downstream of the model helped to determine the free-stream flow. Entry conditions slightly upstream of the model were considered to be uniform following the results of preliminary calibration work in the empty working section.

The tunnel reference pressure difference (RPD) in mm of water, measured using a Betz manometer connected between two pressure tappings along the upstream contraction, determined the free-stream working section conditions in front of the model.

Calibration in the empty working section using a pitot-static tube on the tunnel centre-line at mid chord location, revealed a linear variation of total pressure given by

$$H = .046 \times RPD \text{ in mm} \qquad - 2.1$$

and for static pressure

$$P = 1.184 \times RPD \text{ in mm} \qquad - 2.2$$

Applying the blockage correction suggested by Pankhurst and Holder(25), p. 334, the blockage factor

$$e_s = (.822/2)(1+c/t)(t/h)^2 \qquad - 2.3$$

where c is chord, h is tunnel height (= 2.1m) and t is the maximum aerofoil thickness; e_s = .00805 and the mid-chord dynamic pressure is

$$Q_{mc} = 1.156 \times \text{RPD in mm} \qquad - 2.4$$

Hence the mid-chord static pressure is given by

$$P_{mc} = 1.110 \times \text{RPD in mm} \qquad - 2.5$$

The longitudinal static pressure gradient in the working section was measured on a sloping multitube manometer using six pressure tappings located along the far side-wall. With the model in the working section, the gradient based on chord length was found to be 4.0% of the dynamic pressure. This gave a chord-wise static pressure correction

$$p' = p + .04(x/c - 0.5)/q_{mc} \qquad - 2.6$$

where p is the measured static pressure on the aero-foil a distance x behind the leading edge.

2.2.2 Jet Blowing Momentum Coefficient

The blowing coefficient C_j is defined as

$$C_j = \frac{\dot{m} V_{jfs}}{q_{mc} bc} \qquad - 2.7$$

The mass flow rate $\dot{m}$ was measured using individually calibrated standard orifice plates as specified in reference (26). The pressure difference across the plates was read using vertical U-tube water manometers permanently connected to each plate.

The jet velocity V_{jfs} is that due to an isentropic expansion from plenum stagnation conditions to free-stream static pressure given by

$$V_{jfs} = (2nRT_o(1 - (p_{fs}/p_o)^{-n}))^{1/2} \qquad - 2.8$$

where n is 3.5 for air. It has become adopted by convention as suggested in reference (24) because of the difficulty in many test situations of measuring the ambient static pressure at the slot.

2.2.3 Pressure Distribution

The 79 static pressure tappings located around the model centre-line are shown in Fig.2.11. They were connected to the data acquisition system using two scanivalves as described in section 2.1.5. The numbering is anti-clockwise around the model as shown, starting with tapping number 1 slightly upstream of the TE blowing lip. Station 0 is a fictitious tapping at the lip, used to pad either end of the pressure integration routine. The table included in Fig.2.11 gives the chordwise position of each tapping. Each scan consisted of a satisfactory datum reading, before stepping both scanivalves simultaneously through ports 1 to 46. A dwell time of 250ms at each port allowed the transducers to settle before sampling for one second.

During the scan, it was necessary to check that the tunnel conditions and the blowing supply remained stable, and to read the pressure difference across the orifice plates and the plenum stagnation pressure and temperature. These values determined the blowing coefficient, C_j, calculated using the relationship described in section 2.2.2.

Following a scan, the program would decode the readings and calculate the mean and RMS values so that data could be stored or analysed immediately.

Before integrating, the static pressure was corrected using equation 2.6 to take account of the longitudinal pressure gradient.

The subroutine to calculate the normal and chordwise force coefficients C_N and C_X divided the surface into 79 panels each extending between the respective pressure tapping locations.

Stepping around the model calculating the resultant normal and chordwise forces, the integration routine placed a cubic curve through the four data points either side of each panel and then integrated across the panel area.

The normal force coefficient C_N was assumed equivalent to the lift coefficient C_L, while the chordwise force coefficient C_X was modified to take account of the pressure across the blowing slot. The slot exit pressure p_s was measured on tapping 79 and corrected using equation 2.6 to give p_s'. The static pressure across the slot is to a first approximation given by

$$p = p_s' - \rho V_j y / R \qquad - 2.9$$

where ρ is density, y the distance normal to the surface, R the radius of curvature of the flow (approximately 25mm) and V_j the jet velocity at the slot found by substituting p_s' for p_{fs} in equation 2.8. Equation 2.9 with $y = h/2$ estimates the mean slot exit pressure p_j at mid-slot height. With $y = h$ then p

approximates to the pressure at the lip which was used to pad the integration routine.

The chordwise force correction term due to the slot exit pressure is given by

$$C_{D_{pj}} = -(p_j - p_{fs})h/q_{mc}c \qquad - 2.10$$

which was found experimentally to be linear against C_j with a slope of 0.21 so that a modified force coefficient taking account of the slot pressure is

$$C_X' = C_X + 0.21C_j \qquad - 2.11$$

Resolving parallel to the tunnel axis takes account of the drag contribution from the normal force and assuming $\cos\alpha_g = 1$ gives the pressure drag coefficient

$$C_D' = C_X' + C_N \sin\alpha_g \qquad - 2.12$$

The inclusion of skin-friction gives the profile drag coefficient

$$C_{D_p} = C_D' + C_f \qquad - 2.13$$

and subtracting the induced drag leaves the sectional drag coefficient

$$C_{D_s} = C_{D_p} - C_{D_i} \qquad - 2.14$$

Englar(27) suggests correcting the sectional drag to take account of the thrust due to the jet blowing momentum defined as

$$C_{D_j} = C_j / \bar{V}_{jfs} \qquad - 2.15$$

where $\bar{V}_{jfs} = V_{jfs}/U_\infty \qquad - 2.15(a)$

so that the drag which relates directly to the momentum deficit in the wake is given by

$$C_{D_w} = C_{D_s} - C_{D_j} \qquad - 2.16$$

Equation 2.16 shows that with high blowing rates the net drag may be negative, representing a thrust component.

The power necessary to produce the kinetic energy of the jet is considered by Englar(28) as an incremental drag coefficient,

$$C_{D_{ke}} = \frac{1}{U_\infty} \frac{d(KE)}{dt} \qquad - 2.17$$

so that a corrected equivalent drag coefficient is

$$C_{D_e} = C_{D_w} + \frac{\bar{V}_{jfs}}{2} C_j \qquad - 2.18$$

Equation 2.18 allows comparison of the lift to drag ratio with conventional aerofoils.

2.2.4 Induced Drag

A major source of error when measuring the drag of CCAs is estimating the effective incidence which is related to the overall lift of the model. Small errors in α_e lead to large variations in the induced drag.

Comparison of the mid-section ($0.2 < x/c < 0.8$) pressure distribution with inviscid potential flow theory allows an estimate for α_e to within $\pm 0.5^\circ$. An example of this is shown in Fig. 2.12 for Run 45 where the theoretical distribution is drawn with $\alpha_e = -3^\circ$ and -5°. A first approximation is $\alpha_e = -4.0^\circ$.

Collecting all the available data and assuming a linear relationship between the induced drag and the lift coefficient squared, where

$$C_{D_i} = C_N \sin \alpha_i \qquad - 2.19$$

resulted in an empirical relationship where

$$C_{D_i} = .082\ C_N^2 \qquad - 2.20$$

as shown in Fig.2.13.

Substituting into equation 2.19 allowed a revised value for the effective incidence since

$$\alpha_e = \alpha_g - \sin^{-1}(.082\ C_N) \qquad - 2.21$$

which for Run 45 led to the modified value of $\alpha_e = -4.1^\circ$. This method gave a grid of effective incidence against lift coefficient with variation of geometric incidence as shown in Fig.2.14.

2.2.5 Skin Friction Measurement

Following a review of available methods given in reference (29) and by Winter(30), the razor blade technique described by East(31) was adopted as a means of measuring the skin friction drag. The method is based on measurement of total pressure close to the surface. The razor blade is placed parallel to the surface with the sharp edge just covering the static pressure tapping hole.

Eight razor blades araldited to pvc-tape were attached to the model surface. This gave a secure hold with the blade mounted 0.2 to 0.4mm above the surface and also allowed easy removal by simply peeling away the tape. The blades designated S1 to S8 were staggered and slightly offset from the centre line as shown previously in Fig.2.8.

The pressure p_r measured at S1 to S8 as part of each scan was subtracted from the adjacent mid-span pressure tapping to determine $(p - p_r)$. Dimensional analysis shows that this difference in static pressure compared with the undisturbed pressure in the boundary layer can be related to the local skin friction as a function of:

h - height of the sharp edge above the surface.

d - diameter of the pressure tapping hole.

l - length.

b - width of the razor blade.

x'- distance of the leading edge of the blade behind the front edge of the hole.

East(31) found that with $b/h > 30$, $b/d > 5$ and $x' = 0$ the relationship was

$$c_f^* = -0.23 + 0.618\ p^* + .0165\ p^{*2} \quad - 2.22$$

where $c_f^* = \log_{10}(c_f' h^2/\rho v^2)$

where $c_f^* = \log_{10}(c_f' h^2/\rho v^2)$ - 2.22(a)

and $p^* = \log_{10}((p-p_r)h^2/\rho v^2)$ - 2.22(b)

The main consideration when adopting this technique was that the change in pressure due to the expected shear stress should be measurable using the pressure transducers.

Considering the model as a flat plate immersed in a turbulent boundary-layer suggested a maximum local skin friction value of about $3N/m^2$. Using equation 2.22 with h = 0.2mm then $(p - p_r)$ is 10mm H_2O which compares favourably with the 0.25mm H_2O resolution of the pressure transducer.

Experimental verification of equation 2.22 using an annular calibration tunnel suggested a slightly modified relationship as shown in Fig.2.15. The experimental points compare two similar razor blades with h varying from .075 to .312mm.

The variation of the curve from that of East is probably due to slightly different blade geometry.

East found that if $x'/h < 0.5$ then the error in measuring pressure was less than 5%.

The calibration work gave a linear relationship of the form

$$c_f^* = 0.85p^* - 1 \qquad - 2.23$$

Equation 2.23 shows that a 10% error in measuring h leads to a 3.0% error in the value of c_f'. Similarly a 10% error in $(p - p_r)$ leads to a 8.5% error in c_f'.

2.2.6 Wake Traverse

Measurement in the wake of the model was performed using the 0.38m span rake described in section 2.1.5. The static probes were calibrated with respect to an adjacent wall tapping, which was used as a datum to eliminate fluctuations in free-stream static pressure due to slight variations in tunnel conditions during each run.

A scan consisted of first moving the rake into position using the traversing mechanism. Following a check on the atmospheric datum at scanivalve port 0, the transducer measured the static reference pressure, the four static probes and the three pairs of yaw head tubes. There was then a new datum check before scanning the 22 total pressure probes. The duration of a scan was about one minute and typically another minute was required to reposition the rake and check the tunnel conditions before continuing. Between three and seven scans were necessary to satisfactorily define the wake distribution, with the rake moved 12.5mm (1/2") between each scan.

Calculation of the drag coefficient from the measured total and static pressure in the wake was derived using equation 2.24 proposed by Jones(32)

$$C_{D_r} = \int_{wk} C'_{D_r} \, d(y/c) \qquad - 2.24$$

where the integral is across the wake and

$$C'_{D_r} = 2(g - p)^{1/2}(1 - g^{1/2}) \qquad - 2.24(a)$$

$$g = \frac{H_{wk} - H_{fs}}{Q_{fs}} \qquad - 2.24(b)$$

$$p = \frac{P_{wk} - P_{fs}}{Q_{fs}} \qquad - 2.24(c)$$

Equation 2.24 is a simplified expression based upon earlier work by Betz(33). Both methods are discussed by Schlichting(34) pp. 758-762 and have proved to be satisfactory when determining profile drag for both in-flight and wind-tunnel measurements. The rake coefficient C_{D_r} represents the momentum deficit of the fluid in the wake of the model and is assumed equivalent to the wake drag coefficient C_{D_w} defined in equation 2.16.

The method of Jones was checked by traversing in the wake of a cylinder, which was mounted vertically in the tunnel with one end fixed through the roof to the drag balance above the working section as shown in Fig.2.16. The free end of the cylinder was just clear of the tunnel floor so that the effective two-dimensional drag per unit span C_{D_b} could be measured directly from the balance reading.

Three runs labelled CRUN-1 to 3 were recorded with free-stream velocities similar to the proposed CC-model testing conditions. The results are summarised in Table 2.3. CRUN-2 is at a slightly higher tunnel speed compared with CRUN-1 while CRUN-3 is a repeat of CRUN-2.

Reynolds number R_d is based on the diameter d (= 41.1mm) and the column b'/d represents the wake width as defined later in equation 2.25(c). As shown in the table, slight variation in C_{D_r} was possible depending upon where one chose to place the wake limits y_1 and y_2. In general a 5% error in determining the wake width could result in a 1% error in C_{D_r}.

The drag coefficient $C_{D_r} = 1.1$ is as expected from published two-dimensional cylinder data. (Refer, for example, to Hoerner(35) p. 3-9). In practice the drag measured using the balance should be slightly less than that derived from the rake measurements because the boundary-layer along the tunnel roof and floor lead to a reduced effective aspect ratio for the cylinder. The percentage difference of 5-7% shown in column 4 for CRUN-2 and 3 merely reflects that C_{D_b} does not directly equate with C_{D_r}. As discussed below, the optimistic value for CRUN-1 is within the proposed mean error of the measurement method, but may also be due to Reynolds number effects.

The total pressure distribution for CRUN-3 is seen in Fig.2.17, which shows the raw data points for each of five scans as well as a calculated mean distribution and an empirical relationship within the wake of the form

$$H_{wk} = H_{pk} \cos^{2.6}(\pi (y-y_o)/b') + H_{fs} \quad - 2.25$$

where

$$H_{pk} = H_{max} - H_{fs} \quad - 2.25(a)$$

$$y_o = (y_1 + y_2)/2 \quad - 2.25(b)$$

$$b' = (y_2 - y_1) \quad - 2.25(c)$$

The static pressure distribution shown in Fig.2.18 is defined empirically in terms of the measured mean pressure within and outside of the wake.

The linear relationship

$$P_{wk} = \text{constant} = P_{mean} \quad - 2.26(a)$$

is compared with the empirical relationship

$$P_{wk} = 1.8(P_{mean} - P_{fs})\cos^2(\pi (y-y_o)/b') + P_{fs} \quad - 2.26(b)$$

Considering CRUN-3 and substituting the measured mean total distribution into equation 2.24(b), and equation 2.26(a) into equation 2.24(c) results in a drag coefficient $C_{D_r} = 1.141$ which compares with the balance drag $C_{D_b} = 1.065$. Applying equation 2.26(b) instead leads to an almost negligible increase in C_{D_r} of less than 1%. This suggests that using a mean

static pressure across the wake is perfectly reasonable. However, note that the table does not show that a 5% error in measuring the static pressure results in a 4% error in C_{D_r}.

The preceding discussion shows that the proposed wake traverse method was consistent and adequate for the proposed CC-drag investigation and that, provided care was employed in measuring the static pressures, accuracies to within 3 or 4% were possible.

Finally, observation of the flow angle shown in Fig.2.19 for CRUN-2 reveals a characteristic shape due to the reduced static pressure within the wake causing the flow to move towards the centre-line. Again, under such steady conditions, a resolution to within $\pm 0.1^{o}$ was possible.

3. EXPERIMENTAL RESULTS.

3.1 INTRODUCTION

The following chapter describes a selection of the results from the experimental work. These were obtained using the 20% elliptic CC-model at Bath University which is described in chapter 2.

The objectives of the work were:

(1) To obtain detailed pressure measurements around the trailing edge (TE) in the vicinity of the separation region.

(2) To integrate the mid-spanwise pressure distribution around the model and determine the lift and drag components of the resultant force.

(3) To measure the skin-friction distribution with respect to chord location and thus obtain an estimate for the skin friction drag coefficient C_f.

(4) To measure the momentum deficit in the wake of the model and compare the rake drag C_{D_r} (see equation 2.24) with the resultant wake drag coefficient C_{D_w} (see equation 2.16).

The work involved:

(1) Modification of the original model used by Wood(15).

(2) Development of an "on-line" data acquisition and analysis system for taking pressure measurements around the model and downstream in the wake.

(3) Investigation of skin friction measurement techniques and calibration of both razor blades and Preston tubes using a small annular calibration tunnel.

(4) Calibration of orifice plates used to measure the mass flow into the model's plenum chamber.

(5) Calibration of various pressure transducers used with the scanivalves.

(6) Calibration of the empty tunnel working section.

(7) Development of a method for reducing spanwise flow variations using endplate blowing.

(8) Flow visualization using titanium-dioxide in oil and paraffin to reveal both endplate interference effects and surface streamline patterns around the model.

(9) Development and calibration of a rake with total pressure, static pressure and yaw head tubes, mounted on a manually operated traversing mechanism located downstream of the model.

Section 3.2 presents the results of measurements on the model with no blowing, then TE blowing only and finally LE blowing only.

The RUN numbers were recorded in chronological order. Not all are included as some were repeats of previous conditions to check the consistency of the data and measurement technique.

Section 3.3 covers results from measurements made in the wake of the model and the presentation is limited to a selection of the results available. These are labelled as DRUN with numbering in chronological order.

Section 3.4 presents the overall performance of the model for lift, drag and pitching moment. It includes a comparison between the drag measured around the model (C_{D_w}) and drag using the rake (C_{D_r}).

The notation used with the graphic presentation of the results has had to be slightly modified due to limitations of the plotting routine - suffices and greek symbols were not available. A revised notation list is not included because the alterations should be self-explanatory.

The graphs when subdivided into quadrants are labelled alphabetically reading from left to right with (a) as top left and finally (d) as bottom right.

3.2 MODEL MEASUREMENTS

3.2.1 No Blowing (Figs.3.1 to 3.3 and Table 3.1)

The mean experimental pressure distribution is plotted against chord x/c% in Fig.3.1 with the model at four different geometric incidences. Comparison is made with theoretical potential flow for a pure 20% ellipse. There are irregularities due to the model having rounded leading and trailing edges, and the presence on the upper surface of the LE and TE blowing slots. An alternative presentation is shown in Fig.3.2 where the pressure distribution is plotted with respect to the distance normal to the chord line.

The skin friction in Fig.3.3 shows transition from laminar to turbulent boundary-layer by a sharp increase in the local coefficient of skin friction with $c_f' < .002$ representative of a laminar boundary-layer. A turbulent boundary-layer with an adverse pressure gradient eventually leading to separation is shown by a gradual decrease in c_f', for example the upper surface distribution in RUN-65 shown in Fig.3.3(d).

3.2.2 TE Blowing Only

3.2.2.1 TE Blowing at 0^{o} (Figs.3.4 to 3.7 and Table 3.2)

The empirically derived effective incidence (see equation 2.21) in conjunction with the measured normal force coefficient shows a good agreement between the experimental and theoretical pressure distribution in the region $0.2 < x/c < 0.8$ as seen in Fig.3.4. The same pressure distribution plotted against normal distance y/c% is shown in Fig.3.5.

The TE mean pressure plots show details around the TE wall-jet measured in radians from the lip. The RMS pressure distribution is included below each plot. The magnitude along the vertical axis in N/m^2 is dimensional which means that direct comparison between runs is inappropriate due to variation in free-stream dynamic pressure.

In Fig.3.6(a) for RUN-48 the pressure distribution around the TE wall-jet is too weak to be distinguished by its characteristic peak. This starts to develop in Fig.3.6(b) with a slightly higher blowing coefficient. The respective RMS plots are shown in Figs.3.6(c) and (d). In Fig.3.7 the peak in the TE RMS pressure for RUN-46 and RUN-44 reflects the disturbed nature of the wall-jet/boundary-layer interaction in the vicinity of separation.

The results are summarised in Table 3.2. There is no data for the skin friction distribution as the razor blades were not mounted to the model before RUN-49.

3.2.2.2 TE Blowing at -6.8^{o} (Figs.3.8 to 3.12 and Table 3.3)

The pressure distribution at negative geometric incidence is shown in Figs.3.8 and 3.9 with details of the TE pressure in Figs.3.10 and 3.11. In Fig.3.12 one must be wary of direct comparison of the skin friction due to changing Reynolds number, R_c: RUN-56 and RUN-59 were at similar values. The reduced Reynolds numbers for RUN-57 and RUN-58 favour a laminar boundary-layer. Despite these limitations on the results it is evident from Fig.3.12 that, as would be expected, increased TE blowing stabilises the upper surface boundary-layer and draws the point of transition downstream. The lower surface seems to be relatively unaffected.

3.2.2.3 TE Blowing at $+3.7^{o}$ (Figs.3.13 to 3.16 and Table 3.4)

Results with a positive geometric incidence are limited to one unblown case RUN-69 and two blown cases RUN-74 and RUN-73. Figure 3.13 shows the experimental mean pressure distribution which is in good agreement with the potential flow distribution. In Fig.3.14 the pressure is plotted against distance normal to the chord line. Figure 3.15 shows an irregular TE pressure distribution suggesting spanwise variations due to the

alternate spacing of the pressure tappings which has already been discussed in section 2.1.1.

The skin friction distribution is shown in Fig.3.16. The upper surface experiences an adverse gradient and is "tripped" by the protruding LE blowing slot so that the boundary-layer is completely turbulent throughout.

The lower surface is more susceptible to variation of free-stream Reynolds number and TE blowing coefficient. In Fig.3.16(a) with no TE blowing, transition on the lower surface occurs near $x/c = 0.4$. In Fig.3.16(b) with $C_j = .015$ the lower surface skin friction distribution is unchanged. In Fig.3.16(c) with $C_j = .028$ the same distribution has become completely laminar. This is partly due to the 16% reduction in free-stream Reynolds number and partly due to the blockage effect of the TE wall-jet as it moves further around onto the lower surface before separating downstream.

3.2.3 LE Blowing Only

3.2.3.1 LE Blowing at 0^{o} (Figs.3.17 to 3.21 and Table 3.5)

Figure 3.17 shows the mean pressure distribution with LE blowing. The effect on the lifting performance of the model is negligible as the LE wall-jet has limited influence on the pressure distribution beyond $x/c = 0.1$.

Fig.3.18 shows that the LE wall-jet moves onto the lower surface and removes the LE stagnation point resulting in a net reduction of the drag coefficient C_X. The LE pressure distribution in Figs.3.19 and 3.20 shows considerable spanwise variation with the alternate positioning of the pressure tappings highlighted by joining with a solid and a dashed line respectively.

In Fig.3.21 the LE blowing disrupts the laminar boundary-layer over the front part of the model thus increasing the skin friction drag coefficient C_f. There is small change in skin friction distribution with increased blowing.

3.2.3.2 LE Blowing at 3.7^{o} (Figs 3.22 to 3.26 and Table 3.6)

With a positive geometric incidence the LE wall-jet is distinguished by the return of a LE stagnation point where $C_p = +1$. This is shown in Fig.3.22 and more

clearly in Fig.3.23 when plotted against distance normal to the chord line.

The LE distribution for the no blowing case in RUN-69 (Fig.3.24(a)) shows a smooth mean-pressure distribution with stagnation at s/R = 1.6 radians from the LE blowing slot and a continuous low RMS pressure distribution. The LE pressure distribution for RUN-71 in Fig.3.24(b) shows a reversed LE wall-jet with a spanwise variation of the separation point. The solid line shows an increasing pressure coefficient, with the RMS distribution suggesting LE separation close to the blowing slot at s/R = 0.3. The dotted line joining tappings at a slightly different spanwise location (moved 3.3% of the total span) shows a decreasing pressure coefficient with a peak $C_p = -1.0$ at s/R = 0.4 where the wall-jet is still attached and LE separation occurs slightly further around at s/R = 0.5. For RUN-70 in Fig.3.25(a) and (c) one again needs to consider the alternate spacing of the tappings in order to interpret the results. The smooth curve for RUN-72 in Fig.3.25(b) is probably due to fortuitous location of the pressure tappings relative to the spanwise variation of the LE separation line.

The skin friction measurements in Fig.3.26 show that with the LE wall-jet folding back along the upper surface there is small change in the lower surface

distribution with increased LE blowing. Transition is maintained at about one-third of the distance along the chord. The upper surface is initially turbulent for the unblown case in RUN-69 and, though the measured skin friction is reduced when the LE blowing is applied, the upper surface boundary-layer is probably turbulent for all four cases shown in Fig.3.26.

3.3 WAKE MEASUREMENTS

3.3.1 No Blowing (Figs.3.27 to 3.30)

Results from one of three wake traverses behind the unblown model at zero geometric incidence are shown in Fig.3.27 for DRUN-6. The total pressure in mm of water below atmosphere is plotted against the normal distance measured as a percentage of the chord length from the tunnel centre line. The data collected during seven scans, with the rake moved 12.5mm (1/2") between each, defines a mean distribution with an upper and lower wake limit, similar to the method described in section 2.2.6 for the cylinder. The table of experimental results includes the assumed total pressure H_{fs} across the wake in absence of the model. This is calculated as the mean of four readings (two either side) adjacent to the wake limit. The width b' is given as a fraction of the chord. The lift coefficient is calculated by measuring the difference in pressure between the mid-chord tappings on the upper and lower surface of the model and using the empirical relationship,

$$C_L = 1.44(C_{P_l} - C_{P_u}) \qquad - 3.1$$

The static pressure for DRUN-6 is plotted on a similar scale to the total pressure and shown in Fig.3.28. The results measured, using four static pressure probes on

the rake, show a slight reduction in pressure within the wake. The algorithm for the integration routine to calculate the drag coefficient C_{D_r} assumes a constant distribution as shown by the dotted line, where the experimental points are used to calculate a mean static pressure in the wake (P_{wk}) and in the free-stream (P_{fs}).

Total pressure profiles with variation of geometric incidence are shown in Fig.3.29 for increments of 2.5^{o} from -7.5^{o} to $+7.5^{o}$. The peak reading represents a loss in total pressure equivalent to about 15% of the dynamic pressure which was maintained relatively constant at 73mm of water.

Fig.3.30 shows the flow angle across the wake with model incidence at -7.5^{o}, 0^{o} and $+7.5^{o}$. The positive flow angle depicts streamlines moving from the upper-surface side towards the lower-surface side. The slight offset from zero for DRUN-6 is due to the rake not being exactly aligned with the free-stream. The reduced static pressure in the wake induces flow towards the wake centre-line thus increasing the angle at the upper wake limit and reducing it at the lower limit. For DRUN-6 this variation was 1^{o} while for DRUN-30 it was about 3^{o}.

3.3.2 TE Blowing Only

3.3.2.1 TE Blowing at 0^{o} (Figs.3.31 and 3.32)

The variation of the mean total pressure distribution across the wake with increasing TE blowing coefficient is shown in Fig.3.31.

The mean wake static pressure increased from 77.6mm of water below atmosphere to 80.4mm with maximum TE blowing. However, the non-dimensional wake static pressure remained constant so that,

$$\bar{p}_{wk} = P_{wk} / Q_{wk} = 1.040 \pm .005 \qquad - 3.2$$

Fig.3.32 presents the variation of the flow angle across the wake showing movement to the side, and increased flow angle at the traverse plane with increased TE blowing.

3.3.2.2 TE Blowing at -5^{o} (Figs.3.33 and 3.34)

Fig.3.33 shows the mean total pressure across the wake with the model at -5^{o} geometric incidence. The flow angle is shown in Fig.3.34.

3.3.2.3 TE Blowing at -7.5^{o} (Figs.3.35 and 3.36)

Fig.3.35 shows the mean total pressure across the wake with the model at -7.5^{o} geometric incidence. The flow angle is shown in Fig.3.36.

3.4 OVERALL PERFORMANCE

3.4.1 No Blowing

The lift performance of the unblown model is shown in Fig.3.37 and comparison is made with earlier work by Wood(15) and the two-dimensional lift-curve slope predicted by Hoerner(35). The slight increase in lift-curve slope when compared with the work by Wood reflects the improved efficiency of the end-plate blowing slots.

Comparison between the wake drag coefficient C_{D_w} and rake drag coefficient C_{D_r}, both plotted against geometric incidence, is shown in Fig.3.38. Both methods include some scatter, but their similarity suggests an accuracy in C_D to within ± 0.002 with a minimum drag coefficient $C_{D_o} = .0120$ at -2^o geometric incidence. The offset is due to the asymmetric contour of the model with upper-surface blowing slots. The skin friction component represented about 40% of the minimum drag coefficient.

3.4.2 TE Blowing Only

The lift performance of the 20% elliptic CCA with TE blowing is shown in Fig.3.39 for geometric incidence of -6.8^{o}, 0^{o} and $+3.7^{o}$. With TE blowing coefficient limited to 0.05, the measured maximum lift coefficient of 1.2 is well below stall. Comparison is made with the work by Wood(15) on the same model with two lower slot heights both at zero geometric incidence. The reduced performance for the present investigation agrees with the speculation by Wood that an optimum slot height to chord ratio for this specific model is about .0020. The graph highlights the benefit of a smaller slot height for obtaining larger augmentation rates. Wood measured dC_N/dC_j up to 70 at the lowest slot height, compared with 36 for the present investigation.

The mid-chord pitching moment is shown in Fig.3.40 plotted against lift coefficient with variation of geometric incidence. The unblown model shows the conventional characteristic of positive (nose-up) pitching with increased angle of attack. TE blowing has a nose-down influence thus increasing the moment about the elastic axes for CCAs when operating at negative geometric incidence. The linear relationship shows the independance between pitching moment due to geometric incidence and that due to blowing.

Fig.3.41 shows the centre of pressure location due to TE blowing. The limited movement (<3% of chord) suggests that it is almost independent of both geometric incidence and blowing coefficient. Note that it is important to distinguish between the centre of pressure due to blowing and that due to geometric incidence.

3.4.2.1 TE Blowing only at 0^{o}

Fig.3.42 shows a direct comparison between the wake drag and rake drag coefficients plotted against TE blowing coefficient for the model at zero geometric incidence.

3.4.2.2 TE Blowing only at -6.8^{o}

Fig.3.43 summarises the drag results for the model with TE blowing at negative geometric incidence. The rake measurements at -5^{o} and -7.5^{o} show a slight decrease in drag with increased blowing rate. The wake drag measured at -6.8^{o} reveals a slightly spurious scatter which is discussed further in section 5.3.

3.4.3 LE Blowing Only.

In Fig.3.44 comparison is made between the LE and TE blowing performance. Figure 3.44(a) shows that the LE wall-jet alone does not produce any significant lift. However, Fig.3.44(b) shows that it does reduce the chordwise force C_X and increases the mid-chord pitching moment as shown in Fig.3.44(c). The effect of the TE wall-jet alone is also shown (but at a different slot height).

The performance with the model at $+3.7^{\circ}$ is similarly shown in Fig.3.45. The mid-chord moment in Fig.3.45(c) reveals an unexpected reduction with increased LE blowing. This is discussed further in section 5.4.1.

4. THEORETICAL DISCRETE VORTEX MODEL.

4.1 INTRODUCTION

The model presented in this section has been developed from the original concept suggested by Smith(21) for a circular cylinder with a blowing slot at top dead centre (TDC). Discrete vortices, with a strength related to the blowing coefficient, are shed sequentially from the lip with a frequency determined by the time-step of the program. Before each time-step, image vortices of equal but opposite strength to their respective external vortices are located so as to maintain zero flow across the surface boundary. The velocity vector at each external vortex is calculated by summing the induced velocity due to the remaining vortices and the free-stream potential flow. The external vortices are then relocated, assuming a constant velocity during the time-step. A new vortex is shed from the lip, and respective image vortex location and strength are calculated before continuing with the next time-step.

The earliest reference to modelling a shear layer by discrete vortices was made by Rosenhead(36) when dealing with the Helmholtz instability of two parallel streams flowing in opposite directions. Extension of this work was later performed by Birchoff(37) and Hama(38).

Smith(21) gives a brief history of discrete vortex modelling with numerous references showing that the technique has been used in treating a variety of two-dimensional shear layer problems. He showed that when applied to the prediction of the Coanda flow due to a wall-jet on a circular cylinder, the vortex development approached a steady-state condition. He predicted the blowing momentum coefficient by considering the induced velocity on the surface at the slot, and the lift coefficient by finding the point of zero induced velocity around the trailing edge (TE) surface. Artificial viscosity and a time-dependent vortex decay rate helped to stabilise the vortex development and simulated the dissipative effects encountered in real fluids.

Performance was comparable with the experimental work of Levinsky and Yeh(5) indicating that the technique was essentially correct. However, semi-empirical determination of the decay rate detracted from the initial simplicity of the model.

4.2 MODEL DEVELOPMENT

4.2.1 The Starting Process.

The experimental work by Wood(15) suggested that under certain blowing conditions the vortex sheet, formed at the lip due to the shear between the jet and upper-surface boundary-layer, was rapidly broken down and rolled up to form discrete vortices as shown in Fig.4.1(a).

Considering a slot height h, with a blowing coefficient C_j resulting in a jet velocity V_j then

$$C_j = \dot{m}(V_j - V_p)/q_\infty c \qquad - 4.1$$

where m is the mass flow rate in kg/s per unit span and V_p the free-stream potential flow velocity at the lip. Expanding equation 4.1 and considering incompressible flow where the free-stream and jet exit densities are equal, leads to

$$\bar{V}_j = (\bar{V}_p + (\bar{V}_p^2 + 2C_j/\bar{h})^{1/2}) \; / \; 2 \qquad - 4.2$$

For a cylinder with a blowing slot at TDC, $\bar{V}_p = 2$ and equation 4.2 becomes

$$\bar{V}_j = 1 + (1 + C_j/2\bar{h})^{1/2} \qquad - 4.2(a)$$

where the $\bar{}$ denotes a non-dimensional form so that

$$\bar{V}_j = V_j \; / \; U_\infty \quad \text{and} \quad \bar{h} = h/c$$

Let s be the length of the vortex sheet before breaking down to form the first discrete vortex, which is relocated at the lip as shown in Fig.4.1(b).

The induced velocity due to the adjacent image vortex is

$$V_i = \gamma_o / (2\pi.2h) \qquad - 4.3$$

where γ_o is the strength of the first vortex and 2h an approximation to the distance between this vortex and its image.

The starting length s can be related to the time-step Δt by

$$s = (V_p + V_i)\Delta t \qquad - 4.4$$

Defining the excess jet velocity by

$$V_e = V_j - V_p \qquad - 4.5$$

and assuming that the vorticity along the sheet is rolled into a concentrated vortex, then

$$\gamma_o = V_e\, s \qquad - 4.6$$

Substituting frequency f, with the inverse of time step $(1/\Delta t)$ and for convenience using an equivalent frequency velocity

$$V_f = 4\pi h f \qquad - 4.7$$

leads to

$$\gamma_o = V_p \frac{V_e}{(V_f - V_e)} \frac{V_f}{f} \qquad - 4.8$$

hence relating vortex strength with frequency.

The relationship between the vortex core size r_o and the starting length s is critical in determining the frequency f. The simplest relationship satisfying the boundary conditions is

$$\frac{r_o}{s} = \text{constant} = k \qquad - 4.9$$

where the core diameter ($2r_o$) is equivalent to the lip thickness d.

The resulting relationship for frequency has two terms

$$f = \frac{kV_p}{r_o} + \frac{V_e}{4\pi h} \qquad - 4.10$$

where the first term is considered to be a threshold frequency dependent upon free-stream velocity and slot geometry. The second term is a function of blowing strength and slot height.

Fig.4.2 shows the relationship of frequency for blowing coefficient up to 0.5 at U_∞ = 44m/s. The three plots are with k = 0.35, 0.30 and 0.25. Each shows variation with slot height (1, 2 and 3mm) and initial core radius (0.4, 0.6 and 0.8mm). Preliminary work revealed that with $k > 0.4$ the vortices started pairing unrealistically close to the lip, and with $k < 0.2$ the spacing was so large that pairing was not initiated during the intended development of the vortices downstream.

Increasing slot height h, and lip thickness d, hence r_o, decreases the shedding frequency. With increasing slot height the frequency augmentation rate df/dC_j is reduced. At low slot heights the frequency becomes unrealistically high for the proposed flow regime and it is suggested that the stability of the vortex sheet increases due to the proximity of the surface, thus delaying the roll up into discrete vortices and altering the condition set by equation 4.9.

4.2.2 Vortex Growth and Pairing

The strength of the vortices is determined by an exponential time dependent decay as suggested by Smith(21) with

$$\gamma = \gamma_0 \exp(-Kt) \qquad - 4.11$$

where K is a decay rate constant and t, the age of the vortex in seconds.

The core size is calculated assuming a conservation of angular momentum H, so that

$$H = \gamma_o r_o^2 = \gamma r^2$$

and $$r = r_o \exp(Kt/2) \qquad - 4.12$$

Eventual overlapping of the vortices starts a pairing process involving a summation of the cross-sectional core area and again conservation of angular momentum.

For pairing between the j^{th} and $j+1^{th}$ vortex the new radius r' is given by

$$r' = (r_j^2 + r^2_{j+1})^{1/2} \qquad - 4.13$$

and new strength by

$$\gamma' = (\gamma_j r_j^2 + \gamma_{j+1} r^2_{j+1})/r'^2 \qquad - 4.14$$

The new position is such that the distance to the new vortex location x' is inversely proportional to the original radii for both vortices; if x is the distance from a colinear datum then

$$x'r' = (x_j r_j + x_{j+1} r_{j+1}) \qquad - 4.15$$

4.2.3 Lift Prediction

It is shown in Appendix A section 8.1.3 that the circulation about a cylinder due to a discrete vortex pair is equivalent to the image vortex strength $\gamma m^2/s$. The total circulation due to blowing can therefore be related to the sum of the image vortices within the flow-field so that

$$\Gamma = \sum_{i=1}^{n} \gamma_i \qquad - 4.16$$

Remembering the relationship $L = \rho U_\infty \Gamma$

then

$$C_L = \frac{2\Gamma}{U_\infty c} \qquad - 4.17$$

and the lift coefficient due to blowing can be expressed independently of incidence effects as,

$$\Delta C_{L_{blowing}} = \frac{2}{U_\infty c} \sum_{i=1}^{n} \gamma_i \qquad - 4.18$$

4.3 PERFORMANCE OF A CYLINDER WITH CIRCULATION CONTROL

For comparison with the experimental work by Levinsky and Yeh(5) calculations were made for a condition where vortices were shed from the lip of a cylinder, with radius 76.2mm and a slot at its top dead centre of height 1.14mm, in a horizontal free-stream velocity of 44.2m/s.

Equation 4.2 with $\bar{h} = h/2R = .0075$ limits C_j to 0.5 for subsonic slot flow. Equation 4.10 shows that with a starting length s equal to the slot height, the threshold frequency is 76kHz increasing to 91kHz with maximum blowing coefficient. The initial vortex strength from equation 4.8 is 0.25 m^2/s, resulting in an induced surface velocity at the slot of 200m/s.

Fig.4.3 shows the external and image vortex distribution after 20 time-steps for a blowing coefficient of 0.2 and a shedding frequency of 85kHz. The slot surface velocity is 211m/s and the vortex strength, $0.14m^2/s$. The vortex path curls to form the characteristic "starting vortex" which is carried downstream before a steady-state solution is reached.

The programme continues shedding vortices and after each time-step checks the vortex spacing. The pairing process described in section 4.2.2 starts when adjacent vortices overlap. The distribution after 500 time-steps is shown in Fig.4.4.

Pairing results in a rapid dissipation of the vortex strength thus reducing the significance of the vortices. As these disappear downstream of a cut-off line they are removed from the computation. The downward slope of the vortex path is due to the induced velocity from the starting vortex which has only just passed the cut-off line. The stabilised distribution immediately downstream of the slot is shown in Fig.4.5(a) for comparison with Fig.4.3. The vortex strength and growth in core size is shown in Figs.4.5(b) and (c): Z is the distance along the vortex path from the lip.

Fig.4.5(d) summarises the results after 500 iterations. The six digit run-number (542035) describes the main variables. Reading from left to right the first digit is the number of iterations in hundreds (e.g. 5 for 500). The second digit represents the free-stream velocity (all runs with 4 were at 44.2 m/s). The next two digits (20) show the blowing coefficient 0.20. The final two digits describe the starting length ratio 0.35.

During the first 5.9ms, (500 time-steps) there were 346 pairings, leaving 93 vortices distributed downstream with a summed strength of $9.98 m^2/s$. The remaining 61 vortices had passed the cut-off line.

A steady-state solution is approached after 9.4ms (800 time-steps) as shown in Fig.4.6 for run 842035. The vortex path is aligned with the free-stream having recovered from earlier influence by the starting vortex which was still evident after 500 iterations. The circulation due to the remaining 89 vortices is 9.82 m^2/s which from equation 4.20 predicts a lift coefficient of 2.91. The steady-state distribution of vortex strength and core size is shown in Fig.4.7(a). The spikes show that pairing is not instantaneous but depends on a semi-random sequence with some vortices remaining single for longer than others. Fig.4.7(b) shows the resulting growth in vortex size representing the breakdown of the discrete vortex structure to a large scale eddy flow in the wake.

Before the final iteration the model is "seeded" with a passive point grid. The velocity and direction is calculated at each passive point and plotted as pressure coefficient and flow angle with respect to the adjacent surface. The grid consists of 75 points in three rows of 25 each. The radial distances are one, two and three slot heights from the surface, starting at 70^o from the lip with an angular spacing of 2.5^o up to 130^o.

Fig.4.7(c) shows the pressure coefficient for the three rows adjacent to the surface. The TE separation point where $C_p = +1$ has moved 1.5^o onto the lower surface. The lower surface distribution is due to free-stream potential flow while the upper surface shows a reduction in C_p due to the induced vortex velocity.

Fig.4.7(d) shows the flow angle with respect to the adjacent surface. The lines represent the three grid rows, and depict the flow which changes from being almost parallel with the surface before separation, to moving perpendicularly and finally to being in a reversed orientation with respect to the TE on the lower surface. The small movement of the stagnation point reflects the early breakdown of the vortices due to pairing, which started about 67^o from the lip.

Fig.4.8 shows the effect of increasing the blowing coefficient to 0.3 with the stagnation point moving about 3^o on to the lower surface.

Fig.4.9 shows performance after 500 iterations with k varying from 0.30 to 0.38 and with blowing coefficient up to 0.3. Comparison is made with the experimental work of Cheeseman(3) and Levinsky and Yeh(5). The accompanying table summarises the results showing also the shedding frequency and the initial vortex strength predicted by the model.

The overall performance of the cylinder with a fixed starting length ratio k = .35 is shown in Fig.4.10. At the two lowest blowing rates of C_j = 0.1 and 0.2 only a minor change is achieved by extending the number of iterations beyond 500. The effect of 800 iterations is shown with C_j = 0.2 to produce .05 reduction in C_L. With C_j = 0.3 the model required 800 iterations to reach a steady-state solution. Finally with C_j = 0.4 predicted C_L is above the extrapolated curve. The vortex development shown in Fig.4.11 reveals incomplete breakdown of the vortex structure.

The performance results are limited in scope and more work is required to reduce the computation time and clarify the relationship between vortex size, strength and frequency. However, they represent an extension of the work by Smith(21) and are an attempt to impose physical constraints on a theoretical concept thereby extending its application into an engineering environment. The work provided experience in methods of stabilising vortex models and result presentation. It was also a useful stepping stone for developing the theoretical model applying to elliptic aerofoils which is described in the next section.

4.4 PERFORMANCE OF AN ELLIPSE WITH CIRCULATION CONTROL

The effect of vortex shedding from an elliptic aerofoil was investigated by first considering the potential flow around a cylinder, and then using conformal transformation to calculate the equivalent flow around an ellipse. A programme listing together with explanatory comments is given in Appendix B section 8.2.

The vortices were shed into the potential flow from the lip located at 96.5% chord. Positioning of the image vortices was slightly modified due to the changing curvature, the criterion being that the line joining the external vortex with its image was perpendicular to the surface at the point of intersection. The radial distance was then calculated by extending this line to the x-axis and using the relationship $R^2 = R_i.R_j$ where R is the distance from the x-axis intersection to the surface and R_i, R_j are the respective distances to the image and external vortex.

The equation for predicting the vortex strength and frequency is described in section 4.2. Using the present experimental model as an example with a typical slot height to chord ratio of .0012 and a blowing coefficient of 0.02 in a tunnel free-stream of 30m/s leads to a slot exit velocity of 120m/s.

The free-stream potential flow at the lip is about 40m/s and with a starting length equal to the slot height, this leads to a threshold frequency of 65kHz.

The elliptic model DVM-ellipse was developed with a slot to chord ratio of .00125 based on a 20% ellipse with chord .6096m (24") and at a free-stream velocity of 30m/s. The preliminary work with a starting ratio of 0.35 and a core radius of 0.2mm (representative of the lip thickness), led to premature pairing. Reducing the starting ratio to 0.25 resulted in a shedding frequency of 45kHz at a blowing coefficient of $C_j = 0.01$.

The numbering of the elliptic model is similar to that used for the cylinder model. For run number "330125" the first digit "3" represents 300 iterations, the second digit "3" shows that the free-stream velocity was 30m/s. The next two digits "01" describe the blowing coefficient $C_j = 0.01$ and the final two digits "25" show that the starting ratio $k = 0.25$.

Fig.4.12 shows the vortex development downstream of the elliptic CCA after 300, 400 and 500 iterations. Fig.4.12(a) exhibits two classic features of discrete vortex models; the rolling up of the tail end into a "starting vortex", and the tendency of the path to curl into a S-shape. This is a characteristic mode of

instability leading to possible breakdown of the vortex path.

The programme gradually removes the older vortices by checking, after each time-step, the vortex path and removing the last vortex if the path extends beyond the cut-off line. The position of this line is estimated by considering the breakdown of the vortices. Locating the line too close to the model results in the premature removal of vortices which still influence the TE flow pattern. Locating the cut-off line too far downstream leads to unnecessary computation.

After 500 iterations (about 11.1ms) the model has reached a steady-state solution with the vortex path separating from the lower surface.

An extension of the passive point grid technique discussed in section 4.3 is shown in Fig.4.13. The grid is distributed about X_{TE} in four rows with angular spacing of 5^{o}, starting 20^{o} above the TE. Row 1 is on the ellipse surface and the remaining rows are located 2h, 4h and 6h distance from the surface. The point X_{TE} lies at the intersection of the x-axis and the line perpendicular to the ellipse surface passing through the blowing slot location (not shown). It has been adopted as a convenient reference point with regards to the TE geometry and is also used in

conjunction with the algorithm for calculating the location of the image vortices to ensure that there is no flow across the ellipse surface.

Inset Fig.4.13(a) is a plot of the pressure distribution for Row 1 plotted as angle in degrees about X_{TE}. The separation point is 20^{o} below the TE.

Fig.4.14 reveals how the pairing process gradually dissipates the strength of the vortices as they flow downstream. Plots (a), (b) and (c) show strength against distance Z for the three runs already discussed in Fig.4.12. The initial slope is due to the exponential decay determined by the decay rate K. Pairing starts 42.3mm downstream of the lip after about 1.0ms and remains unaffected by the later developments downstream.

Fig.4.15 shows the vortex path after 300 iterations for two partially developed flows both with C_j= 0.01. Increasing k to 0.30, changes the frequency from 45.0 to 53.0kHz and moves the onset of pairing from 42.3mm downstream of the lip after 1.0ms to 36.0mm after only 0.83ms. It also reduces the induced velocity on the lower surface and the location of the TE separation point as shown by the surface pressure distribution in Fig.4.15(a). The relationship between the TE separation point S and the lift coefficient is not

certain. Potential theory states that

$$C_L = 2\pi(1+t/c) \sin \eta \qquad - 4.19$$

where the angle η is as shown in Fig.4.15. Using equation 4.19 to predict the lift coefficient at such an early stage of the vortex development is unrealistic due to the proximity of unpaired vortices. These will disappear downstream when the steady-state solution has been reached.

Such a condition is shown in Fig.4.16 after 600 iterations which is equivalent to 11.3ms "real-time". The vortex path and strength are compared with the situation after 300 iterations. Inset Fig.4.16(a) is a comparison between the vortex strength plotted against distance along the path. Note that the axes have been shifted by +5 units for 330130 to separate the graphs. The resultant flow pattern around the TE is shown in Fig.4.17. This can be compared with Fig.4.13 which is after 500 iterations but at a lower frequency and represents 11.1ms "real-time". Run 530125 seems to be fully developed judging by the vortex strength (Fig.4.14(c)). However, the lift coefficient based upon the separation point is well above any realistic value (=1.27). Run 630130 with a shedding frequency of 53.0kHz and C_j= 0.01 predicts C_L= 0.52 and shows that the induced flow around the TE has stabilised following some initially large fluctuations.

In Fig.4.18, the vortex path is shown with $C_j = 0.02$ after 600 and 800 iterations and compared with the previously discussed Run 630130 (Fig.4.17). Changing C_j from .01 to .02 increases the frequency from 53.0 to 55.5kHz and also extends the time needed to reach a steady-state solution.

The path shown by 60230 after 10.8ms "real-time" is still irregular, and the downward slope towards the end of the path is due to the earlier influence of the starting vortex. The situation after 800 iterations 830230 (14.4ms) is a slightly undulating path, which is beginning to re-align itself with the free-stream. The vortex strength is still in the process of dissipating and a steady-state lift coefficient will be slightly lower than the value of 1.27 as shown and would be attained after about 18ms of "real-time".

It is regrettable that limitation on time has reduced the available performance data. However, this section is intended to show the potential of the discrete vortex modelling technique for predicting the performance of CCAs.

5. DISCUSSIONS OF RESULTS

5.1 INTRODUCTION

This chapter considers the results obtained during the present study. The discussion also draws on the experience of other researchers so as to develop an understanding of the main parameters which determine the drag of a circulation-controlled aerofoil(CCA).

A turbulent boundary-layer model has been used for comparison with the skin friction measurements and prediction of the TE separation point. This is based upon a method proposed by Truckenbrodt(39). Two differential equations (given in reference (34) as equations 22.11(a) and (b)) are solved using a fourth-order Runge-Kutta method. The initial conditions are assumed from the experimental data at transition and boundary-layer development determined by the measured pressure distribution. From the transition point the model steps downstream calculating: Reynolds number R_e (based on the energy thickness of the boundary-layer), a modified shape factor H, and the coefficient of local skin friction. Separation can be assumed when the shape factor is in the region $0.74 > H > 0.72$. In general $H < 1$ represents flow subject to an adverse pressure gradient and $H > 1$ a favourable pressure gradient. The calculations continue step-by-step until separation at $H = 0.723$ as suggested by reference (34) equation 22.6.

In addition to quantitative measurements the discussion includes results from flow visualization work using titanium-dioxide powder mixed with oleic acid and paraffin. This revealed details of the flow pattern which helped interpretation of the experimental results.

Section 5.2 presents drag results for the unblown model together with some typical boundary-layer development along the upper surface. Measured results are compared with those predicted by the turbulent boundary-layer model.

Section 5.3 is devoted to a more detailed discussion of the results obtained for the model with TE blowing. Because of the quality of the results it was decided to include some of the aspects which, though not directly related to the drag, may be of interest to others doing similar work. Originally it was anticipated that this section would also include results from the theoretical Discrete Vortex Model described in chapter 4. Limitations on time, rather than on the proposed model, has meant that this has had to be postponed. However, the recommendations for future work in chapter 6, include suggestions based on the experiences gathered during the present study which should be useful if the work is to be continued.

Section 5.4 is included because of current interest in the LE wall-jet in conjunction with the application of CC-symmetrical rotor-blades which require dual blowing.

5.2 NO BLOWING

5.2.1 The Unblown Drag

The experimental lift-curve slope of 3.60 (shown in Fig.3.37) for the unblown model is as would be expected slightly lower than the two-dimensional value of 4.0 predicted by Hoerner(35).

Experimental drag data for elliptic profiles is limited to work on struts at Reynolds numbers less than 0.2×10^6, compared with 1.0×10^6 for the present study. Such work is described in references (40) and (41). Hoerner(42) suggests 0.016 for the minimum drag coefficient. This is assuming a completely turbulent boundary-layer with the model at zero geometric incidence. The measured value of 0.012 (see Fig.3.38) includes a partly laminar boundary-layer and is considered to be in good agreement.

As will be shown in section 5.3 the resultant chordwise force due to the pressure distribution (C_X), can be defined empirically as a function of geometric incidence and lift coefficient, (see equations 5.7 and 5.8). The derived relationship is shown in Fig.5.1(a) together with the measured experimental results.

Assuming a linear lift-curve slope of the form

$$C_N = a\alpha_g \qquad - 5.1$$

as shown in Fig.3.37 where a = 3.60 x π/180 and α_g is in degrees, then C_X can be simplified to a function of geometric incidence which is shown in Fig.5.1(b) and reproduced from equation 5.10 using the coefficients given in equation 5.11. The experimental points are also given for comparison. This curve is redrawn in Fig.5.1(c) together with the expression for streamwise drag given by

$$C_D' = C_X \cos\alpha_g + C_N \sin\alpha_g \qquad - 5.2$$

Equation 5.2 represents the force due to the pressure distribution which acts along the tunnel axes. For small angles (<10°), $\cos\alpha_g$ is taken as unity. The minimum value occurs at -1.2° geometric incidence due to the asymmetry of the model.

The two-dimensional, sectional, wake drag coefficient C_{D_w} is calculated as shown in section 2.2.3. For the unblown model, the relationship simplifies to

$$C_{D_w} = C_X + C_N \sin\alpha_g - .082C_N^2 + C_f \qquad - 5.3$$

This is the sectional streamwise drag, minus the induced drag, plus the skin friction. The last term was found to be almost constant at .0050 for the unblown model. Equation 5.3 is shown in Fig.5.1(d) along with the calculated value for C_{D_w} and the measured rake drag coefficient C_{D_r}. These have already been shown in Fig.3.38. Equation 5.3 has an unrealistic turning point at +6.1°. The most likely source for

such error is thought to be in the term for induced drag. This observation is discussed further in section 5.3 when considering the more complicated condition with TE blowing.

5.2.2 Boundary-Layer Development

To help understand the turbulent boundary-layer model used in section 5.3 a simple presentation from RUN-69 with the unblown model at $+3.7^{o}$ geometric incidence is included in this section. The pressure distribution along the upper surface is shown in Fig.5.2(a) (see also Fig.3.1(c) and Fig.3.22(a) for the same plot). Transition is assumed to occur at x/c = .09 with the local coefficient of skin friction c_f = .004. The measured skin friction is shown as the solid line in Fig.5.2(b) (see also Fig.3.3(c) and Fig.3.26(a)), the dotted line is that predicted by the turbulent boundary-layer model. Fig.5.2(c) shows the growth of the energy thickness, defined by the Reynolds number R_e, which has been scaled by its value at transition. The plot reveals a modest growth in the size of the boundary-layer. Fig.5.2(d) presents the modified shape factor H plotted against chordwise location. This shows a stable boundary-layer which (because H < 1) is subjected to a slight adverse pressure gradient. With H considerably greater than 0.74 at the final iteration point (x/c = .91), separation occurs even further downstream, which is as would be expected.

5.3 TE BLOWING

5.3.1 The Overall Drag Performance

Experimental results from the two different methods for measuring the drag have already been presented in chapter 3. Figure 3.42 shows that with the model at zero geometric incidence then comparison of drag with increased TE blowing is excellent. With the model at negative geometric incidence (shown in Fig.3.43), the proposed method for reduction of C_{D_w} is missing a correction term dependent upon geometric incidence. The quality and consistency of the rake measurements suggest that C_{D_r} is representative of the correct drag. To explain why the measurements do not agree we must consider the individual terms which represent the wake drag coefficient C_{D_w}. These have already been presented as equations 2.10 to 2.16 in section 2.2.3. Summarising we have

$$C_{D_w} = C_X + C_N \sin\alpha_g - C_{D_i} + C_f + C_{D_{pj}} - C_{D_j} \qquad - 5.4$$

Two of the terms ($C_{D_{pj}}$ and C_{D_j}) are dependent upon C_j and have limited influence because they almost cancel each other out. It was found that

$$C_{D_{pj}} = \frac{C_j^{1/2}}{20.2} \qquad - 5.5(i)$$

and

$$C_{D_j} = 0.21\ C_j \qquad - 5.5(ii)$$

With a maximum blowing coefficient of 0.04, the sum of these two terms constituted only an additional .0015 to the value of C_{D_w}. The skin friction component C_f was found to vary from .0050 to .0080, being primarily dependent upon free-stream Reynolds number rather than blowing coefficient or geometric incidence. It is reasonable to assume a constant value of .0065 for these three terms.

The induced drag (C_{D_i}) has been discussed in section 2.2.4. The curve in Fig.2.13 shows a linear relationship with respect to the lift coefficient squared so that equation 5.4 can be rewritten in the form

$$C_{D_w} = C_X + C_N \sin \alpha_g - k\, C_N^2 - k_o \qquad - 5.6$$

where k = .082 due to induced drag and k_o = .0065 is from the jet and skin friction contribution. The term C_X can be large compared with C_{D_w} and is difficult to measure accurately. It represents the force due to the pressure distribution acting along the chordline. The second term resolves this force to the drag acting parallel to the tunnel axis. A plot of the measured experimental points for C_X against C_N is shown in Fig.5.3 with geometric incidences -6.8^o, 0^o and $+3.7^o$. From inspection it is sensible to assume that the relationship can be described in the form

$$C_X = f_o + f_1\, C_N + f_2\, C_N^2 \qquad - 5.7$$

where the coefficients f_o, f_1 and f_2 have a linear relationship with respect to the geometric incidence so that

$$f_o = a_o + a_1 \alpha_g \qquad - 5.8(i)$$

$$f_1 = b_o + b_1 \alpha_g \qquad - 5.8(ii)$$

and $$f_2 = c_o + c_1 \alpha_g \qquad - 5.8(iii)$$

Considering each of the three experimental cases with $\alpha_g = -6.8$, 0 and $+3.7^o$; using a method of least squares to estimate the coefficients f_o, f_1 and f_2, then linear regression to find the coefficients a, b and c with suffixes o and 1, produced the empirical coefficient

$$a_o = .00959 : b_o = .004208 : c_o = .074345 \qquad - 5.9(i)$$

$$a_1 = .00079 : b_1 = -.015607 : c_1 = -.005046 \qquad - 5.9(ii)$$

This empirical relationship is also shown in Fig.5.3.

The case of no blowing, with variation of geometric incidence has already been mentioned in section 5.2.1. It was considered by substituting equation 5.8 for 5.7 and assuming a linear lift-curve slope as given in equation 5.1. Equation 5.7 can be written as a cubic in α_g with the form

$$C_X = d_o + d_1 \alpha_g + d_2 \alpha_g^2 + d_3 \alpha_g^3 \qquad - 5.10$$

where

$$d_o = a_o = .009590 \quad - 5.11(i)$$

$$d_1 = a_1 + b_o a = .001054 \quad - 5.11(ii)$$

$$d_2 = a(b_1 + c_o a) = -.000687 \quad - 5.11(iii)$$

$$d_3 = a^2 c_1 = -.000020 \quad - 5.11(iv)$$

Equation 5.10 has already been drawn in Fig.5.1(b) and (c). It has a maximum when $\alpha_g = 0.74^o$ where $C_X = .009986$. Note that because of the cubic relationship there is also a second turning point when $\alpha_g = -23.74^o$.

The relationship between C_N and C_j shown in Fig.3.39 approximates to the empirical relationship

$$C_N = a\alpha_g + 36\, C_j - 200\, C_j^2 \quad - 5.12$$

where a is $(3.60 \times \pi/180)$ the unblown lift-curve slope per degree. With C_j limited to 0.04 then equation 5.12 can be approximated by a linear relationship with the form

$$C_N = a\alpha_g + q\, C_j \quad - 5.13$$

where q is an approximate lift augmentation rate taken as 32. Equation 5.13 reflects the independence between lift due to geometric incidence and lift due to blowing which was found to exist for this particular experimental model. Both equations 5.12 and 5.13 are shown in Fig.5.4.

Substituting equations 5.7 and 5.8 in equation 5.6 leads to

$$C_{D_w} = (f_o - k_o) + (f_1 + \sin\alpha_g)\, C_N + (f_2 - k)C_N^2 \qquad - 5.14$$

Differentiating with respect to C_N (assume partial derivatives where appropriate),

$$\frac{dC_{D_w}}{dC_N} = (f_1 + \sin\alpha_g) + 2(f_2 - k)\, C_N \qquad - 5.15$$

At fixed geometric incidence,

$$\frac{dC_{D_w}}{dC_j} = \frac{dC_{D_w}}{dC_N}.\frac{dC_N}{dC_j} \qquad - 5.16$$

where $\frac{dC_N}{dC_j} = q$ from equation 5.13 so that

$$\frac{1}{q}\frac{dC_{D_w}}{dC_j} = (f_1 + \sin\alpha_g) + 2(f_2 - k)(a\alpha_g + q\, C_j) \qquad - 5.17$$

with $\alpha_g = 0$ this simplifies to

$$\frac{1}{q}\frac{dC_{D_w}}{dC_j} = b_o + 2(c_o - k)q\, C_j \qquad - 5.18$$

Equation 5.18 describes the gradient of the empirical curve for C_{D_w} against C_j based on the experimental results presented in Fig.3.42. With no blowing the empirical slope is slightly positive because from equation 5.9(i) $b_o > 0$. However with $k > c_o$, increased blowing reduces the drag C_{D_w} as shown in Fig.3.42.

Returning to the more general equation 5.17 with $\alpha_g < 0$ then f_2 is increased so that the term $(f_2 - k) > 0$ which means that C_{D_w} will start increasing with more blowing. The measurements using the rake show that this is not the case. Comparison with Fig.3.43 suggest that the gradient dC_{D_w}/dC_j should be almost independent of the geometric incidence in the measured range where $C_j < 0.04$.

Reconsidering equation 5.4 and taking note of the above discussion, it is questionable whether the derived value for the induced drag C_{D_i} is correct. Barbour(7) found that predicted induced drag did not produce a linear relationship with respect to the lift coefficient squared. This linear relationship has been the basis for the present method as described in section 2.2.4. If one considers k (see equation 5.6) to be a function of geometric incidence with the form,

$$k = k_1 + k_2 \alpha_g \qquad - 5.19$$

where $k_1 = .082$ and $k_2 = -.003$, then a modified expression for induced drag becomes

$$C_{D_i} = (k_1 + k_2 \alpha_g)\, C_N^2 \qquad - 5.20$$

The original empirical relationship for the wake drag coefficient is shown in Fig.5.5 with dashed lines drawn for the three incidences which were

investigated. Two of these lines ($\alpha_g = 0^o$ and -6.8^o) can be compared with the measured experimental results in Figs.3.42 and 3.43 respectively. The third line with $\alpha_g = +3.7^o$ has been extrapolated by using the assumed relationship for C_X from equation 5.7. The modified relationship for estimating C_{D_i} using equation 5.20 is shown for the same cases with solid lines in Fig.5.5. These do not agree exactly with the measured rake drag coefficient, but they show that similar trends of reduced wake drag with increased TE blowing can be obtained by slight alterations of induced drag.

Fig.5.6 shows the resulting modified relationsip between lift coefficient and effective incidence, together with the original relationship which has already been shown in Fig.2.14. The change is small, but has a great influence on the predicted wake drag coefficient.

5.3.2 The LE Stagnation Point

Flow visualization around the LE with TE blowing revealed that the spanwise distribution of the LE stagnation point was uniform. Fig.5.7 shows the location of the stagnation point, measured in arc angle (radians) from the lip, plotted against effective incidence for the unblown case and with TE blowing at -6.8^{o}, 0^{o} and 3.7^{o}. The circular profile of the LE makes it impracticable to compare the plot with theory. However, it is interesting to note that the stagnation point can be uniquely defined as a function of geometric incidence and blowing coefficient.

For the present study, with modest blowing rates and angles of attack, the empirical relationship is

$$\vartheta_{o} = 1.36 + 0.0685\,\alpha_{g} + 7.25\,C_{j} \qquad - 5.21$$

where α_{g} is measured in degrees.

Equation 5.21 shows that measuring the location of the LE stagnation point to within 1^{o} one can check the geometric incidence to within $1/4^{o}$ or the TE blowing coefficient to within 0.0025, which is equivalent to 6.5% of the maximum value of 0.04 measured during the present study.

5.3.3 The Upper Surface Boundary Layer

The upper surface boundary-layer is subject to a favourable pressure gradient except when the model is at a large positive geometric incidence with a low TE blowing momentum coefficient.

For much of the work at negative geometric incidence the boundary-layer was laminar with $R_c < 10^6$. At positive incidence the boundary-layer "tripped" at the LE blowing slot and remained turbulent. An example of this is shown in Fig. 5.8 where comparison is made between the measured and theoretically derived boundary-layer development for RUN-73 at $+3.7^o$ geometric incidence with TE blowing: Figure 5.8(a) shows the experimental pressure distribution and Fig.5.8(b) compares the coefficient of local skin friction with the theoretical boundary-layer model. The slight difference is considered to lie within the expected experimental error and both curves show an almost constant value along the chord length.

The Reynolds number R_e in Fig.5.8(c) is interesting when considering the influence of the boundary-layer on the lift augmentation capability of the model. The theoretical discrete vortex model in section 4.2.1 calculates lift coefficient using the velocity difference between the jet and the potential flow at the lip. Wood(43) extends the relationship and

suggests that the ratio of jet-momentum to the boundary-layer momentum deficit determines the lift increment due to blowing. An exact relationship is not known but it is suggested that consideration of energy levels may be useful. If the energy thickness of the boundary-layer is reduced, this should increase the wall-jet effectiveness (which may be considered in terms of kinetic energy). The lift augmentation rate should therefore increase slightly when the geometric incidence becomes more negative because this will tend to reduce the upper surface boundary-layer growth. This cannot be confirmed using the experimental results from the present study because there is not enough detail of lift performance with low blowing rates typically $C_j < 0.01$.

The shape factor in Fig.5.8(d) shows that the boundary-layer is stable. This is due to the re-energising effect of the TE blowing slot.

5.3.4 The Lower Surface Boundary Layer

The lower surface has a relatively clean profile which, with a favourable pressure gradient (as is the case when geometric incidence is positive), leads to a laminar boundary-layer over a large portion of the surface. A feature of the boundary-layer is its change from being almost two-dimensional to being a distinctly three-dimensional flow regime when approaching the TE wall-jet. This is a recognized problem when testing CCAs, the extent of which may be underestimated when considering the validity of "two-dimensional" data. An extreme example is shown by flow visualization in Fig.5.9. Photograph (a), taken during some preliminary work at the start of the present study, shows the lower surface near the TE and bottom endplate junction. The main feature is the spanwise (downward) movement of the lower surface flow towards the bottom endplate. A strong root-vortex emanates perpendicularly to the TE surface and extends downstream with a clockwise rotation (when viewed looking from upstream). The strength of this vortex is shown by the strong transverse flow pattern along the endplate. Note also the distinct line separating the upper and lower surface flow.

Photograph (b) was taken following inclusion of the endplate boundary-layer control blowing slot. This

counteracted the rotation of the root-vortex and considerably reduced the spanwise flow on the lower surface.

Analysis of the boundary-layer using a typical case of TE blowing at -6.8° incidence is shown in Fig.5.10 for RUN-59. Figure 5.10(a) is the experimental pressure distribution showing an adverse gradient. Transition was found experimentally to occur at $x/c = 0.3$ where the local skin friction coefficient is 0.004. The measured local skin friction is noticeably less than that predicted by the two-dimensional boundary-layer model. The results are not surprising when one considers the already mentioned spanwise movement which will tend to reduce the predicted value. The Reynolds number in Fig.5.10(c) shows a thickening boundary-layer, and the shape factor in Fig.5.10(d) shows that the flow is near to separation.

5.3.5 The TE Wall-Jet

Investigation of the TE wall-jet was limited to pressure measurements and flow visualization work. The pressure distribution, when moving around the TE from the blowing slot, exhibits a characteristic suction peak before a sharp fall (rise in pressure) followed by separation when approaching the lower surface boundary-layer. Figure 5.11 is a photograph of the TE wall-jet viewed looking onto the mid-span region of the upper surface blowing-lip and TE tube. The free-stream flow is moving from right to left. The photograph was taken following a modest blowing rate $C_j = 0.02$. The white streaks show the two-dimensional wall-jet emerging from the slot. The denser white area is the almost stagnant lower surface flow. The spanwise (vertical) sinusoidal path of the separation line was observed throughout the flow visualization work and is discussed further in section 5.3.6. A notable feature of the wall-jet is how the streamlines move spanwise when close to the separation line. This would suggest the development of longitudinal streamwise vortices emanating from the TE surface and being conveyed downstream in the wake. An example from the preliminary work performed at the start of the present study did in fact reveal eight of these vortices evenly distributed across the span. Two of these (near the mid-span region) are shown in Fig.5.12 which is a

view looking upstream onto the TE tube. The vertical white line to the right is the TE blowing lip and the white area on the left is the oncoming lower-surface boundary-layer. Sellotape covering the static pressure tappings during the flow visualization work is evident and obviously influences the location of the separation point. These longitudinal vortices may be due to strong endplate root vortices which induce spanwise flow variations. Alternatively this is a phenomenon which is also present on fully two-dimensional CCAs.

5.3.6 The TE Separation Point

Extension of the turbulent boundary-layer model to predict the TE wall-jet provided useful comparison with the experimental results for estimating the TE separation point. Initial conditions assume that the TE wall-jet becomes turbulent at the blowing slot. The model steps around the TE, calculating skin friction, Reynolds number and shape factor at each pressure tapping location. The method progresses up to the point of separation where H = 0.723.

The measured separation point from the RMS pressure distribution for RUN-56 is seen in Fig.5.13(a) and compared with the shape factor H in Fig.5.13(c). The curve is extrapolated to H = 0.723 and predicts separation at s/R = 0.8 with C_j = .016.

A similar trend is shown in Figs.5.13(b) and (d) for RUN-59 with a blowing coefficient C_j = .041. The peak near s/R = 1.0 in the RMS measurements around the TE coincides with the location of the TE separation point predicted by the boundary-layer model.

Figure 5.14 shows the predicted boundary-layer growth and local skin friction coefficient for the same two runs discussed above. The boundary-layer growth in Figs.5.14(a) and (b) remains comparatively steady. The local skin friction calculated in N/m^2 shows (see

Figs.5.14(c) and (d)) a shallow peak followed by a gradual reduction in both cases. This is similar to trends measured by Warsop and Marrero Santo(44) during earlier work on the same experimental model. A sample of this is reproduced in Fig.5.15 showing skin friction measured around the TE tube plotted against angle from the blowing slot. The higher maximum values from their measurements is due to a lower slot height and increased blowing coefficient.

Figure 5.16(a) is a photograph showing the spanwise distribution of the TE wall-jet separation line. There is no obvious relationship between the sinusoidal distribution and the internal layout of the TE plenum chamber. Figure 5.16(b) is a close-up photograph of the mid-span section showing detail of the spanwise movement of the separation line.

5.3.7 The Wake Structure

Measurements in the wake of the model revealed regular mean trends which provided sensitive drag values and indicated flow direction.

The experimental work showed large fluctuations of total pressure in the core region of the wake. Damping the pressure transducer signal with a low-pass filter, extending the sampling time and performing several scans produced a reasonable mean total pressure distribution. This led to some very satisfactory results as shown for example in Figs.3.31, 3.33 and 3.35. However, the apparatus was not capable of measuring details relating to the rotational nature of the flow.

Extending the hypothesis for the flow structure proposed by the theoretical discrete vortex model and considering the physical constraints on such flow, suggests that the original discrete vortices initially pair as shown by the model. The ideal two-dimensional flow conditions rapidly break down, and the vortices turn longitudinally and break up to produce a large "eddy-flow" reminiscent of the breakdown of the two-dimensional discrete vortex model but on a three-dimensional level. This means that detailed investigation of the wake must be done using a three-dimensional wake traverse method capable of measuring flow angle and having a frequency response upto 100kHz.

By considering conservation of momentum upstream and downstream of the CCA, one should relate the angular momentum of the flow in the wake to the jet blowing momentum. This is best understood by first considering ideal conditions with no blowing: In which case there should be no rotational component in the wake flow. If we now start blowing, the extra momentum due to the jet is transferred into discrete vortices which have a finite strength, size and frequency. These pair downstream with conservation of angular momentum and are only subject to viscous losses predicted by the vortex strength decay rate. There should therefore be a relationship between the blowing momentum and the angular momentum of the flow in the wake.

5.4 LE BLOWING

5.4.1 The LE Wall-Jet

A limited amount of work was done to investigate the behaviour of the LE wall-jet. The results described in sections 3.2.3 and 3.4.3 have confirmed earlier observations by Wood(15) that there are two types of LE flow. The first is when the LE wall-jet is too weak to move around onto the lower surface and is therefore forced by the oncoming free-stream to fold-back along the upper surface. This means that there is a re-attachment point somewhere downstream of the blowing slot as shown in Fig.5.17(a). The extent of the recirculation region will vary. Figures 3.22(b) and (c) show that there is a "bubble" of disturbed flow lying over the LE blowing lip and extending downstream to about 15% chord. This leads to an increased mid-chord pitching moment as shown in Fig.3.45(c). With increased LE blowing coefficient, the extent of the recirculating region decreases and the re-attachment point moves close to the LE blowing slot. This is shown by the LE pressure distribution in Fig.3.22(d). The LE wall-jet is still flowing back along the upper surface, but there is only slight disturbance downstream of the LE blowing slot. Hence a reduced mid-chord pitching moment as shown in Fig.3.45(c).

Further increase of the LE blowing coefficient leads to the wall-jet moving around the LE and onto the lower surface as shown in Fig.5.17(b). The velocity ratio $V_j:U_\infty$ when this change occurs depends upon which type of flow exists when one starts to change the parameters. There is a hysteresis situation.

5.4.2 The LE Stagnation Point

The LE pressure distributions showed (see Figs.3.19, 3.20, 3.24 and 3.25) that the flow varied with spanwise location. The experimental results suggest that when the LE wall-jet folds back (see run 70, 71 and 72) then there exists a sinusoidal LE stagnation line similar to the flow type found with the TE wall-jet. This of course disappeared once the LE wall-jet moved completely around onto the lower surface in which case the LE stagnation point becomes indeterminate as was the case for run 51, 52 and 53. This latter type of LE flow resulted in a suction peak around the LE tube (see Fig.3.17) and hence a marked decrease in the drag value.

6. CONCLUSIONS AND RECOMMENDATIONS

6.1 THE EXPERIMENTAL WORK

An experimental investigation has been carried out on a 20% elliptic circulation-controlled aerofoil with both leading and trailing edge blowing slots. Detailed pressure measurements have been made around the model and downstream in the wake. These provided experimental data relating drag measured on the model with the resulting momentum deficit in the wake.

Integration of the surface static pressure distribution showed that lift performance compared favourably with previous results and confirmed trends found by other researchers.

Measurement of shear stress using flush-mounted razor blades provided a simple but effective means for determining the magnitude of the skin friction drag C_f.

A method for calculating the momentum deficit from the rake measurements was initially checked by measuring the drag of a cylinder using a drag balance. Results suggested an experimental error of less than 4%. The overall drag for the unblown model agrees with limited previous work.

Reduction of the results when calculating drag with TE blowing has included a discussion showing the correction terms necessary due to tunnel constraints and the

jet-blowing momentum. The results were sensitive to the value of effective incidence and induced drag. A slightly non-linear relationship between induced drag versus (lift coefficient)^2, helped to equate drag measured on the model with the value measured downstream using the rake.

The results showed that the resultant force due to pressure acting along the chordline can be approximated by a quadratic relationship with the lift coefficient.

Details of the pressure distribution around the trailing edge showed that separation of the TE wall-jet from the TE surface could be recorded by measuring the RMS of the fluctuating static pressure.

The experimental separation line was shown (using flow visualization) to exhibit a sinusoidal spanwise pattern which was not related to the internal geometry of the blowing slots. It is not clear whether the spanwise variation is due to endplate interference or a characteristic phenomenon associated with the TE Coanda flow.

The experimental pressure distribution along the lower surface was used as input to a two-dimensional turbulent boundary-layer model. This predicted the boundary-layer development and showed that the measured skin friction was (on approaching the TE

wall-jet) lower than the predicted value. This suggests a spanwise movement of the lower surface flow when close to separation. This was confirmed by flow visualization even after improvements to the endplate/boundary-layer control blowing system.

The turbulent boundary-layer model was also used to predict the TE separation point which agreed with the value suggested from the TE RMS pressure measurements.

Comparison of predicted TE skin friction distribution with that measured previously on the same model, but with a rougher TE surface and higher blowing coefficients at a lower slot height, shows similar trends but with lower magnitudes.

The aerodynamic characteristics of a CCA can be distinguished between those parameters due to incidence changes and those due to blowing. Specifically it has been shown that for the experimental conditions investigated then lift, mid-chord pitching moment, centre of pressure and location of the leading edge stagnation point are four such parameters.

6.2 THE THEORETICAL WORK

The present study has extended the theory that discrete vortices control the development of the Coanda flow associated with a circulation-controlled aerofoil.

The work has included development of a theoretical model which simulates shear between the upper surface boundary-layer and the TE wall-jet using discrete vortices. These are shed from the TE lip with frequency and strength determined by the blowing parameters and TE geometry. Vortices of equal but opposite strength, located inside the aerofoil section, maintain no-flow across the TE surface. It is shown that for a cylinder their summed strength is equal to the circulation and hence lift due to the blowing coefficient. The vortices develop downstream influenced by the induced velocity and potential flow. Viscosity and entrainment is modelled by a nominal decay constant. Vortex strength and size is related to conservation of angular momentum with eventual overlapping resulting in a pairing process. Once initiated this process rapidly breaks down the discrete vortex structure resulting in a large-scale eddy flow representative of the flow in the wake of the model.

Performance results for the model, when applied to a circular cylinder with a blowing slot at top dead

centre, showed good agreement with previous experimental work.

The theoretical analysis suggests that lift should be related to the total strength of the discrete vortices and is independent of the location of the TE separation point.

Extension of the model for comparison with a 20% elliptic CCA has led to realistic vortex development. Prediction of separation and overall lift performance is similar to the present experimental study. Limitations on time has meant that detailed results are not yet available. However, it is hoped to continue the work and publish extensive performance results in the not too distant future.

6.3 RECOMMENDATIONS FOR FUTURE WORK

The present study has developed the work of Wood(15) and Smith(21) in an effort to confirm the presence of discrete vortices around the TE of a circulation-controlled aerofoil by relating their influence to the resultant pressure distribution and hence drag of such aerofoils.

Extended performance measurements with lift coefficients greater than 1.5 is not recommended on the present model at Bath, due to the low aspect ratio which adversely affects the two-dimensional nature of the flow. However, the work has suggested several features of the vortex structure, such as frequency, size and strength, which can be confirmed by means of detailed measurements immediately downstream of the blowing lip using hot-wire or holography methods.

There is still only limited experimental data relating to low-speed aerodynamic characteristics of CCAs with forward facing blowing slot. The present model could provide valuable information by investigating the two-different types of LE wall-jet flows which have been found. This work could be supplemented by adapting the discrete vortex model to predict the LE flow pattern.

REFERENCES

1. Lockwood, V.E.
Lift Generation on a circular cylinder by tangential blowing from surface slots.
NASA Tech. Note D-244, 1960.

2. Jones, A.F. and Buckingham, W.R.
Some exploratory tests on a two-dimensional blown cylinder model in the RAE 2ft x 1.5ft transonic wind tunnel.
ARC CP 889, December 1964.

3. Cheeseman, I.C.
Circulation control and its application to stopped rotor aircraft.
The Aeronautical Journal, Vol. 72, pp 635-646, July 1968.

4. Dunham, J.
Experiments towards a circulation control lifting rotor. Part I-Wind tunnel tests.
The Aeronautical Journal, Vol. 74, pp 91-103, January 1970.

5. Levinsky, E.S. and Yeh, T.T.
Analytical and experimental investigation of circulation control by means of a turbulent Coanda jet.
NASA CR-2114, September 1972.

6. Osborne, A.R.
An interim review and appraisal of two-dimensional tests on circulation controlled sections.
NGTE NT.678, February 1968.

7. Barbour, D.
A study of circulation control by blowing at the trailing edge of elliptic aerofoils, and its application to fixed wing aircraft.
MSc. Thesis, Southampton University, 1973.

8. Williams, R.M.
Two-dimensional subsonic wind-tunnel test on a 20-percent thick, 5-percent cambered circulation control airfoil. NSRDC AL-176, August 1970.

9. Englar, R.J.
Two-dimensional subsonic wind-tunnel test on a cambered 30-percent thick circulation control airfoil.
NSRDC AL-201, May 1972.

10. Ottensoser, J.
Two-dimensional subsonic evaluation of a 15-percent thick circulation control airfoil with slots at both leading and trailing edges.
NSRDC Report 4456, July 1974.

11. Englar, R.J.
Circulation control - An updated bibliography of NSRDC research and selected outside references.
NSRDC Report 84-052, September 1984.

12. Bachalo, W.D.
An experimental investigation of circulation control flow fields using holographic interferometry.
NASA CR-166482, October 1982.

13. Kind, R.J.
A proposed method of circulation control.
Ph.D Thesis, Cambridge University, 1967.

14. Jones, D.G.
The performance of circulation controlled airfoils.
Ph.D Thesis, Cambridge University, 1970.

15. Wood, N.J.
The aerodynamics of circulation control airfoils.
Ph.D Thesis, Bath University, 1981.

16. Dunham, J.
A theory of circulation control by slot blowing applied to a circular cylinder.
Journal of Fluid Mechanics, Vol. 33, pp 495-514, 1968.

17. Kind, R.J.
A calculation method for circulation control by tangential blowing around a bluff trailing edge.
Aeronautical Quarterly, pp 205-223, August 1968.

18. Ambrosiani, J.P.
Analysis of a circulation controlled elliptical aerofoil.
Aerospace Engineering TR-30, April 1971.

19. Dvorak, F.A. and Kind, R.J.
Analysis method for viscous flow over circulation controlled airfoils.
Journal of Aircraft, Vol. 16. No. 1, January 1979.

20. Dvorak, F.A. and Choi, D.A.
The analysis of circulation controlled airfoils in transonic flows.
AIAA paper 81-1270, June 1981.

21. Smith, R.V.
A theoretical and experimental study of circulation control with reference to fixed wing application.
Ph.D Thesis, Southampton University, 1978.

22. Soliman, M.E.
A theoretical study of circulation controlled airfoils and experimental application to a symmetrical aerofoil.
MSc. Thesis, Southampton University. 1980.

23. Smith, R.V. et al.
Discrete vortex modelling applied to the prediction of circulation control.
Paper submitted to the Journal of Fluid Mechanics. 1980.

24. Englar, R.J. and Williams, R.M.
Test techniques for high-lift, two-dimensional airfoils with boundary-layer and circulation-control for application to rotary wing aircraft.
NSRDC 4645. July 1975.

25. Pankhurst, R.C. and Holder, D.W.
Wind-tunnel technique.
SBN 273 43353 9, Pitman Press, 1968.

26. Methods for the measurement of fluid flow in pipes.
British Standard 1042, 1964.

27. Englar, R.J.
Subsonic two-dimensional wind tunnel investigation of the high lift capability of circulation-control wing sections.
NSRDC Report ASED-274, April 1975.

28. Englar, R.J.
Two-dimensional transonic wind tunnel test of three 15% thick circulation-control airfoils.
NSRDC Report ASED 182, December 1970.

29. Review of wall shear stress measurement.
Journal of Fluid Mechanics, Vol. 35, pp. 737-757.

30. Winter, K.G.
Techniques available for skin friction measurements.
Progress in Aerospace Science, Vol. 18, pp. 1-57.

31. East, L.F.
Measurement of skin friction at low subsonic speeds by the razor blade technique.
RAE TR 66277.

32. Jones, M.
The measurements of profile drag by the pitot-traverse method.
R & M. 1688, Cambridge University laboratory. 1936.

33. Betz, A.
A method for the direct determination of profile drag.
Zeitschrift fur Flugtechnik und Motorluftschiffahrt, Vol. 16, p 42, 1925.

34. Schlichting, H.
Boundary-layer theory (seventh edition)
ISBN 0-07-055334-3, McGraw-Hill. 1979.

35. Hoerner, S.F.
Fluid Dynamic Lift.
Hoerner Fluid Dynamics, 1975.

36. Rosenhead, L.
The formation of vortices from a surface of discontinuity.
Proc. Roy. Soc. A., Vol. 134, p 170, 1931.

37. Birkhoff, G.
Do vortex sheets roll up ?
Rendi. Cir. Math. Palermo, Series 2, Vol. 8, p 77, 1959.

38. Hama, F.R.
On the rolling-up of a vortex sheet.
Tech. Note, BN-220, University of Maryland, 1960.

39. Truckenbrodt, E.
Neuere erkenntnisse uber die berechnung von Stromungsgrenzschichten mittels einfacher quadraturformeln.
Part I: Ing-Arch. 43, 9-25, 1973.
Part II: Ing-Arch. 43, 136-144, 1974.

40. Zahm, A.F., Smith, R.H., Louden, F.A.
Forces on elliptic cylinder in uniform air stream.
NACA Tech. Rpt. 289. 1928.

41. British Aeronautical Research Council.
Resistance of certain strut forms.
ARC RM 1599, 1934.

42. Hoerner, S.F.
Fluid-Dynamic Drag.
Hoerner Fluid Dynamics, 1965.

43. Wood, N.J. and Nielsen, J.
Circulation control airfoils, past, present, future.
Paper 85-0204, AIAA 23rd Aerospace Sciences Meeting, Jan 1985.

44. Warsop, C. and Marrero Santo, G.
Measurement of the surface shear stress around the trailing edge of a circulation controlled aerofoil.
Report No: 526, School of Engineering, University of Bath, June 1981.

THE DRAG OF A CIRCULATION CONTROLLED AEROFOIL

Submitted for the degree of Ph.D
by

C.W.Hustad, BSc. May 1986

Part 2 - List of Tables
- List of Figures
- Appendices
- Tables
- Figures

L I S T O F T A B L E S

Chapter 2.

Chapter 3.

L I S T O F F I G U R E S

Chapter 3.

8 APPENDICES

8.1 Appendix A

8.1.1 The Induced Velocity due to a Discrete Vortex

Consider a vortex I with strength γ m^2/s (+'ve is clockwise) which is located at the point I(R_i,Φ_o). The origin of the polar co-ordinate system is at O as shown in Fig.A1.

The point P can be described as P(r,Φ) with respect to O, or as P(s,β) with respect to the polar co-ordinate system with its origin at I.

Considering the stream function Ψ due to the vortex I it is evident that the radial velocity at any point P(s,β) is zero so that,

$$\frac{1}{s}\frac{\partial \Psi}{\partial \beta}=0 \qquad \text{A1.1}$$

It can be readily shown that the tangential velocity at P is q_t

where,

$$q_t = \frac{\gamma}{2\pi s} \qquad \text{A1.2}$$

Resolving q_t to its velocity components tangential and radial about O it is shown by geometry that

$$v_r = q_t \sin\Theta \qquad \text{A1.3}$$

which can be written as

$$v_r = q_t \frac{R_i \sin\alpha}{s} \qquad \text{A1.4}$$

similarly

$$v_t = q_t \cos\Theta \qquad \text{A1.5}$$

so that

$$v_t = q_t \frac{r - R_i \cos\alpha}{s} \qquad \text{A1.6}$$

Thus providing expressions for the radial and tangential velocity induced at P about the origin O by the vortex I.

8.1.2 The Induced Velocity due to a Discrete Vortex Pair

Consider a vortex pair I and J, where J is of equal but opposite strength to I lying on the extension of line OI at a radial distance R_j from the origin O.

Take the point P(r,Φ) where the distance IP is S_i and JP is S_j as shown in Fig.A2. The stream function at P due to each vortex is Ψ_i and Ψ_j respectively, so that using equation A1.4 the radial velocity at P due to I and J is,

$$v_r = \frac{\gamma \sin\alpha}{2\pi}\left[\frac{R_i}{S_i^{\,2}} - \frac{R_j}{S_j^{\,2}}\right] \qquad \text{A2.1}$$

if

$$\frac{R_i}{S_i^{\,2}} = \frac{R_j}{S_j^{\,2}} \qquad \text{A2.2}$$

then the radial velocity at P is zero for all values of α. This is the condition for a cylindrical surface streamline.

Expanding equation A2.2

$$\frac{R_i^{\,2} + r^2 - 2R_i r\cos\alpha}{R_i} = \frac{R_j^{\,2} + r^2 - 2R_j r\cos\alpha}{R_j} \qquad \text{A2.3}$$

Hence

$$\frac{R_i^{\,2} + r^2}{R_i} = \frac{R_j^{\,2} + r^2}{R_j} \qquad \text{A2.4}$$

Cross-multiplying and re-arranging gives

$$R_i R_j (R_j - R_i) = r^2 (R_j - R_i) \qquad \text{A2.5}$$

Provided $R_i \neq R_j$ then

$$R_i R_j = r^2 \qquad \text{A2.6}$$

Hence if r=R is constant then the locus of P is a circle with radius R which represents a cylinder within the flow field.

By using equation A1.6 the tangential velocity along the surface at the cylinder is,

$$v_t = \frac{\gamma}{2\pi} \left[\frac{R - R_i \cos\alpha}{S_i^2} - \frac{R - R_j \cos\alpha}{S_j^2} \right] \qquad \text{A2.7}$$

Using the relationship in equation A2.2 leads to

$$v_t = \frac{\gamma R}{2\pi} \left[\frac{1}{S_i^2} - \frac{1}{S_j^2} \right] \qquad \text{A2.8}$$

Equation A2.8 represents the tangential velocity around a circle with center O and radius R due to a vortex pair located so that the radial velocity is zero.

Expanding equation A2.8

$$v_t = \frac{\gamma R}{2\pi} \left[\frac{1}{R_i^2 - 2RR_i \cos\alpha + R^2} - \frac{1}{R_j^2 - 2RR_j \cos\alpha + R^2} \right] \qquad \text{A2.9}$$

Using the substitution $R^2 = R_i R_j$ from equation A2.6 then,

$$v_t = \frac{\gamma R}{2\pi}\left[\frac{1}{R_i}\frac{1}{(R_j + R_i - 2R\cos\alpha)} - \frac{1}{R_j}\frac{1}{(R_j + R_i - 2R\cos\alpha)}\right] \qquad \text{A2.10}$$

Re-arranging equation A2.10

$$v_t = \frac{\gamma R}{2\pi}\left(\frac{1}{R_i} - \frac{1}{R_j}\right)\left[\frac{1}{R_j + R_i - 2R\cos\alpha}\right] \qquad \text{A2.11}$$

$$= \frac{\gamma R}{2\pi}\left(\frac{R_j - R_i}{R^2}\right)\left[\frac{1}{R_j + R_i - 2R\cos\alpha}\right] \qquad \text{A2.12}$$

$$= \frac{\gamma}{2\pi R}\left(\frac{R_j - R_i}{R_j + R_i}\right)\left[\frac{1}{1 - \dfrac{2R\cos\alpha}{(R_j + R_i)}}\right] \qquad \text{A2.13}$$

Let

$$A = \frac{2R}{R_j + R_i} \qquad \text{A2.14(a)}$$

and

$$B = \frac{2R}{R_j - R_i} \qquad \text{A2.14(b)}$$

so that

$$v_t = \frac{\gamma}{2\pi R}\left(\frac{A}{B}\right)\left[\frac{1}{1 - A\cos\alpha}\right] \qquad \text{A2.15}$$

8.1.3 The Circulation about a Cylinder due to a Vortex Pair.

The circulation within a closed system is defined by the relationship

$$\Gamma = \int v_t \, dc \qquad \text{A3.1}$$

where v_t is the tangential velocity along the small increment of circumference dc .

Considering the cylinder mentioned in Appendix A (section 8.1.2) and using the relationship for v_t from equation A2.15 then

$$\Gamma = \frac{\gamma}{2\pi}\left[\frac{A}{B}\right]\int_{-\pi}^{\pi} \frac{d\alpha}{1 - A\cos\alpha} \qquad \text{A3.2}$$

where $d\alpha$ is the angle at the origin subtended by the increment of circumference dc . Using the substitution

$$t = \tan\frac{\alpha}{2} \qquad \text{A3.3}$$

so that

$$d\alpha = \frac{2dt}{1+t^2} \qquad \text{A3.4}$$

and

$$\cos\alpha = \frac{1-t^2}{1+t^2} \qquad \text{A3.5}$$

Then substitution into equation A3.2 leads to

$$\Gamma = \frac{\gamma}{2\pi}\left[\frac{A}{B}\right]\int_{-\infty}^{\infty}\frac{2dt}{(1-A)+(1+A)t^2} \qquad \text{A3.6}$$

Let

$$a^2 = \frac{(1-A)}{(1+A)} \qquad \text{A3.7}$$

Re-arranging equation A3.6,

$$\Gamma = \frac{\gamma A}{\pi B(1+A)}\int_{-\infty}^{\infty}\frac{dt}{a^2+t^2} \qquad \text{A3.8}$$

$$\Gamma = \frac{\gamma A}{\pi aB(1+A)}\left[\tan^{-1}\left(\frac{t}{a}\right)\right]_{-\infty}^{\infty} \qquad \text{A3.9}$$

$$\Gamma = \frac{-\gamma A}{aB(1+A)} \qquad \text{A3.10}$$

By squaring equation A2.14(a) and using the substitution $R^2 = R_j R_i$ then it is readily shown that

$$(1-A^2)^{\frac{1}{2}} = \frac{R_j - R_i}{R_j + R_i} \qquad \text{A3.11}$$

Taking equation A3.10 and using equation A3.7, then

$$\Gamma = \gamma \frac{A}{B} \left[\frac{(1+A)}{(1-A)} \right]^{\frac{1}{2}} \frac{1}{(1+A)} \qquad \text{A3.12}$$

$$\Gamma = \gamma \frac{A}{B} \left[\frac{1}{(1-A)(1+A)} \right]^{\frac{1}{2}} \qquad \text{A3.13}$$

using equations A2.14(a) and (b) leads to

$$\Gamma = \gamma \frac{(R_j - R_i)}{(R_j + R_i)} \frac{1}{(1-A^2)^{\frac{1}{2}}} \qquad \text{A3.14}$$

Hence from equation A3.11 we have

$$\Gamma = \gamma \qquad \text{A3.15}$$

In other words the resultant circulation about a cylinder due to a vortex pair is equal to the strength of the image vortex.

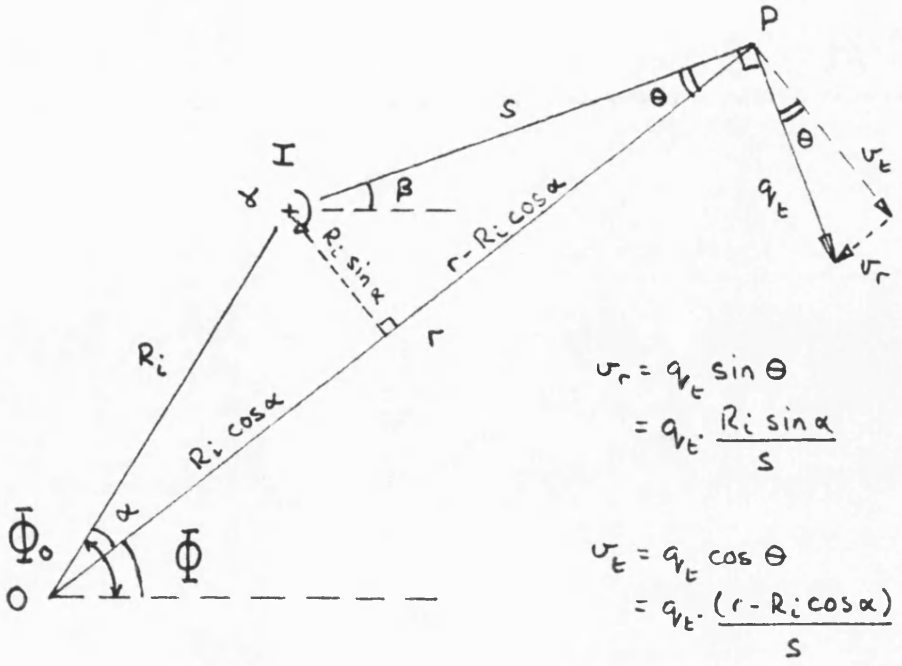

Fig.A1: Induced velocity at P due to the vortex I.

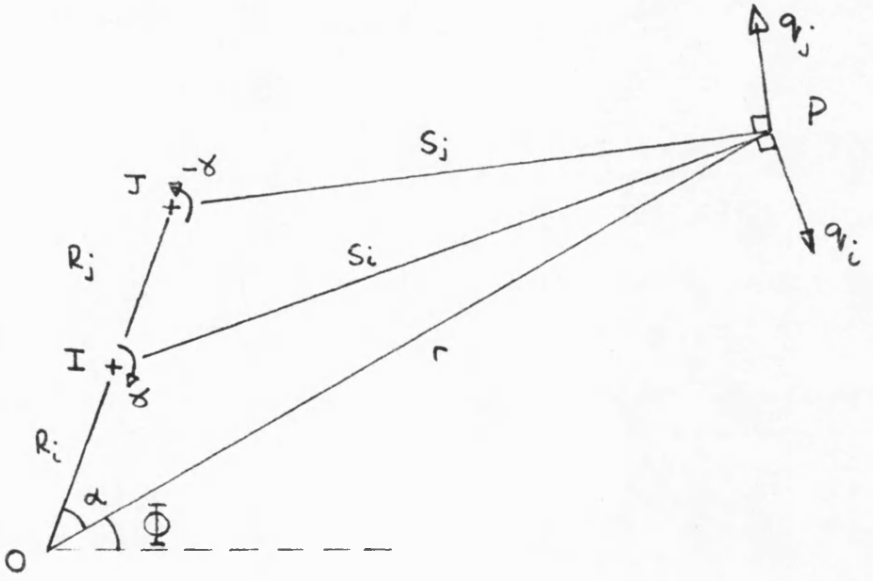

Fig.A2: Induced velocity at P due to the vortex pair I and J.

8.2.1 DVM-Ellipse Programme Listing

```
10 ' Program developed by C.W.Hustad, Bath University, 1984.
20 ' Applies Discrete Vortex Modelling(DVM) to a 20 % ellipse.
30 ' Similar to experimental work of the present study.
40 ' Incorporates pairing as proposed by Wood(15).
45 ' Frequency is determined by the blowing parameters.
50 ' Slot height is 0.762mm (.030") at 96.5 % chord.
60 ' Freestream velocity is 30 m/s.
70 ' Maximum number of vortices N1 is 400.
80 ' Maximum number of passive points P2 is 80.

100 DIM R(401)              ' Radius of vortex core in m.
110 DIM Z(401)              ' Length along vortex sheet in m.
120 DIM G(802)              ' Strength of each vortex at T0=t
130 DIM T(802)              ' Age of each vortex
140 DIM U(80),V(80)         ' Passive point velocity components
150 DIM X(1,880),Y(1,880) ' Location of vortices at T0=t in column 0
                            and T0=t+dt in column 1 of the arrays.
160 DIM D(40)               ' Dummy array for variables

170 REM ****** Listing of the D() array variables ********
```

Array No.	Variable	Comments
1	R	TE radius wrt XTE (see D(27)).
2	H	Slot height, h.
3	R0	Radius to the lip (ie. R+H).
4	L1	No. of external vortices.
5	N2	No. of passive point rows.
6	P2	No. of passive points.
7	P	No. of pairings.
8	L0	Tabulation step for print out of results (default=1).
9	T0	No. of iterations.
10	T1	Time-step, dt.
11	F1	Frequency, 1/dt.
12	K2	Starting length ratio, ro/s.
13	C1	Lift coefficient, CL.
14	Not used	
15	C3	Blowing coefficient, Cj.
16	W3	Jet-exit velocity.
17	K3	Downstream cut-off line.
18	V0	Free-stream velocity.
19	A3	Angle between passive points wrt XTE.
20	G	Total circulation in m2/s.
21	G0	Initial vortex strength.
22	K1	Decay rate.
23	R1	Initial vortex core radius, ro.
24	S0	Artificial viscosity.
25	Q0	Angle to slot from chord line.
26	Q1	Angle to first passive point.
27	X0	TE axes datum, XTE.
28	C	Chord length.
29	D(29)	Percentage thickness, t/c.
30	Not used	
31	Not used	

Array No.	Variable	Comments
32	H1	Distance between passive point rows.
33	C9	Chordwise slot location.
34	Not used	
35	Not used	
36	F4	Flag used when running as absentee job.
37	F5	Flag set to display induced velocity.
38	F6	Flag set to show pairing process.
39	F7	Flag set to show image vortices.
40	D(40)	If =1 then quits program.

```
200 REM ****** Set the default input parameters in D() array ******

210 D(2)=.03*.0254                  ' Slot height h in m.
220 D(5)=4 : D(6)=80                ' 80 passive points distributed in
                                      four rows around the TE.
230 D(8)= 1                         ' Tabulation step used when printing
                                      results.
240 D(9)=600                        ' Number of iterations.
250 D(12)=.20                       ' Initial vortex spacing K2.
260 D(15)=.01                       ' Blowing coefficient Cj.
270 D(17)=2.1                       ' Downstream cut-off line K3.
280 D(18)=30                        ' Freestream velocity in m/s.
290 D(22)=100                       ' Decay rate K helps to simulate
                                      entrainment.
300 D(23)=.0002                     ' Initial core radius in m.
310 D(24)=.013                      ' Artificial viscosity - the value
                                      (gamma 0) has been taken from
                                      the work by Smith(21).
320 D(19)= 5*PI/180                 ' Passive point angular spacing.
330 D(26)=15*PI/180                 ' Angle to the first passive point.
340 D(28)=24*.0254                  ' Chord (24") in m.
350 D(29)=20/100                    ' 20% thickness of ellipse.
360 D(32)=D(2)*2                    ' Passive point row spacing (H1)
                                      set to 2h.
370 D(33)=.965                      ' Chordwise location of the TE slot.

380 D(37)=0 : D(38)=0 : D(39)=0 ' When set to 1 then these act as
    flags which are useful  for checking induced velocity, the
    pairing process and the image vortices respectively.

1000 L$="DISCRETE VORTEX MODEL OF A C=C ELLIPSE" ' Title string.

1010 CALL "INIT" (L$,D())   ' This subroutine allows interactive
     use of the program. For listing see section 8.2.2.

1020 if D(40)=1 goto 9900   ' Stops the program.

2000 CALL "MAIN" (X(,),Y(,),Z(),U(),V(),G(),T(),R(),D()) ' This
     routine includes the main number crunching algorithm. For
     listing see section 8.2.3.

6000 CALL "RESULT" (X(,),Y(,),Z(),U(),V(),G(),T(),R(),D()) ' This
     routine presents the results in tables or as data stored on
     files. For listing see section 8.2.4.

6010 if D(36)=0 goto 1000   ' Flag used when doing absentee runs.

9900 end
```

8.2.2 INIT - Subroutine Programme Listing

```
10  SUB "INIT" (L$,D()) ' Initialises program DVM-Ellipse.
20  ' Allows interactive use of program. Displays default input
30  ' data on the terminal and prompts for new input, run or quit.

100 REM ********** Define variables from D() array ************

110 H=D(2)    : K2=D(12)
120 C3=D(15) : V0=D(18) : G=D(20) : C=D(28)
130 F4=D(36)

200 REM ********** Initialise program variables ***************

210 gosub 650 : gosub 500       ' Display on terminal
215 if F4=1 goto 810            ' Exit sub on absentee run
220 print "Enter #1-#11,'value' of parameter" : print
225 print "Enter 12,0 to run program"         : print
230 print "Enter 12,1 to quit program ";      : input i,j

235 REM ***** Waits on line 230 for interactive input ********
240 on i goto 290,300,310,320,330,340,350,360,370,380,390,800

280 REM ***** Change program variables if desired ************

290 C=j/500   : D(28)=C : goto 200      ' Chord in m.
300 D(29)=j             : goto 200      ' Thickness/Chord ratio.
310 D(33)=j/100         : goto 200      ' Chordwise slot position in %.
320 H=j/1000 : D(2)=H   : R0=D(1)+D(2)
325 D(3)=R0             : goto 200      ' Slot height in mm.
330 D(6)=j              : goto 200      ' Number of passive points.
340 D(9)=j              : goto 200      ' Number of iterations.
350 K2=j : D(12)=K2     : goto 200      ' Initial spacing, s=ro/K2
360 C3=j : D(15)=C3     : goto 200      ' Blowing coefficient Cj.
370 V0=j : D(18)=V0     : goto 200      ' Free-stream velocity in m/s
380 D(22)=j             : goto 200      ' Vortex decay constant
390 D(23)=j/1000        : goto 200      ' Initial vortex core size in mm

500 ' ***** Display variables on 80 character width terminal ******
503 print "**************** ";L$;" ***************** " : print
505 print" 1 Half-chord ="; : print using "-####.# mm", D(28)*500;
510 print tab(26); : print using " 2 Thick/Chord =-#.##",D(29);
515 print tab(52); : print using "   TE Axes =-####.# mm",D(27)*1000
520 print" 3 Slot chord  = "; : print using "-##.## %", D(33)*100;
525 print tab(26); : print using " 4 Slot height =-#.## mm",D(2)*1000;
530 print tab(52); : print using " 5 Passive points =-###",D(6)
540 print " 6 Iterations = ";D(9);tab(29);"Vortices    = ";D(4);
550 print tab(55);"Pairings = ";D(7) : print
560 print using "   CL=-#.####",D(13);
562 print tab(29); : print using "CD=-#.####",D(14) ;
565 print tab(52); : print using " 7 ro/s     =-#.##",D(12) : print
570 print tab(52); : print using "   Freq     =-###.# kHz",D(11)/1000
580 print using " 8 C(mu) =-#.###",D(15);
585 print tab(29); : print using "Vj =-###.# m/s",W3;
590 print tab(52); : print using " 9 Ufs      =-###.# m/s",D(18)
600 print using "10 Decay =-####",D(22); : print tab(29);
610 print using "Go =-#.#### m2/s",D(21); : print tab(52);
615 print using "11 Core rad =-#.## mm",1000*D(23)
620 print : return ' End of display routine ************************
```

```
650 REM ************ Subroutine to calculate Blowing parameters ****

660 A=C/2 : B=C*D(29)/2 : X6=D(33)*C-A ' Calculate TE geometry.
662 Y6=B*sqr(1-(X6/A)^2)               ' Slot co-ordinates (x6,y6).
665 Q6=atn(D(29)^2*X6/Y6) : Q0=PI/2-Q6 : D(25)=Q0  ' Angle to slot.
670 X3=Y6/tan(Q0) : R=sqr(X3*X3+Y6*Y6)             ' XTE=x6-x3
672 D(1)=R : D(27)=X6-X3 : D(3)=R+H : R0=D(3) ' R is the distance from
                                                 from XTE on the x-axis
                                                 to the blowing slot.

675 CALL "PFLOW" (U1,V1,X6,Y6,D())       ' Potential flow at the lip.

680 W7=SQR(U1^2+V1^2) : A0=C3*V0^2/(2*H/C)
690 W3=(W7+SQR(W7^2+4*A0))/2 : D(16)=W3   ' Jet exit velocity.
695 D(11)=K2*W7/D(23)+(W3-W7)/(4*PI*H)    ' Frequency (see eqn.4.10).
697 D(10)=1/D(11) : T1=D(10)              ' Time-step dt=1/f.
700 A1=(W3-W7)*T1 : R8=R*R/R0 : B1=2*PI*(R0-R8)
710 IF A0<>0 then goto 730            ' Check for Cj=0.
720 G0=0                : goto 750
730 A2=1/A1 : B2=1/B1 : G0=W7/(A2-B2) ' Initial vortex strength.
750 D(13)=2*G/(C*V0)  : D(21)=G0 ' Calculate lift coefficient CL.
760 return ' End of routine for the blowing parameters **********

800 D(40)=j                               ' j=1 to quit program.


810 SUBEND
```

8.2.3 MAIN - Subroutine Programme Listing

```
10  SUB "MAIN" (X(,),Y(,),Z(),U(),V(),G(),T(),R(),D())
20  ' Main subroutine for DVM-Ellipse. Last edit 28 Nov 1984.
30  ' Applies Discrete Vortex Modelling to a cylinder/ellipse.
40  ' Incorporates pairing as proposed by Wood(15).
50  ' Set F5 to check the induced vortex velocity.
60  ' Set F6 to check the pairing procedure.
70  ' Set F7 to check the image vortices.
75  ' Sets F8 to remove end vortex.
80  ' P2 is number of passive points, N2 is number of rows
85  ' K3 is downstream cut-off point. The empirical relationship
90  ' in line 170 has been derived from experience.

100 REM ************ Declare variables from D() array ************

120 R=D(1)   : R0=D(3)  : N2=D(5)  : P2=D(6)  : T0=D(9)    : T1=D(10)
130 V0=D(18) : A3=D(19) : G0=D(21) : K1=D(22) : R(1)=D(23) : S0=D(24)
140 Q0=D(25) : Q1=D(26) : X0=D(27) : C=D(28)  : H1=D(32)
150 F5=D(37) : F6=D(38) : F7=D(39) : D=2*PI   : F8=0  : T2=0

160 A=C/2 : B=A*D(29) : M2=1-D(29)*D(29)    ' Ellipse geometry.
170 K3=D(17)*D(29)^0.275                    ' Downstream cut-off.
180 P=0                                     ' Reset pairing counter.
190 DIM I$(100)              ' Used to store image format strings.

650 REM ***************** Vortex counters ************************
680 L =P2+2      ' L is total number of vortices in the flow field
690 L1=(L-P2)/2  ' Total number of external vortices
700 L2=L1+1      ' First image vortex
710 L3=L1*2      ' Final image vortex
720 L4=L3+1      ' First passive point

730 S=S0*sqr(G0) ' Artificial viscosity as used by Smith(21).

740 Y(0,1)=R0*sin(Q0) : X(0,1)=R0*cos(Q0)+X0   ' First vortex at lip.
742 G(1)=G0  : T(1)=0             ' Strength and age of first vortex.
745 Y=Y(0,1) : X=X(0,1) : T2=0    ' T2 is set =1 on final iteration
                                    (see line 785).

750 for K=1 to T0 ' ****************** Time Loop ******************
760 R8=R*R/R0 : G(L2)=-G0 : T(L2)=0            ' First image vortex.
770 Y(0,L2)=R8*sin(Q0)    : X(0,L2)=R8*cos(Q0)+X0
775 if K<>T0 goto 835 : X0=D(27)         ' Check for final iteration.

785 T2=1 : for J1=1 to  N2 : N3=int(P2/N2) ' Final iteration only ****
790 for J=L4+(J1-1)*N3 to L4+J1*N3-1 : J2=J-L4 ' Passive points **   R
795 Q=Q1-A3*(J2-N3*int(J2/N3)) ' Angular location in radians.    *   O
800 Z=tan(Q)/B : E2=Z*Z+(1/A)^2                                  *   W
805 E1=-2*X0*Z*Z : E0=Z*Z*X0*X0-1                                *
810 X=(sqr(E1*E1-4*E2*E0)-E1)/(2*E2)                             *   C
812 Y=B*sqr(1-(X/A)^2)                                           *   O
815 X=X-X0                                                       *   U
817 R3=sqr(X*X+Y*Y) ' Radial distance to passive point.          *   N
820 X(0,J)=(R3+(J1-1)*H1)*cos(Q)+X0                              *   T
825 Y(0,J)=(R3+(J1-1)*H1)*sin(Q)                                 *   E
830 next J  ' ************************************************   R

832 next J1 ' ********* PASSIVE POINTS ROW COUNTER ******************
```

```
835 for M=1 to L1+(P2+L1)*T2 ' External vortex loop ******************

840 U=0 : V=0                          ' Total velocity component
850 X9=X(0,M) : Y9=Y(0,M)              ' Local coordinate of vortex M
875 CALL "PFLOW" (U1,V1,X9,Y9,D())     ' Calculate potential flow at M
885 U2=0 : V2=0                        ' Zero induced velocity components

890 if F5=0 goto 920 : print ' Heading for displaying induced velocity.
900 print "    M      N       R2          W2          U2          V2"
910 print "                   mm          m/s         m/s         m/s"

920 for N=1 to L3 ' Vortex induced velocity loop ********************
930 if M=N goto 1050 : if G(N)=0 goto 1050 ' Skip to next vortex    *
940 X2=X(0,N)-X9 : Y2=Y(0,N)-Y9                                     *
950 R2=sqr(X2^2+Y2^2)      ' Distance M to N                        *
955 if R(N)>R2 goto 1050  ' Checks for realistic vortex spacing     *
960 if T(N)=0  goto 990                                             *
970 E=R2*R2/(4*S*T(N))          : if E>10 goto 990 ' Skip exponent  *
980 W2=G(N)*(1-exp(-E))/(D*R2) : goto 1000 '                        *
990 W2=G(N)/(D*R2)                                                  *
1000 U2=U2+W2*Y2/R2 : V2=V2-W2*X2/R2                                *
                                                                    *
1010 if F5=0 goto 1050 '                                            *
1015 I$= " -###   -###   -###.###   -###.###    -###.###    -###.###"
1020 print using I$, M,N,R2*1000,W2,W2*Y2/R2,-(W2*X2/R2)             *
                                                                    *
1050 next N ' End of induced velocity loop ' ************************

1060 U=U1+U2 : V=V1+V2 ' Velocity components at vortex M.

1070 if K=T0  goto 1075 : goto 1090
1075 if M>L3  goto 1080 : goto 1090 ' Final iteration only.

1080 J=M-L3 : U(J)=U : V(J)=V ' Passive points
1090 X(1,M)=X(0,M)+U*T1 : Y(1,M)=Y(0,M)+V*T1 ' New M

1100 if M<>L1  goto 1110
1105 M=L3 ' Skip image vortices and goto the passive points.

1110 next M ' End of exernal vortex loop ****************************

1120 for M=L1 to 1 step -1 ' *** March vortices **********
1130 X(0,M+1)=X(1,M) : Y(0,M+1)=Y(1,M) '                  *
1140 T(M+1)=T(M)+T1  : G(M+1)=G(M)*(1-K1*T1) '            *
1150 R(M+1)=R(M)*(1+K1*T1/2) '                            *
1155 next M ' ******************************************

1160 ' ******** Calculate the vortex spacing *********************
1170 for J=1 to L1 : X=X(0,J+1)-X(0,J) : Y=Y(0,J+1)-Y(0,J)
1180 Z=sqr(X*X+Y*Y) : Z(J+1)=Z(J)+Z
1182 if Z=0 goto 1800  ' Check for error during the pairing process
1184 if K=T0 goto 1500 ' Skip pairing on final iteration

1186 if X(0,J+1)<K3*A goto 1190 : F8=1 ' Remove end vortex if a
                                       external vortex has passed
                                       beyond the cut-off line.

1190 if R(J)+R(J+1)<Z goto 1500 ' Check if adjacent vortices touch.
```

```
1200 REM ********* Calculating the vortex spacing ******************

1210 if F6=0 goto 1290 ' Heading for displaying the pairing process.
1220 print
1224 print "Iteration No ";K;"   No of vortices ";L1
1226 print "  Pair vortices";J;"and";J+1
1230 print : print "    X         Y         Z         R         G"
1240 print "   cm        cm        cm        mm        m2/s" : print
1250 for J1=J to J+1
1255 I$= "-##.###  -##.###  -###.##   -##.###   -#.####"
1260 print using I$,100*X(0,J1),100*Y(0,J1),100*Z(J1),1000*R(J1),G(J1)
1270 next J1 ' ************************************************
1280 print

1290 REM ************* Pair adjacent vortices ******************
1300 Z1=Z*R(J+1)/(R(J+1)+R(J)) : Z(J)=Z(J)+Z1
1310 X(0,J)=X(0,J)+X*Z1/Z : Y(0,J)=Y(0,J)+Y*Z1/Z ' New location.
1320 R(J)=sqr(R(J)*R(J)+R(J+1)*R(J+1))           ' New radius.
1325 T(J)=T(J+1) ' Set time to the oldest of the two vortices.
1330 G(J)=G0*(R(1)/R(J))^2              ' Combined circulation.

1340 if F6=0 goto 1370
1350 print using L$, 100*X(0,J),100*Y(0,J),100*Z(J),1000*R(J),G(J)
1360 print

1370 if J=L1 goto 1410 ' No need to back-step if only the end vortex
                       vortex has paired.

1380 for J1=J+1 to L1  : R(J1)=R(J1+1)       ' Back-step vortices
1390 X(0,J1)=X(0,J1+1) : Y(0,J1)=Y(0,J1+1)   ' when pairing has
1400 T(J1)=T(J1+1) : G(J1)=G(J1+1)           ' occured.
1402 next j1

1404 L=L-2   : L1=L1-1 : L2=L1+1     ' Reset the vortex counters.
1406 L3=L1*2 : L4=L3+1 : P=P+1       ' Increment pairing counter.
1408 goto 1160                  ' Re-calculate the vortex spacing.

1410 if F6=0 goto 1480
1420 print "  M        Z         R         G"
1430 print "          cm        mm        m2/s" : print
1435 I$="-###    -##.###   -#.###   -#.####"
1440 for J1=1 to L1 ' ************************************
1450 print using I$, J1,100*Z(J1),1000*R(J1),G(J1) '       *
1460 next J1 ' ***************************************

1480 L=L-2 : L1=L1-1 : L2=L1+1 : L3=L1*2 : L4=L3+1 ' These two
1482 P=P+1 ' lines reset the vortex counters if the end vortex
           has paired.

1500 next J ' ****** End of the vortex spacing loop *************

1502 if F8=0 goto 1510           ' Remove end vortex if F8=1.

1504 L=L-2 : L1=L1-1 : L2=L1+1 : L3=L1*2 : L4=L3+1
1506 F8=0               ' Reset flag(8) to 0 (see line 1186).
```

```
1510 for J=L2 to L3 ' Image vortex J ****************************
1520 J9=J-L1        ' Exterior vortex of J
1525 X9=X(0,J9+1) : Y9=Y(0,J9+1)
1530 X=X9-X0 : Y=Y9 : R9=sqr(X*X+Y*Y) : Z=Y/X
1532 gosub 1810
1535 M1=Y4/X4/D(29)/D(29) : X0=X9-Y9/M1
1537 if X0<A goto 1540 : X0=D(27) ' Check that XTE is inside ellipse.
1540 X=X9-X0 : Y=Y9 : R9=sqr(X*X+Y*Y) : Z=Y/X
1542 gosub 1810                    ' Repeat iterative procedure once.
1545 X5=X4-X0 : R=sqr(X5*X5+Y4*Y4) : R8=R*R/R9
1550 T9=Y4/X5 : Q=atn(T9) : X(0,J+2)=R8*cos(Q)+X0
1555 Y(0,J+2)=R8*sin(Q) : G(J+2)=-G(J9+1) : T(J+2)=T(J9+1) : X0=D(27)

1560 next J ' ***************************************************

1570 if F7=0 goto 1690
1580 print                        ' Heading for image vortex table.
1585 print " Ext   X     Y     G     T     Im    X     Y     G     T"
1590 print "      cm    cm   m2/s   ms          cm    cm   m2/s   ms"
1595 I$= "-## -#.## -#.## -.### -.###  -## -#.## -#.## -.### -.###"

1600 for J=L2 to L3 : J9=J-L1 ' ************************************
1610 X9=X(0,J9+1)*100 : Y9=Y(0,J9+1)*100 : G9=G(J9+1) : T9=T(J9+1) '*
1615  X=X(0,J+2)*100  :  Y=Y(0,J+2)*100  :  G=G(J+2)  :  T=T(J+2)  '*
1620 print using I$, J9,X9,Y9,G9,1000*T9,J,X,Y,G,1000*T             '*
1625 next j ' ***************************************************

1690 if K=T0 goto 1780 ' Final iteration only

1700 L=L+2 : L1=(L-P2)/2 : L2=L1+1 : L3=L1*2 : L4=L3+1 ' Reset counters

1770 next K ' ****** End of time loop ******************************

1780 G=0 : for J=1 to L1
1785 G=G+G(J) : next J : D(20)=G

1790 D(13)=2*G/(C*V0) : D(4)=L1 : D(7)=P : goto 1830

1795 REM *** Error routines which check for instability ********
1800 D(36)=2  : goto 1830 ' Problem with vortex spacing
1805 D(36)=3  : goto 1830 ' Problem with XTE

1808 REM This routine solves for intercept between the ellipse and *
1809 REM a straight line with slope Z passing through (X0,0).      *
1810 E2=Z*Z+D(29)*D(29) : E1=-2*X0*Z*Z : E0=(X0*Z)^2-B*B           *
1820 X4=(sqr(E1*E1-4*E2*E0)-E1)/(2*E2) : Y4=Z*(X4-X0)             *
1825 return ' ***************************************************

1830 SUBEND
```

8.2.4 RESULT - Subroutine Programme Listing

```
10  SUB "RESULT" (X(,),Y(,),Z(),U(),V(),G(),T(),R(),D())
20  REM Tabulates and stores data on file "ellipse.data".
100 DIM B(80)          ' Flow angle wrt surface
110 DIM C(80)          ' TE pressure coefficient
115 DIM W(80)          ' Passive point velocity in m/s
125 R=D(1) : H=D(2) : R0=D(3) : L1=D(4) : P2=D(6)
130 V0=D(18) : F4=D(36) : N3=int(D(6)/D(5)) : A3=D(19)
140 Q0=D(25) : Q1=D(26) : X0=D(27) : C=D(28)

210 for M=1 to P2 ' ********** Passive points *********************
220 B(M)=atn(V(M)/U(M))*180/D(35) '                               *
222 if U(M)>0 goto 225 : B(M)=B(M)-180 ' Flow angle wrt chord.    *
225 W(M)=sqr(U(M)*U(M)+V(M)*V(M)) '                               *
230 C(M)=W(M)*W(M)/(V0*V0)-1 : next M ' ***************************

250 on F4+1 goto 1000,600,270,280

270 print "Error with vortex spacing" : goto 1800
280 print "Error with Xo "           : goto 1800

300 REM ************************* Tabulate Results ***************
320 print "  M      X        Y         Z        T         G        R"
325 print "        cm       cm        cm     msec      m2/s      mm"
335 I$="###   -##.###  -##.###  -###.##  -##.###   -##.###  -##.###"
340 M=0 : X=100*X(M,1) : Y=100*Y(M,1) : Z=0 : T=0
350 print using I$, M,X,Y,Z,T,G(1),1000*R(1)
370 for M=1 to L1 step D(8) ' ***** External vortices **************
380 X=100*X(1,M) : Y=100*Y(1,M) : T=1000*T(M+1) '                  *
390 print using L$,M,X,Y,100*Z(M+1),T,G(M+1),1000*R(M+1)'           *
400 next M : goto 1000 ' ******************************************

500 print " M     X       Y        W     Beta     Cp       U       V"
505 print "       cm      cm      m/s     deg              m/s     m/s"
507 I$="### -###.## -###.## -###.## -###.## -###.## -###.##  -###.##"
510 for M=1 to P2 : J=M+L1*2 ' ******** Passive points ***************
540 print using I$, M,100*X(1,J),100*Y(1,J),W(M),B(M),C(M),U(M),V(M)
550 next M : goto 1000 ' ******************************************

600 file#1:"ellipse.data"  ' Print data onto file ********************
610 for j=1 to 34 : print #1 :D(j); : next j
620 for j=1 to L1 step D(8)
630 print #1: X(1,j);Y(1,j);Z(j+1);T(j+1);G(j+1);R(j+1);
640 next j
650 for J=1 to P2 : print #1: B(J);C(J);X(1,J+L1*2);Y(1,J+L1*2);
670 next j

690 if F4=0 goto 1000 else goto 2000

1000 print : print "********** dvm table ************" : print
1020 print " #1   Print external vortices"
1030 print " #2   Print passive points"
1035 print " #3   Store data in file"
1040 print " #4   Quit" : print " #5   Continue" : print
1050 print " Enter option #1-#5 "; : input i
1060 on i goto 300,500,600,1800,2000

1800 D(36)=1 ' Set flag F4
2000 SUBEND
```

8.2.5 PFLOW - Subroutine Programme Listing

```
10 SUB "PFLOW" (U,V,X,Y,D()) ' Calculates potential flow.
12 REM ** Written by C.W.Hustad - Bath University, May 1984.
15 REM ** Note that the variables used in this subroutine
20 REM ** are not compatible with the main program.
25 V0=D(18)          ' Free-stream velocity in m/s.
30  C=D(28)          ' Chord length in m.
35  T=D(29)          ' Thickness to chord ratio.
40  K=0              ' Circulation due to rotation (not used).

50  A=(1+T)*C/4 : B=sqr((1-T)*A*C/4)

60 REM ** Transfer (x,iy) in z-plane to (e,in) in the g-plane **
65 REM ** Use transformation z = g + (b^2)/g on the circle IgI=a
70 REM ** in the g-plane where a is radius, z and g are complex.
75 X7=X : Y7=Y : gosub 300 : Q=Q7 : R=R7
80 R1=R*R : Q1=2*Q                              ' z^2
85 X2=R1*cos(Q1)-4*B*B : Y2=R1*sin(Q1)
90 X7=X2 : Y7=Y2 : gosub 300 : Q2=Q7 : R2=R7
95 R3=sqr(R2) : Q3=sgn(Q)*abs(Q2/2)             ' SQR(z^2-4b^2)
98 E=(R*cos(Q)+R3*cos(Q3))/2 : N=(R*sin(Q)+R3*sin(Q3))/2

100 REM ************** Transformation Function ***************
110 X7=E : Y7=N : gosub 300 : M=Q7 : S=R7
120 S1=S*S : M1=2*M : E1=S1*cos(M1) : N1=S1*sin(M1)
130 E2=E1-B*B : N2=N1
140 X7=E2 : Y7=N2 : gosub 300 : M2=Q7 : S2=R7
150 S3=S1/S2 : M3=M1-M2 : T1=S3*cos(M3) : T2=S3*sin(M3)

160 REM ************** Complex Function **********************
165 REM ** Velocity (u-iv) at (e,in) in the z-plane **********
170 S4=V0*A*A/S1 : M4=-M1
180 E5=K*sin(M)/S : N5=K*cos(M)/S
190 X7=E5 : Y7=N5 : gosub 300 : M5=Q7 : S5=R7
200 C1=V0-S4*cos(M4)+S5*cos(M5) : C2=-(S4*sin(M4))+S5*sin(M5)
210 U=C1*T1-C2*T2 : V=-(C1*T2+C2*T1) : goto 400

300 REM ************** Subroutine for arctan *****************
310 if X7=0 goto 370 : if Y7=0 goto 380
320 W=Y7/X7 : if X7>0 goto 340
325 Q7=atn(W)-PI : if Y7<0 goto 390 : Q7=Q7+2*PI : goto 390
340 Q7=atn(W) : goto 390
370 Q7=PI/2*sgn(Y7) : goto 390
380 Q7=PI/2*(1-sgn(X7))
390 R7=sqr(X7*X7+Y7*Y7) : return ' ****************************

400 SUBEND
```

Table 2.1

Tapping No.		Chordwise Location x/c%		Spanwise location from mid span y/b%	Angle from slot in degrees	Arc angle from slot s/R in radians
LE	TE	LE	TE			
-	79	-	96.64	- 2.04	0	0
18	78	2.93	97.07	1.67	6	.105
19	77	2.52	97.48	- 1.67	12	.209
20	76	2.12	97.88	2.04	18	.314
21	75	1.75	98.25	- 1.30	24	.419
22	74	1.40	98.60	2.41	30	.524
23	73	1.09	98.91	- 2.78	36	.628
24	72	.81	99.19	2.78	42	.733
25	71	.57	99.43	- 2.41	48	.838
26	70	.37	99.63	1.30	54	.942
27	69	.21	99.79	- 2.04	60	1.047
28	68	.09	99.91	1.67	66	1.152
29	67	.02	99.98	- 1.67	72	1.257
30	66	0	100.00	2.04	78	1.361
31	65	- .02	- 99.98	- 1.30	84	1.466
32	64	- .09	- 99.91	2.41	90	1.571
33	63	- .21	- 99.79	- 2.78	96	1.675
34	62	- .37	- 99.63	2.78	102	1.780
35	61	- .57	- 99.43	- 2.41	108	1.885
36	60	- .81	- 99.19	1.30	114	1.990
37	59	-1.09	- 98.91	- 2.04	120	2.094
38	58	-1.40	- 98.60	1.67	126	2.199
39	57	-1.75	- 98.25	- 1.67	132	2.304
40	56	-2.12	- 97.88	2.04	138	2.408

Table 2.1: Location of pressure tappings around LE and TE tubes.

Total pressure	Static pressure
19	57
32	159
45	
70	
83	
95	Yawheads
121	
133	0
146	108
172	
184	Distance in mm from either side of the rake centre-line.

Table 2.2: Location of the total, static and yaw head probes on the 0.38m drag rake.

CRUN No.	C_{D_b} (R_d)	C_{D_r}	ΔC_D%	b'/d	Eqn. number from section 2.2.6
1	1.092	1.097	+ 0.5	8.0	2.26(a)
	(81.4×10^3)	1.105	+ 1.2	8.0	2.26(b)
2	1.061	1.122	+ 5.7	8.3	2.26(a)
	(89.3×10^3)	1.129	+ 6.4	8.3	2.26(b)
3	1.065	1.141	+ 7.1	8.3	2.26(a)
	(89.2×10^3)	1.148	+ 7.2	8.3	2.26(b)
		1.133	+ 6.4	8.0	2.26(b)

Table 2.3: Drag of a cylinder measured directly and using the wake traverse method of Jones(32).

RUN	C_{JTE}	C_N	C_x	C_{Dw}	C_{Mmc}	$alpha_g$ deg	$alpha_\infty$ deg	$q_{f\infty}$ N/m²
64	0.000	-.594	-.0459	.0122	-.1786	-8.70	-5.02	693
54	0.000	-.435	-.0223	.0160	-.1362	-6.80	-4.25	600
63	0.000	-.467	-.0224	.0167	-.1354	-6.80	-4.06	691
49	0.000	-.017	.0087	.0145	-.0030	0.00	.08	659
69	0.000	.179	.0051	.0202	.0689	3.70	2.97	700
65	0.000	.451	-.0296	.0249	.1544	7.70	6.18	692
66	0.000	.462	-.0309	.0243	.1544	7.70	6.14	694

Table 3.1: No Blowing with variation of geometric incidence.

RUN	C_{JTE}	C_N	C_x	C_{Dw}	C_{Mmc}	$alpha_g$ deg	$alpha_\infty$ deg	$q_{f\infty}$ N/m²
49	0.000	-.017	.0087	.0145	-.0030	0.00	.08	659
50	.008	.263	.0090	.0064	-.0330	0.00	-1.23	767
48	.011	.280	.0158	.0117	-.0333	0.00	-1.32	358
47	.020	.576	.0343	.0097	-.0664	0.00	-2.71	441
46	.027	.786	.0579	.0099	-.0925	0.00	-3.69	397
45	.027	.854	.0629	.0063	-.0983	0.00	-4.01	693
44	.037	1.099	.0974	.0018	-.1240	0.00	-5.17	685

RUN	C_{DJ}	C_{DpJ}	$C_{Dk\infty}$	L/D_∞	x_{cp} %	LE_{stag} s/R	TE_{sep} s/R
49	0.0000	-.0001	0.0000	-1.1	32.3	1.36	0.00
50	.0041	.0012	.0078	18.5	60.8	1.40	0.00
48	.0052	.0016	.0116	12.0	60.2	1.42	0.00
47	.0069	.0034	.0292	14.8	60.7	1.48	.42
46	.0082	.0048	.0444	14.4	61.2	1.55	.94
45	.0081	.0052	.0451	16.6	60.9	1.55	.94
44	.0094	.0069	.0725	14.8	60.8	1.61	1.15

Table 3.2: TE Blowing at 0 degs. geometric incidence.

RUN	C_{JTE}	C_N	C_x	C_{Dw}	C_{Mmc}	$alpha_g$ deg	$alpha_e$ deg	q_{fs} N/m²
54	0.000	-.435	-.0223	.0160	-.1362	-6.80	-4.25	600
55	.008	-.124	-.0063	.0100	-.1655	-6.80	-6.08	625
56	.016	.140	.0204	.0050	-.1912	-6.80	-7.62	632
58	.021	.262	.0443	.0094	-.2042	-6.80	-8.34	499
57	.031	.498	.0818	.0008	-.2302	-6.80	-9.72	344
60	.041	.713	.1457	.0134	-.2698	-6.80	-10.99	610
59	.041	.741	.1422	.0024	-.2641	-6.80	-11.15	616

RUN	C_{DJ}	C_{DpJ}	C_{Dke}	L/D_e	x_{cp} %	LE_{stag} s/R	TE_{sep} s/R
54	0.0000	.0002	0.0000	-27.2	18.7	.90	0.00
55	.0046	.0018	.0070	-7.3	59.4	.98	.52
56	.0062	.0034	.0205	5.5	59.6	1.05	.73
58	.0072	.0044	.0305	6.6	59.8	1.06	.84
57	.0087	.0060	.0552	8.9	60.1	1.12	.95
60	.0101	.0083	.0832	7.4	61.6	1.14	1.05
59	.0101	.0082	.0836	8.6	60.9	1.14	1.05

Table 3.3: TE Blowing at -6.8 degs. geometric incidence.

RUN	C_{JTE}	C_N	C_x	C_{Dw}	C_{Mmc}	$alpha_g$ deg	$alpha_e$ deg	q_{fs} N/m²
69	0.000	.179	.0051	.0202	.0689	3.70	2.97	700
74	.015	.726	.0046	.0166	.0137	3.70	.75	531
73	.028	1.084	.0239	.0133	-.0190	3.70	-.71	374

RUN	C_{DJ}	C_{DpJ}	C_{Dke}	L/D_e	x_{cp} %	LE_{stag} s/R	TE_{sep} s/R
69	0.0000	-.0001	0.0000	8.8	11.5	1.60	0.00
74	.0061	.0025	.0185	20.7	60.1	1.72	0.00
73	.0082	.0049	.0477	17.8	59.7	1.80	.80

Table 3.4: TE Blowing at +3.7 degs. geometric incidence.

RUN	C_{JLE}	C_N	C_x	C_{Mmc}	$alpha_g$ deg	LE_{stag} s/R	q_{fs} N/m²
49	0.000	-.017	.0087	.0008	0.00	1.36	659
53	.060	-.008	-.0728	.0097	0.00	None	549
52	.089	.001	-.1222	.0150	0.00	None	365
51	.113	-.015	-.1638	.0164	0.00	None	293

Table 3.5: LE Blowing at 0 degs. geometric incidence.

RUN	C_{JLE}	C_N	C_x	C_{Mmc}	$alpha_g$ deg	LE_{stag} s/R	q_{fs} N/m²
69	0.000	.179	.0051	.0689	3.70	1.60	700
71	.031	.229	-.0353	.1124	3.70	1.41	567
70	.038	.223	-.0348	.1139	3.70	1.40	704
72	.044	.173	-.0232	.0768	3.70	1.58	501

Table 3.6: LE Blowing at +3.7 degs. geometric incidence.

1. TE blowing slot.
2. Wall-jet (Coanda flow) separating from the TE surface.
3. TE separation bubble between the wall-jet and the lower surface boundary-layer.

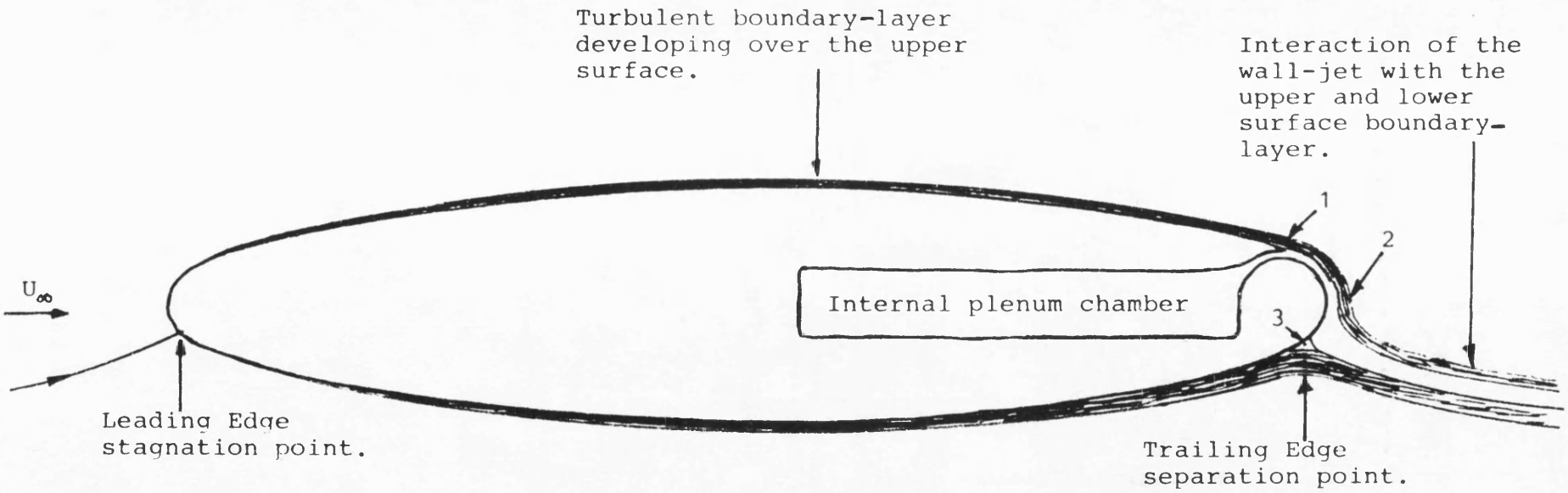

Fig. 1.1: CIRCULATION-CONTROLLED AEROFOIL WITH TE BLOWING.

Fig.1.1

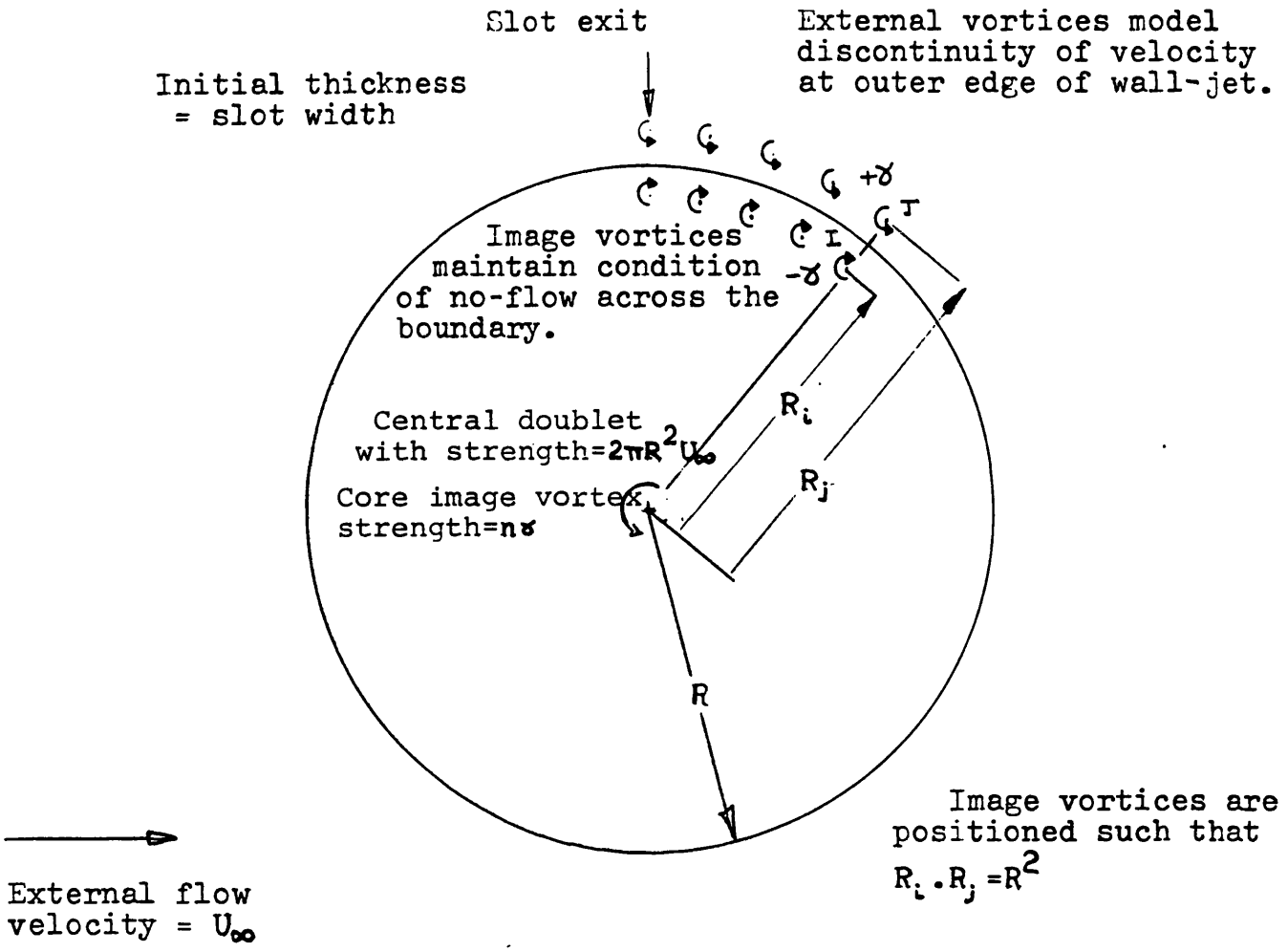

The flow is analysed as a starting problem, a new vortex being introduced after each time step.

Steady Coanda flow of the wall-jet about the cylinder is determined when the configuration of the boundary becomes constant.

n is the number of external vortices.

γ is the strength of each external vortex.

Fig. 1.2: ELEMENTS OF THE DISCRETE VORTEX MODEL PROPOSED BY SMITH(21).

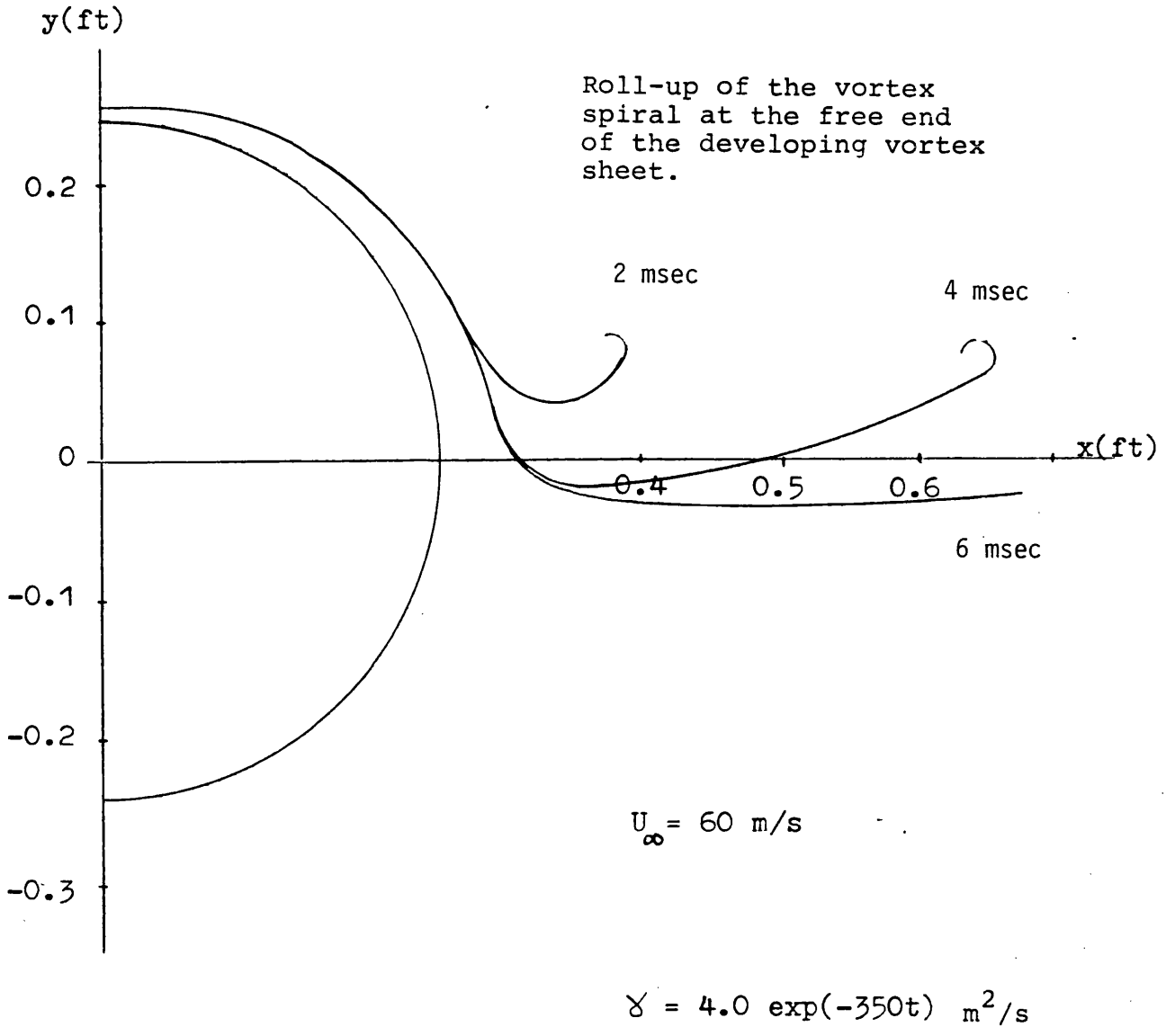

Fig. 1.3: TYPICAL DEVELOPMENT OF THE VORTEX SHEET USING THE METHOD OF SMITH(21).

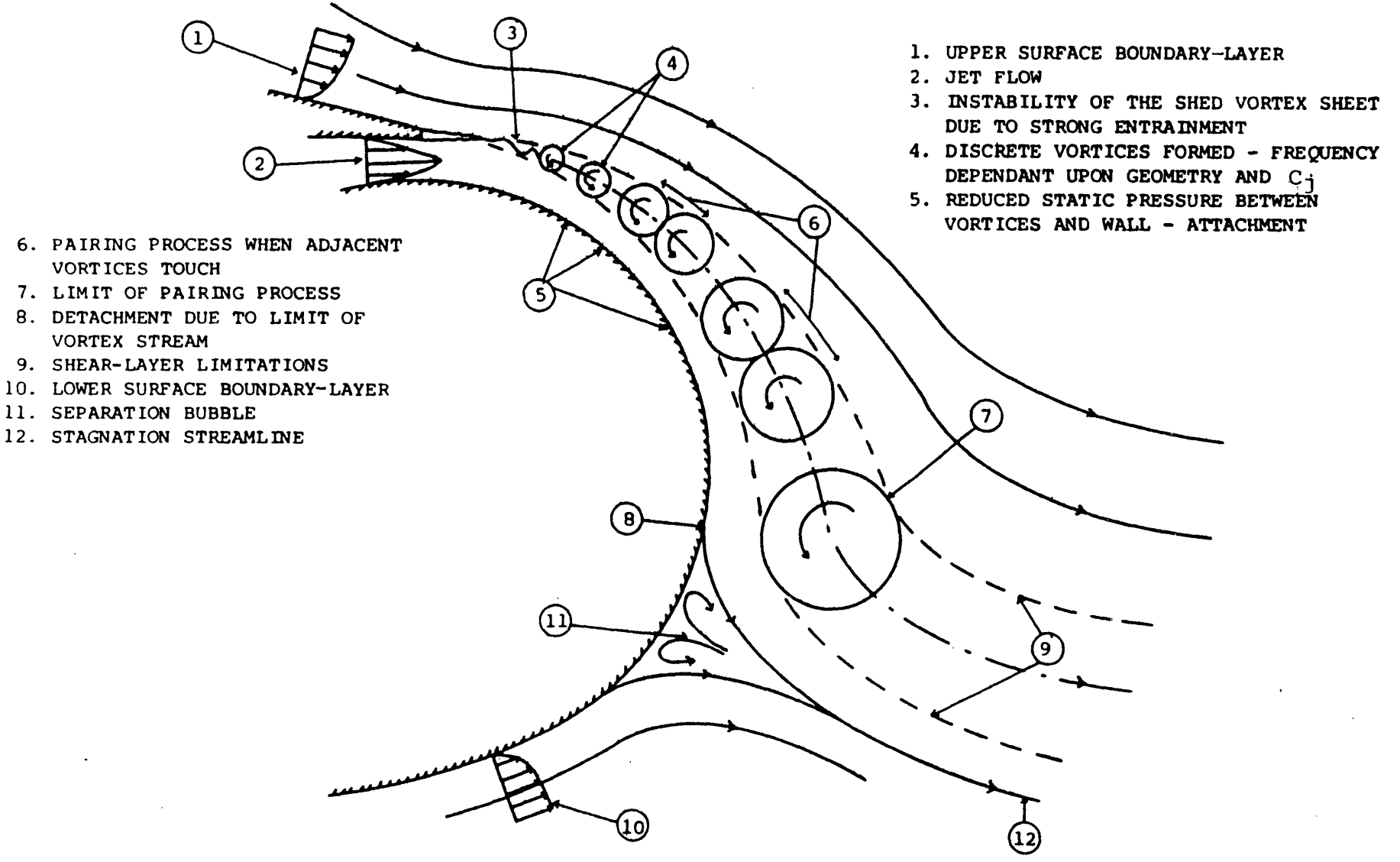

Fig. 1.4: THE TE FLOW-FIELD AS PROPOSED BY WOOD(15).

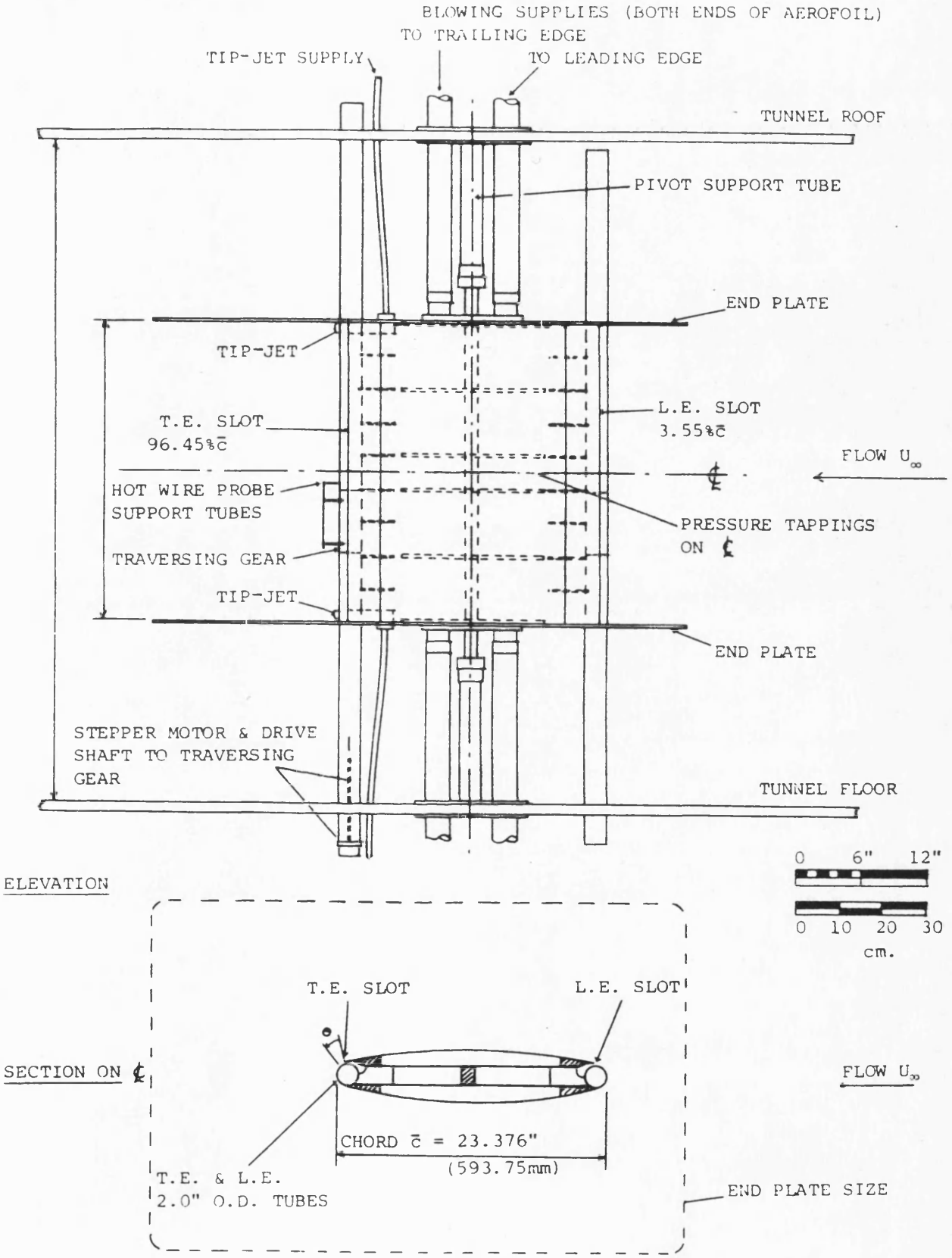

Fig. 2.1: GENERAL ARRANGEMENT OF THE MODEL USED BY WOOD(15).

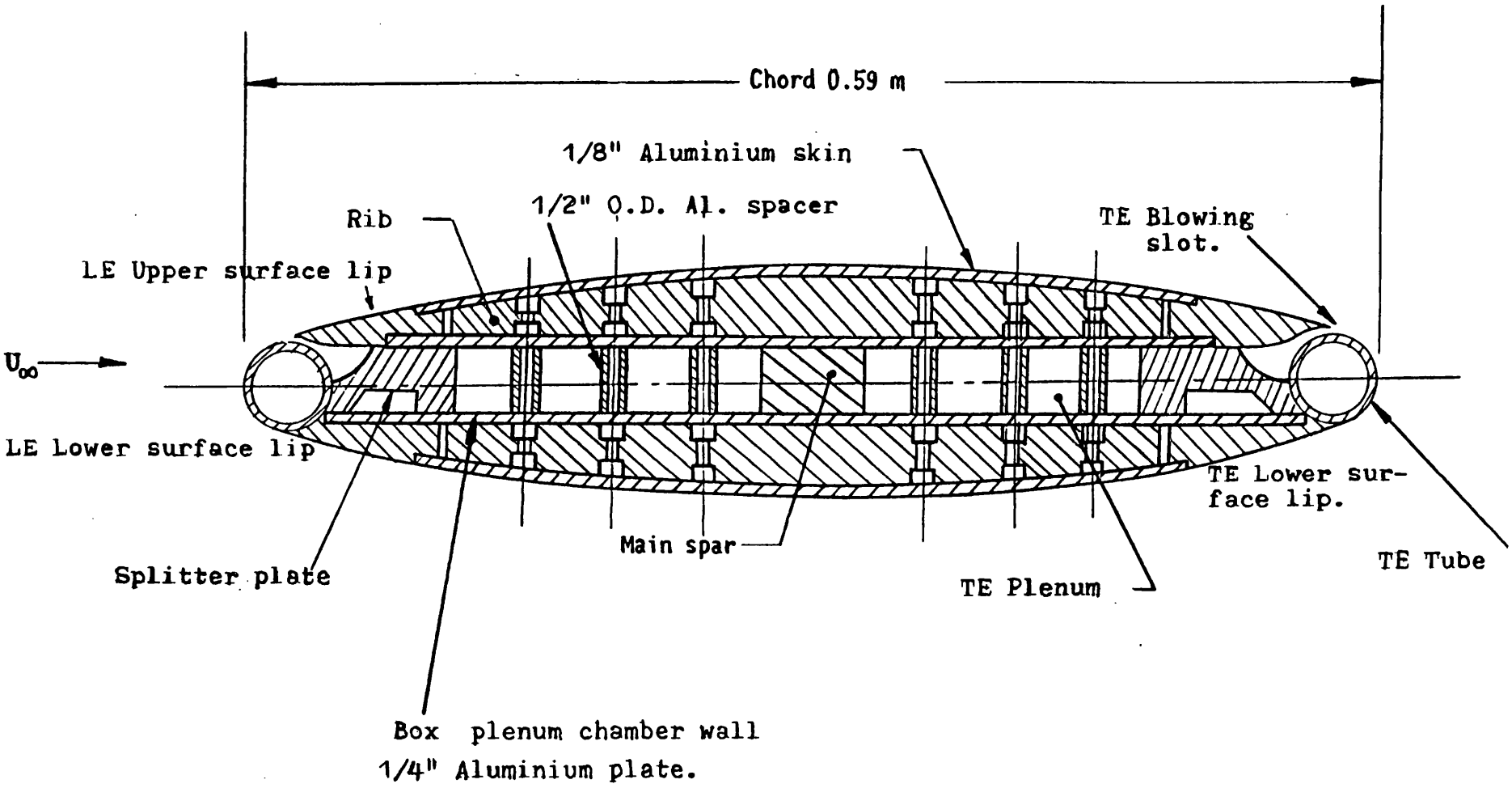

Fig. 2.2: SECTION OF THE MODEL SHOWING INTERNAL PLENUM CHAMBERS.

Fig. 2.2

Dimensions in mm

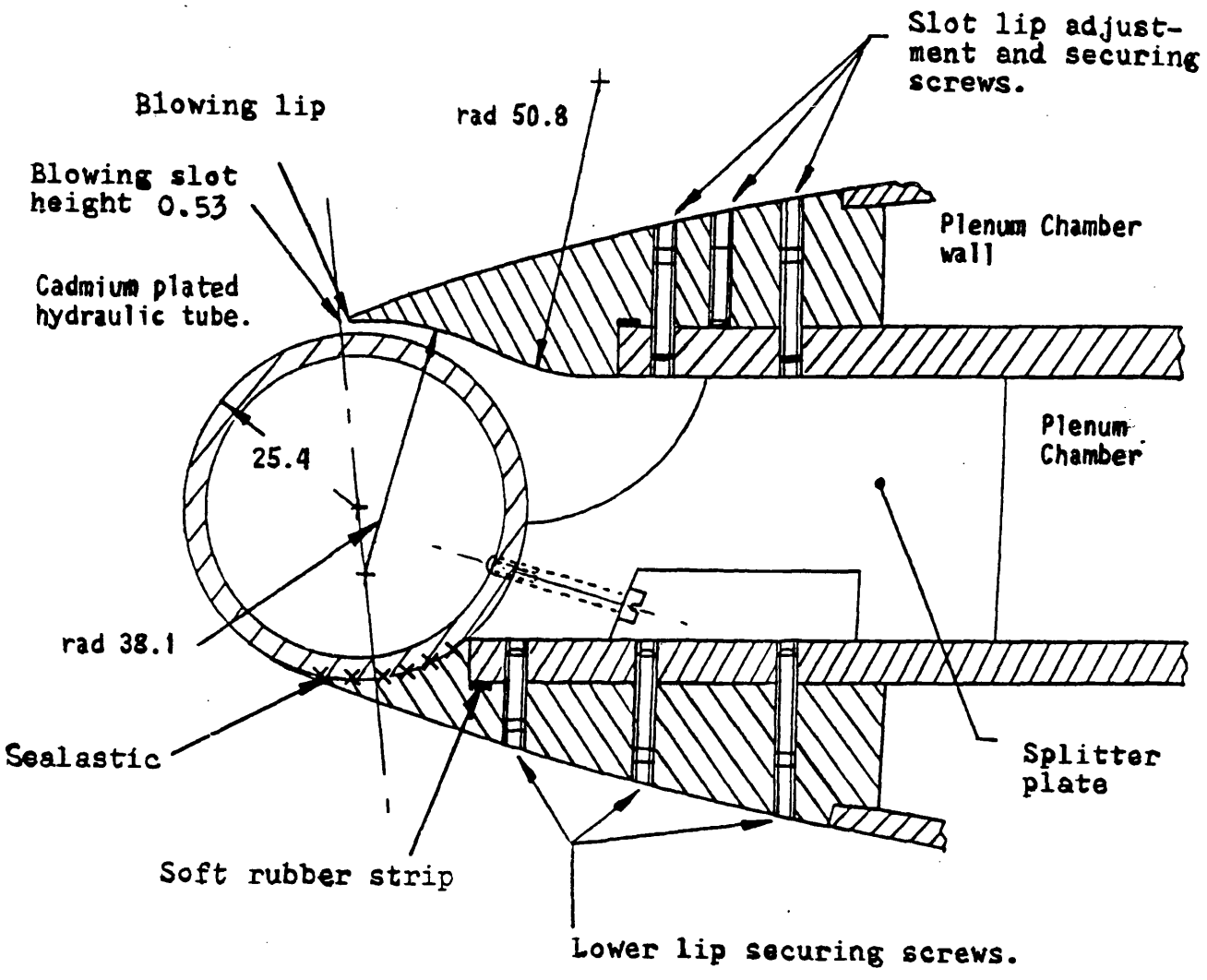

Fig. 2.3: DETAIL OF THE ORIGINAL BLOWING LIP.

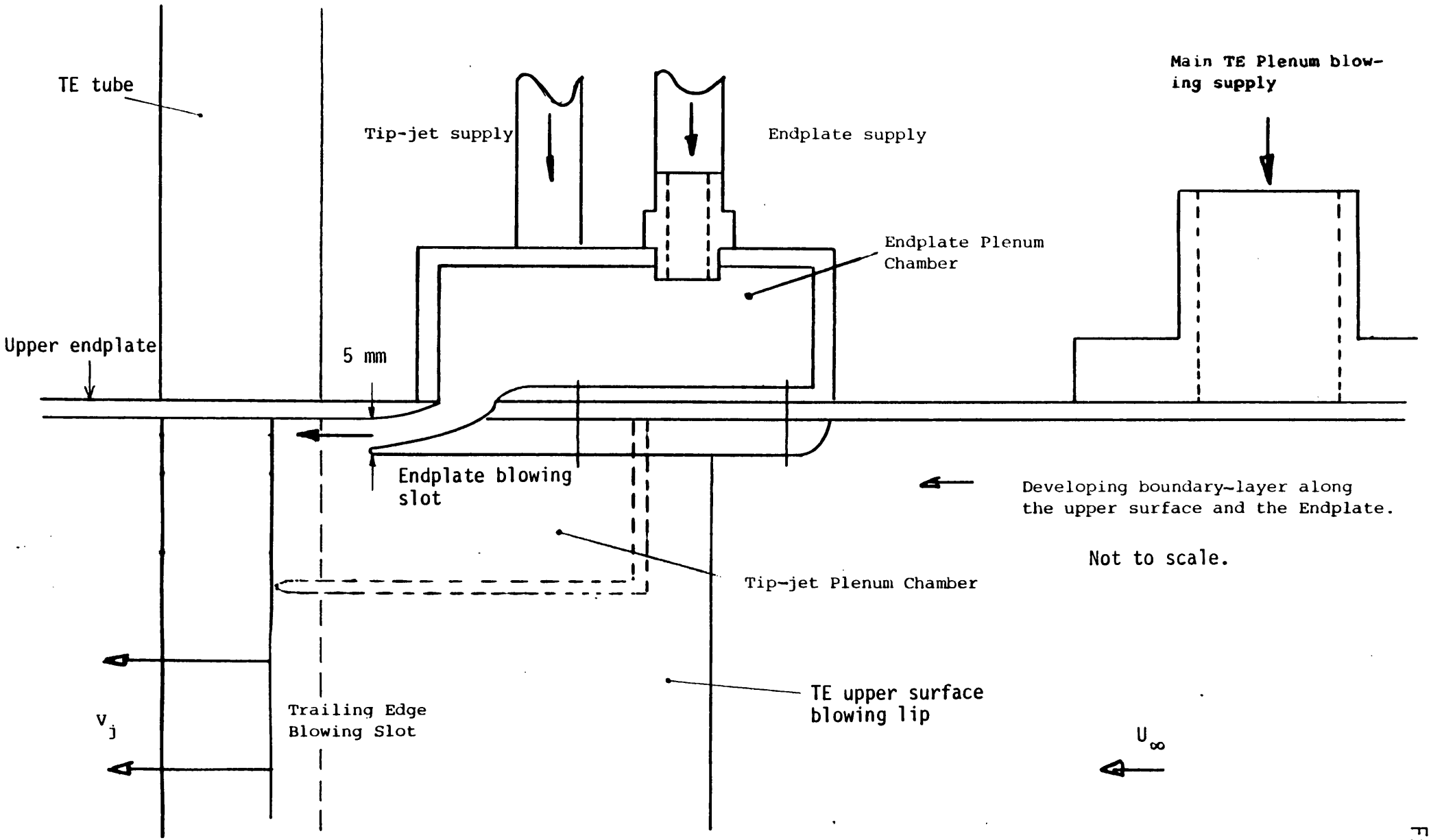

Fig. 2.4: THE MODIFIED BOUNDARY-LAYER CONTROL SYSTEM SHOWING ENDPLATE AND TIP-JET PLENUM CHAMBERS.

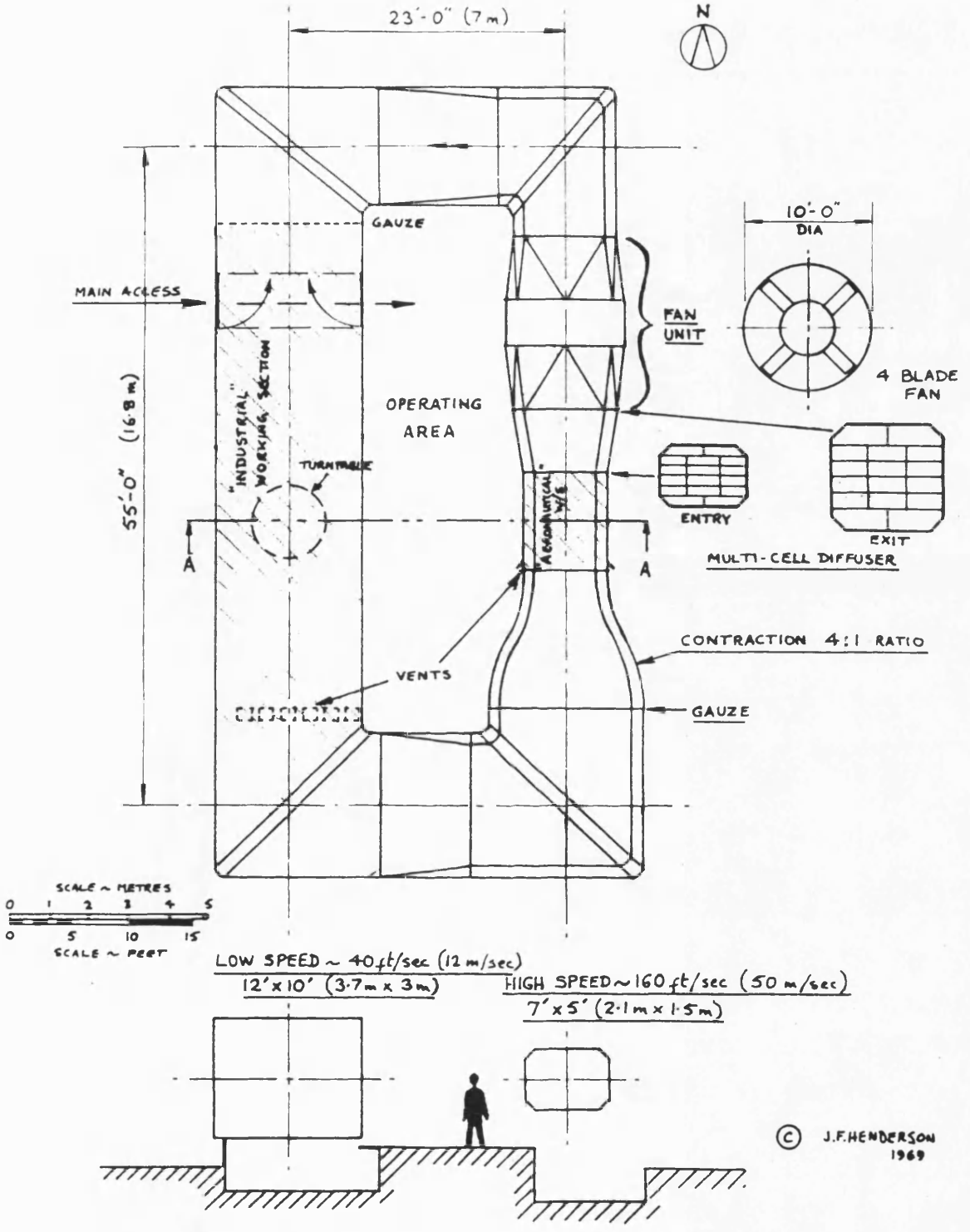

SECTION A-A SHOWING THE TWO WORKING SECTIONS, EITHER OF WHICH MAY BE OPERATED AT AMBIENT PRESSURE, AS REQUIRED

Fig. 2.5: THE DUAL-PURPOSE WIND-TUNNEL AT BATH UNIVERSITY.

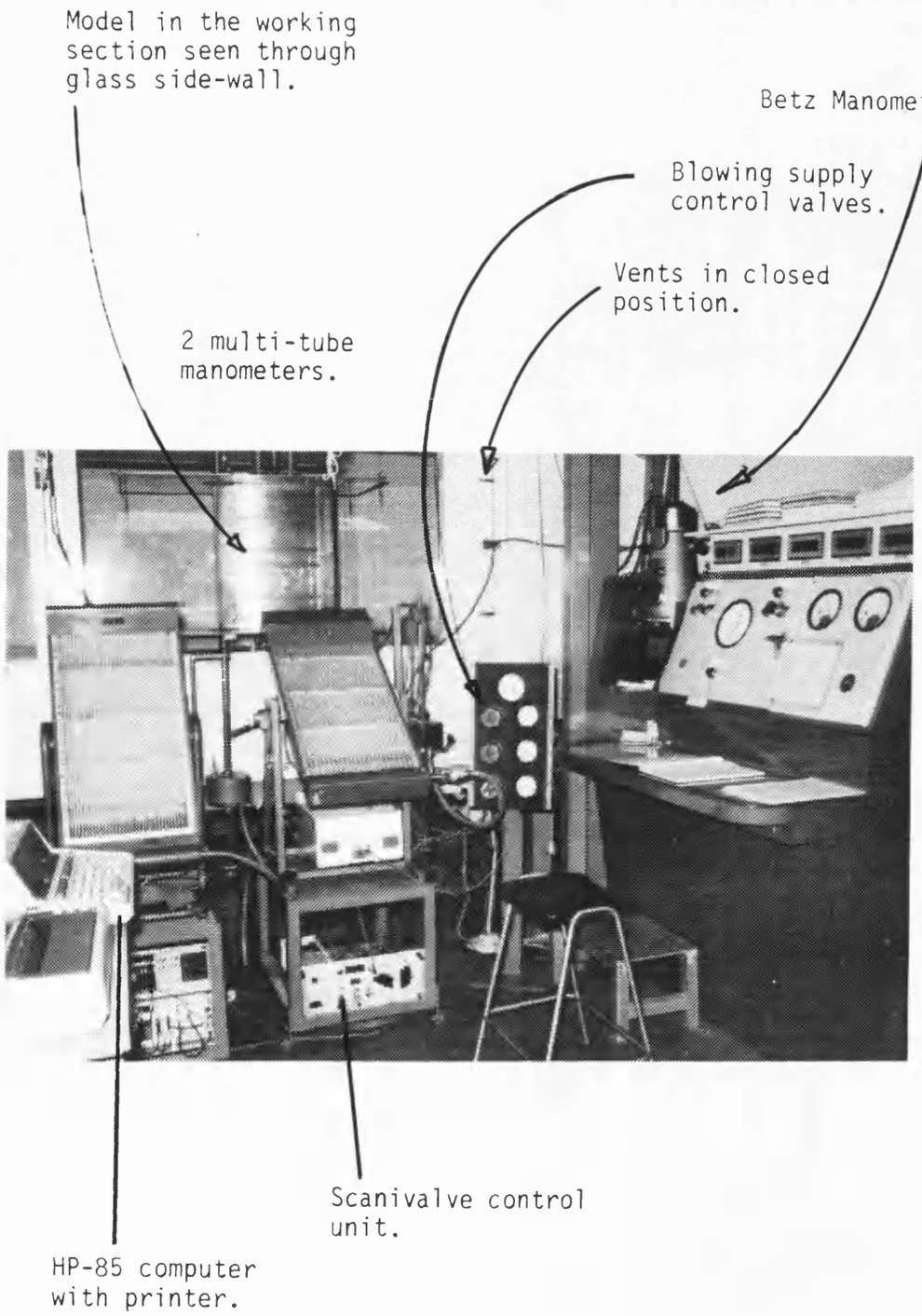

Fig. 2.6: THE TUNNEL OPERATING AREA.

Fig. 2.7

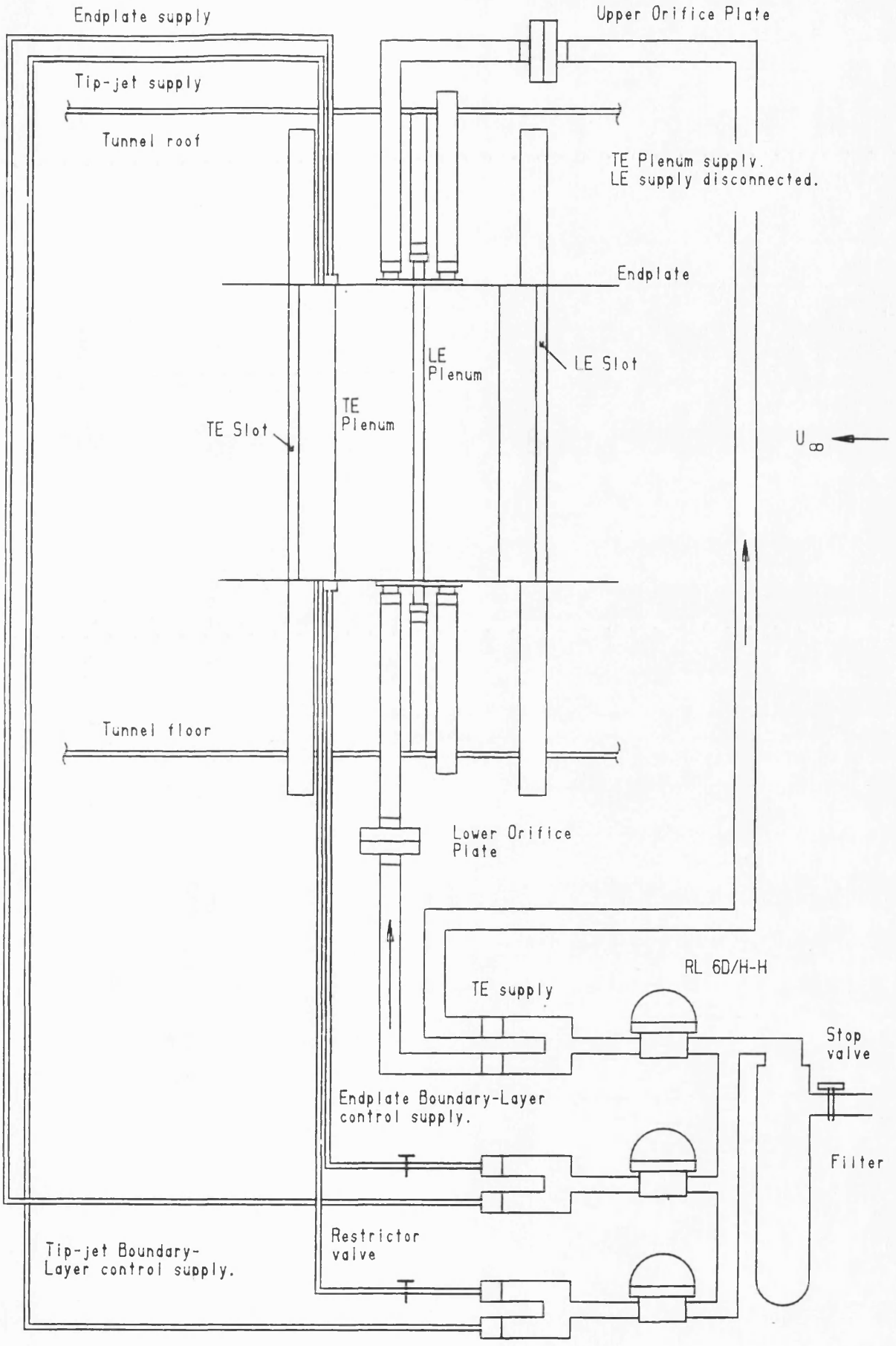

Fig. 2.7: THE BLOWING SUPPLY CONNECTIONS TO THE PLENUM CHAMBERS AND BOUNDARY-LAYER CONTROL SYSTEM.

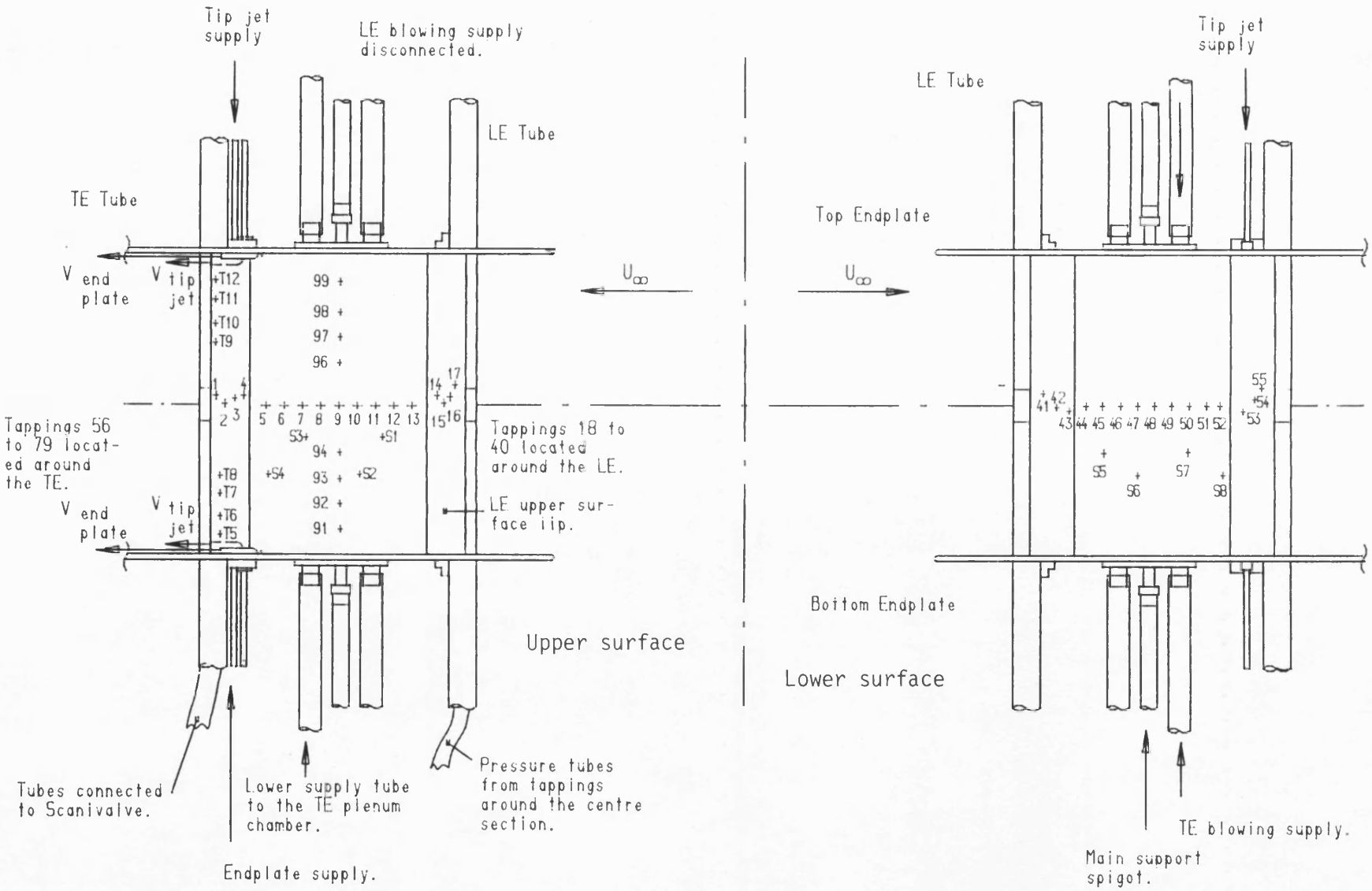

Fig. 2.8: THE MODEL IN THE WORKING SECTION SHOWING LAYOUT OF THE PRESSURE TAPPINGS AND CONNECTIONS.

Fig. 2.8

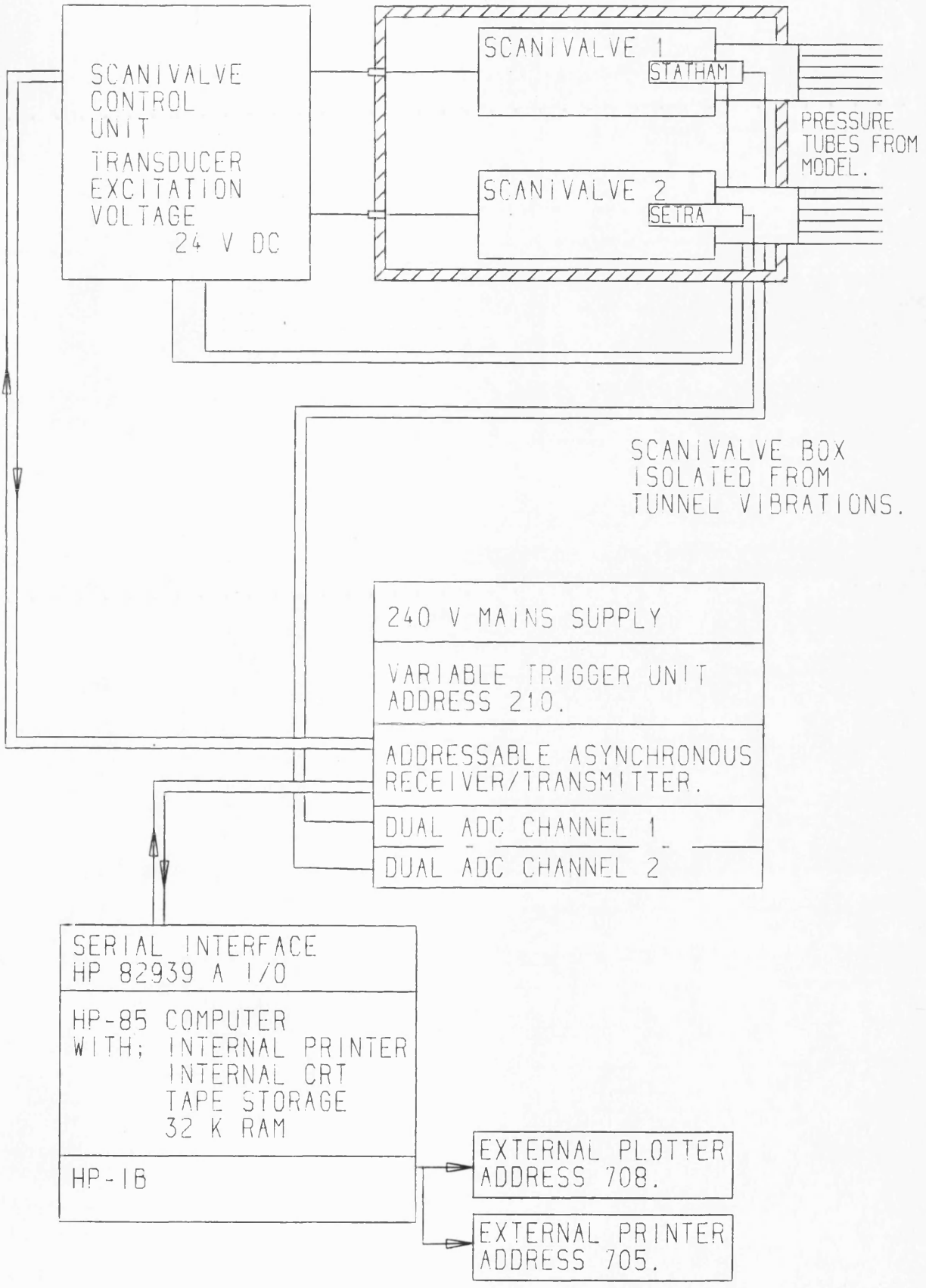

Fig. 2.9: THE DATA ACQUISITION HARDWARE.

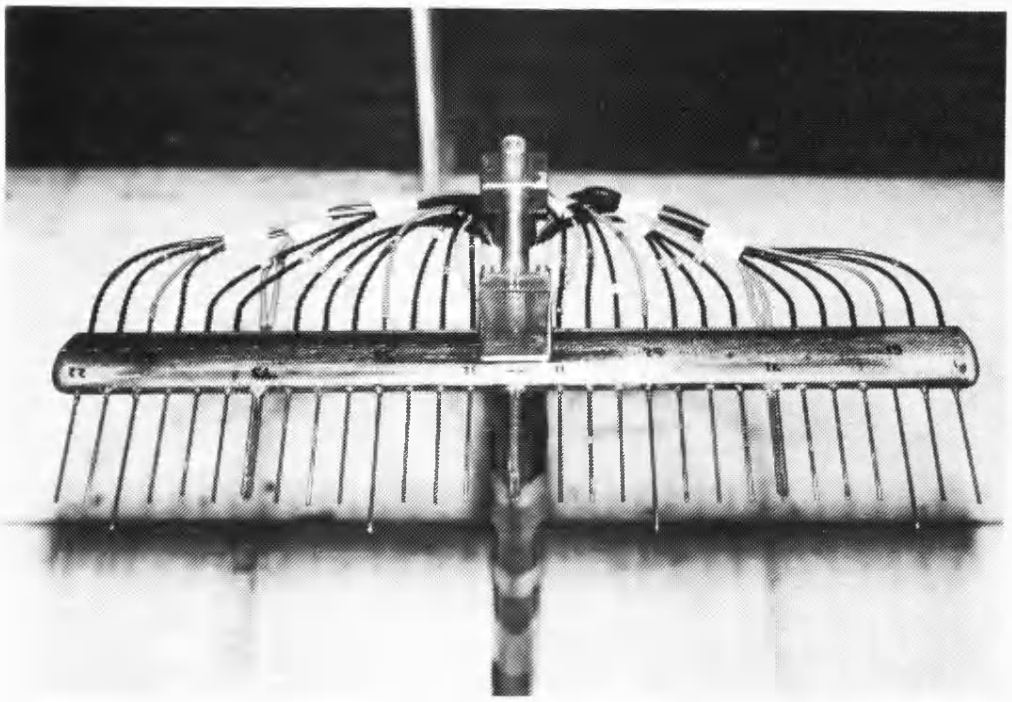

View from front.

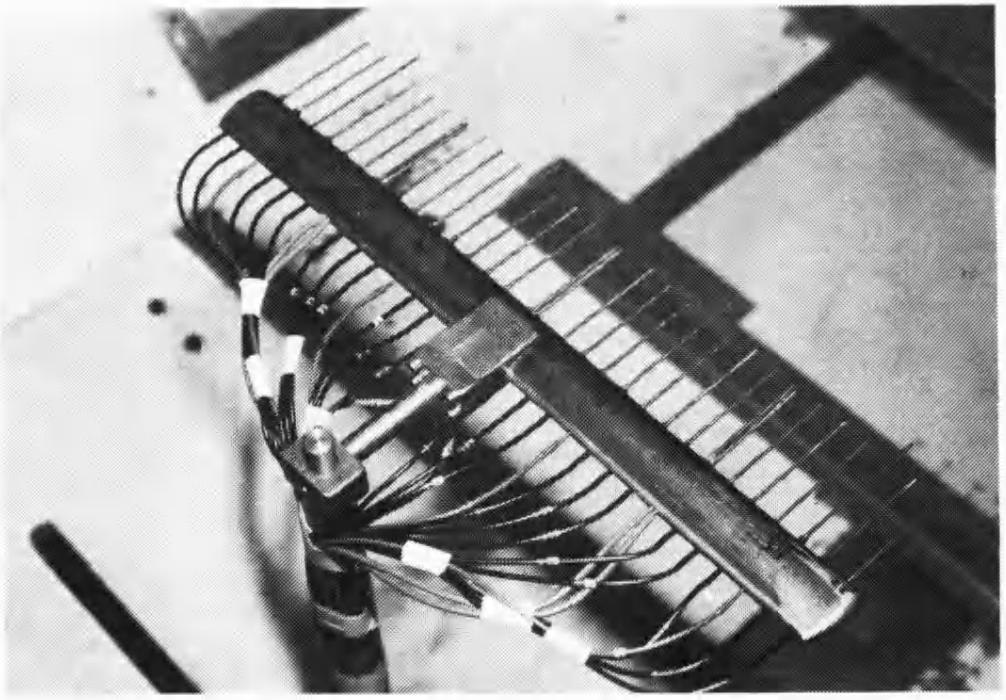

View from above.

Fig. 2. 10: WAKE TRAVERSE RAKE MOUNTED DOWNSTREAM OF THE MODEL IN THE WORKING SECTION.

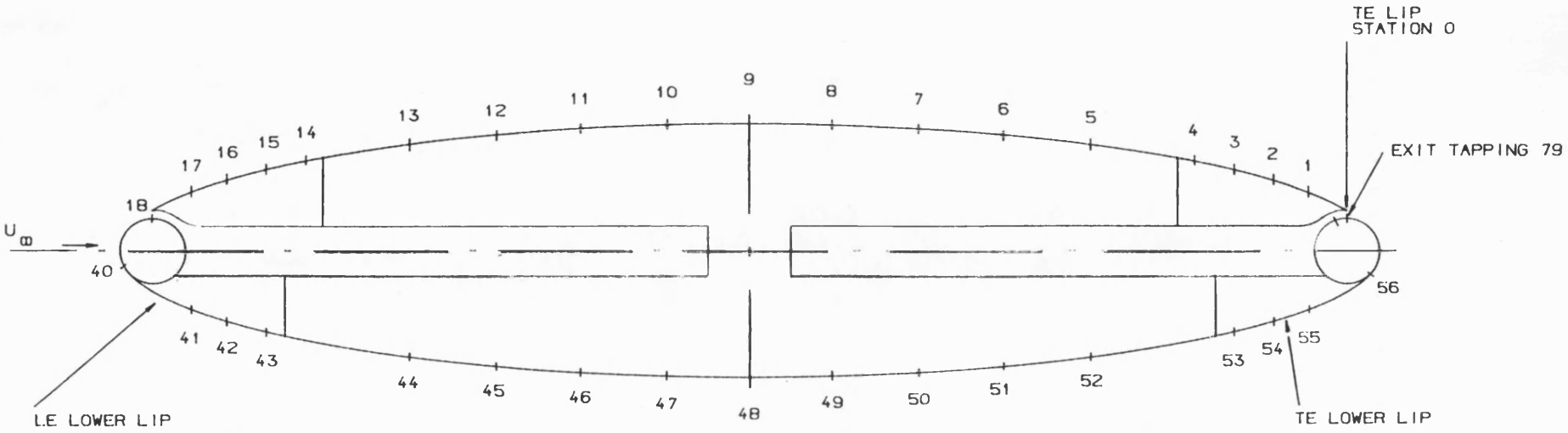

Tapping	No	x/c %	Tapping	No	x/c %	Tapping	No	x/c %	Tapping	No	x/c %
TE lip	0	96.64	Upper	10	43.43	LE lower	41	-8.78	Lower	49	-56.38
	1	94.23	surface	11	36.57	lip	42	-11.90	surface	50	-63.22
	2	91.41		12	29.76		43	-15.03		51	-70.06
	3	88.24		13	22.90					52	-76.90
	4	85.10									
						Lower	44	-22.96	TE lower	53	-84.78
Upper	5	76.84	LE blow-	14	14.78	surface	45	-29.84	lip	54	-87.91
surface	6	70.00	ing lip	15	11.64		46	-36.67		55	-90.99
	7	63.16		16	8.54		47	-43.54			
	8	56.29		17	5.73				TE tube	56 to 79	
									see table 2.1 for		
mid-chord	9	49.85	LE tube	18 to 40		mid-chord	48	-48.96	detailed location		

Fig. 2.11: LOCATION OF THE MID-SPAN PRESSURE TAPPINGS AROUND THE MODEL.

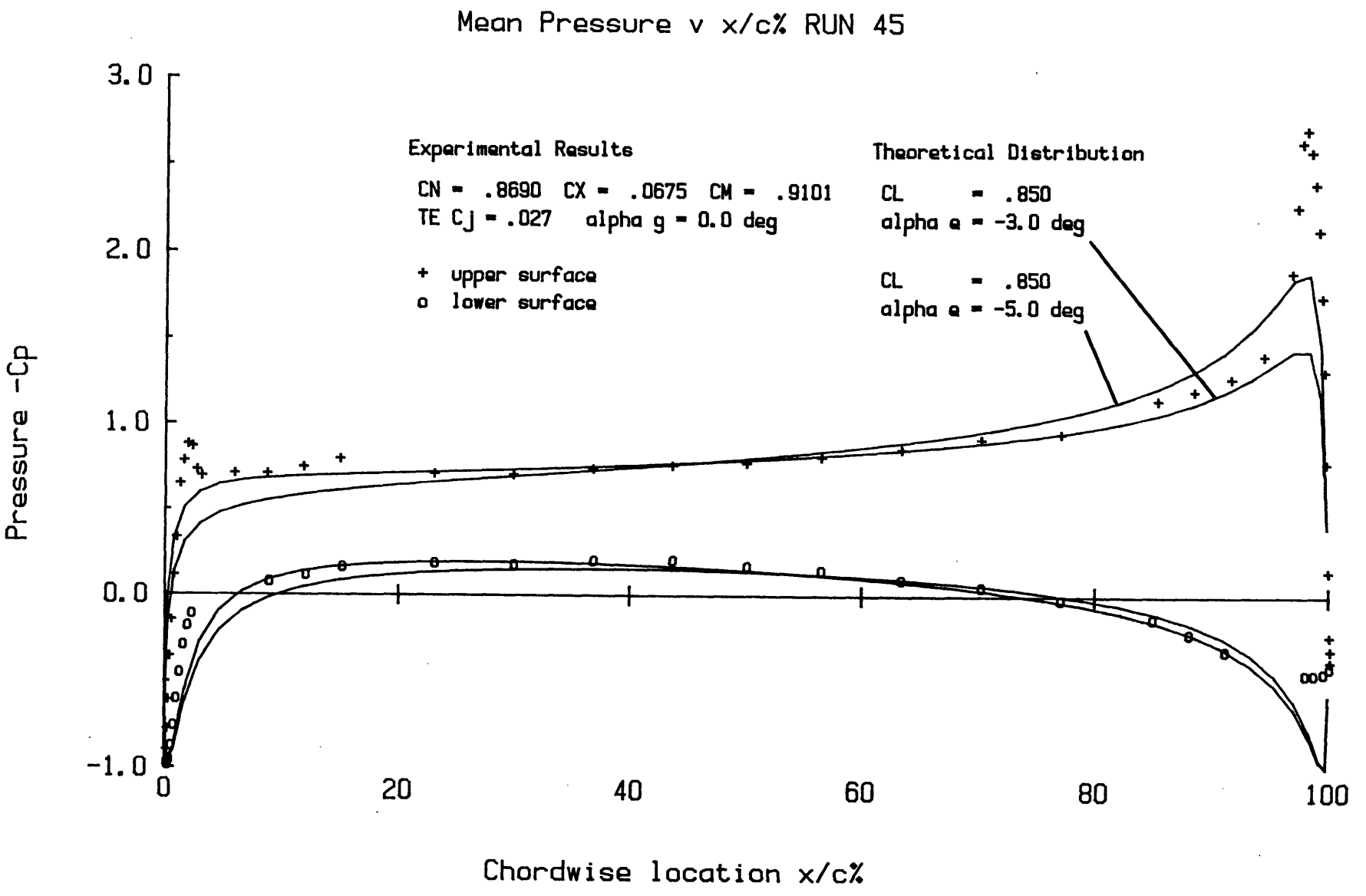

Fig.2.12: EXPERIMENTAL AND THEORETICAL PRESSURE DISTRIBUTION AT ZERO INCIDENCE WITH TE BLOWING.

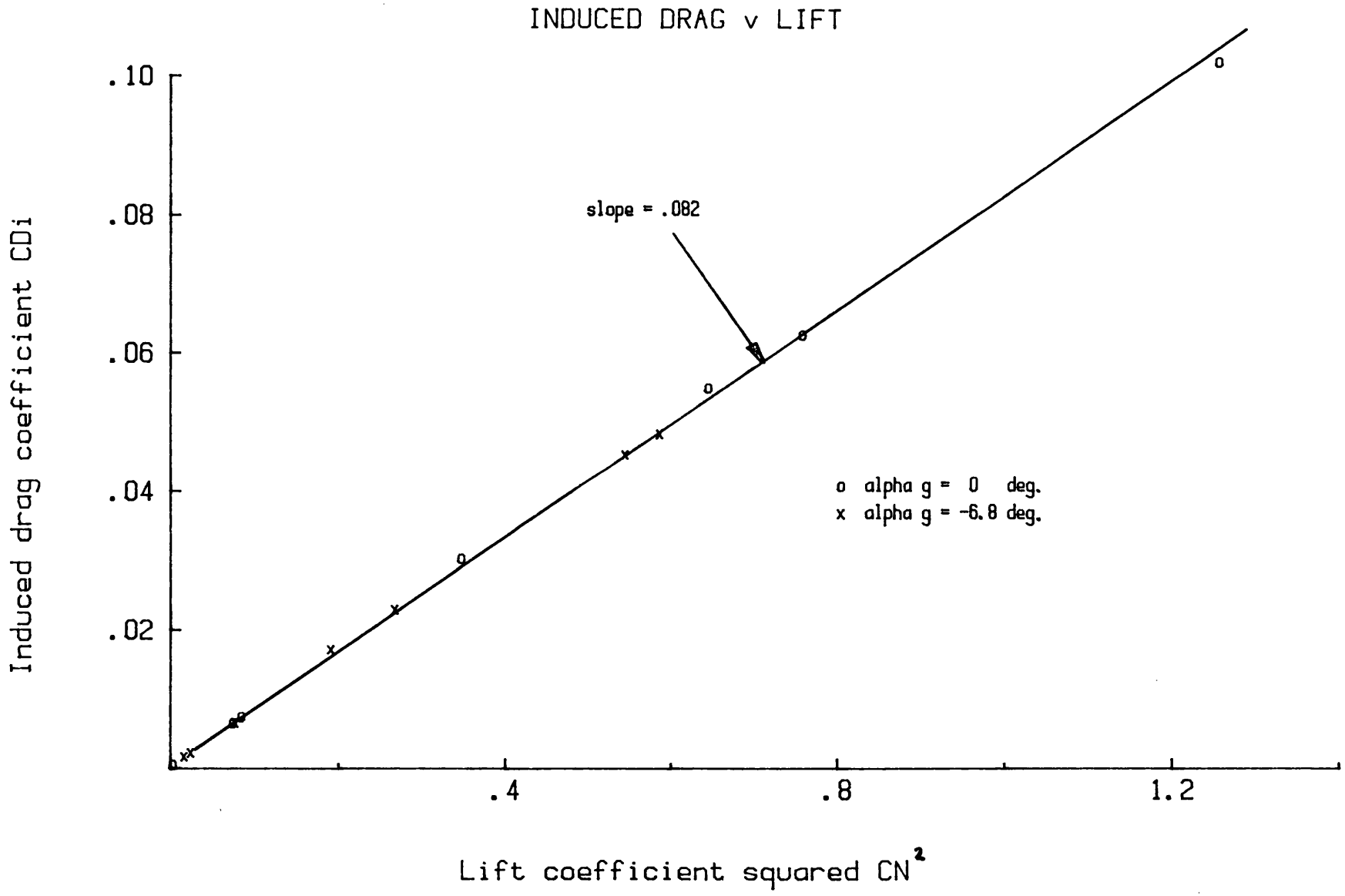

Fig. 2.13: EMPIRICAL RELATIONSHIP BETWEEN INDUCED DRAG AND THE LIFT COEFFICIENT.

Fig. 2.13

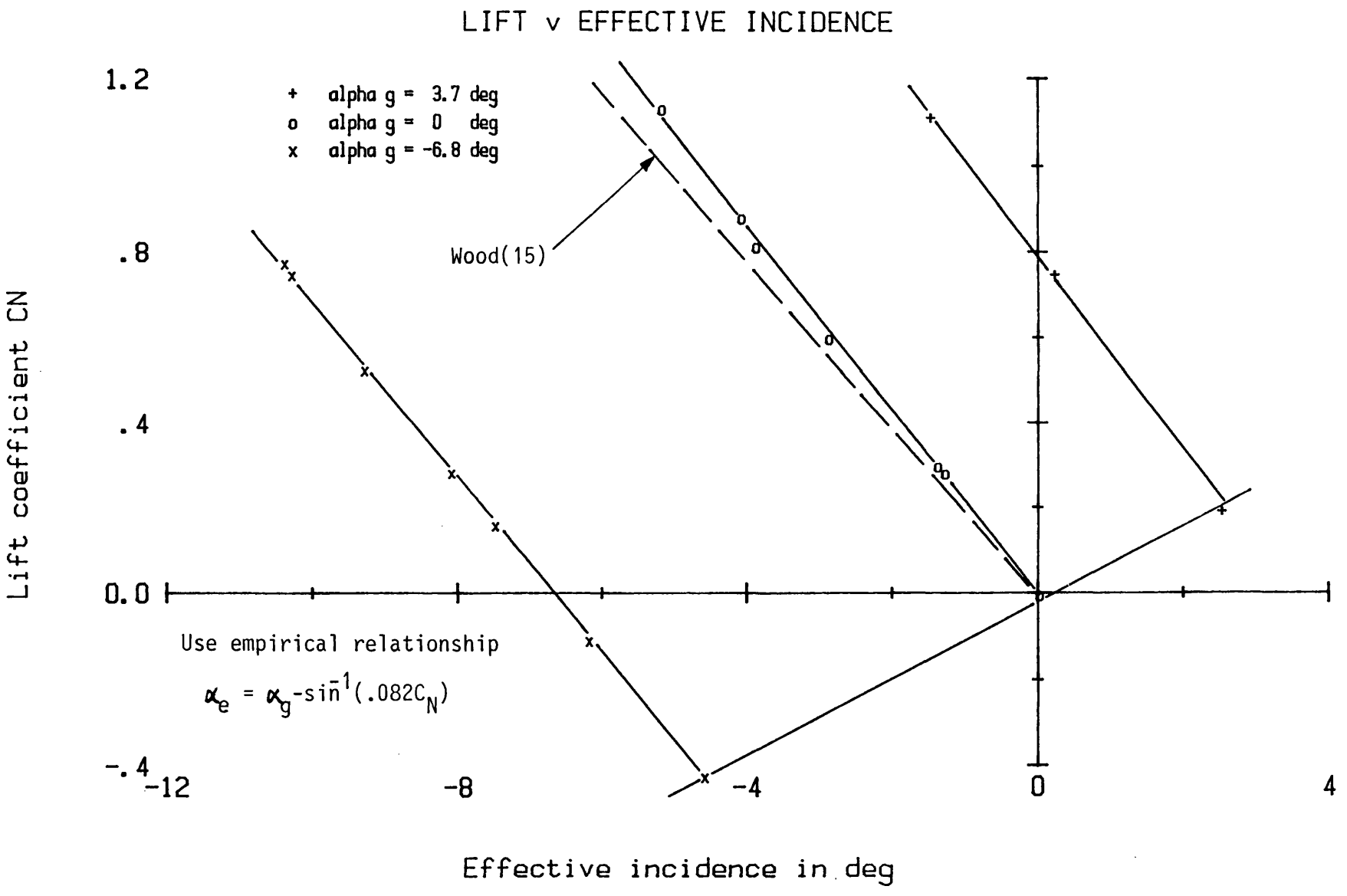

Fig. 2.14: EMPIRICAL RELATIONSHIP BETWEEN LIFT COEFFICIENT AND THE EFFECTIVE INCIDENCE OF THE MODEL.

Fig. 2.14

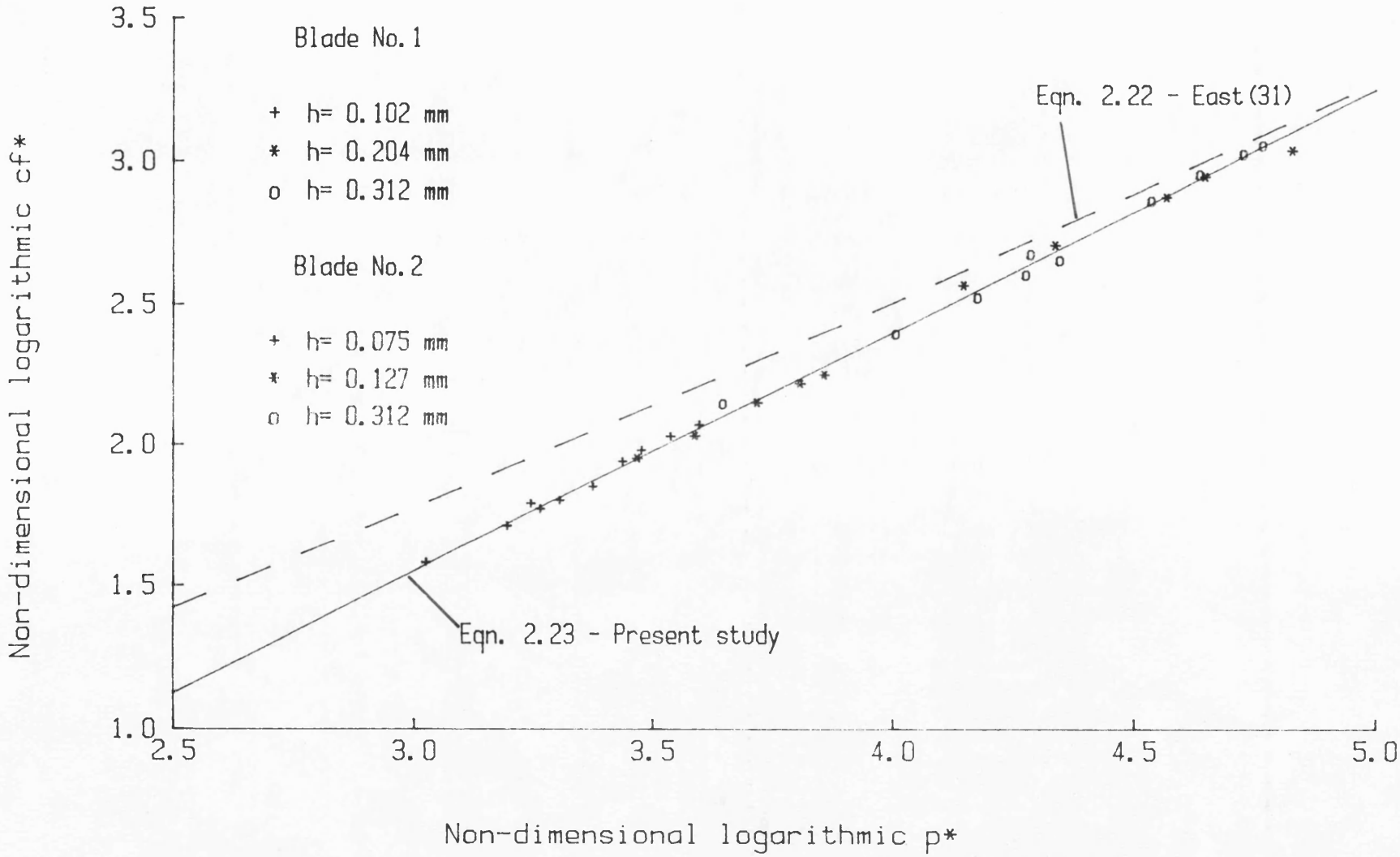

Fig. 2.15: CALIBRATION CURVE OF RAZOR BLADES USED FOR SKIN FRICTION MEASUREMENT.

Fig. 2.15

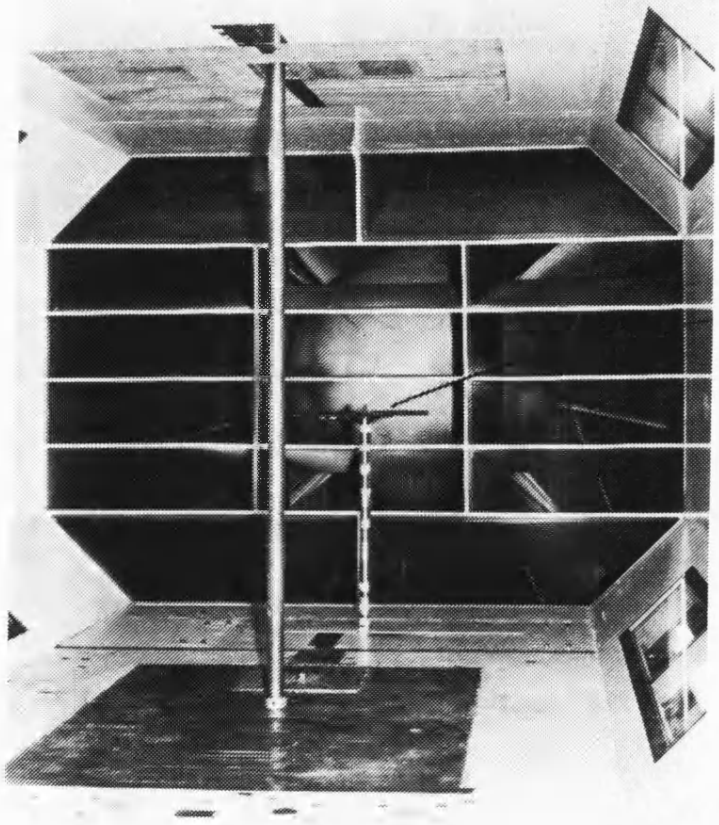

Fig. 2.16: CYLINDER AND RAKE MOUNTED IN THE WORKING SECTION USED TO CHECK THE WAKE DRAG MEASUREMENT.

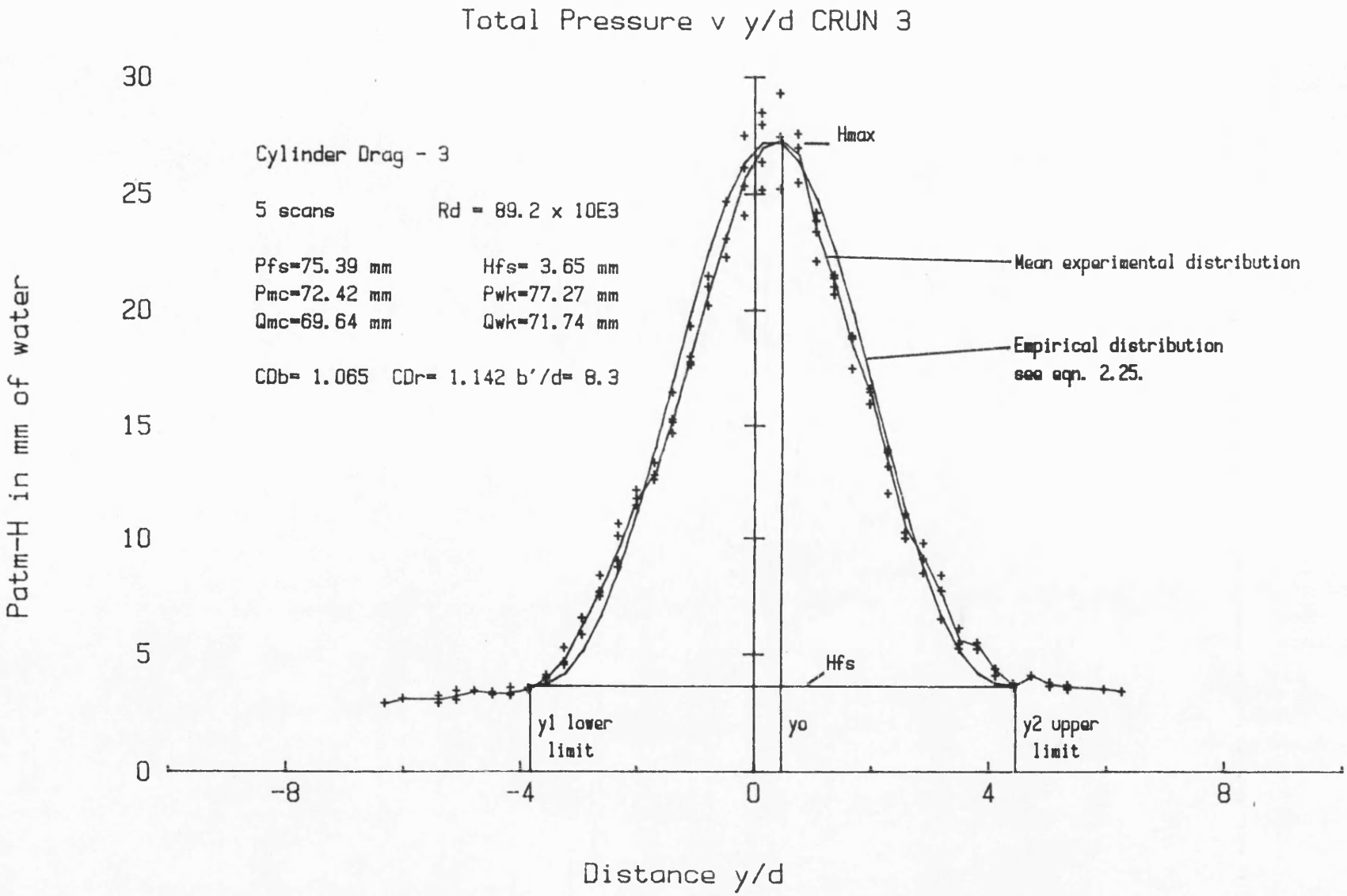

Fig. 2.17: TOTAL PRESSURE DISTRIBUTION IN THE WAKE OF A CYLINDER.

Fig. 2.17

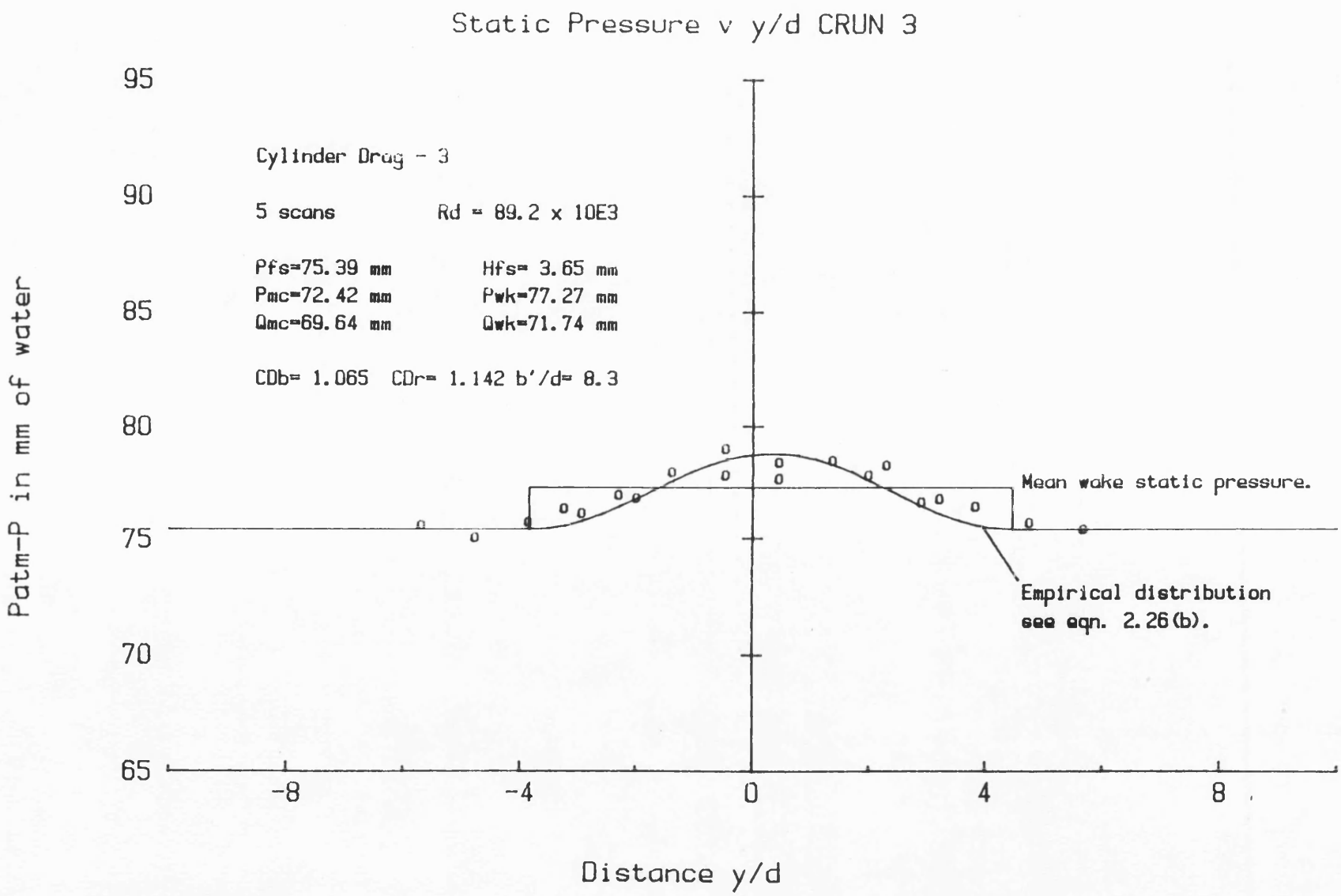

Fig. 2.18: STATIC PRESSURE DISTRIBUTION IN THE WAKE OF A CYLINDER.

Fig. 2.18

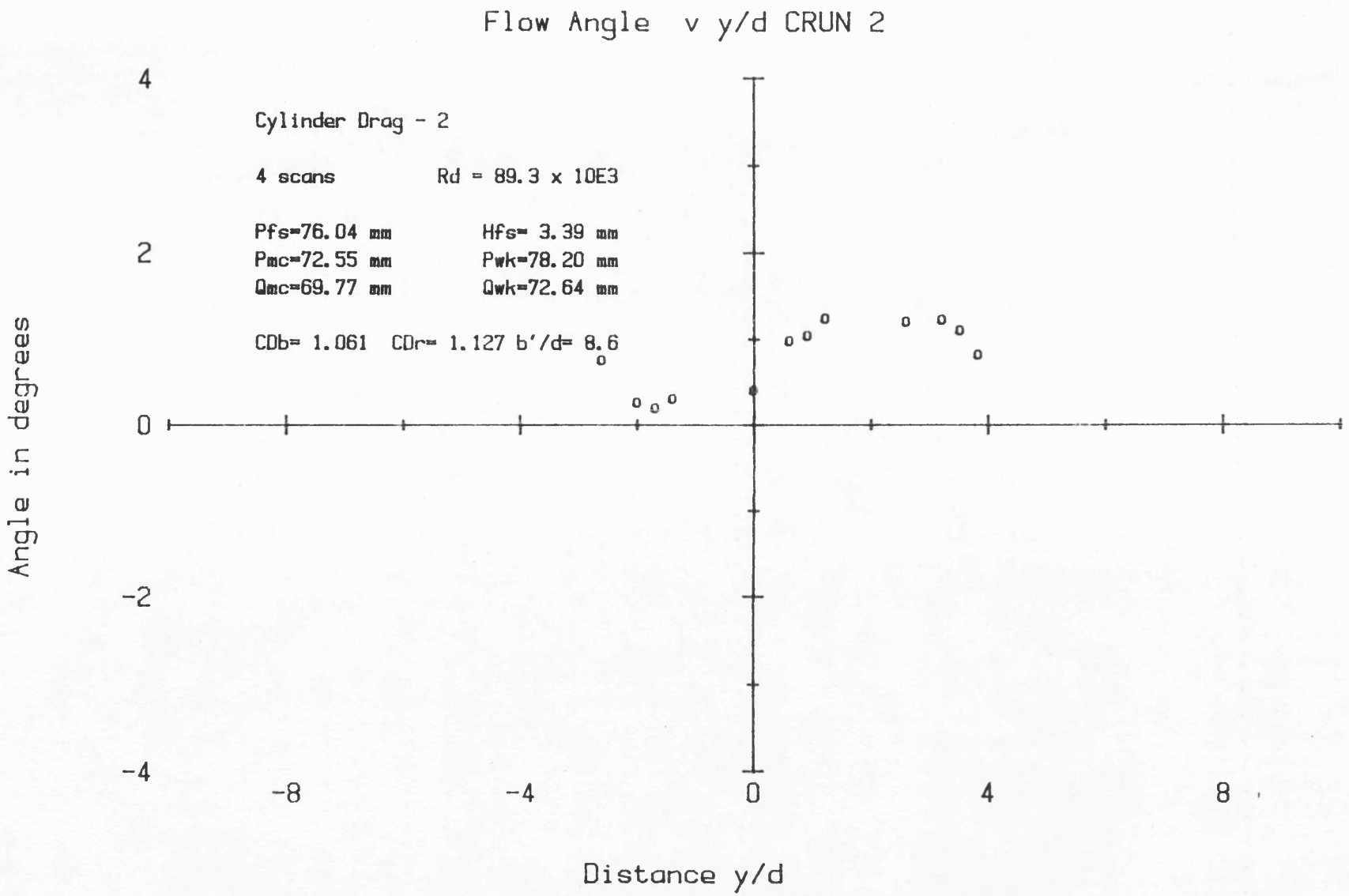

Fig. 2.19: FLOW ANGLE IN THE WAKE OF A CYLINDER.

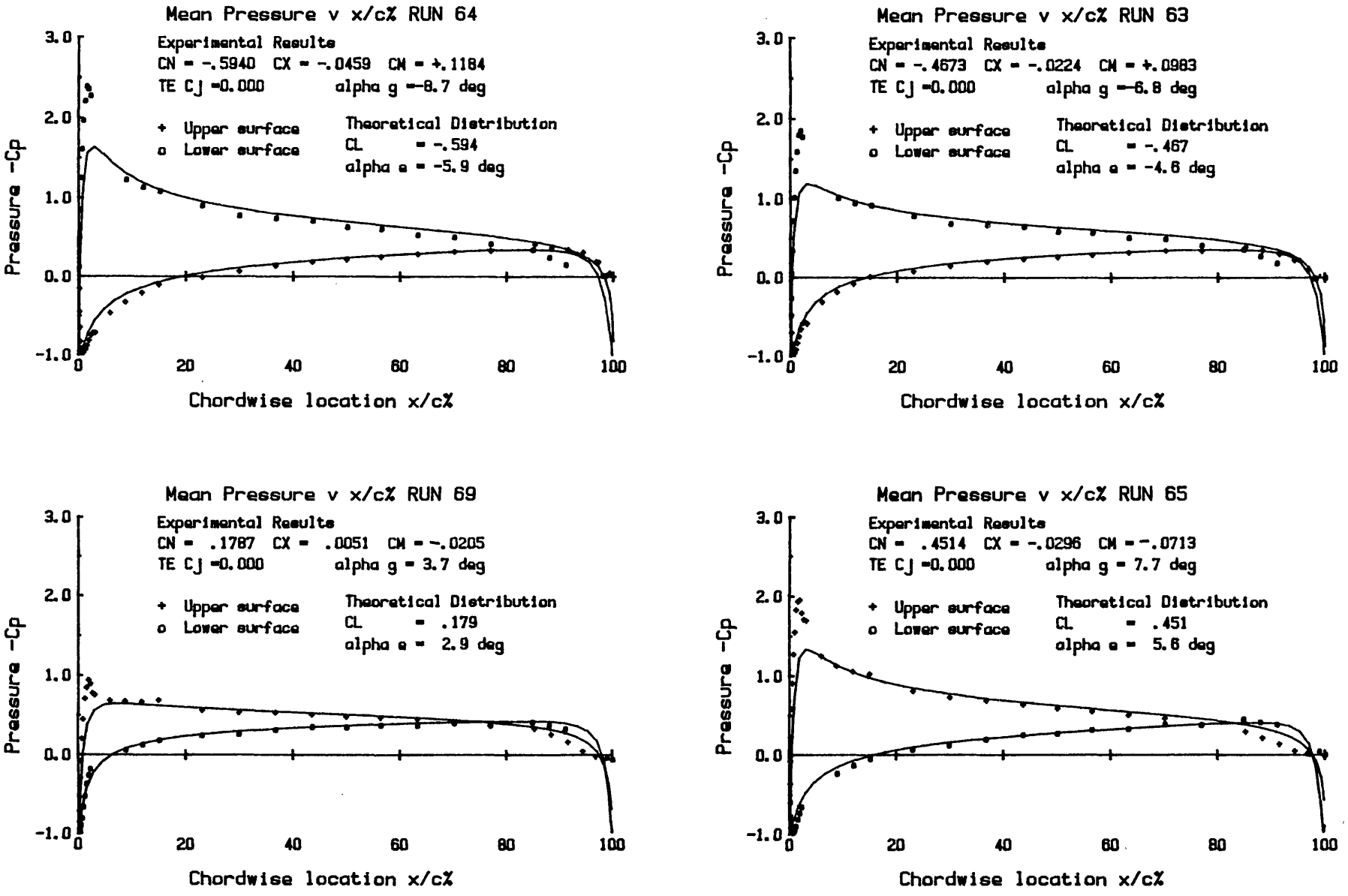

Fig. 3.1: MEAN PRESSURE DISTRIBUTION V X/C% FOR UNBLOWN MODEL WITH VARIATION OF GEOMETRIC INCIDENCE.

Fig.3.1

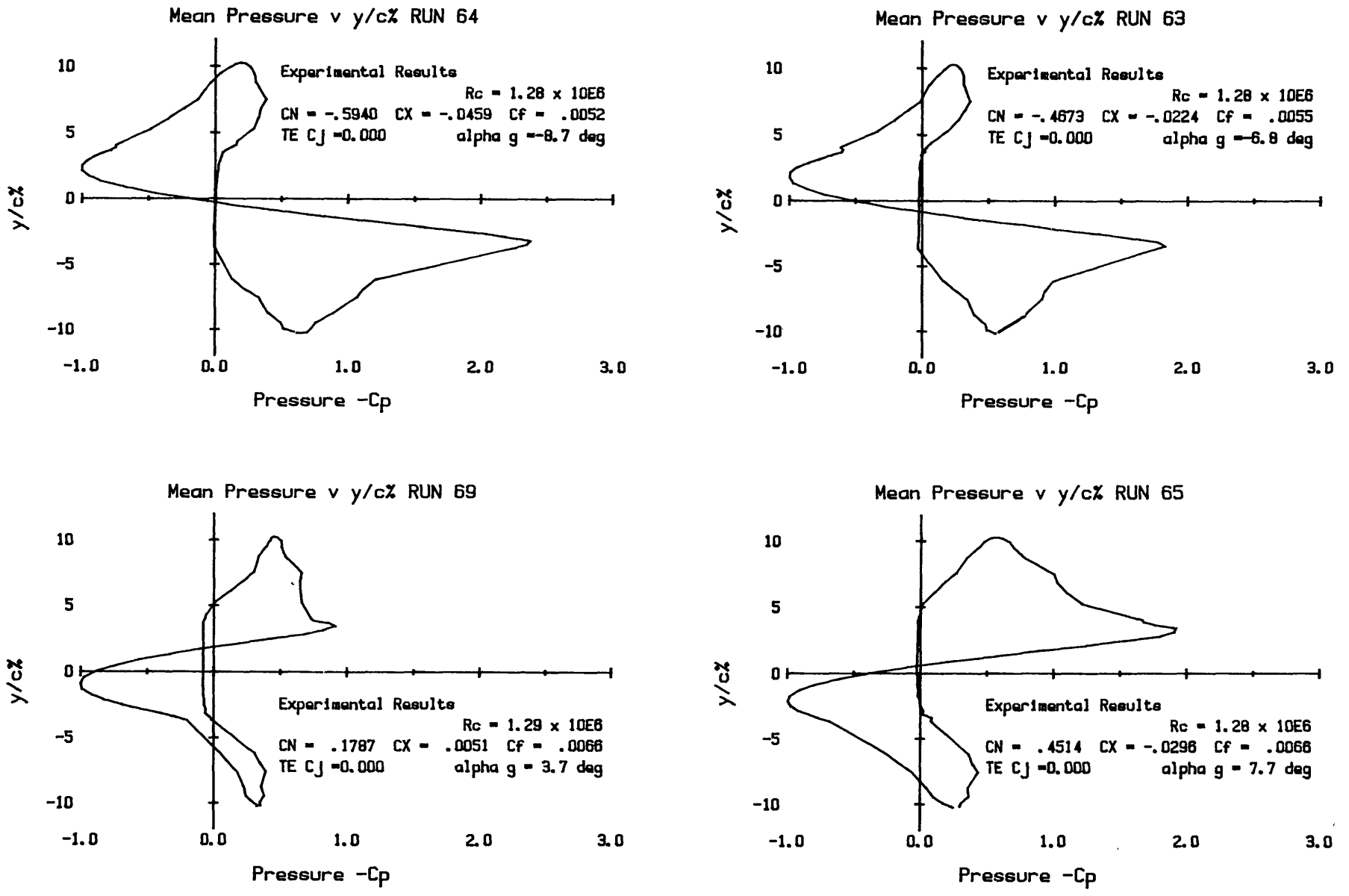

Fig. 3.2: MEAN PRESSURE DISTRIBUTION V Y/C% FOR UNBLOWN MODEL WITH VARIATION OF GEOMETRIC INCIDENCE.

Fig.3.2

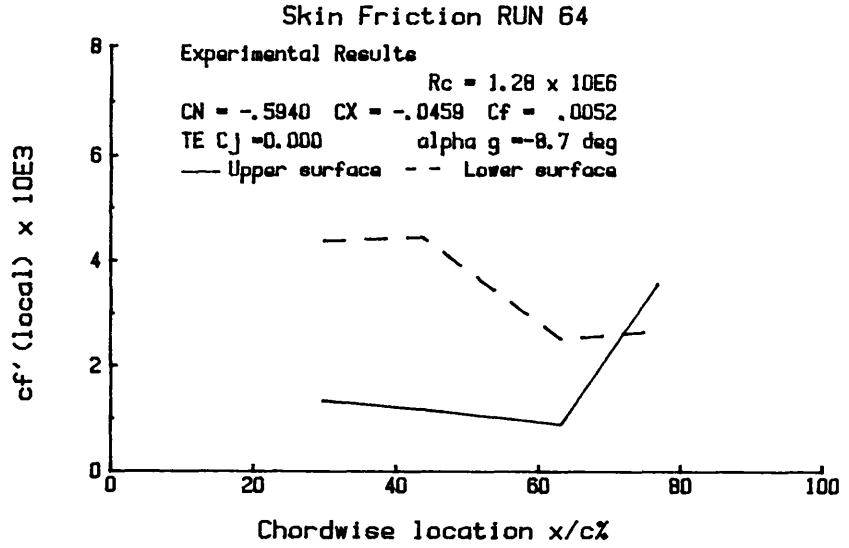

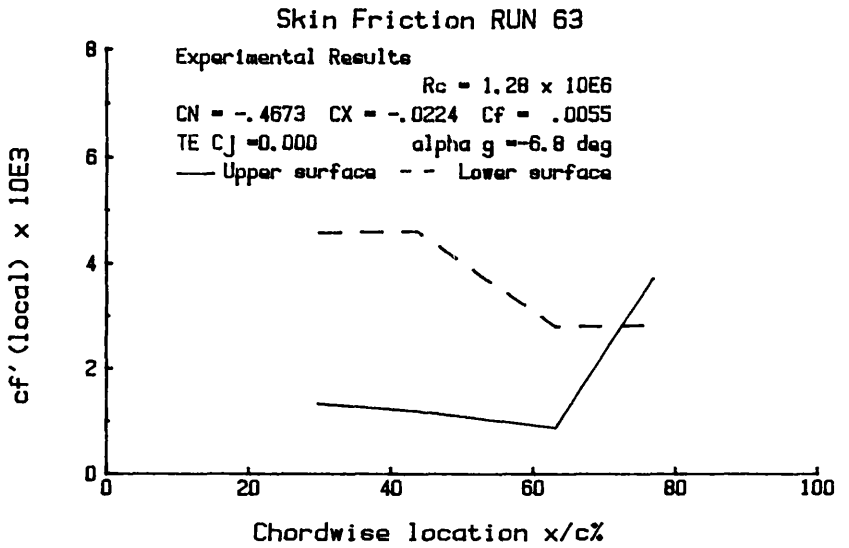

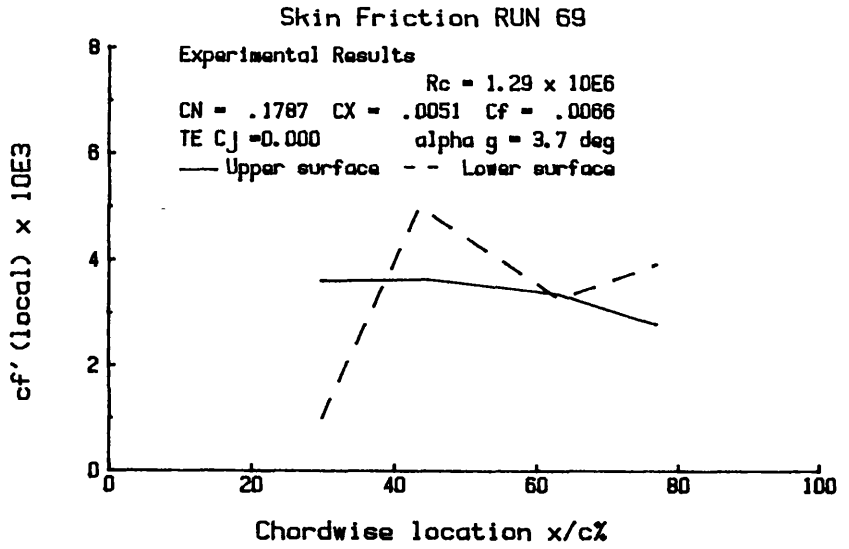

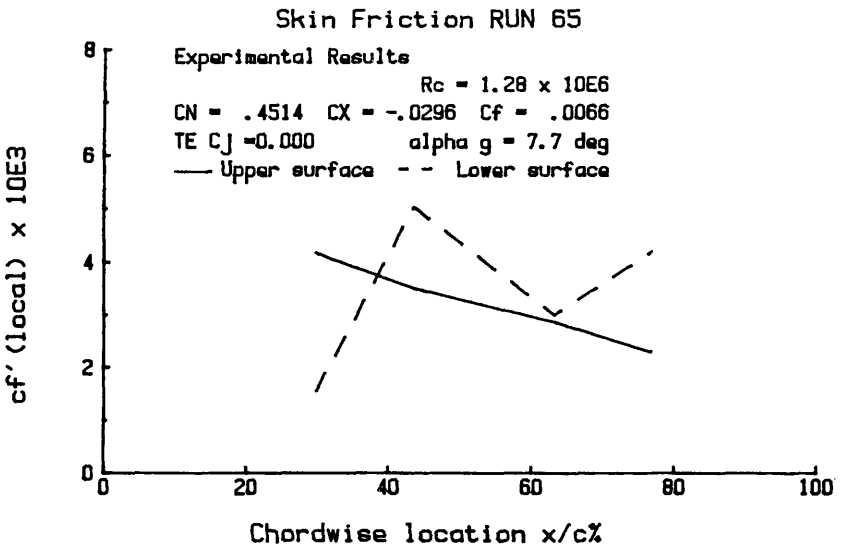

Fig. 3.3: SKIN FRICTION DISTRIBUTION V X/C% FOR UNBLOWN MODEL WITH VARIATION OF GEOMETRIC INCIDENCE.

Fig.3.3

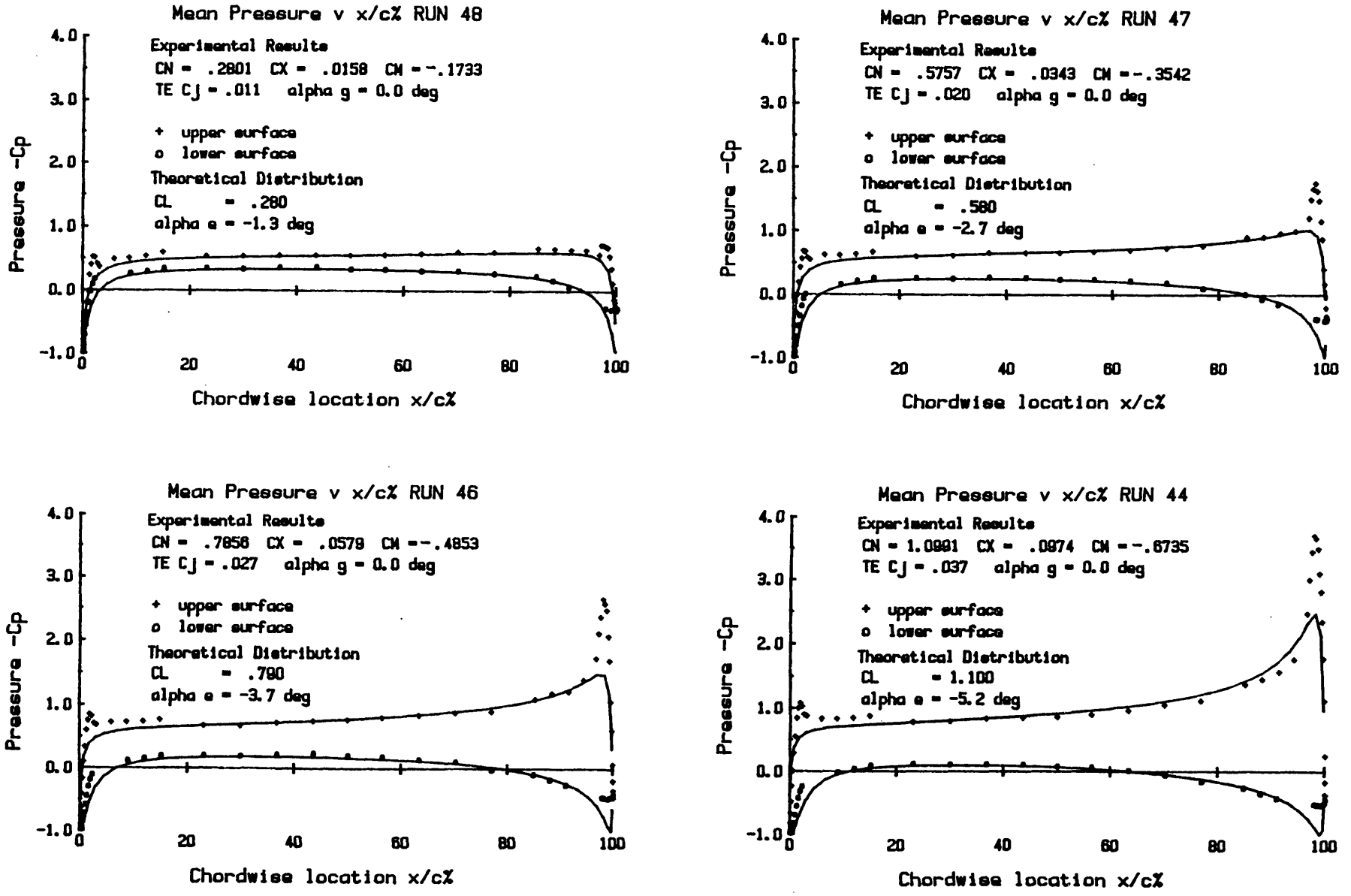

Fig. 3.4: MEAN PRESSURE DISTRIBUTION V X/C% FOR MODEL AT ZERO INCIDENCE WITH TE BLOWING ONLY.

Fig. 3.4

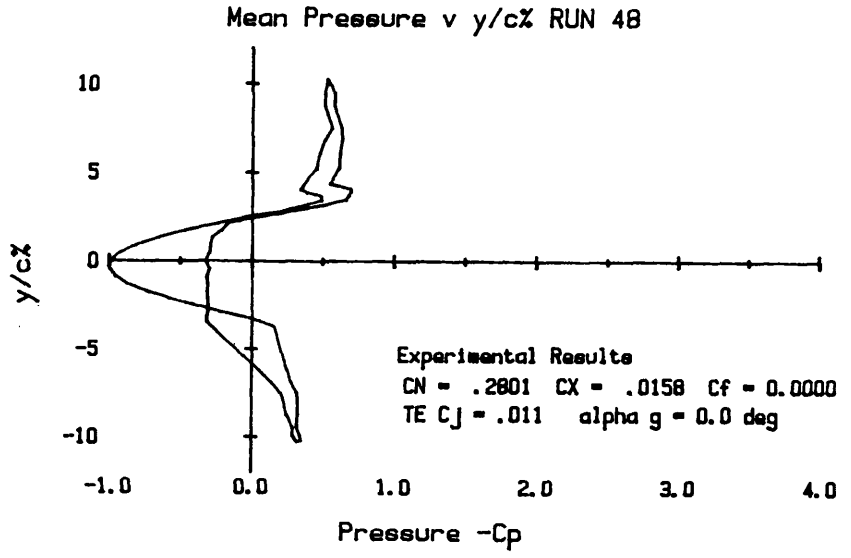

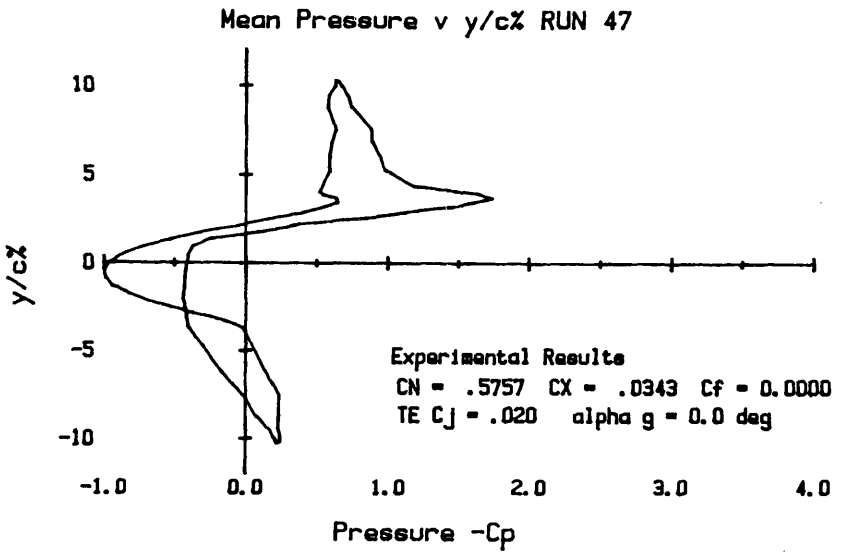

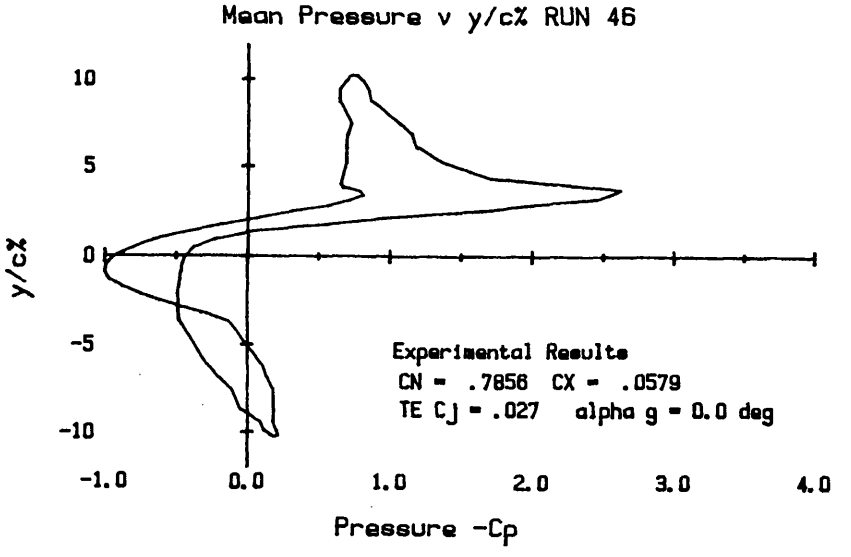

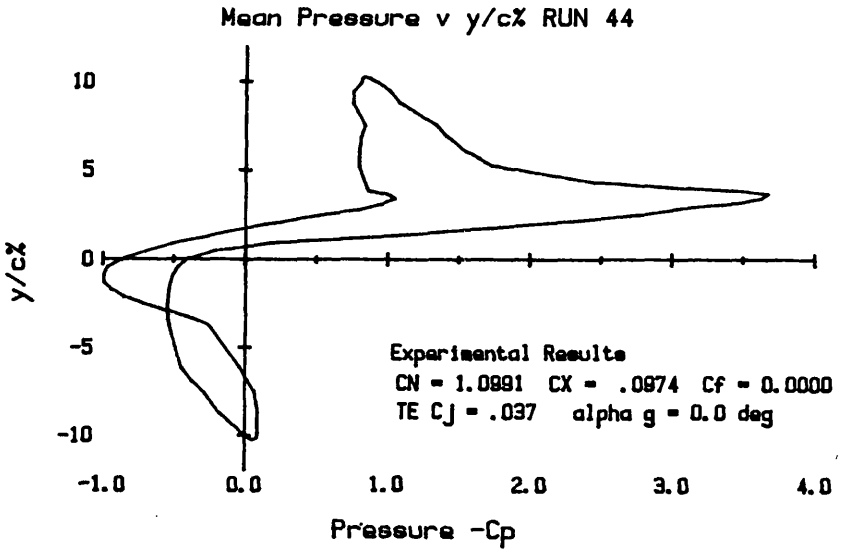

Fig. 3.5: MEAN PRESSURE DISTRIBUTION V Y/C% FOR MODEL AT ZERO INCIDENCE WITH TE BLOWING ONLY.

Fig.3.5

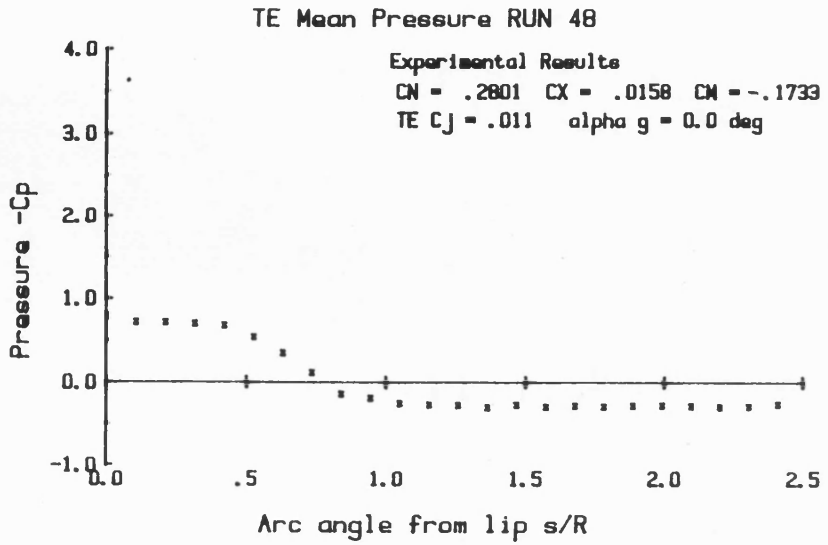

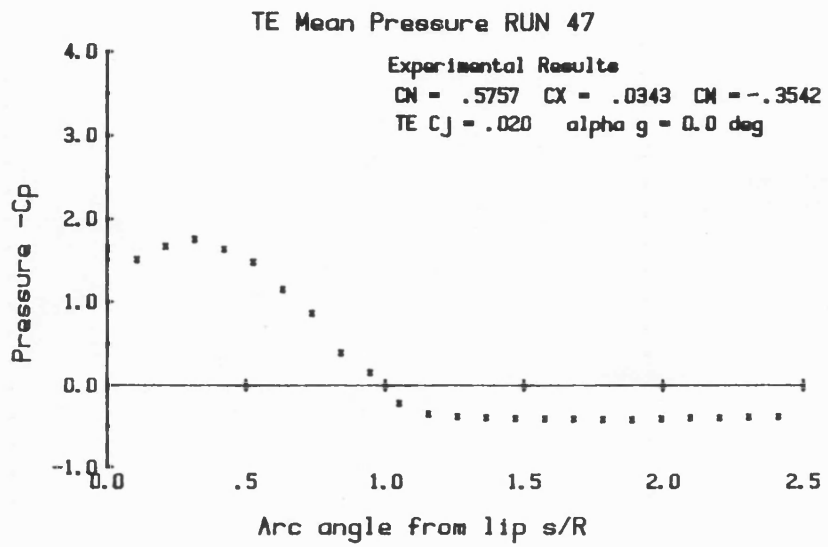

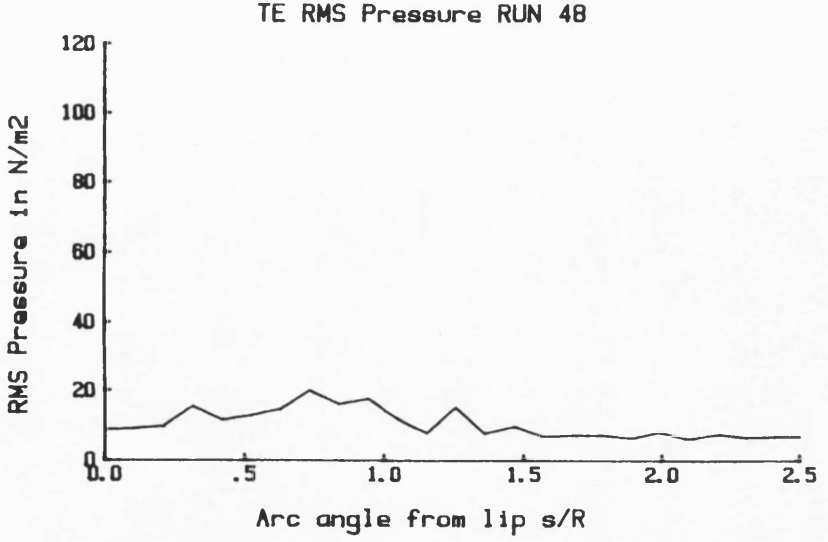

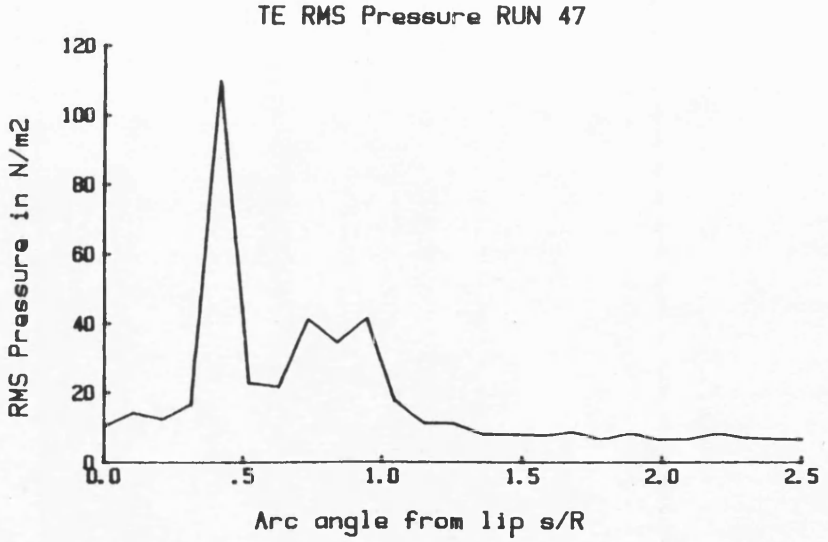

Fig. 3.6: TE PRESSURE DISTRIBUTION V ANGLE FROM LIP FOR MODEL AT ZERO INCIDENCE WITH TE BLOWING ONLY.

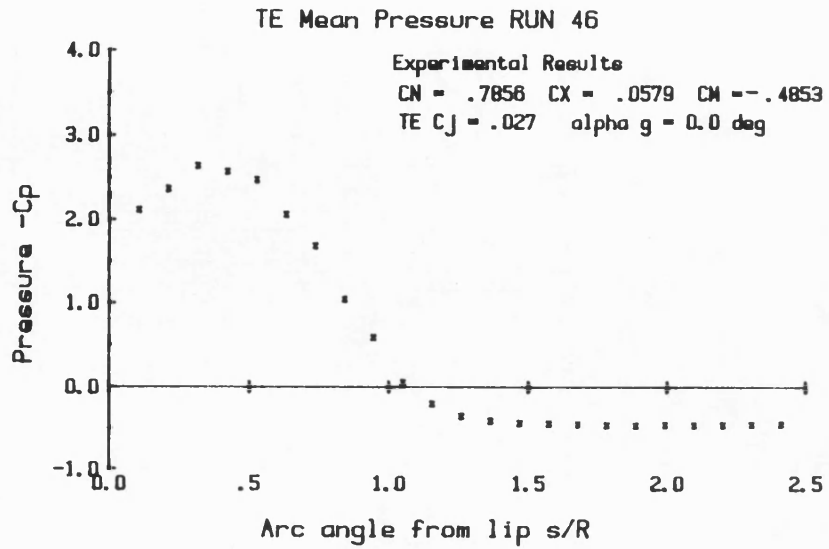

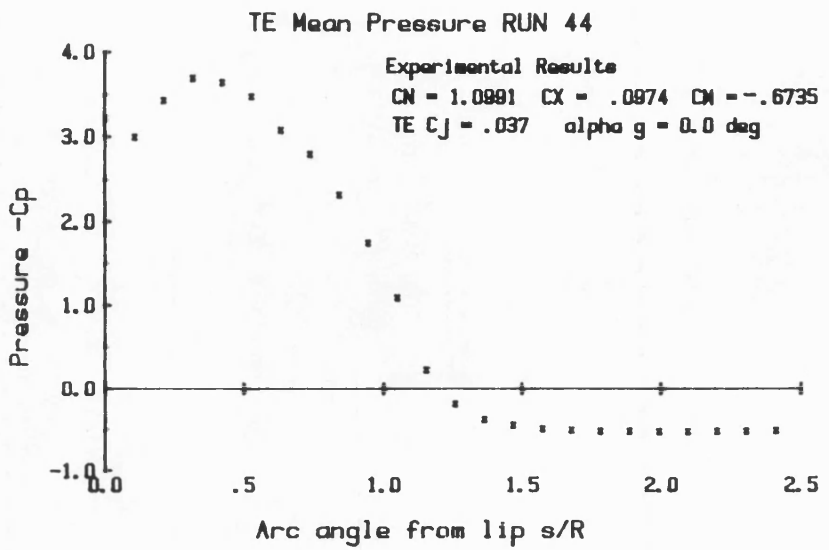

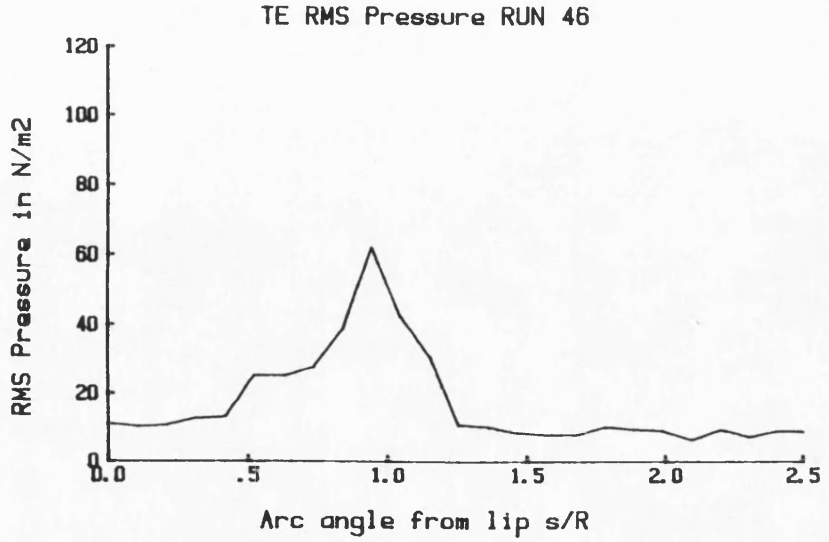

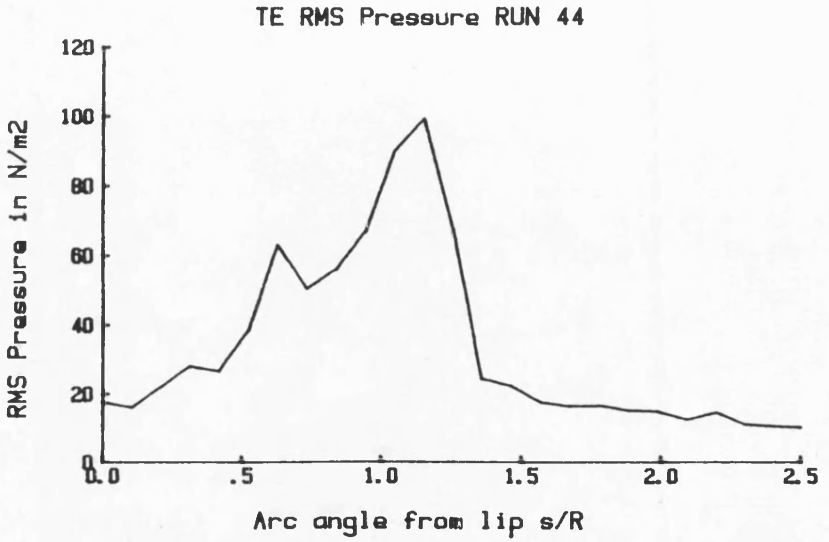

Fig.3.7: TE PRESSURE DISTRIBUTION V ANGLE FROM LIP FOR MODEL AT ZERO INCIDENCE WITH TE BLOWING ONLY.

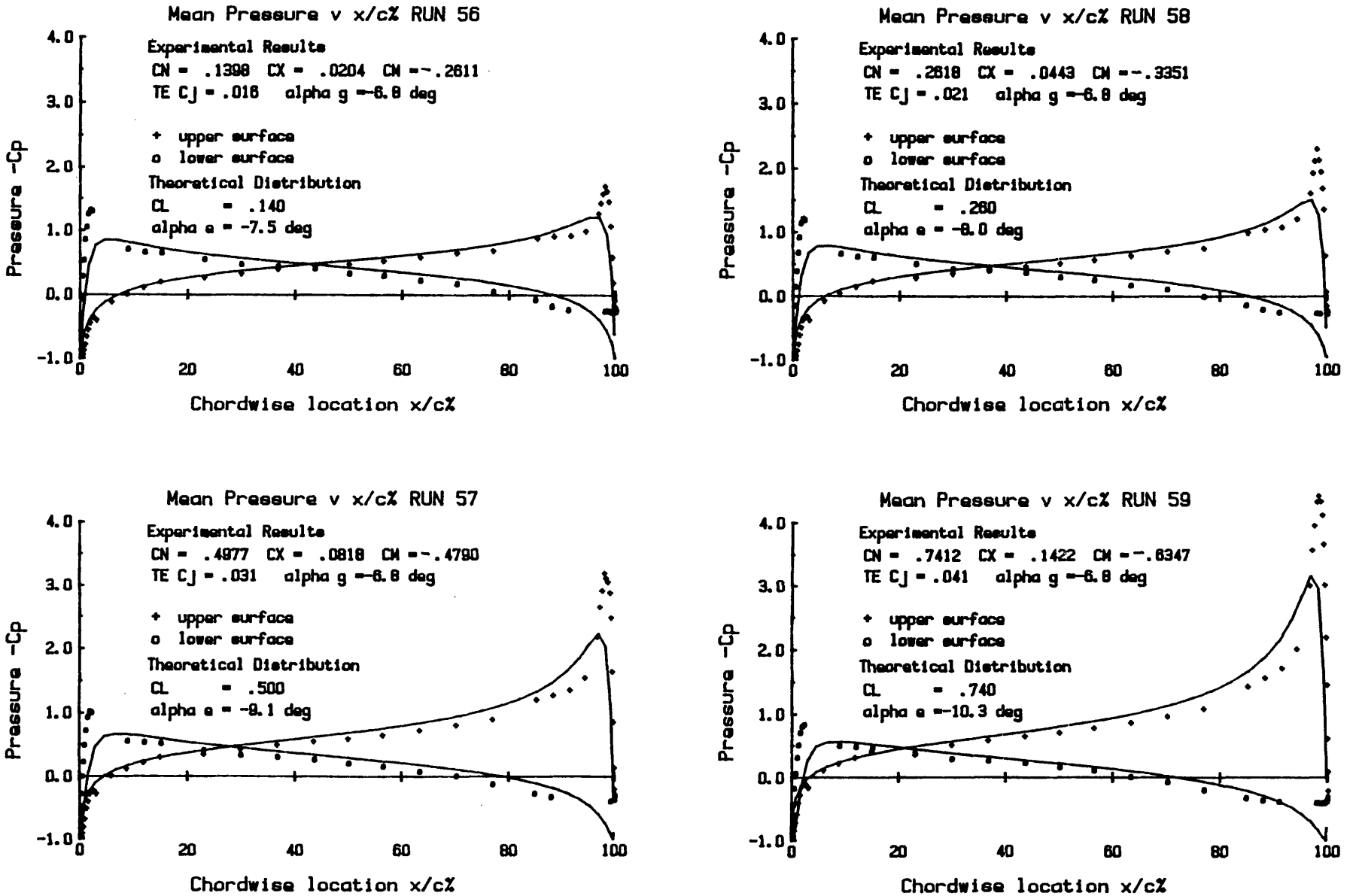

Fig. 3.8: MEAN PRESSURE DISTRIBUTION V X/C% FOR MODEL AT -6.8 DEG. INCIDENCE WITH TE BLOWING ONLY.

Fig. 3.8

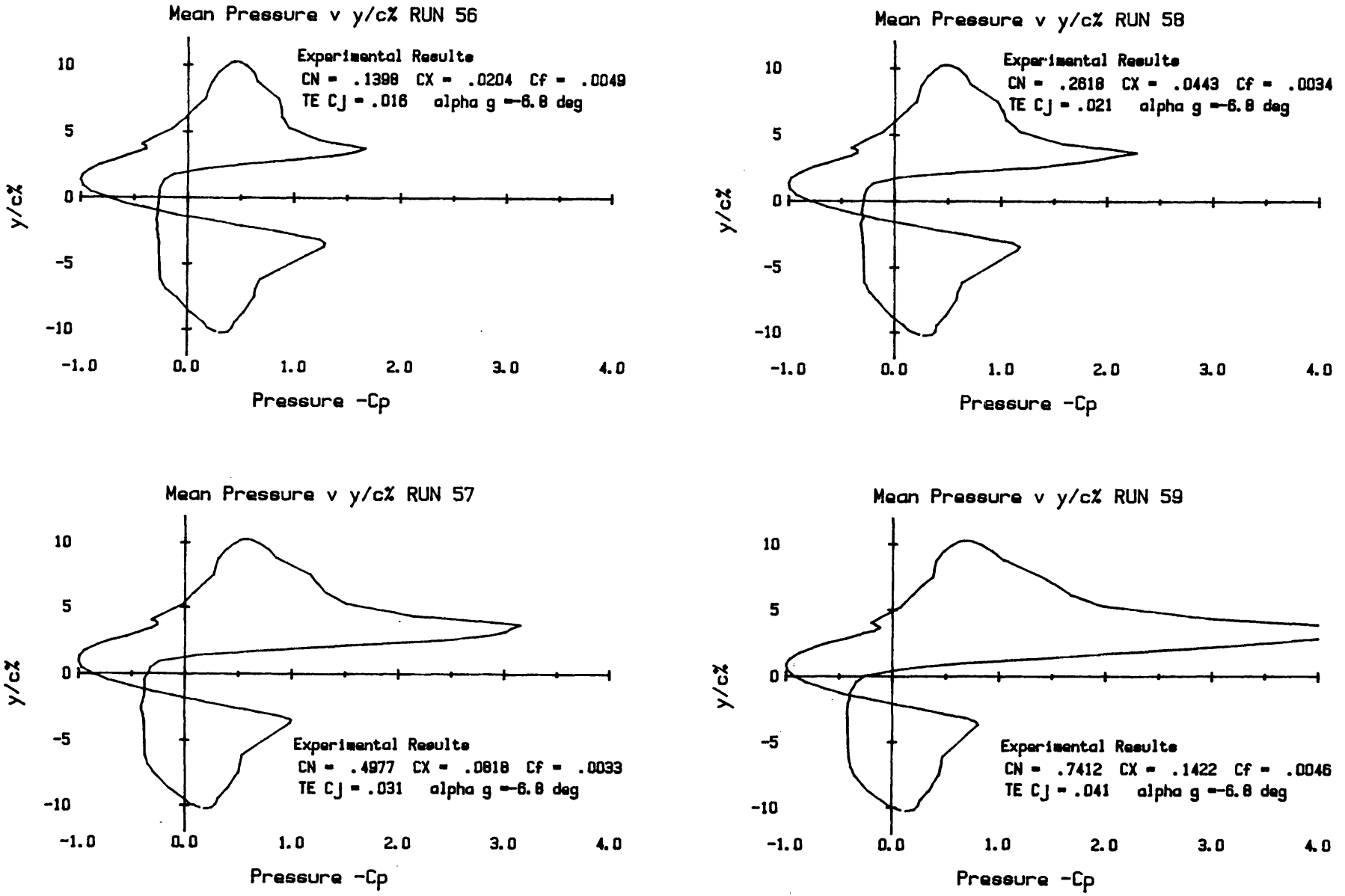

Fig. 3.9: MEAN PRESSURE DISTRIBUTION V Y/C% FOR MODEL AT -6.8 DEG. INCIDENCE WITH TE BLOWING ONLY.

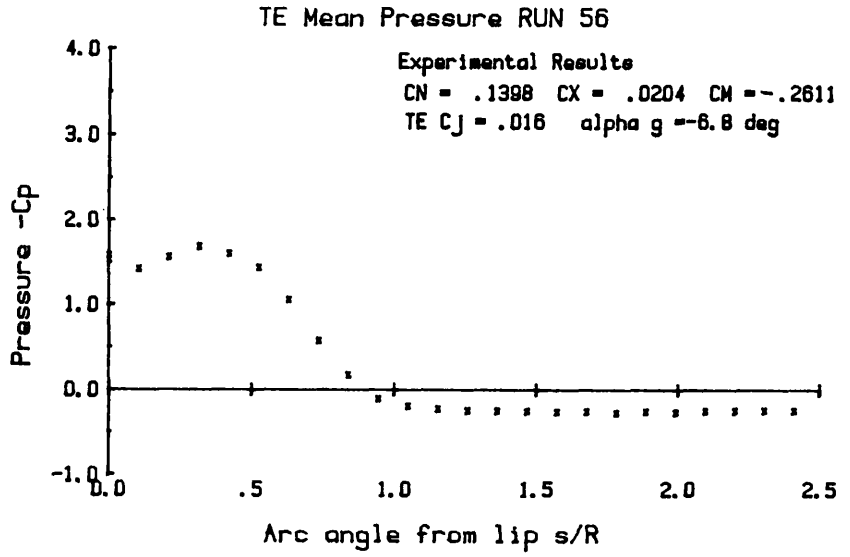

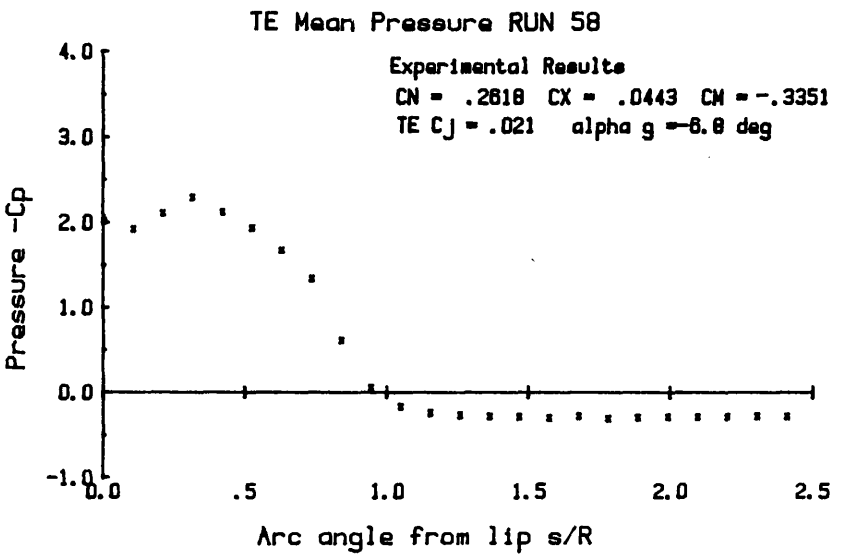

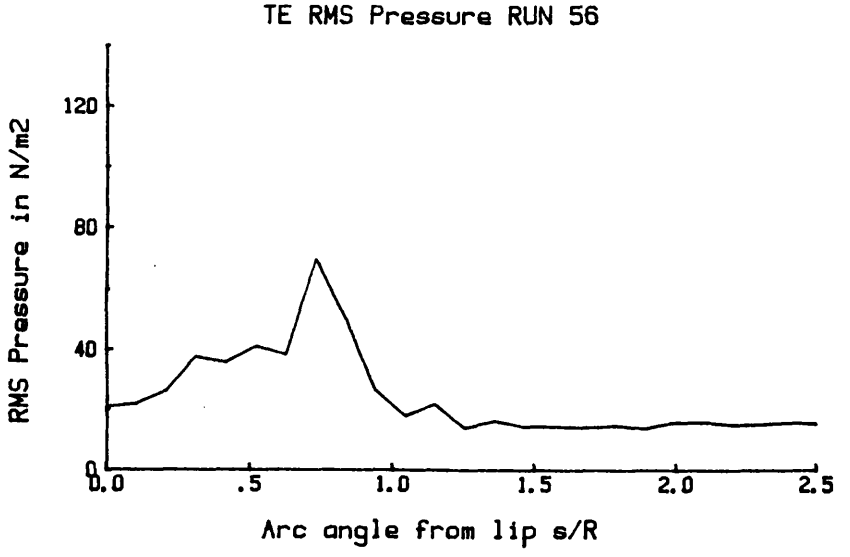

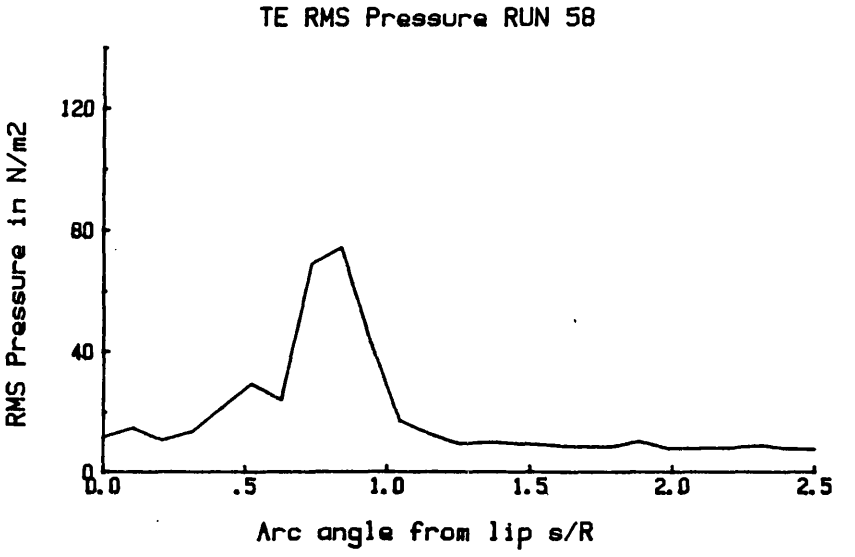

Fig. 3.10: TE PRESSURE DISTRIBUTION V ANGLE FROM LIP FOR MODEL AT -6.8 DEG. INCIDENCE WITH TE BLOWING.

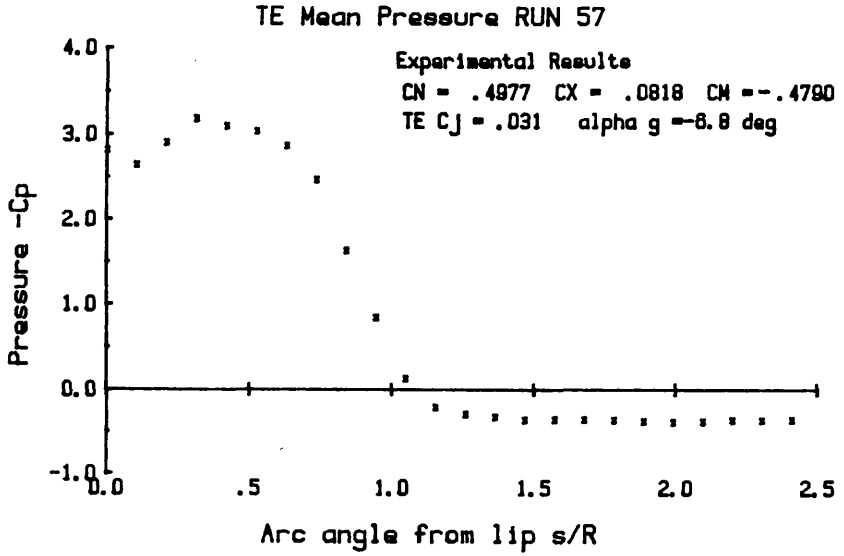

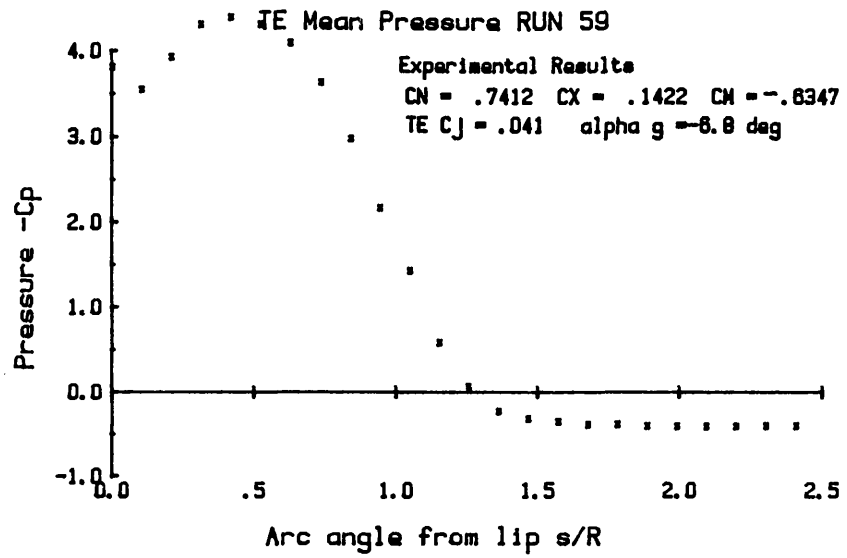

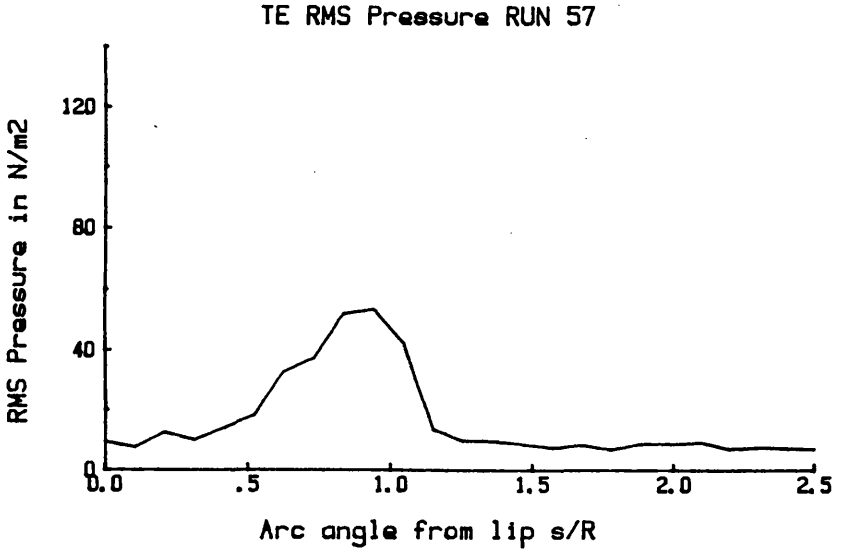

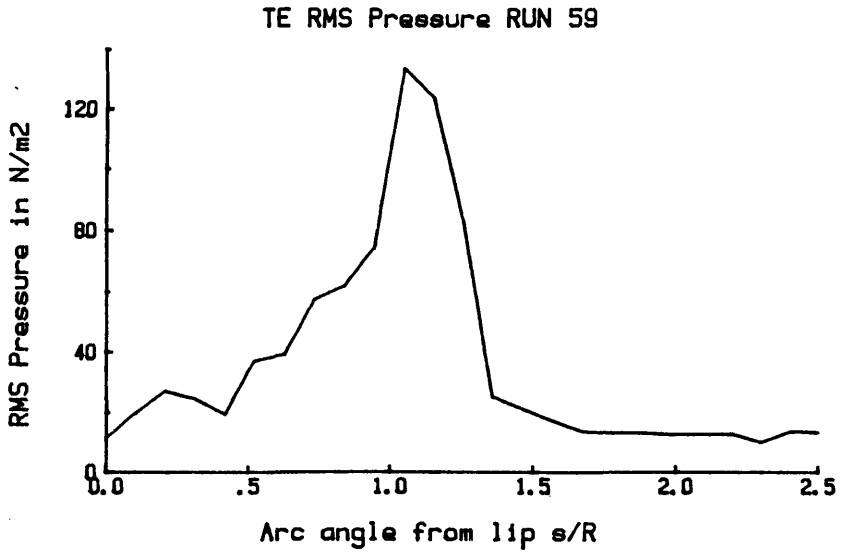

Fig. 3.11: TE PRESSURE DISTRIBUTION V ANGLE FROM LIP FOR MODEL AT -6.8 DEG. INCIDENCE WITH TE BLOWING.

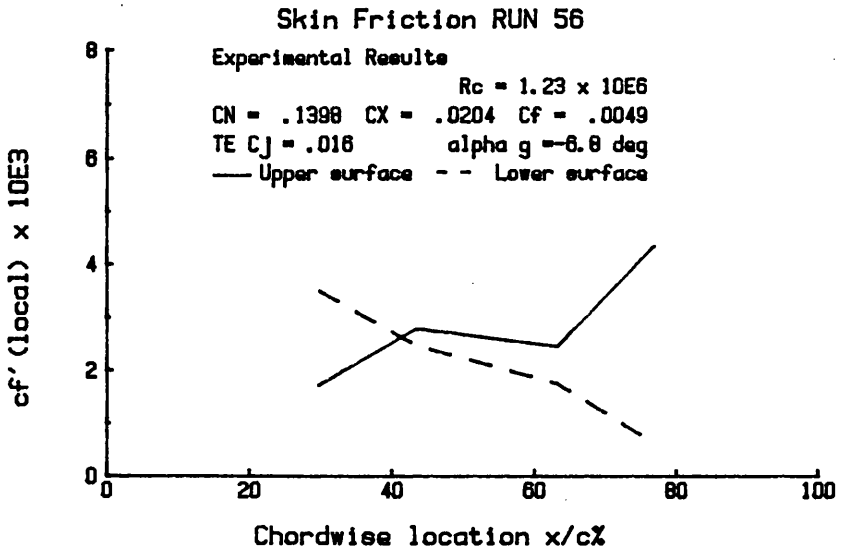

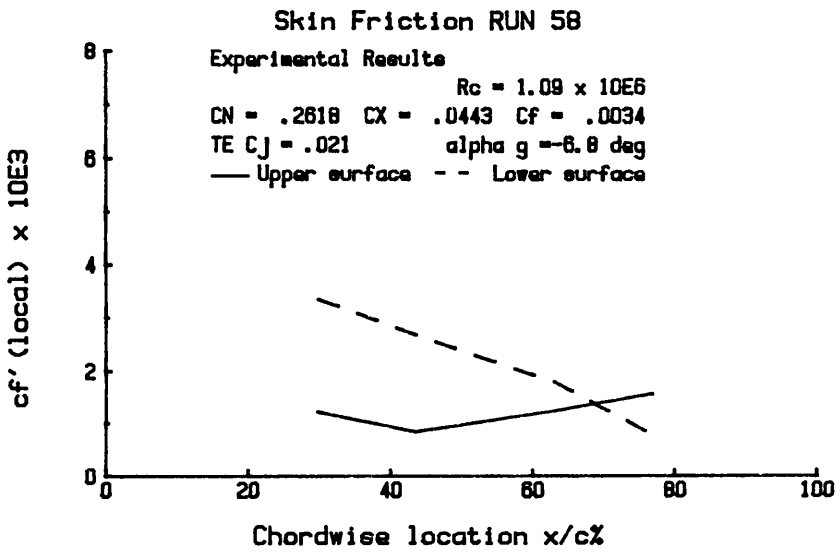

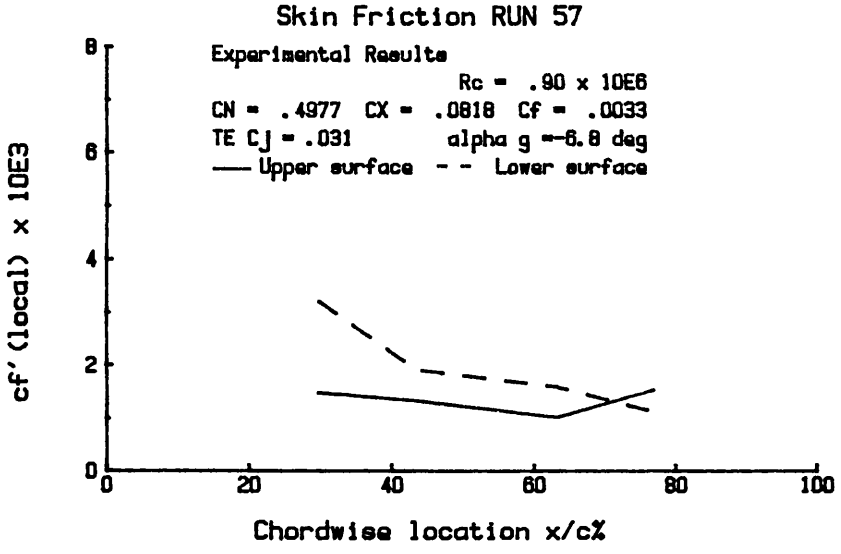

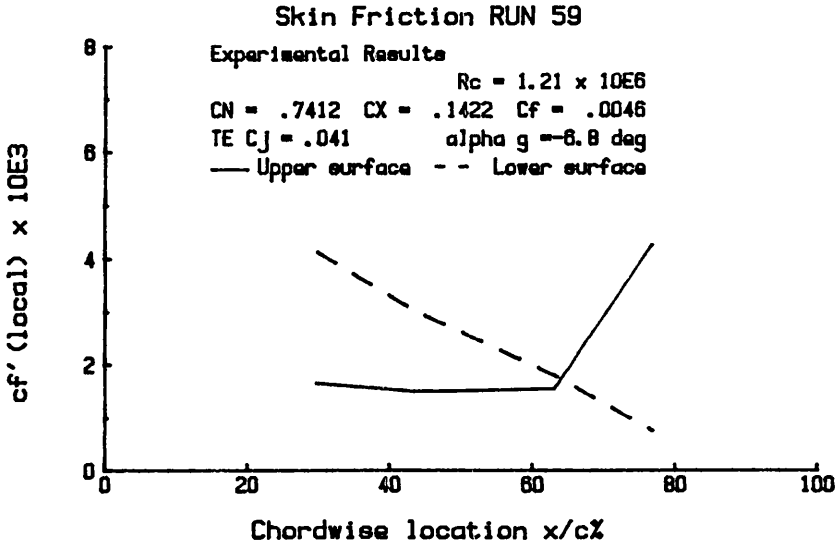

Fig. 3.12: SKIN FRICTION DISTRIBUTION V X/C% FOR MODEL AT -6.8 DEG. INCIDENCE WITH TE BLOWING ONLY.

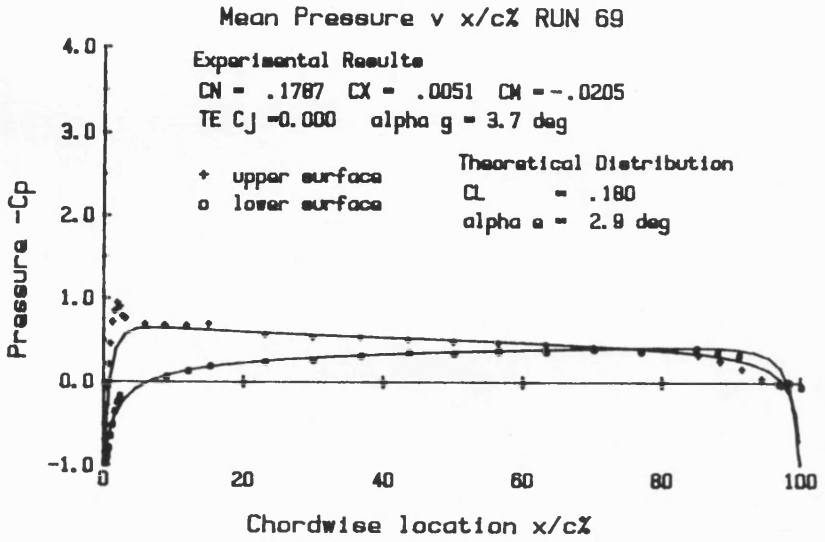

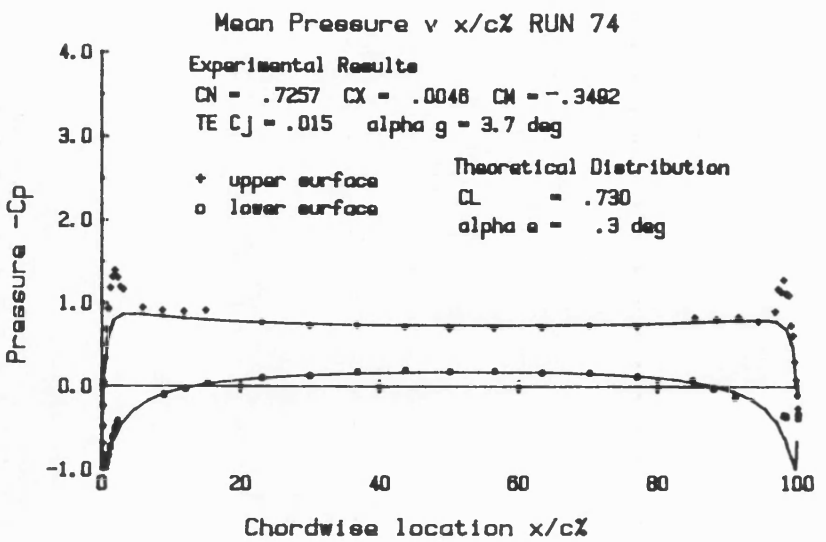

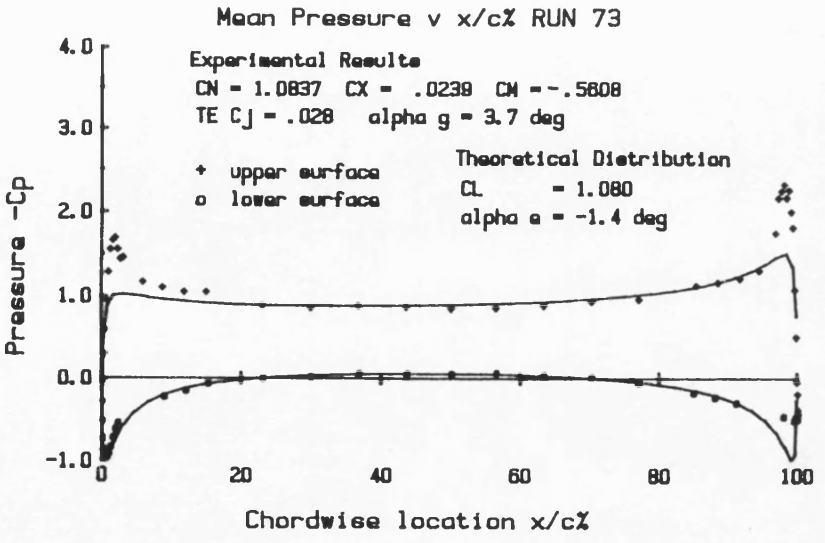

Fig. 3.13: MEAN PRESSURE DISTRIBUTION V X/C% FOR MODEL AT 3.7 DEG. INCIDENCE WITH TE BLOWING ONLY.

Fig.3.13

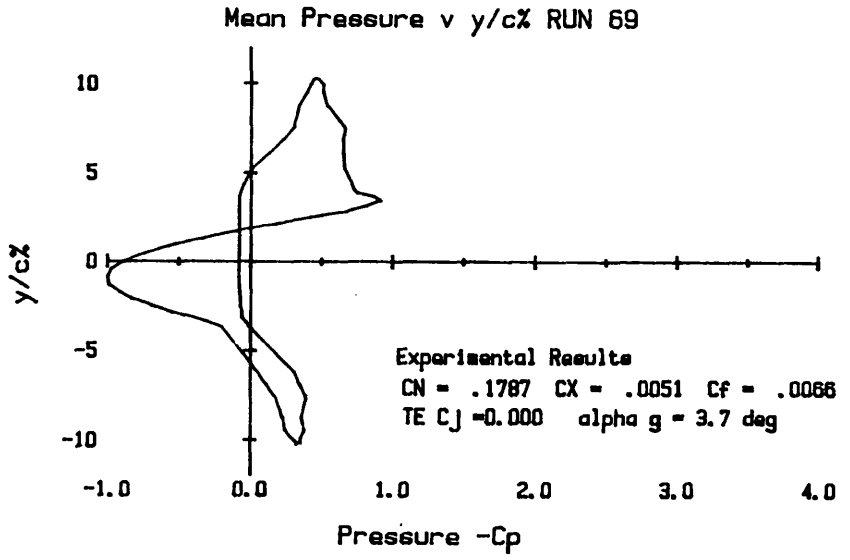

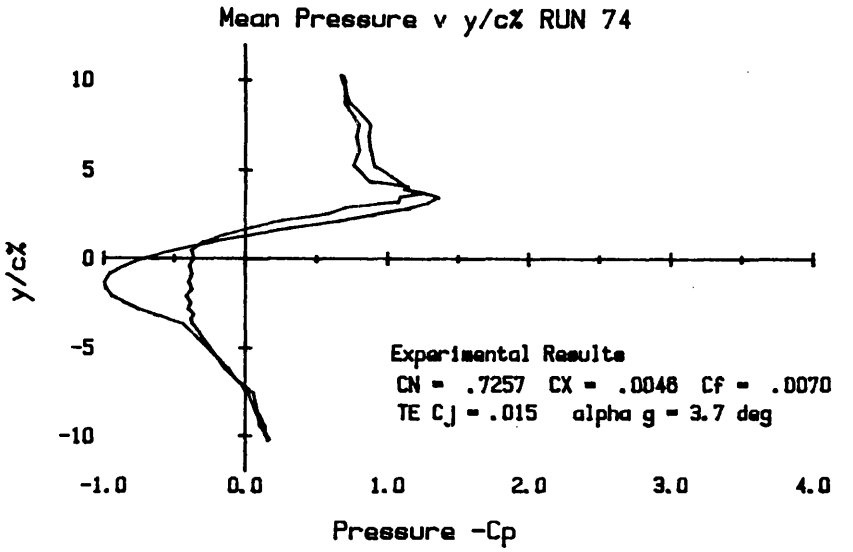

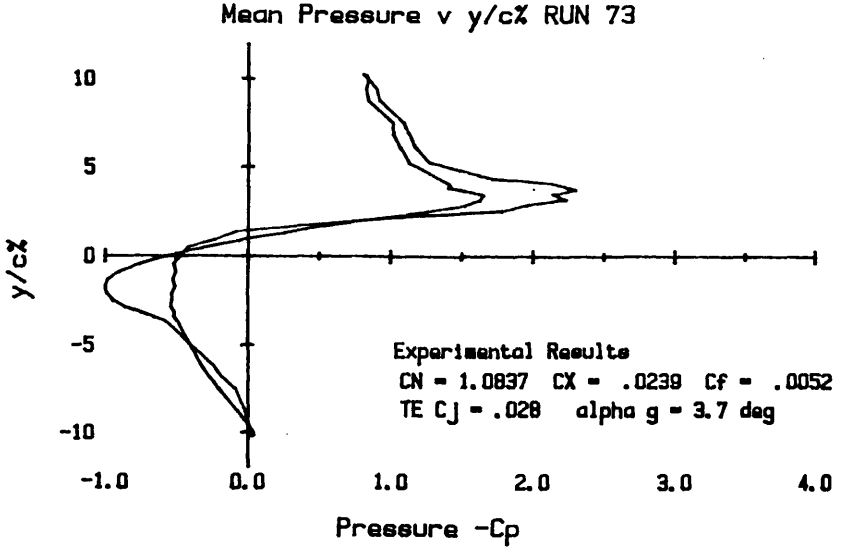

Fig. 3.14: MEAN PRESSURE DISTRIBUTION V Y/C% FOR MODEL AT 3.7 DEG. INCIDENCE WITH TE BLOWING ONLY.

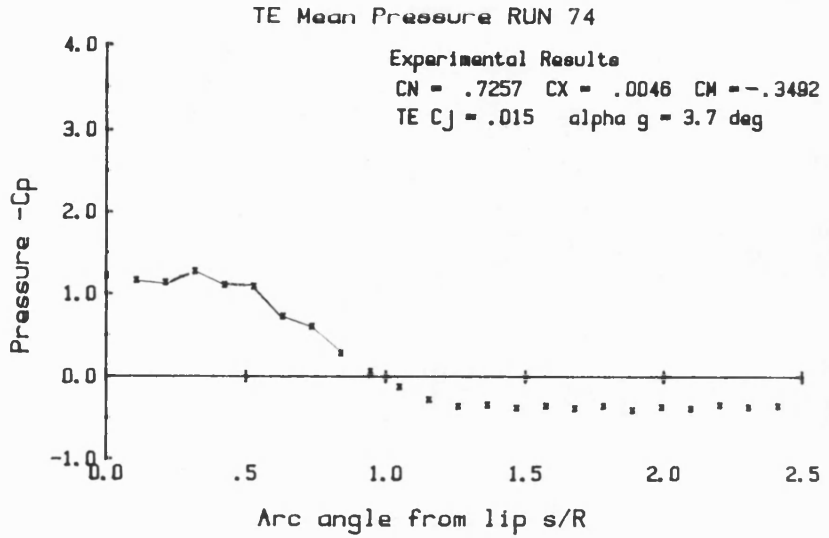

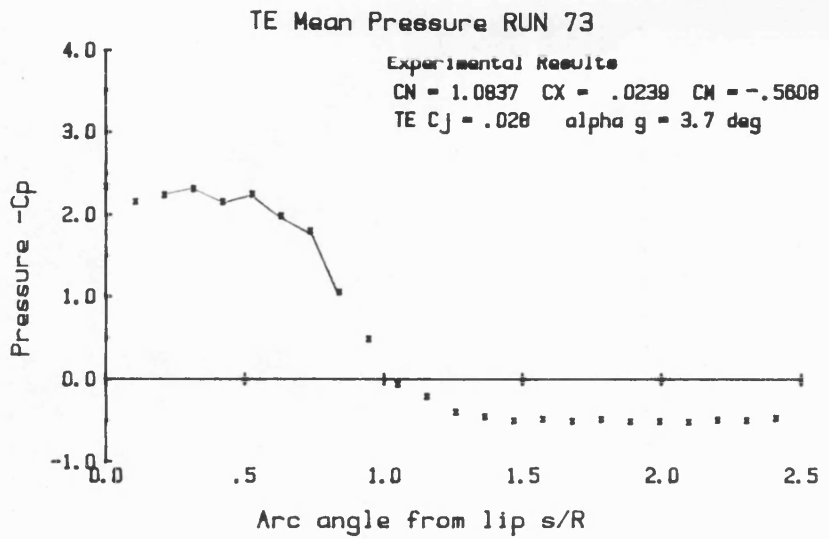

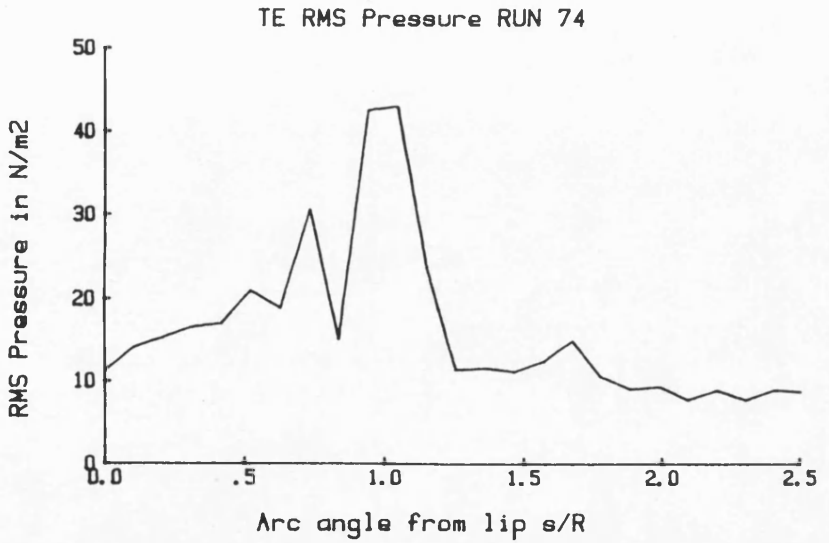

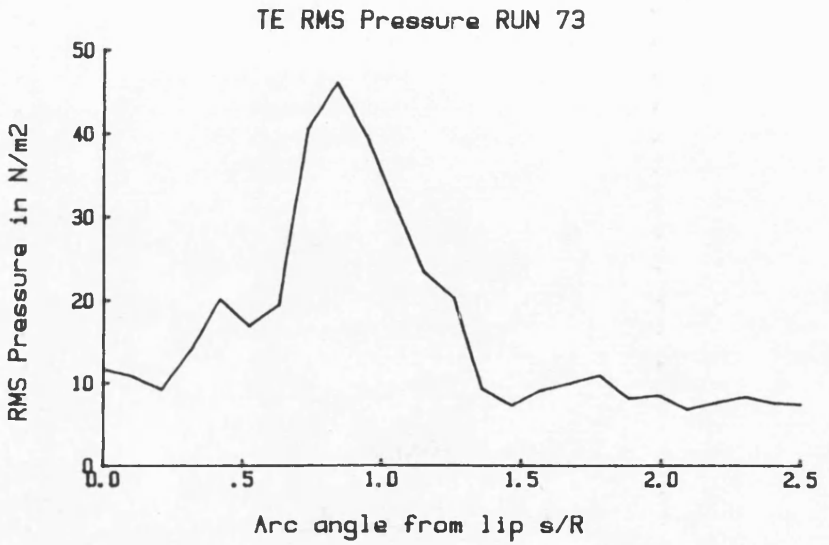

Fig. 3.15: TE PRESSURE DISTRIBUTION V ANGLE FROM LIP FOR MODEL AT 3.7 DEG. INCIDENCE WITH TE BLOWING ONLY.

Fig. 3.15

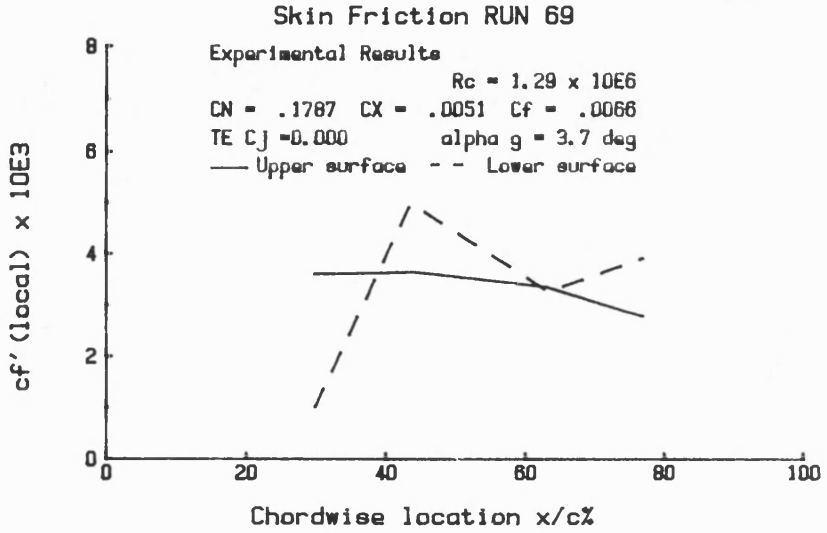

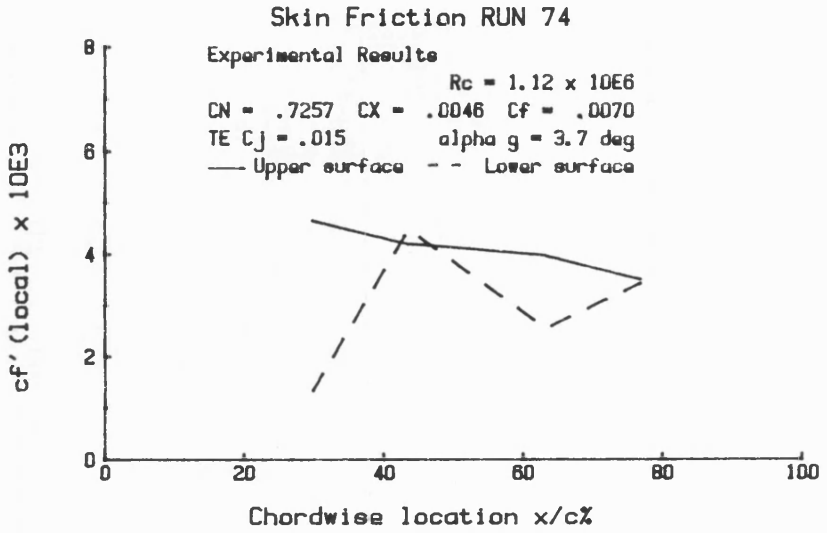

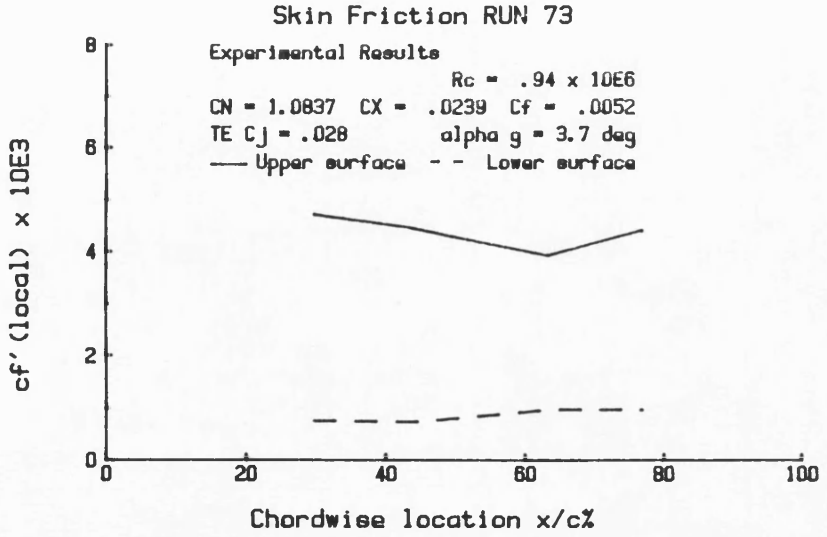

Fig. 3.16: SKIN FRICTION DISTRIBUTION V X/C% FOR MODEL AT 3.7 DEG. INCIDENCE WITH TE BLOWING ONLY.

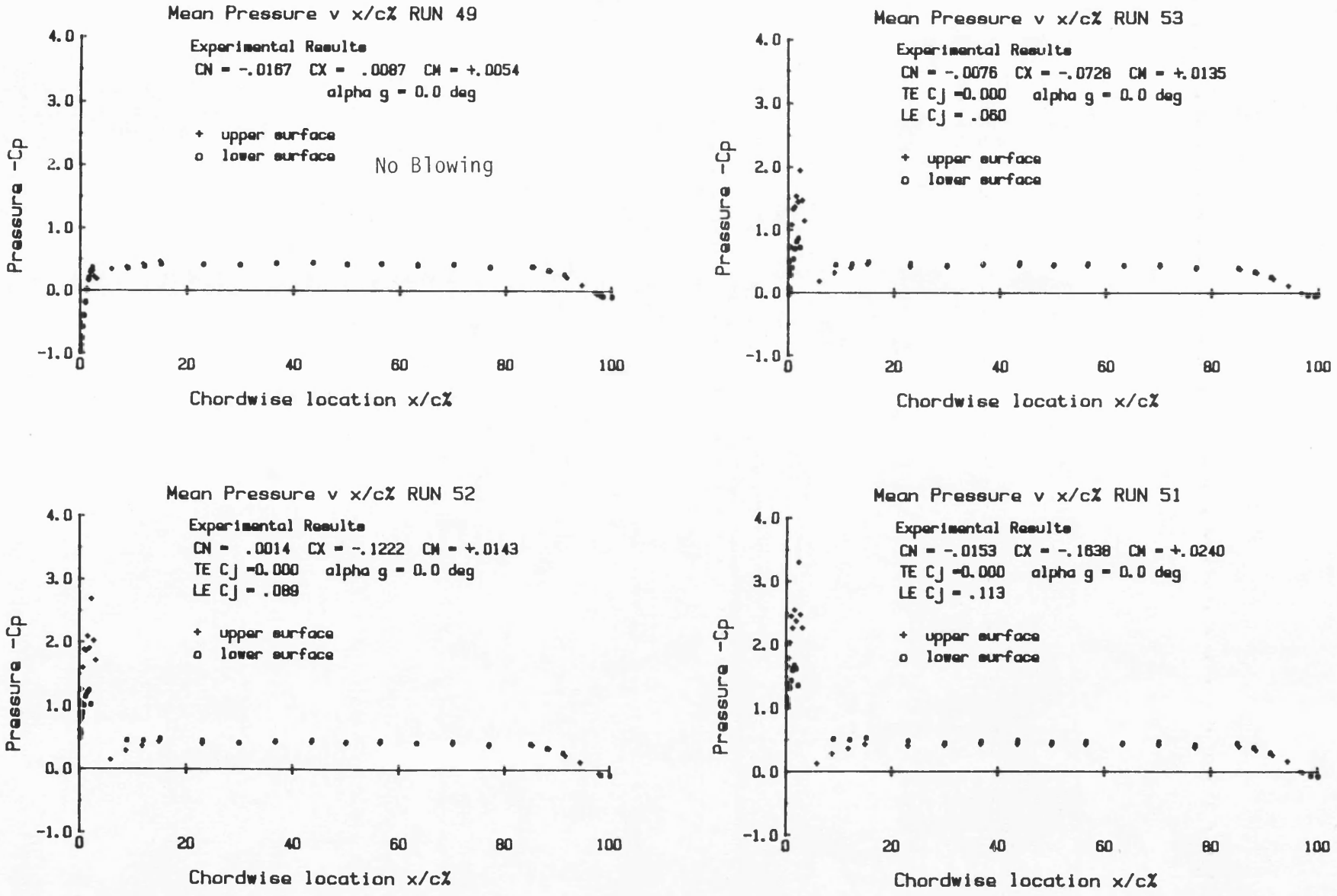

Fig. 3.17: MEAN PRESSURE DISTRIBUTION V X/C% FOR MODEL AT ZERO INCIDENCE WITH LE BLOWING ONLY.

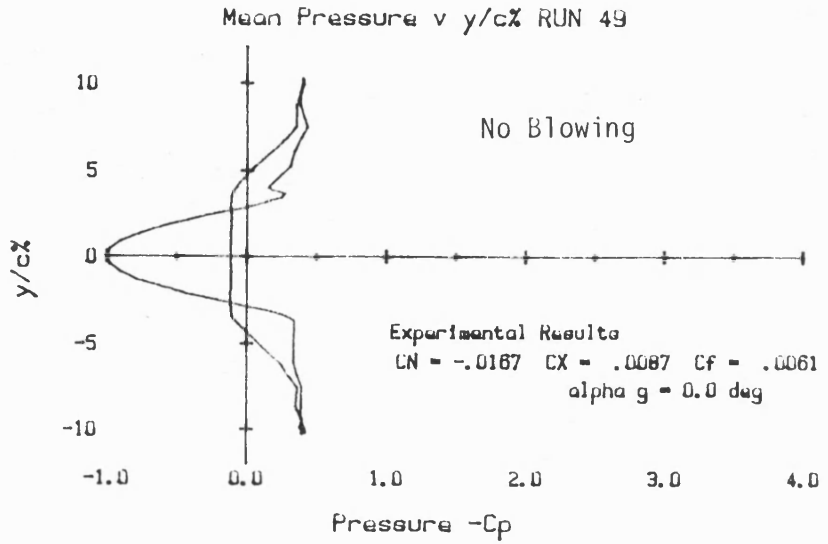

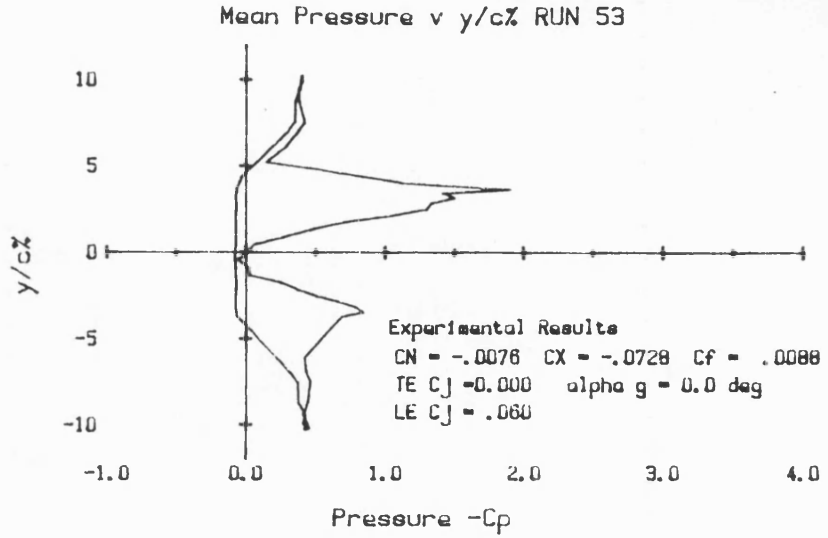

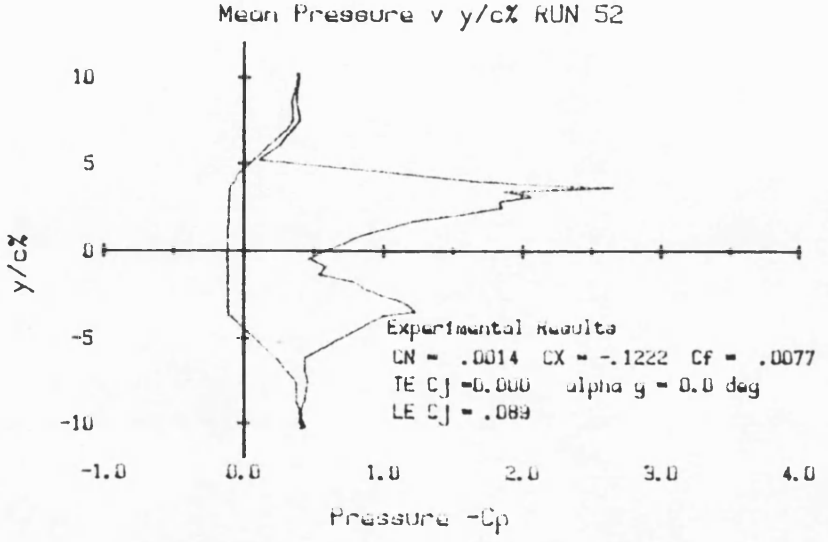

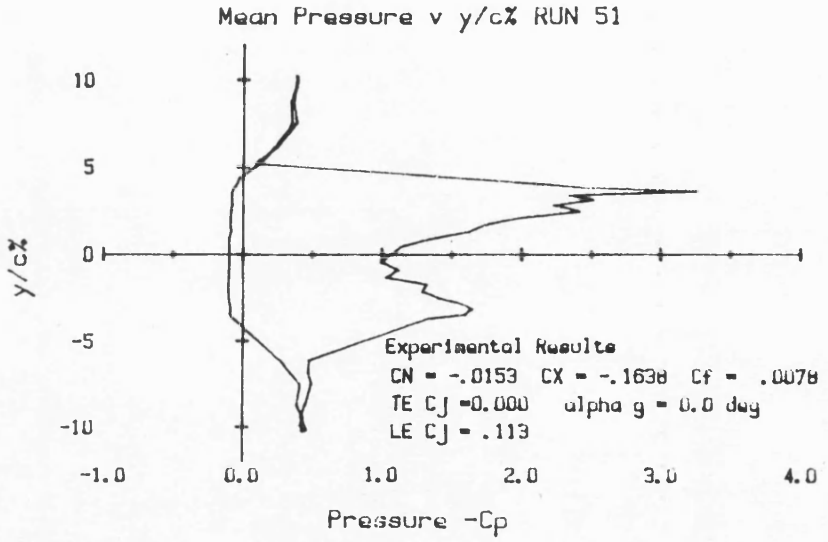

Fig. 3.18: MEAN PRESSURE DISTRIBUTION V Y/C% FOR MODEL AT ZERO INCIDENCE WITH LE BLOWING ONLY.

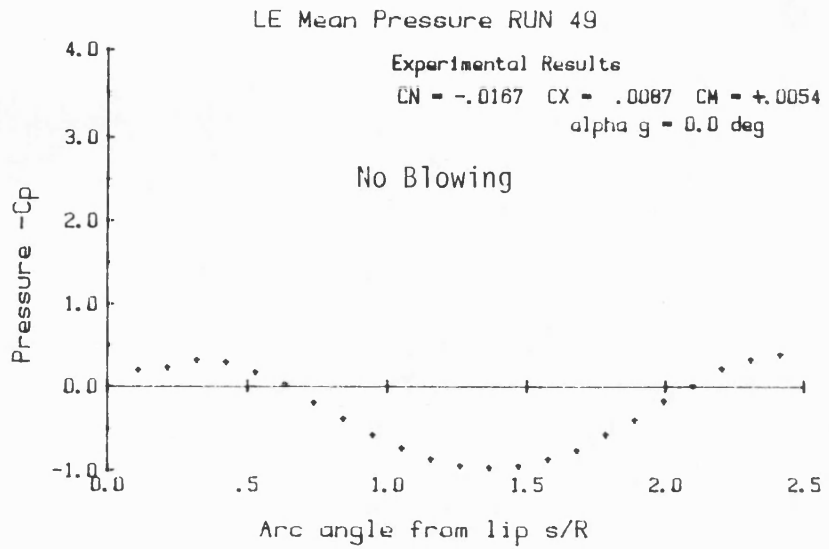

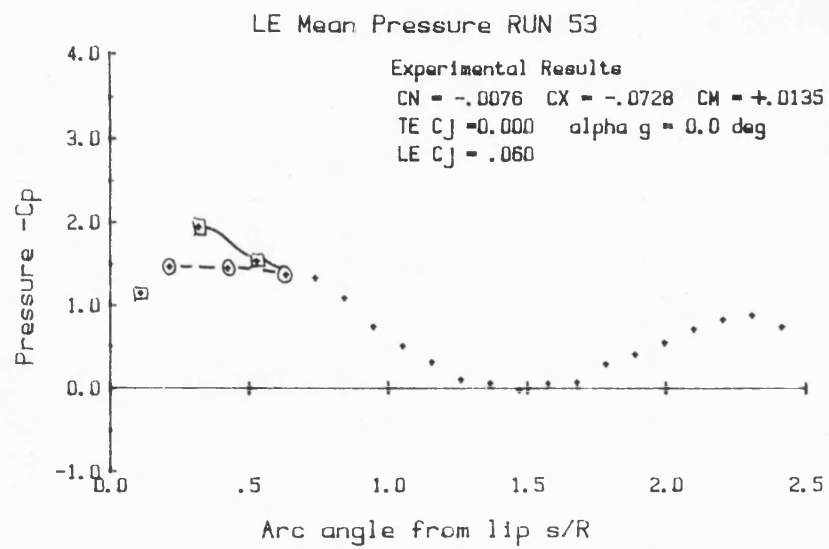

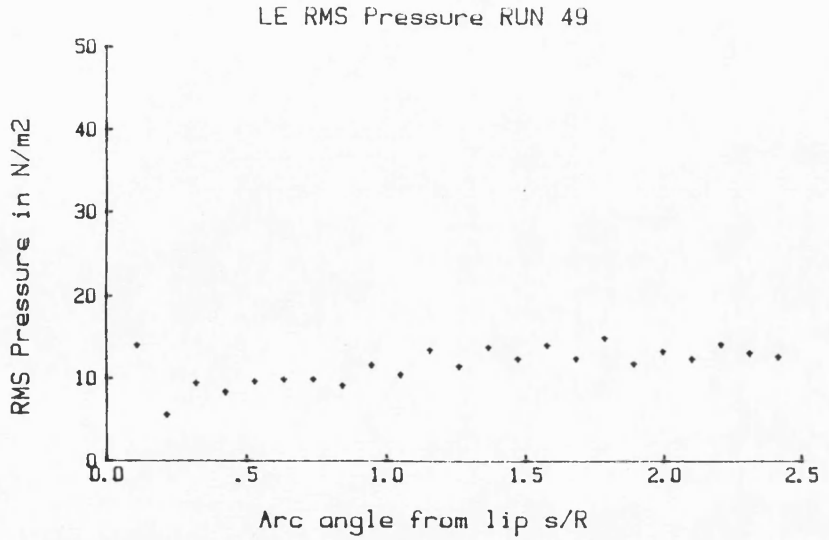

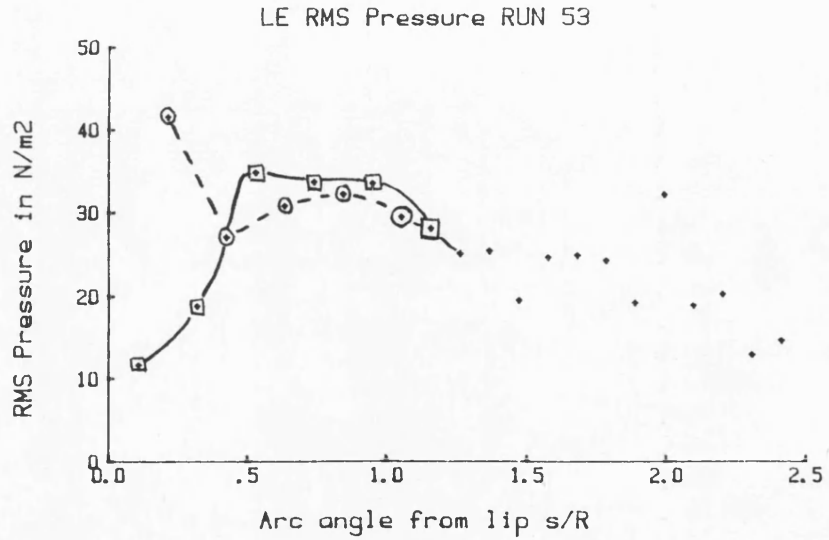

Fig. 3.19: LE PRESSURE DISTRIBUTION V ANGLE FROM LIP FOR MODEL AT ZERO INCIDENCE WITH LE BLOWING ONLY.

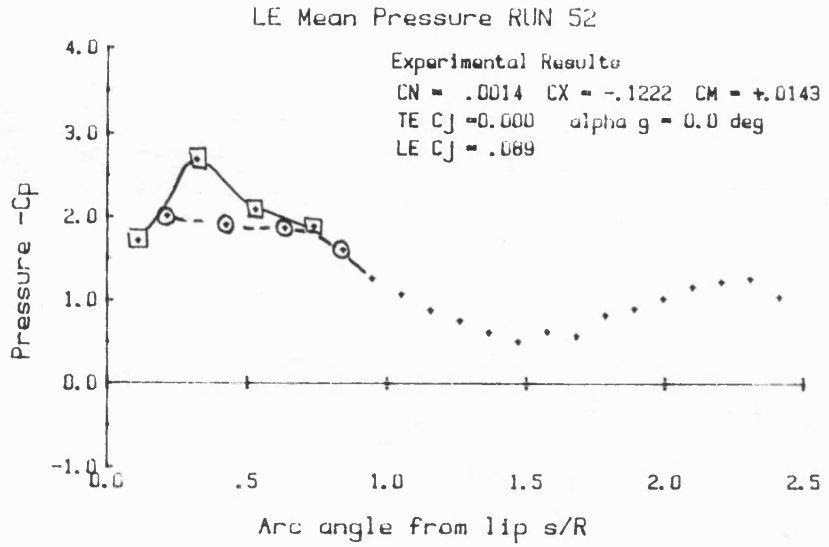

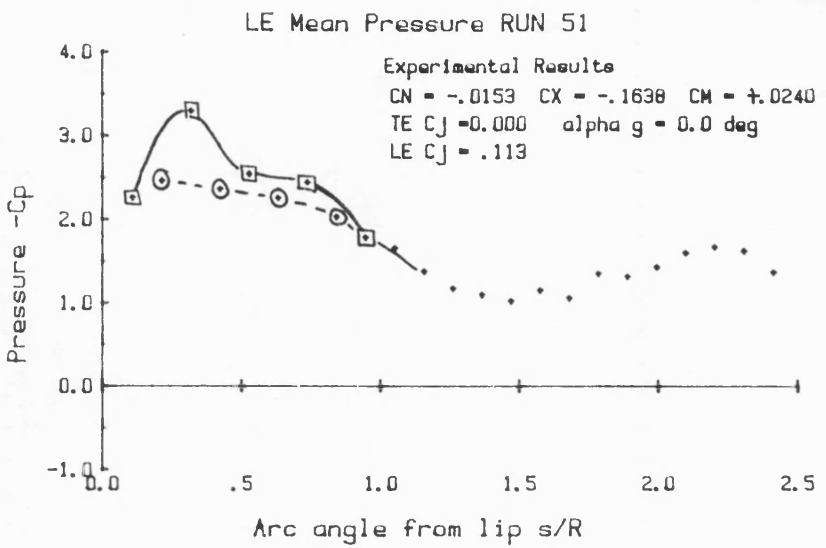

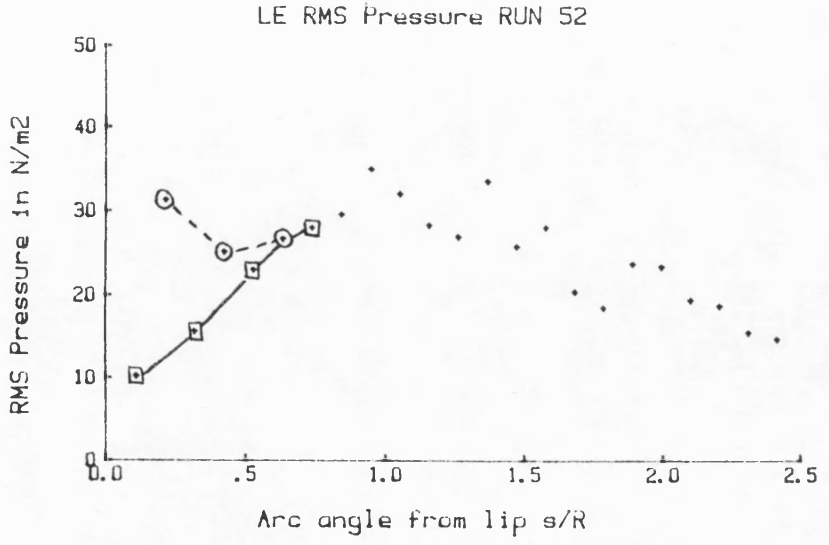

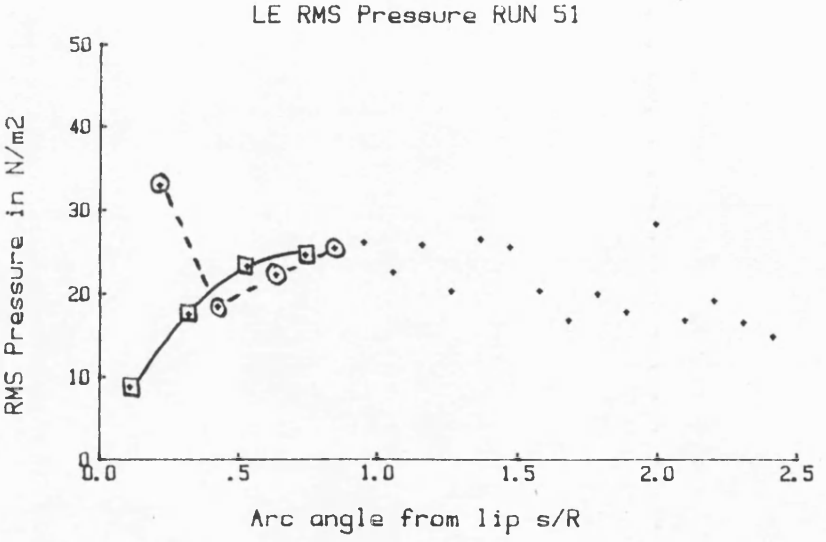

Fig. 3.20: LE PRESSURE DISTRIBUTION V ANGLE FROM LIP FOR MODEL AT ZERO INCIDENCE WITH LE BLOWING ONLY.

Fig. 3.20

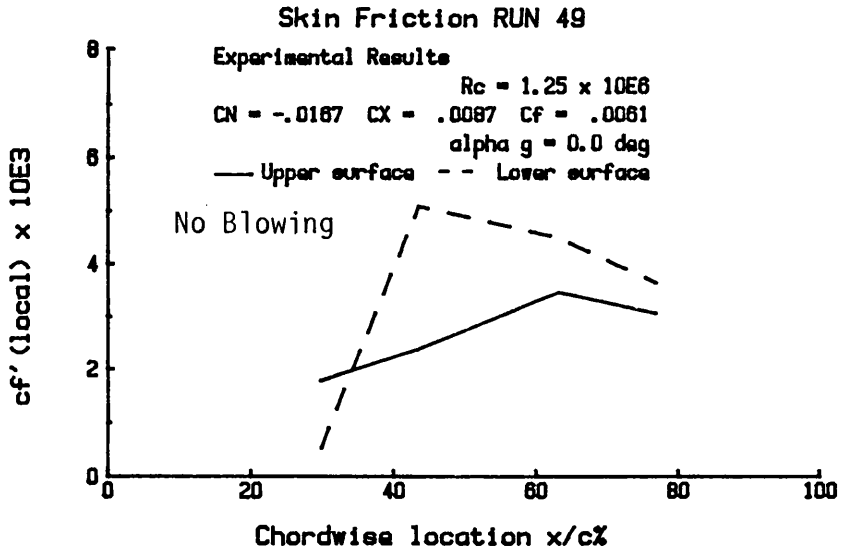

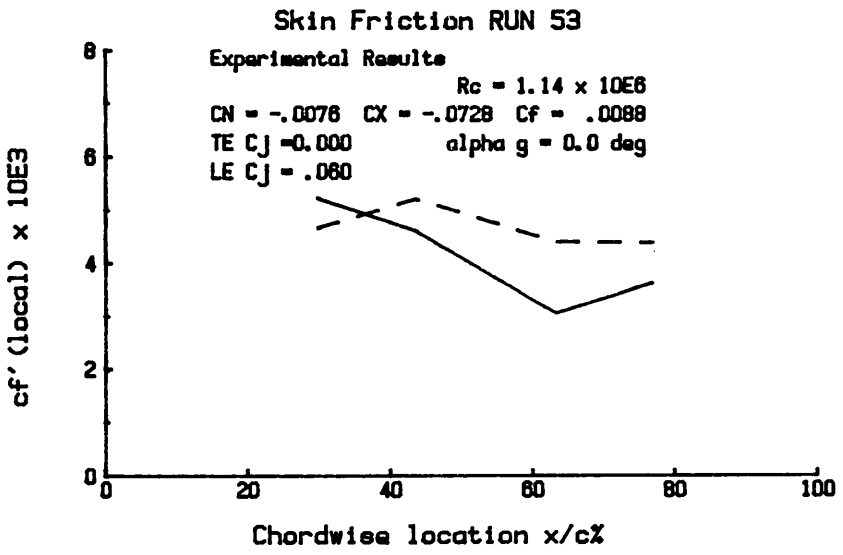

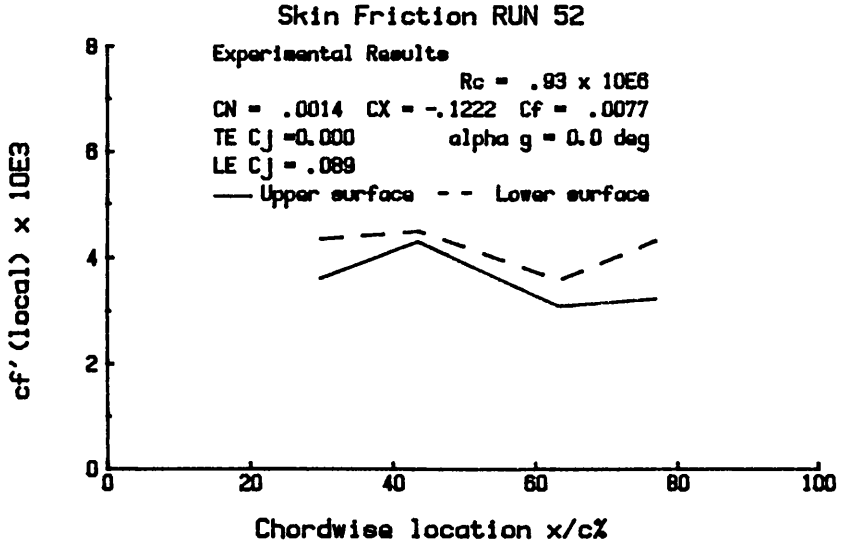

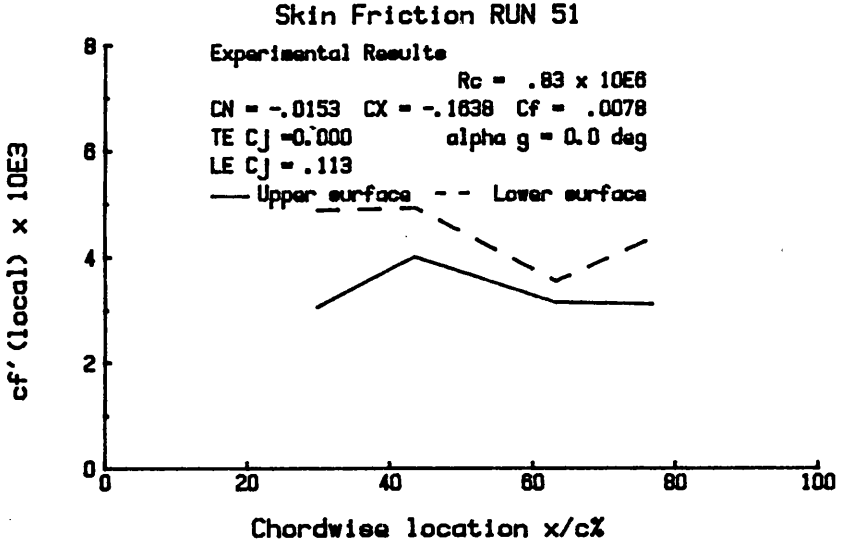

Fig. 3.21: SKIN FRICTION DISTRIBUTION V X/C% FOR MODEL AT ZERO INCIDENCE WITH LE BLOWING ONLY.

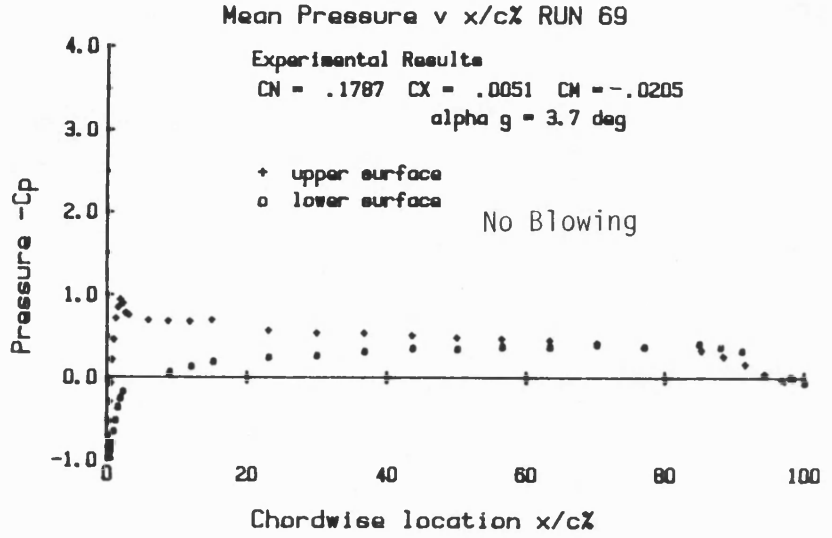

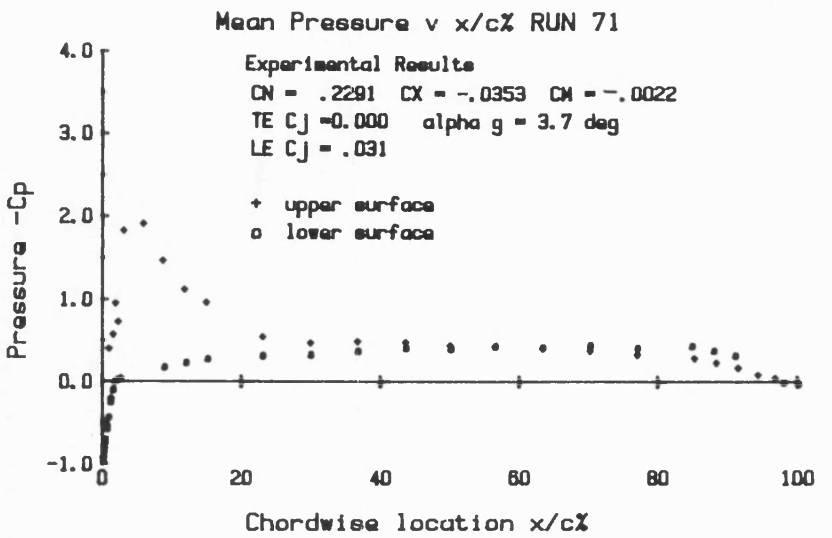

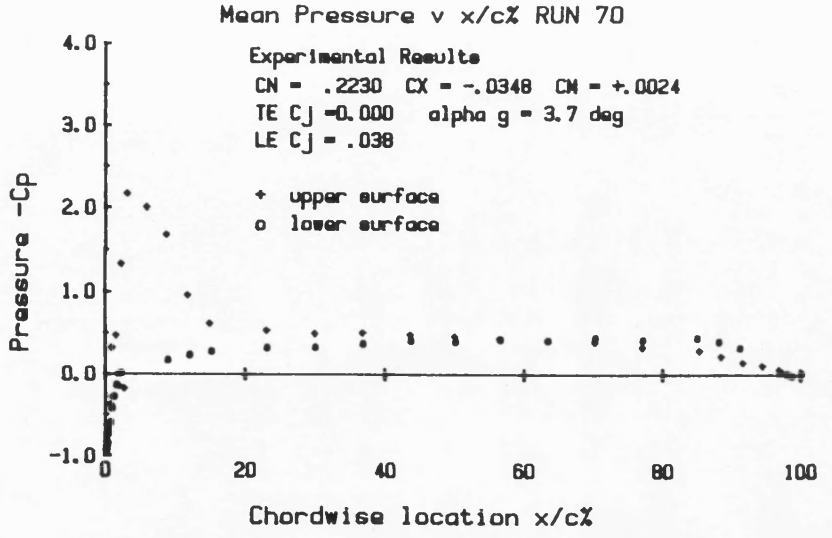

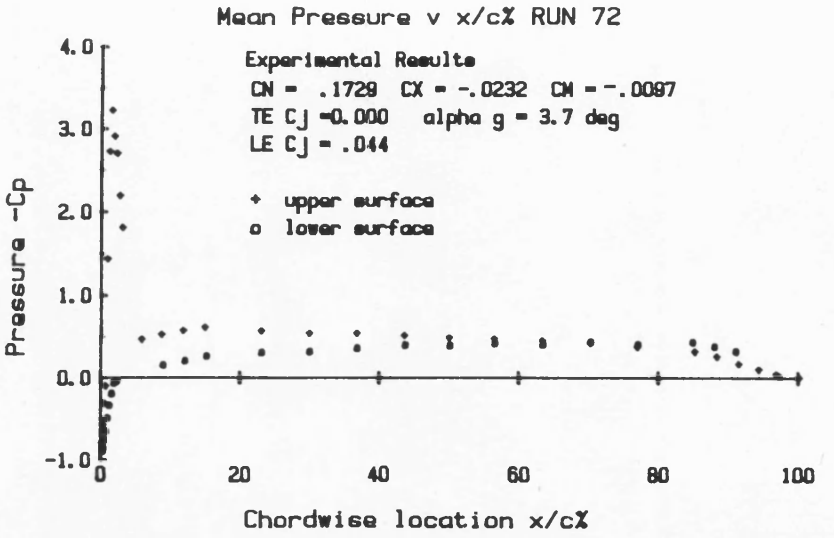

Fig. 3.22: MEAN PRESSURE DISTRIBUTION V X/C% FOR MODEL AT 3.7 DEG. INCIDENCE WITH LE BLOWING ONLY.

Fig. 3.22

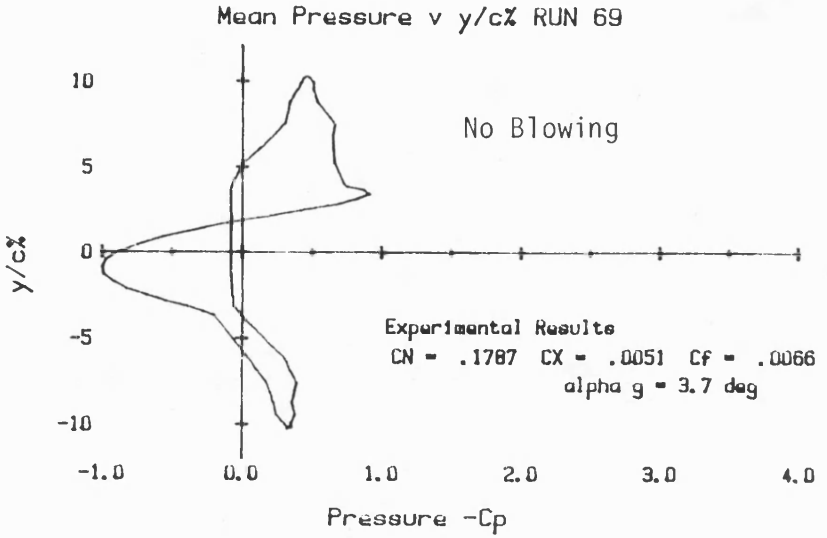

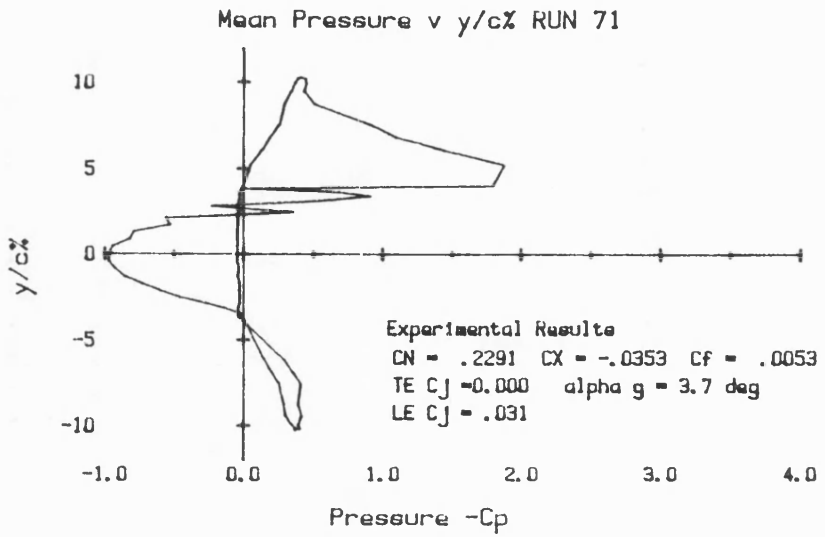

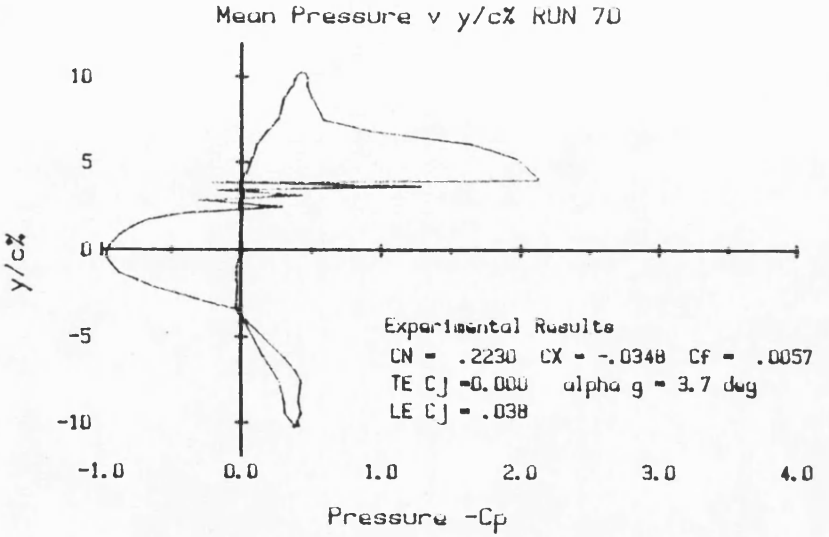

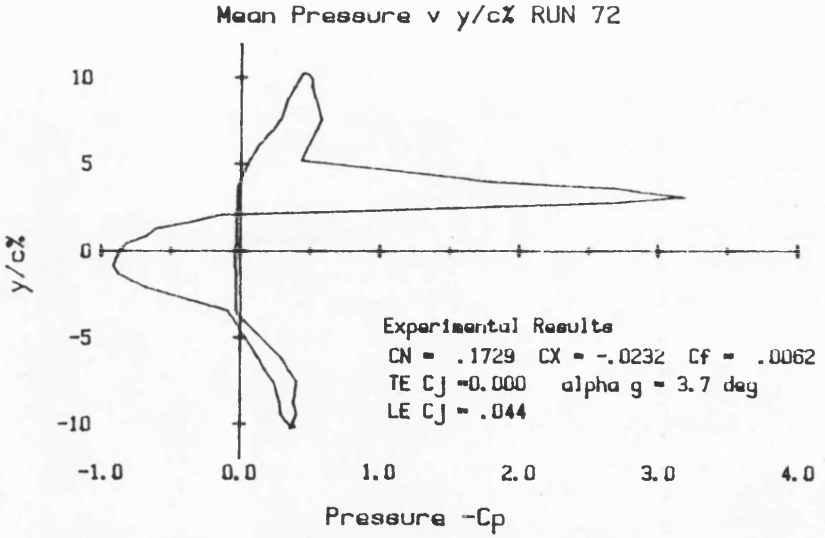

Fig.3.23: MEAN PRESSURE DISTRIBUTION V Y/C% FOR MODEL AT 3.7 DEG. INCIDENCE WITH LE BLOWING ONLY.

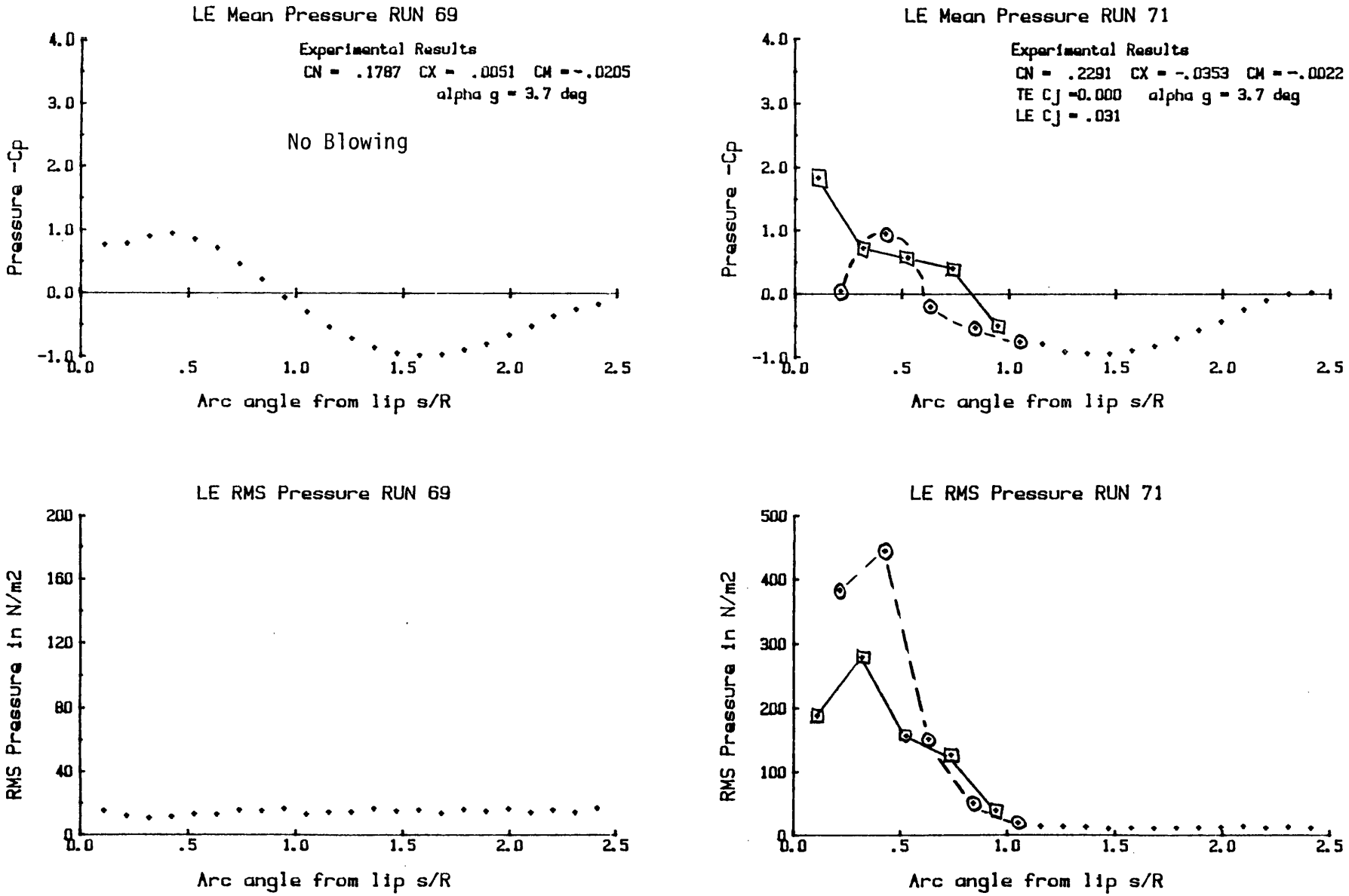

Fig. 3.24: LE PRESSURE DISTRIBUTION V ANGLE FROM LIP FOR MODEL AT 3.7 DEG. INCIDENCE WITH LE BLOWING ONLY.

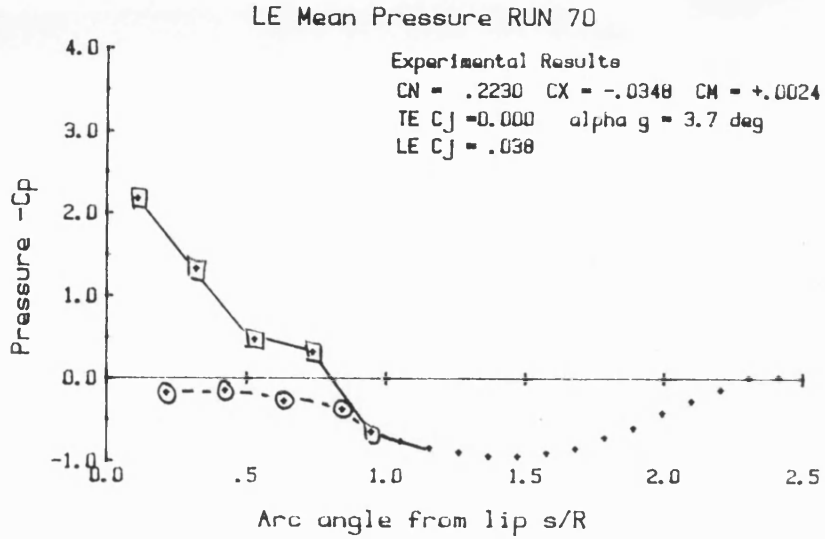

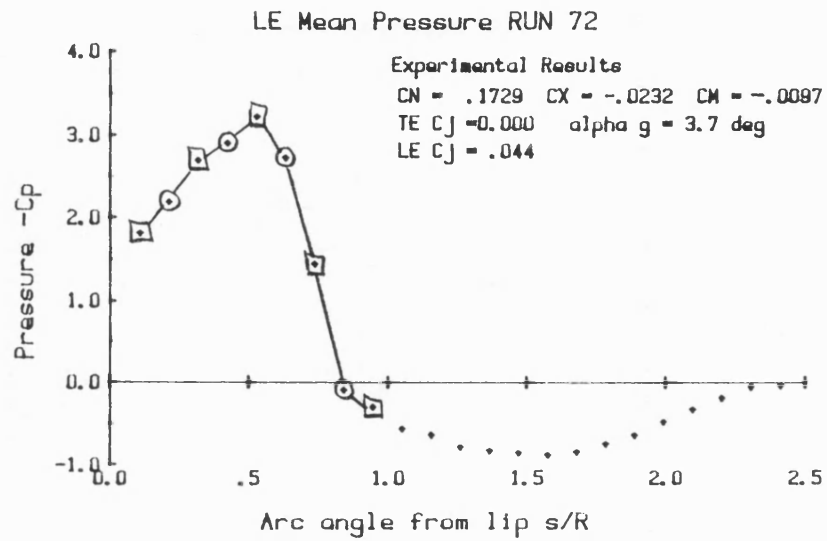

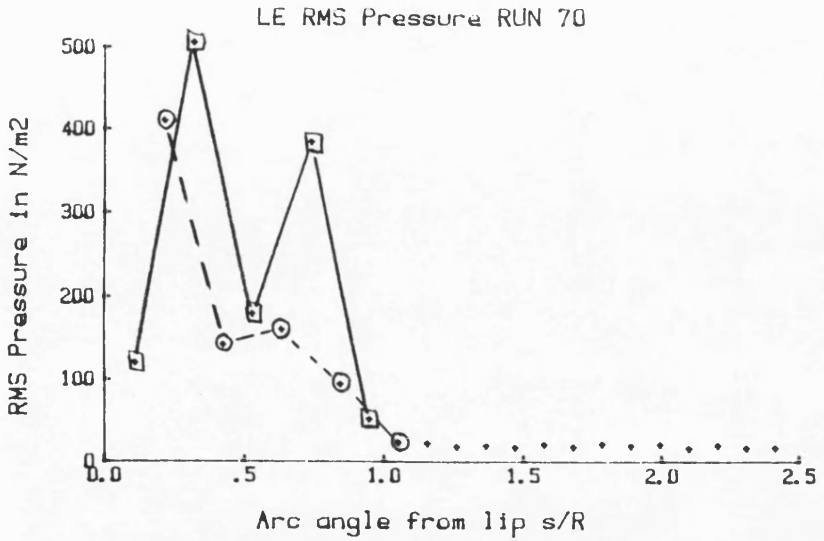

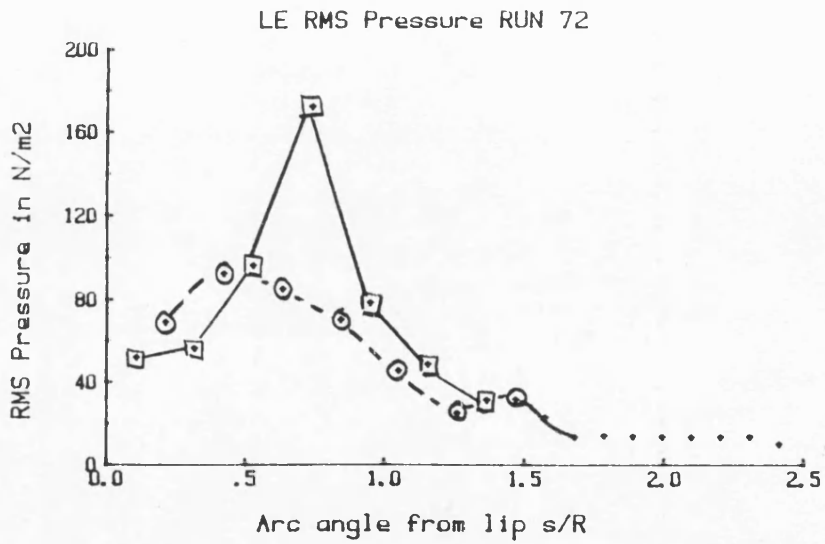

Fig. 3.25: LE PRESSURE DISTRIBUTION V ANGLE FROM LIP FOR MODEL AT 3.7 DEG. INCIDENCE WITH LE BLOWING ONLY.

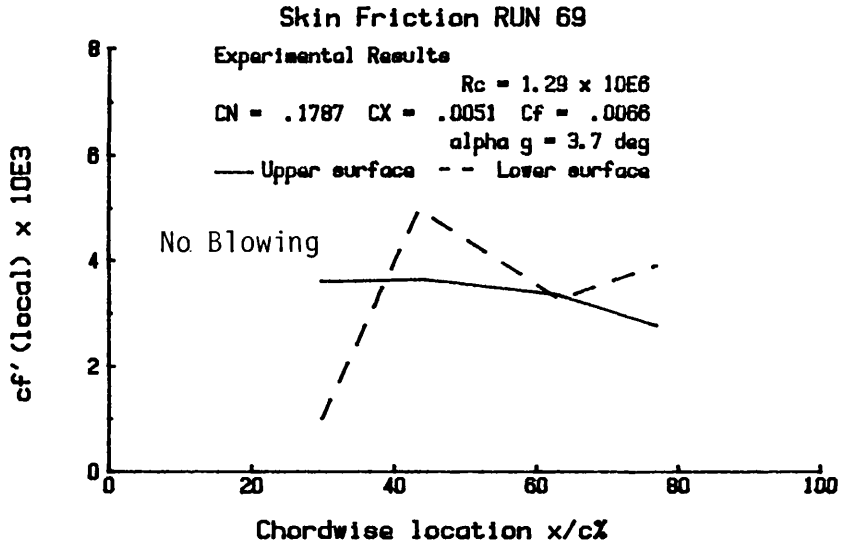

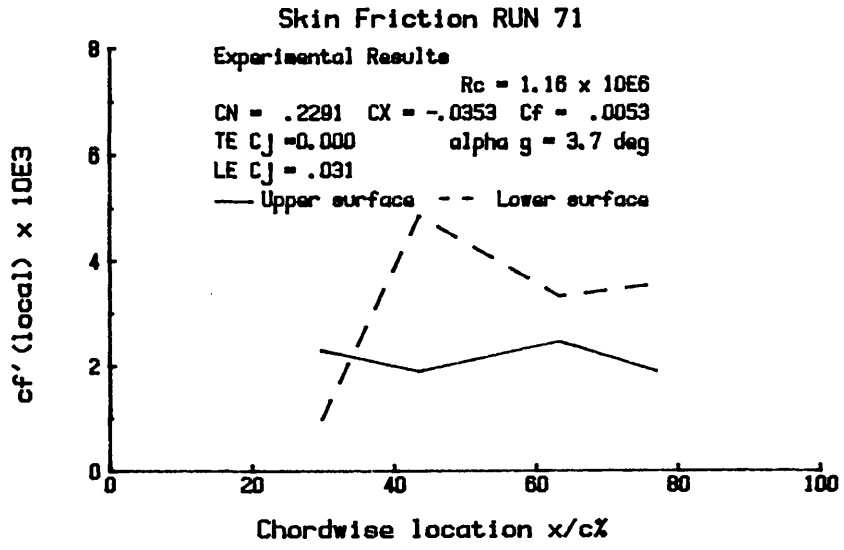

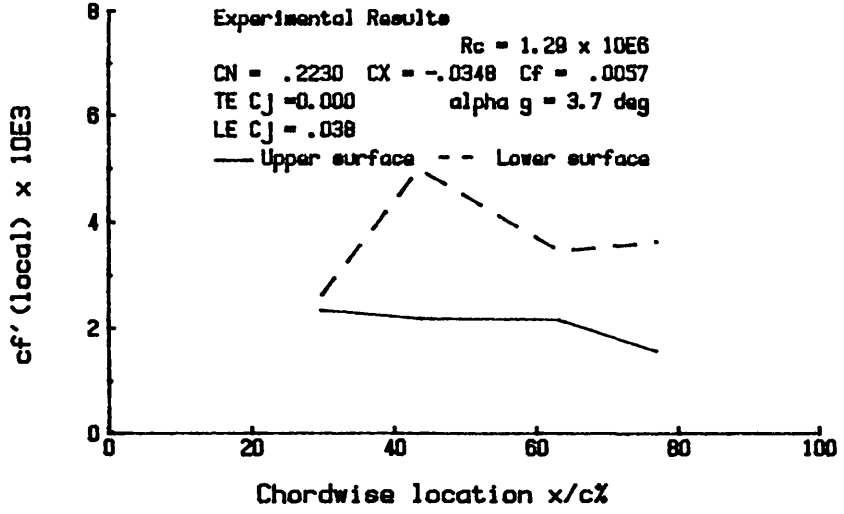

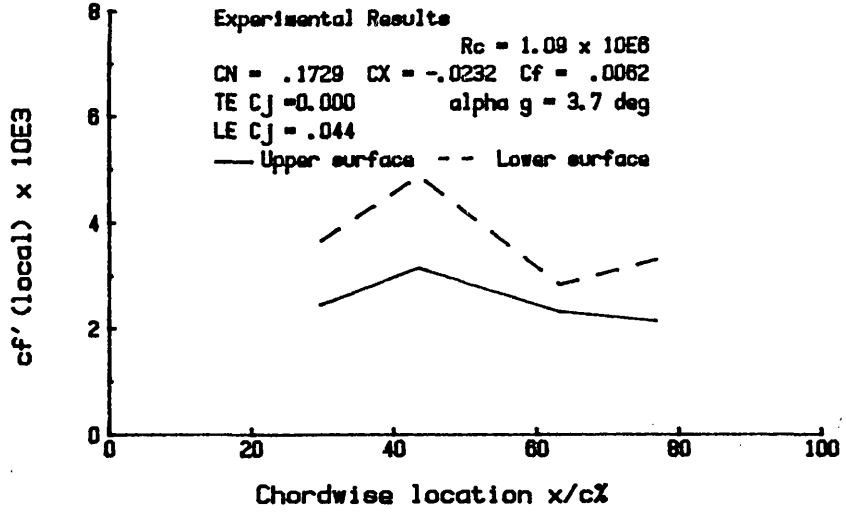

Fig. 3.26: SKIN FRICTION DISTRIBUTION V X/C% FOR MODEL AT 3.7 DEG. INCIDENCE WITH LE BLOWING ONLY.

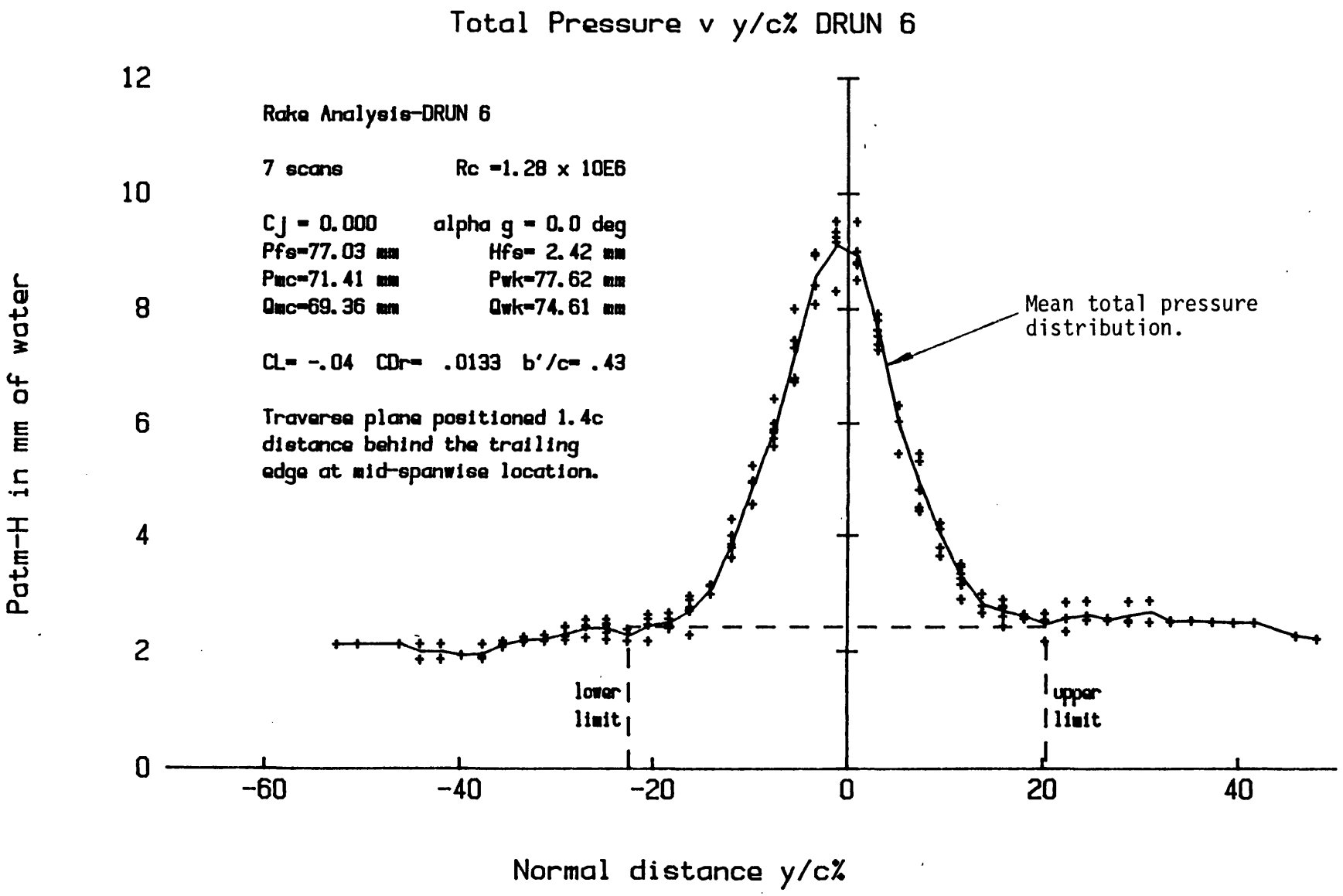

Fig. 3.27: TOTAL PRESSURE DISTRIBUTION IN THE WAKE OF THE UNBLOWN MODEL AT ZERO GEOMETRIC INCIDENCE.

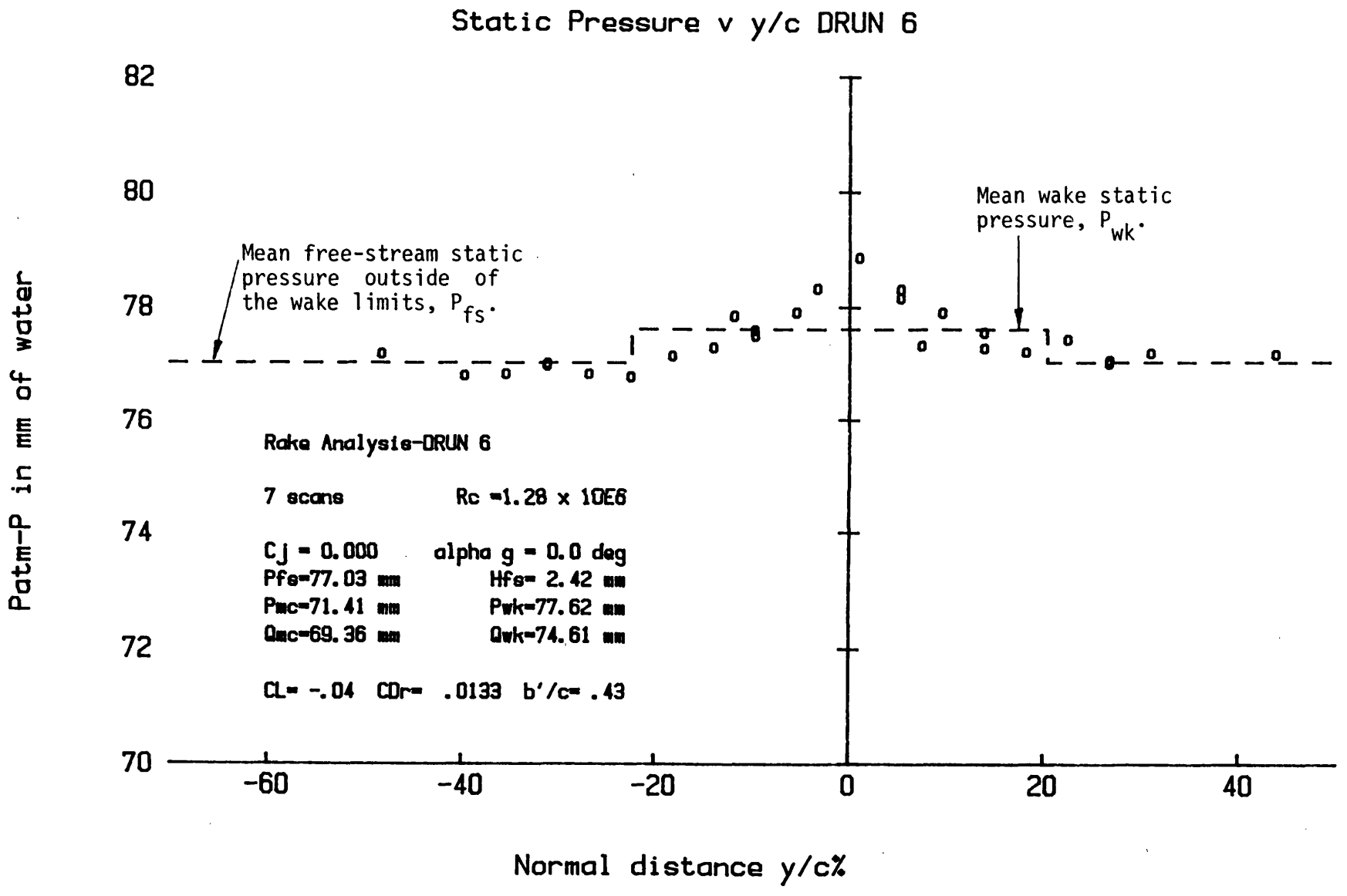

Fig. 3.28: STATIC PRESSURE DISTRIBUTION IN THE WAKE OF THE UNBLOWN MODEL AT ZERO GEOMETRIC INCIDENCE.

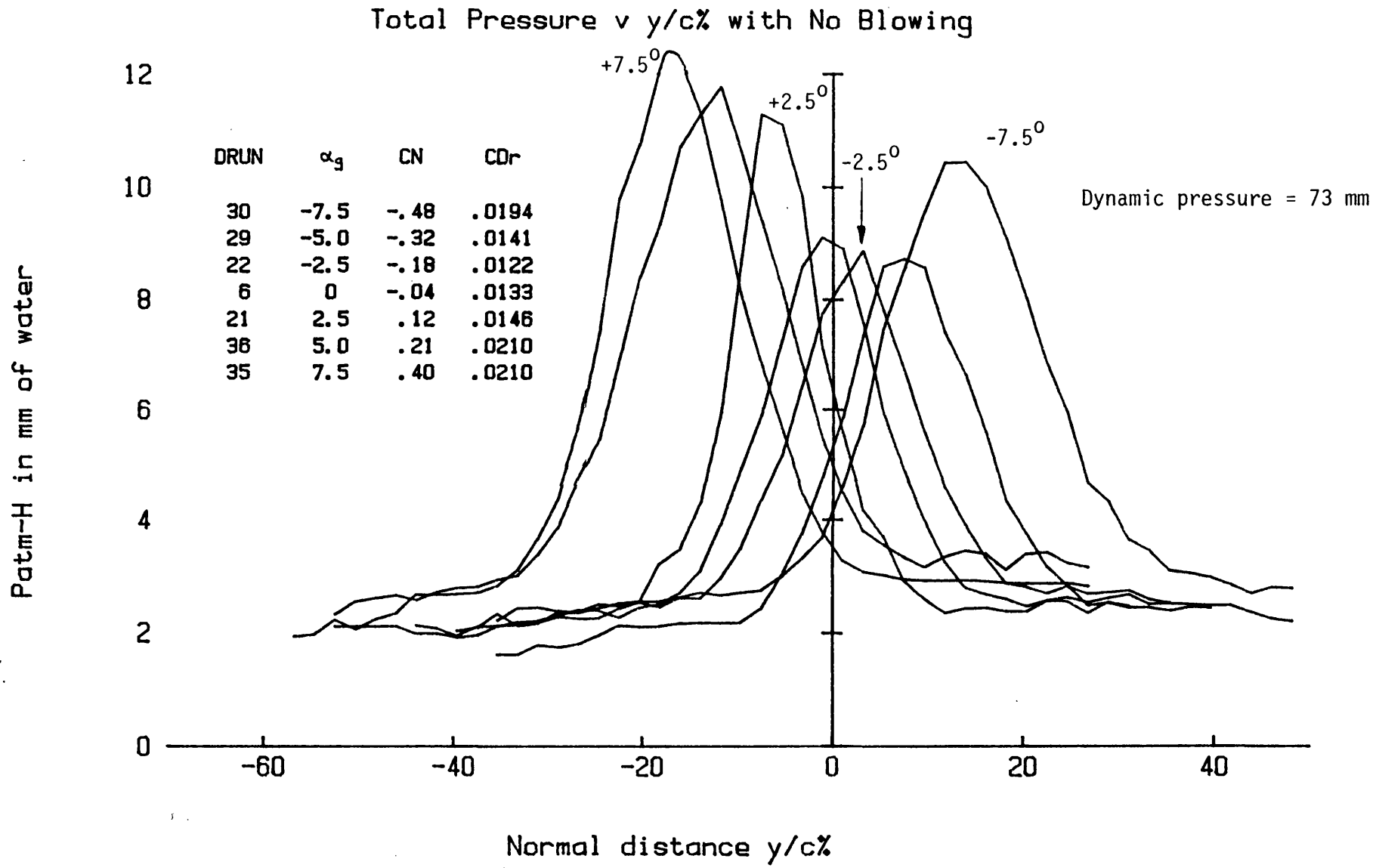

Fig. 3.29: TOTAL PRESSURE DISTRIBUTION IN THE WAKE OF THE UNBLOWN MODEL WITH VARIATION OF INCIDENCE.

Fig. 3.29

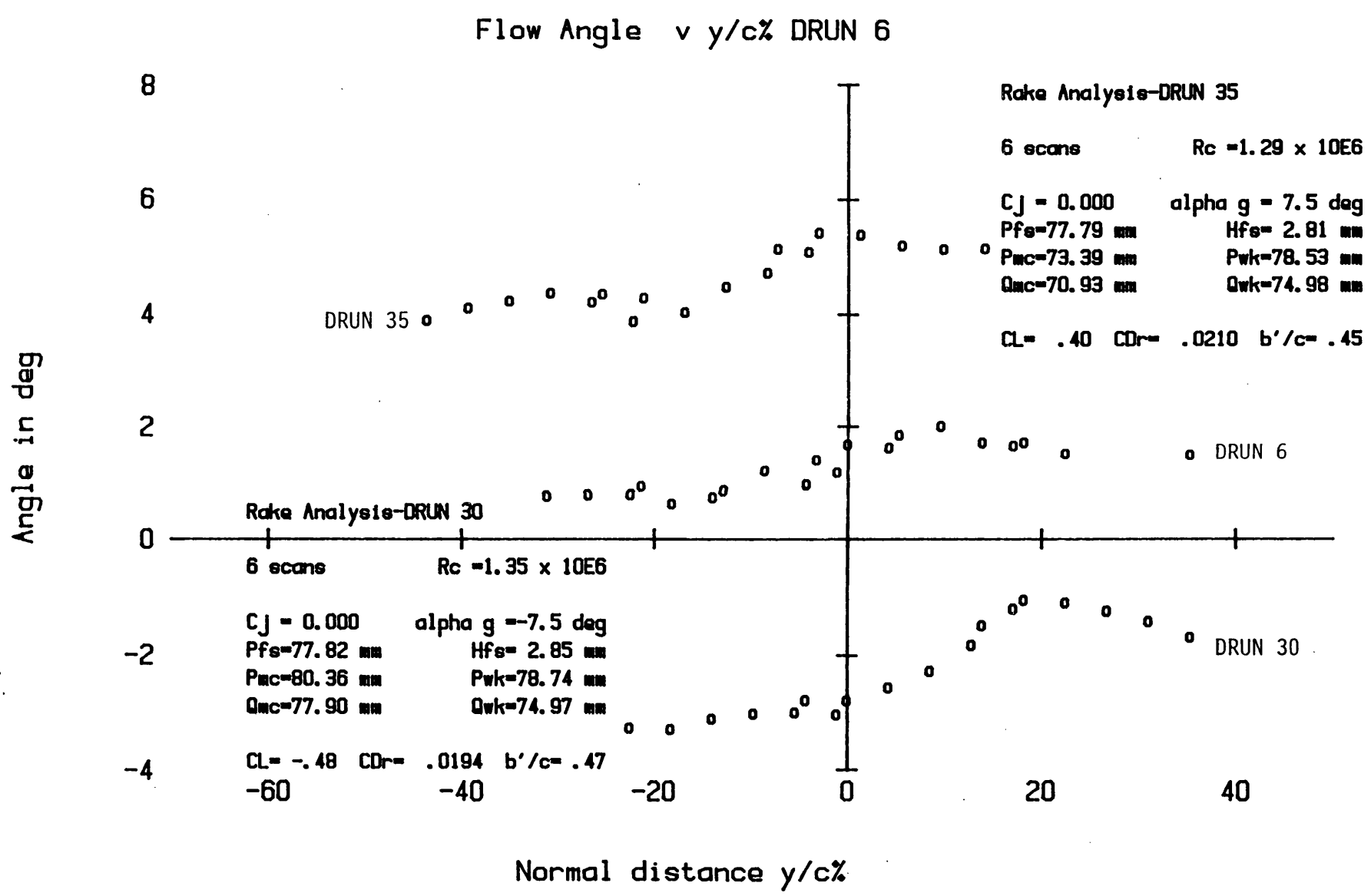

Fig. 3.30: FLOW ANGLE IN THE WAKE OF THE UNBLOWN MODEL AT -7.5 0 AND +7.5 DEGS. GEOMETRIC INCIDENCE.

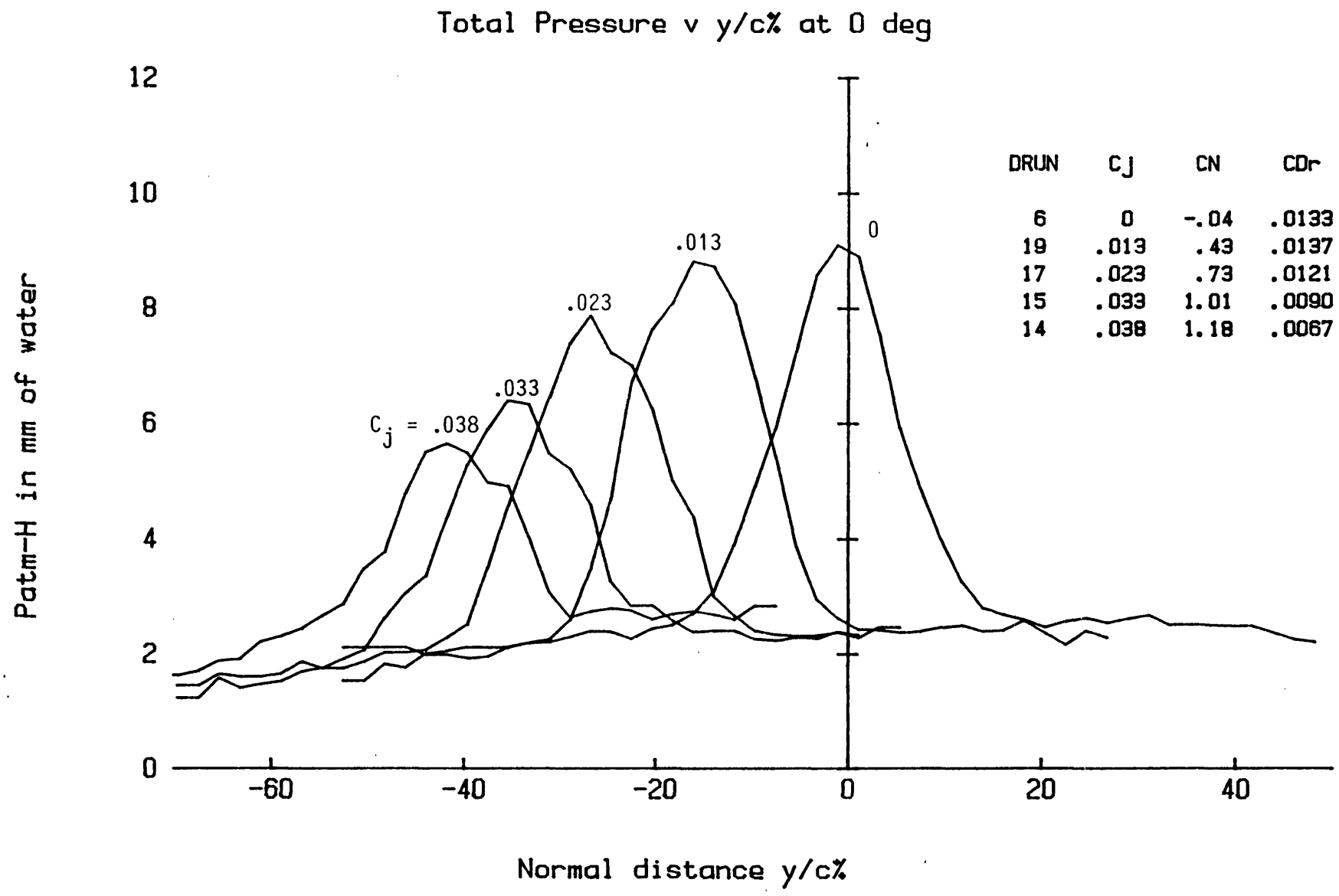

Fig. 3.31: TOTAL PRESSURE DISTRIBUTION IN THE WAKE OF THE MODEL WITH TE BLOWING AT 0 DEG.

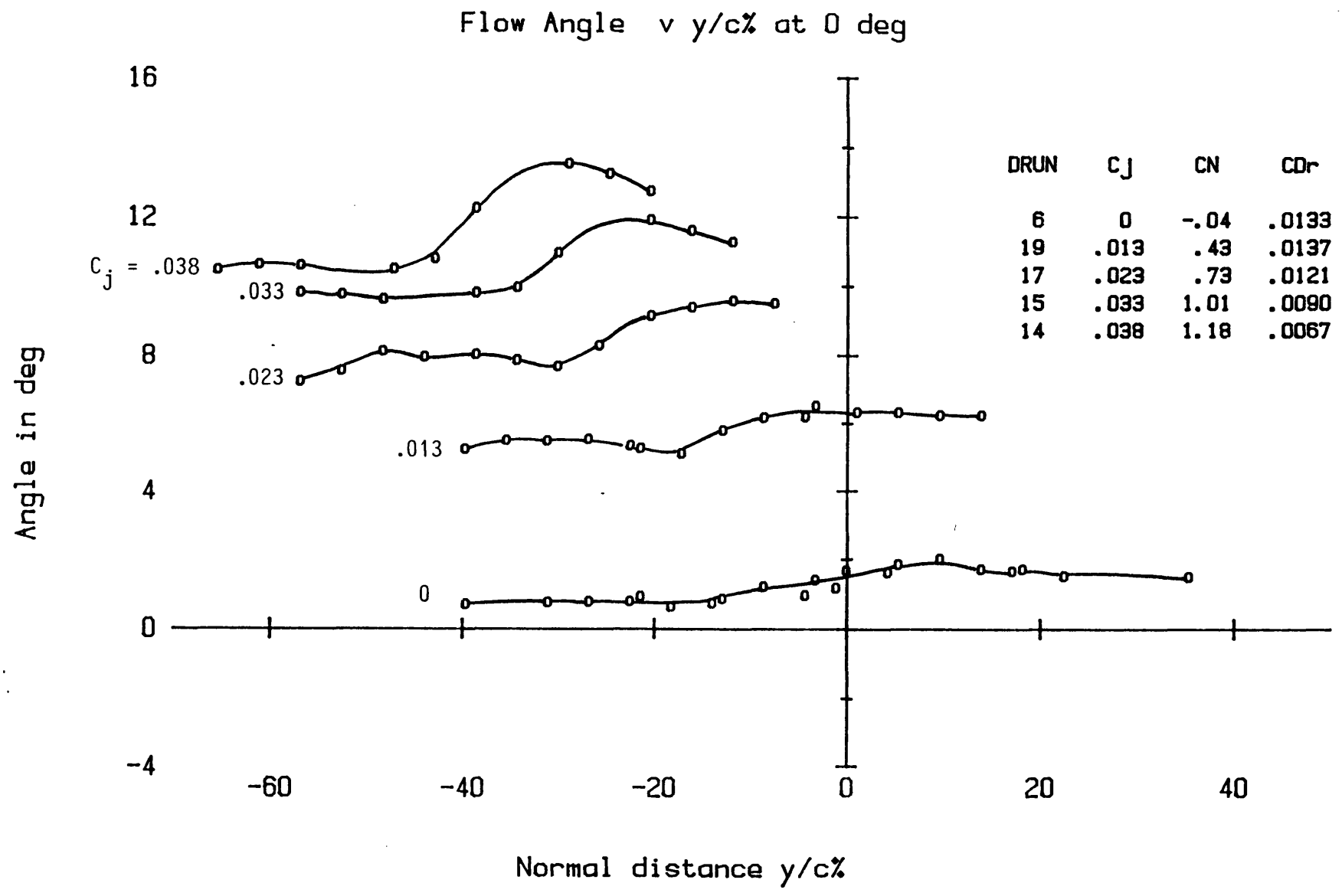

Fig. 3.32: FLOW ANGLE IN THE WAKE OF THE MODEL WITH TE BLOWING AT 0 DEG.

Fig. 3.32

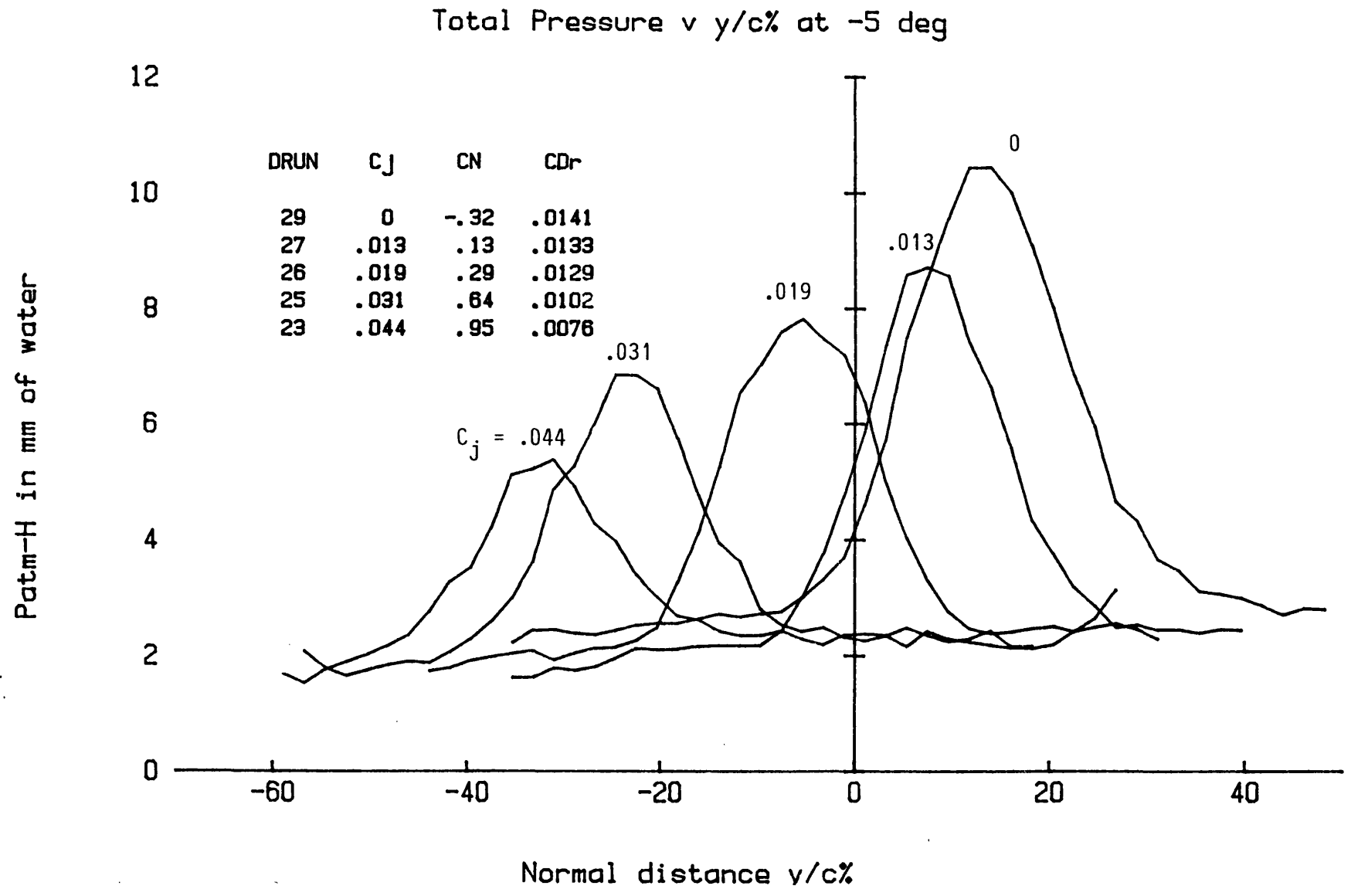

Fig. 3.33: TOTAL PRESSURE DISTRIBUTION IN THE WAKE OF THE MODEL WITH TE BLOWING AT -5 DEG.

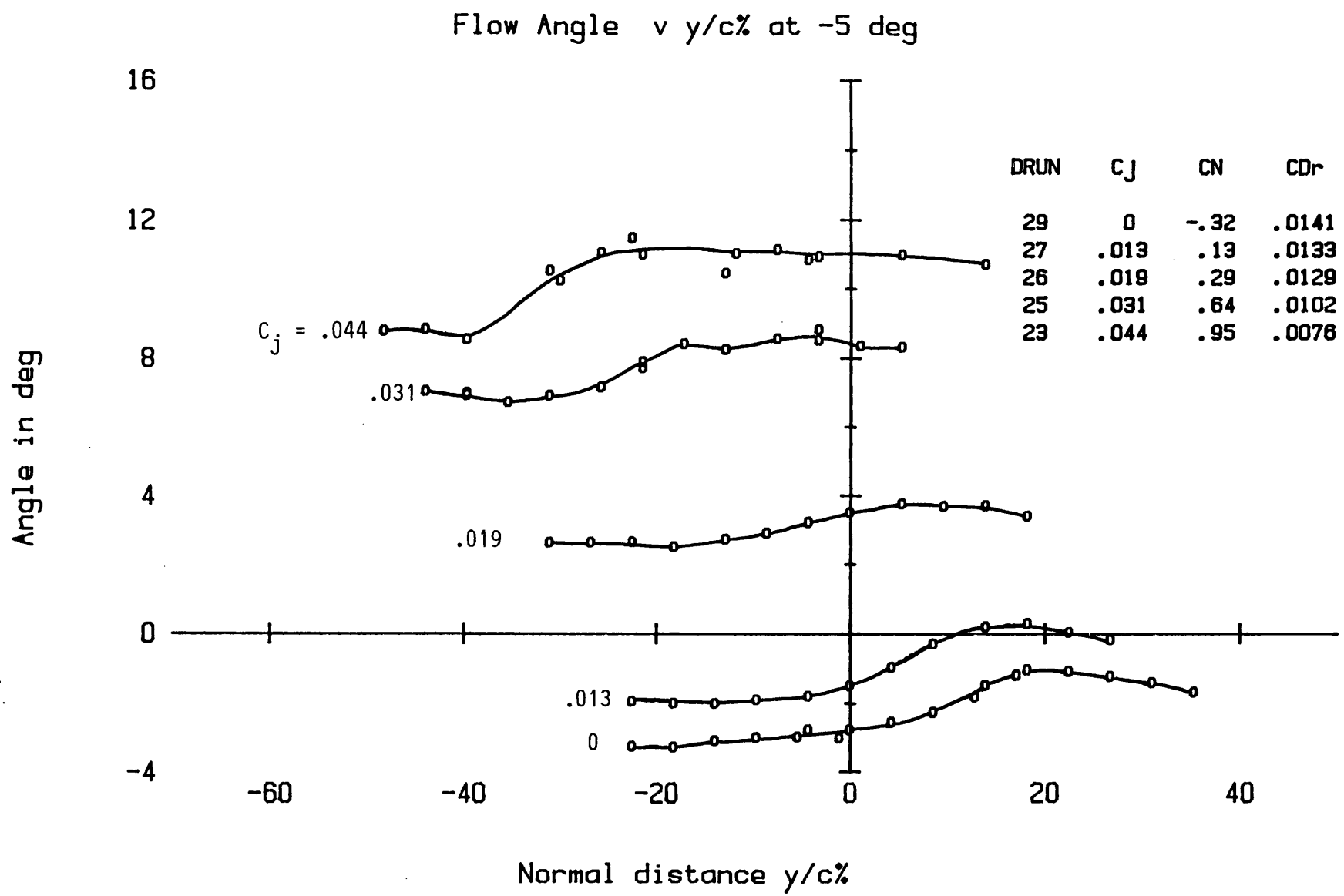

Fig. 3.34: FLOW ANGLE IN THE WAKE OF THE MODEL WITH TE BLOWING AT -5 DEG.

Fig. 3.34

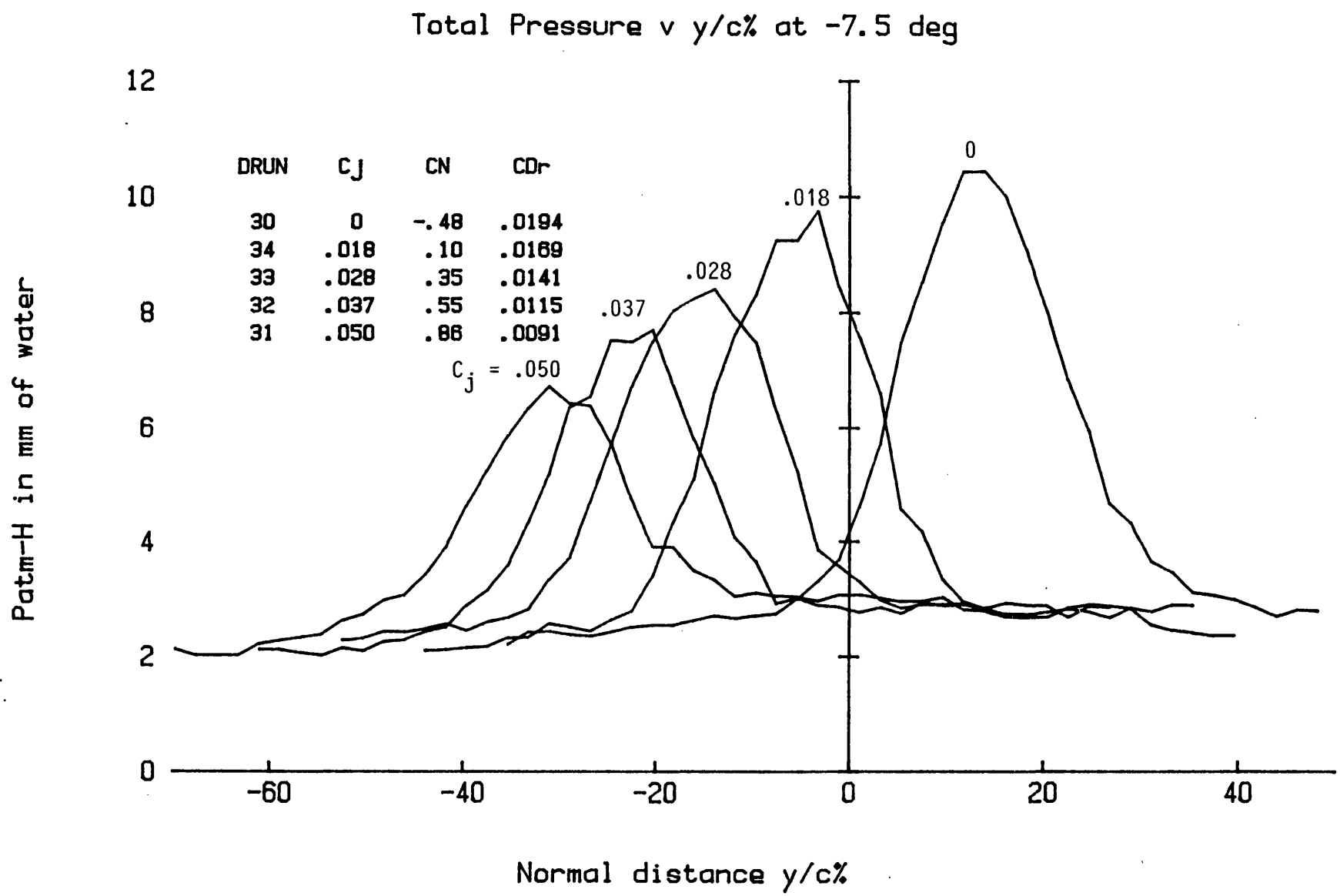

Fig. 3.35: TOTAL PRESSURE DISTRIBUTION IN THE WAKE OF THE MODEL WITH TE BLOWING AT -7.5 DEG.

Fig. 3.35

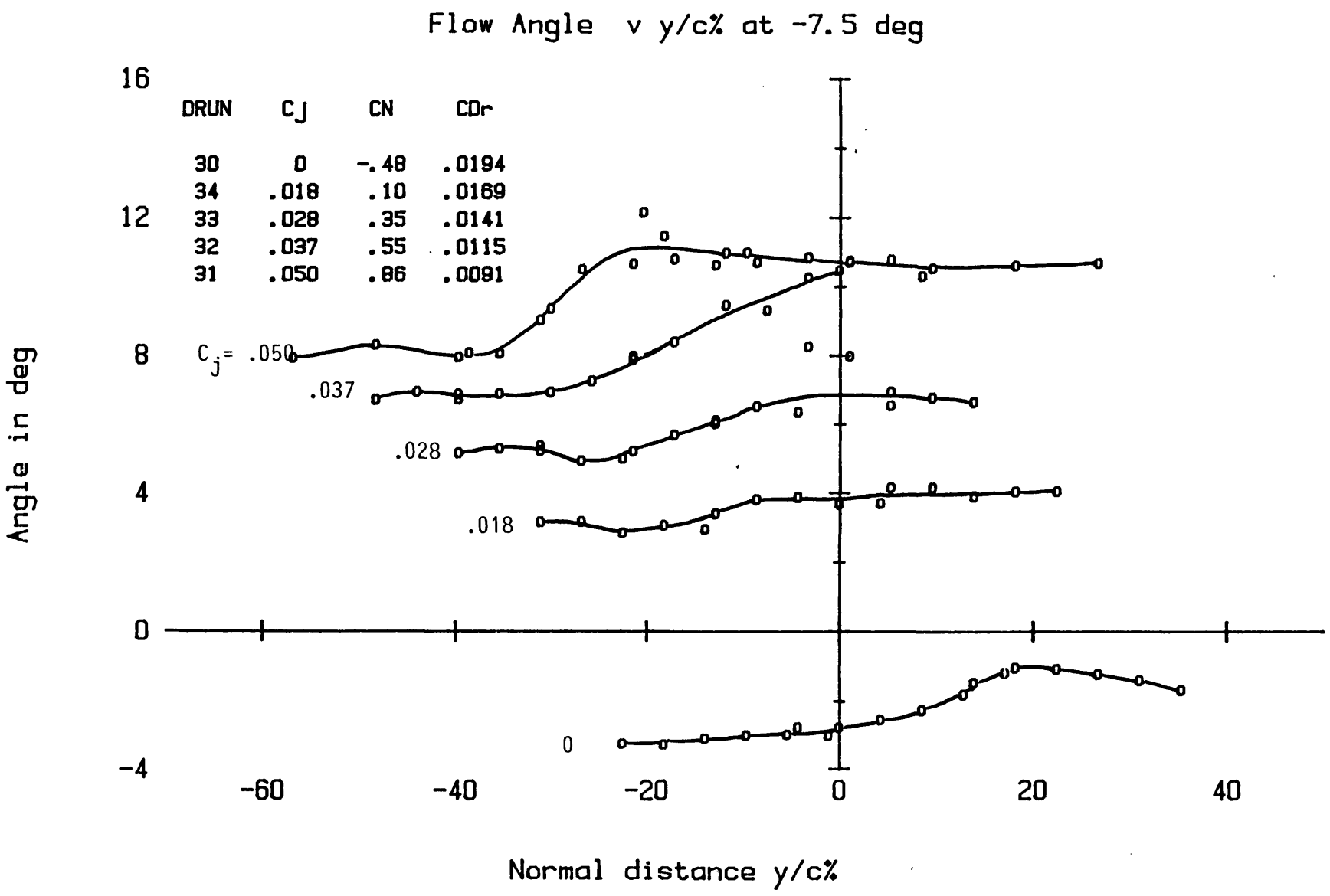

Fig. 3.36: FLOW ANGLE IN THE WAKE OF THE MODEL WITH TE BLOWING AT -7.5 DEG

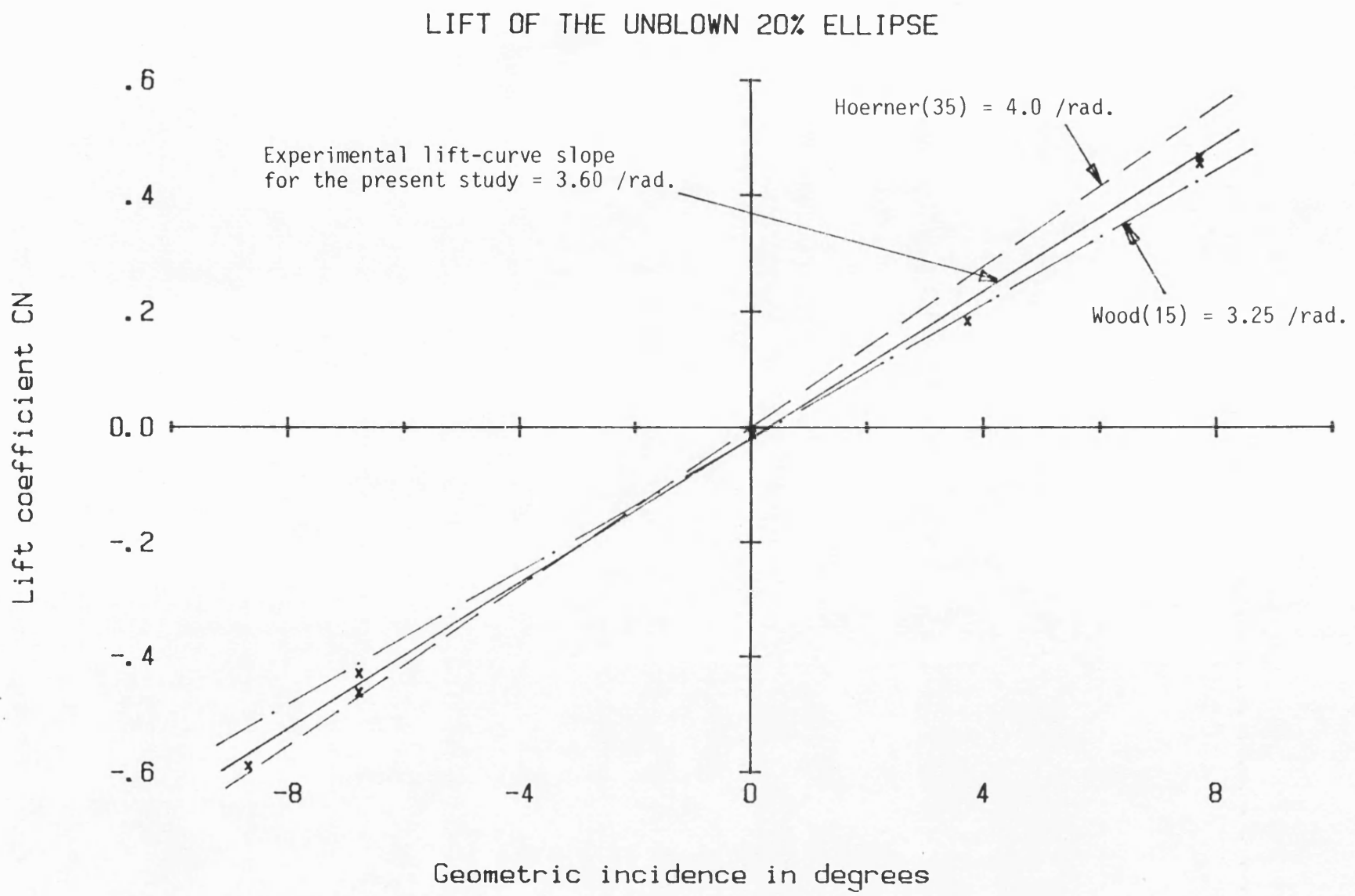

Fig. 3.37: LIFT PERFORMANCE OF THE UNBLOWN MODEL WITH VARIATION OF GEOMETRIC INCIDENCE.

Fig. 3.37

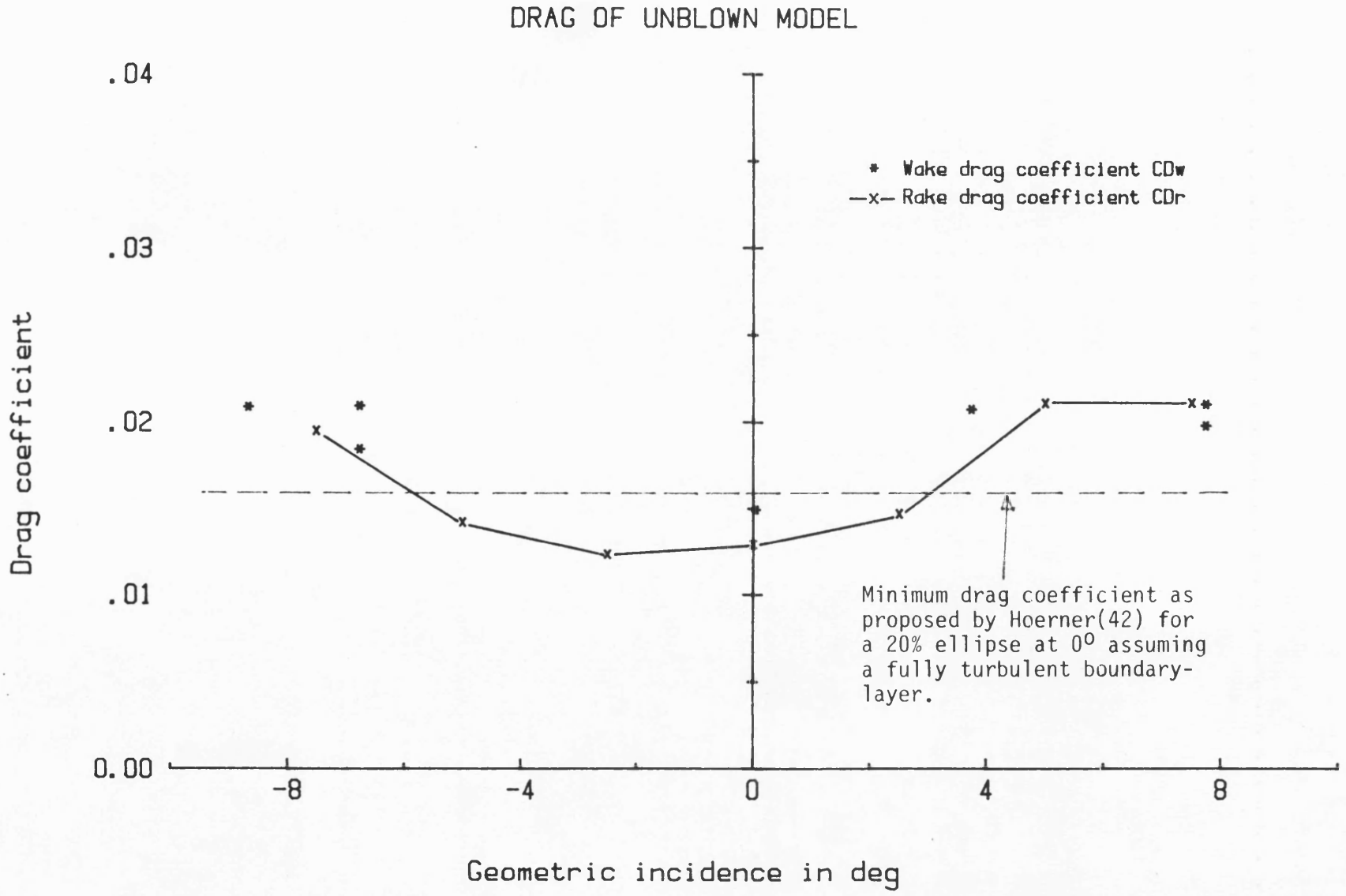

Fig. 3.38: DRAG PERFORMANCE OF THE UNBLOWN MODEL WITH VARIATION OF GEOMETRIC INCIDENCE.

Fig. 3.38

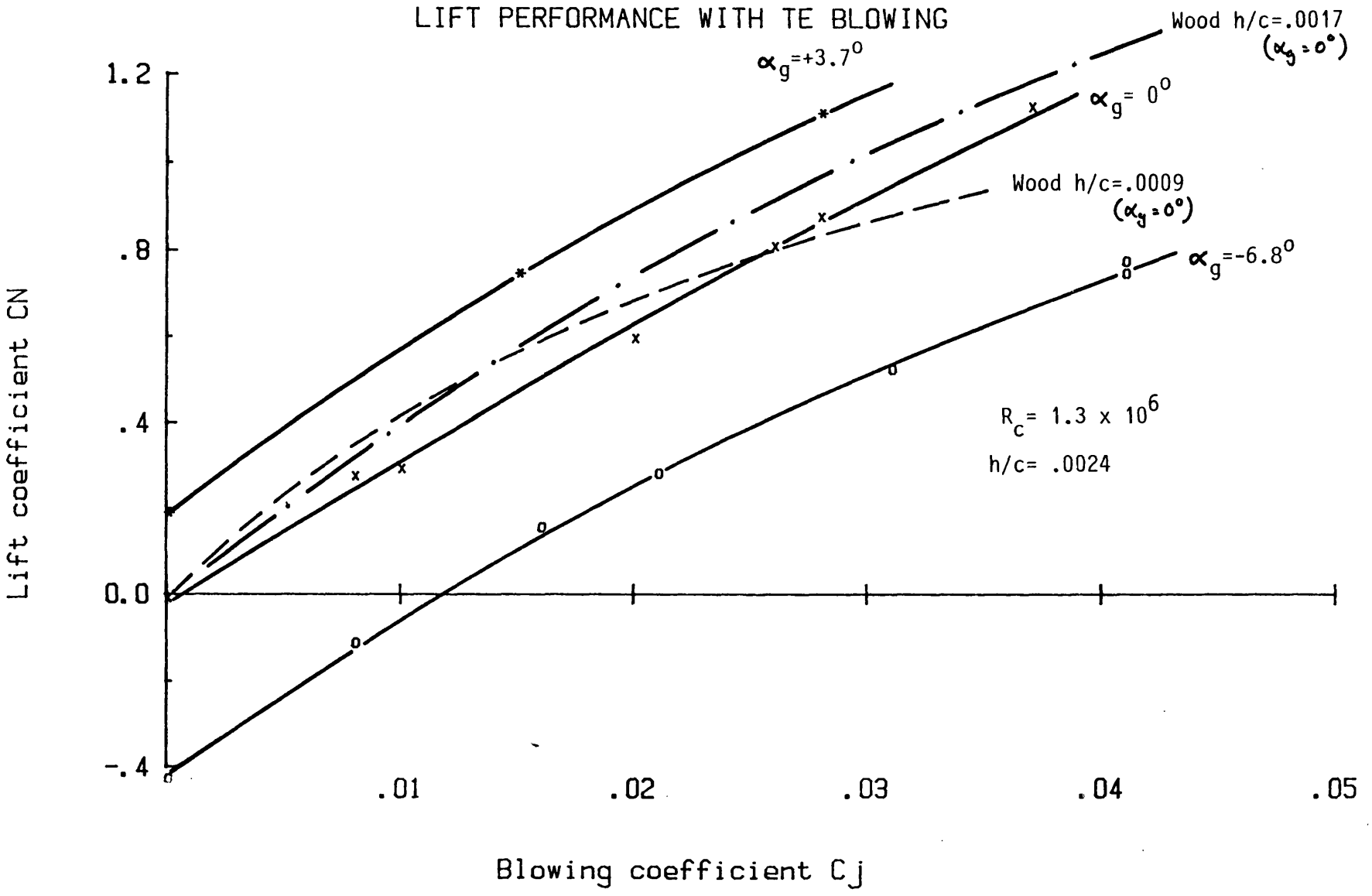

Fig. 3.39: LIFT PERFORMANCE OF THE MODEL WITH TE BLOWING.

Fig.3.39

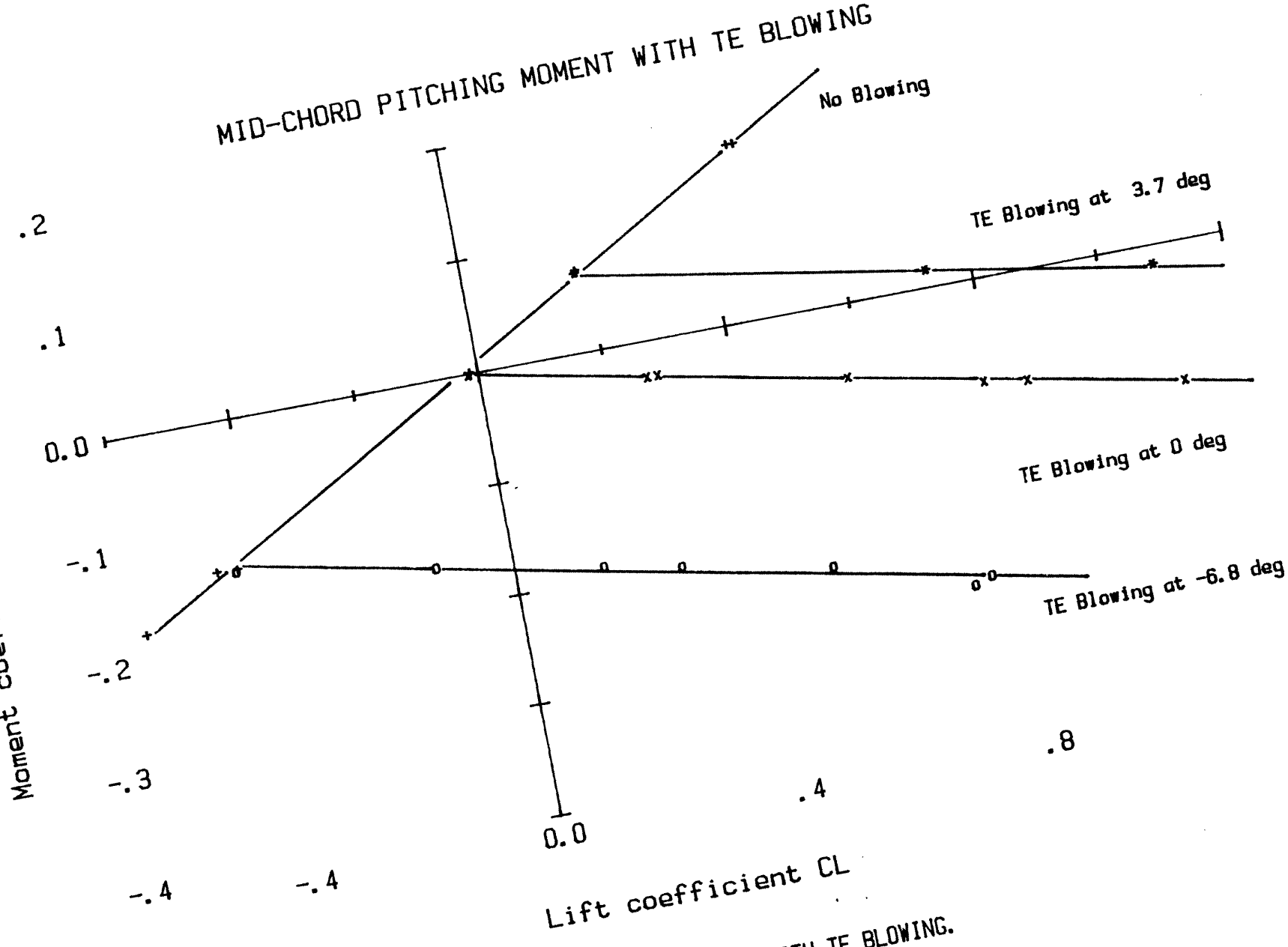

Fig.3.40: VARIATION OF THE MID-CHORD PITCHING MOMENT WITH TE BLOWING.

Fig.3.40

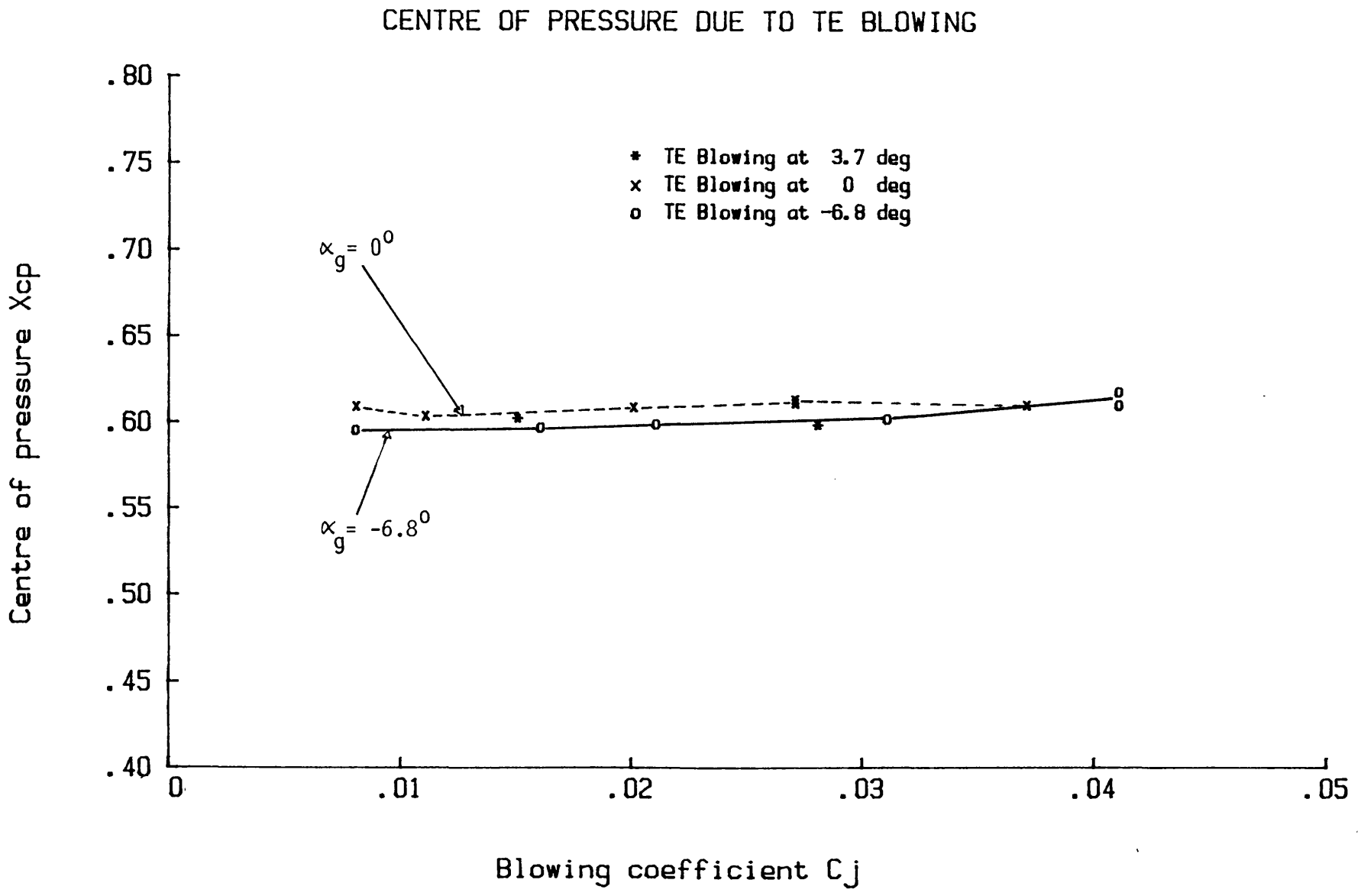

Fig. 3.41: VARIATION OF THE CENTRE OF PRESSURE DUE TO TE BLOWING.

Fig.3.41

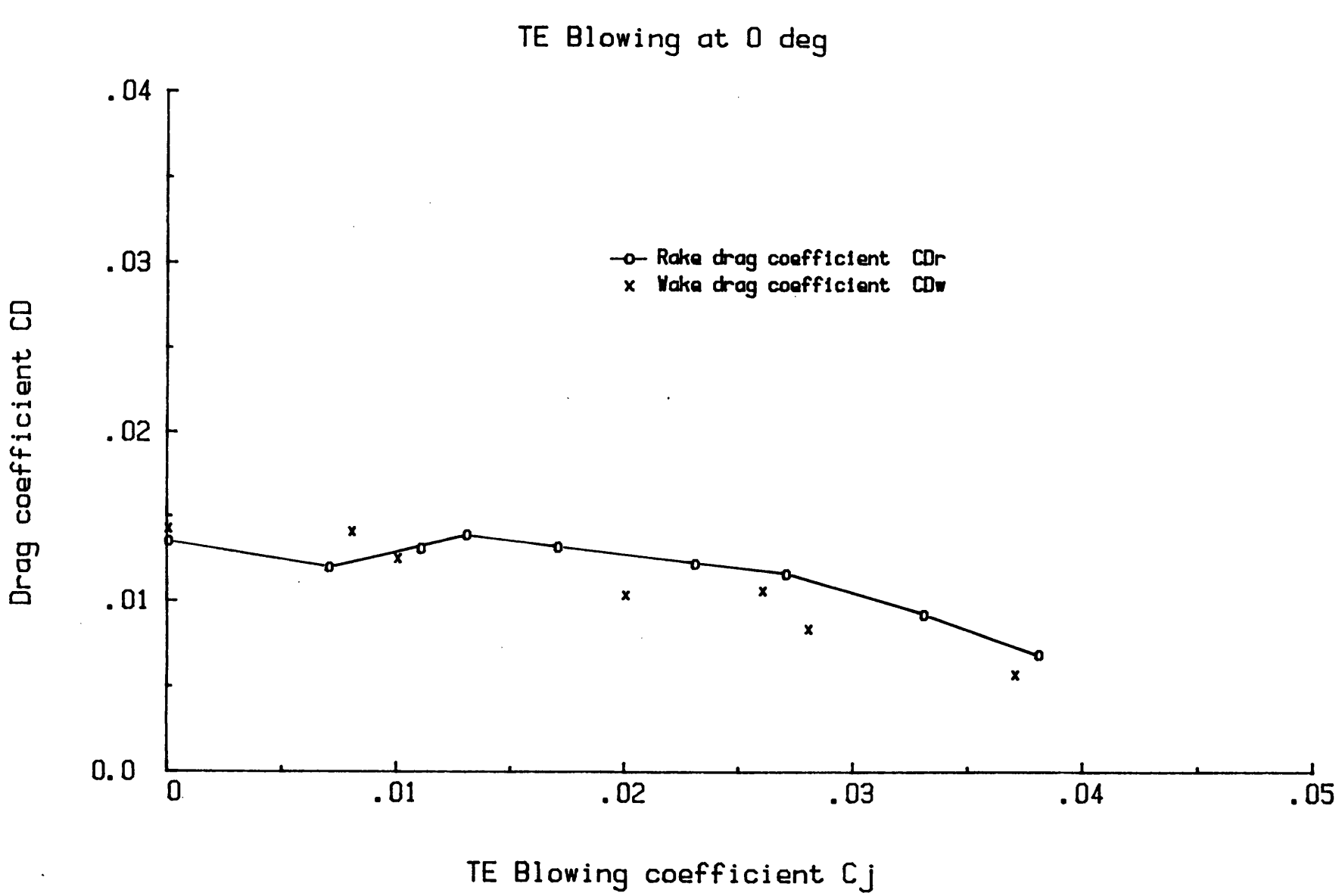

Fig. 3.42: DRAG PERFORMANCE OF THE MODEL WITH TE BLOWING AT ZERO GEOMETRIC INCIDENCE.

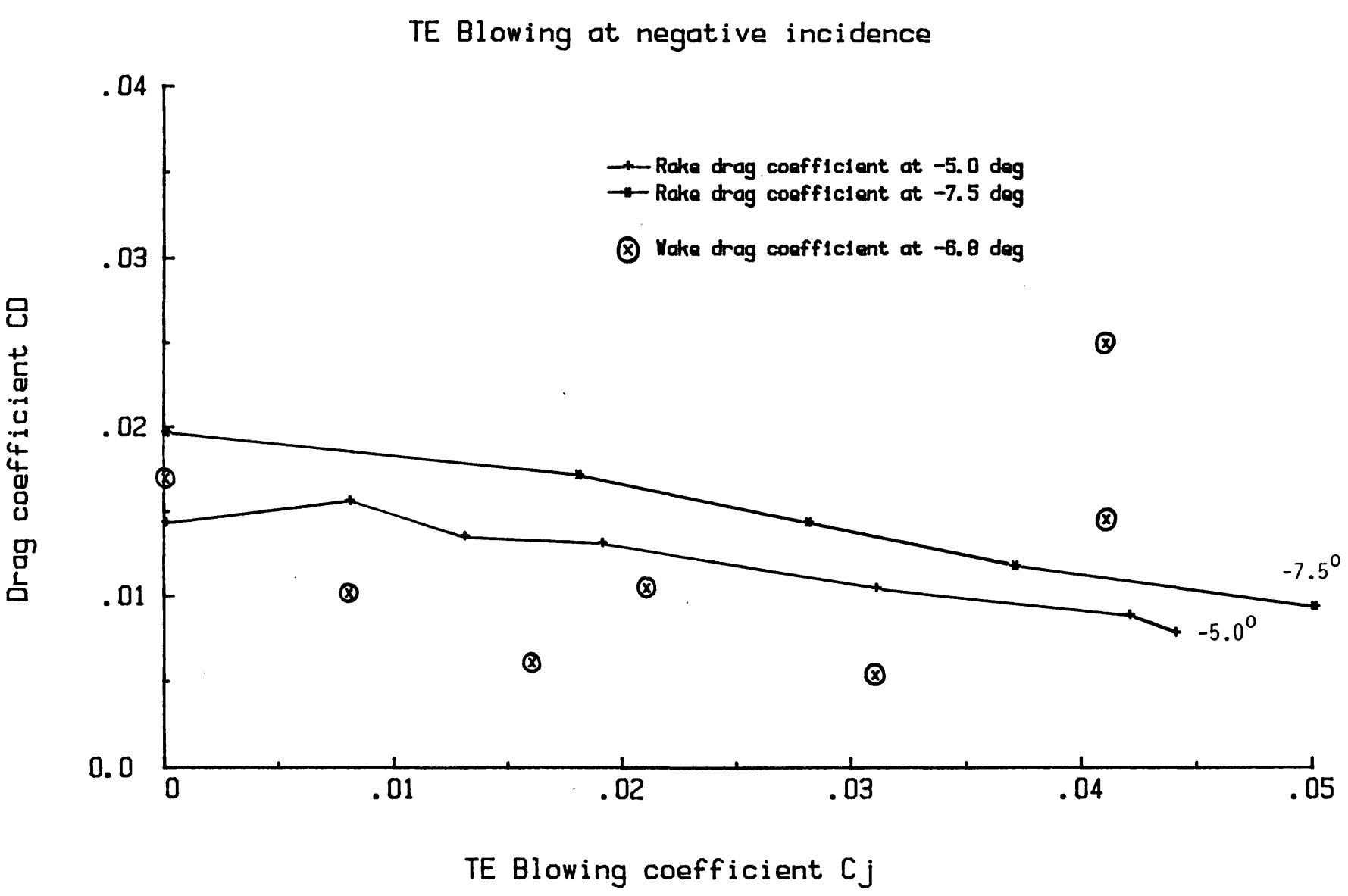

Fig. 3.43: DRAG PERFORMANCE OF THE MODEL WITH TE BLOWING AT NEGATIVE GEOMETRIC INCIDENCE.

Fig. 3.43

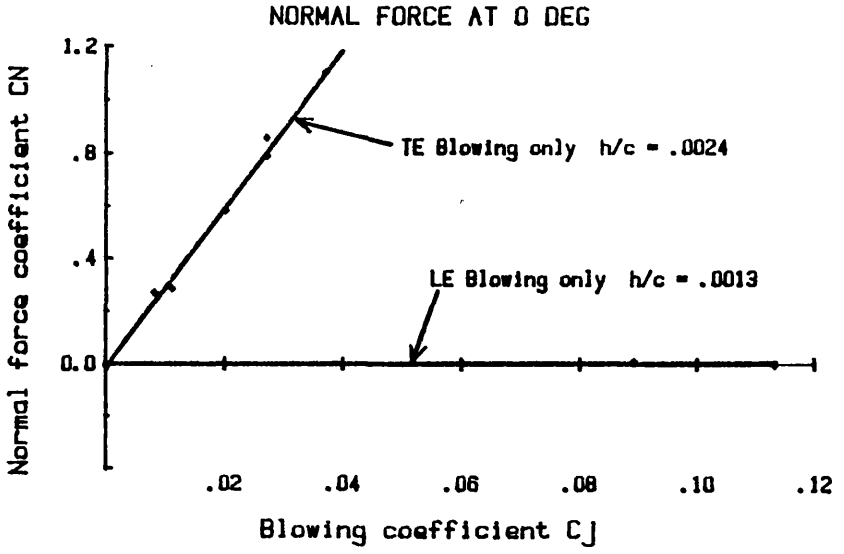

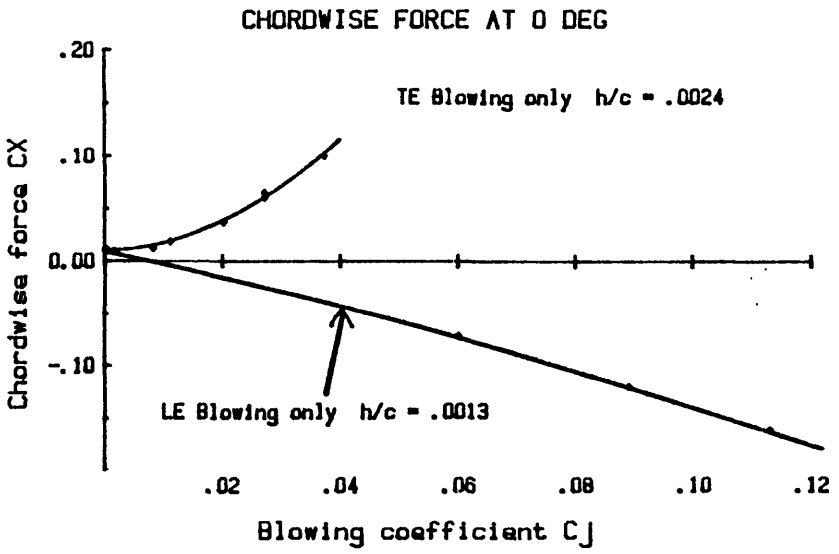

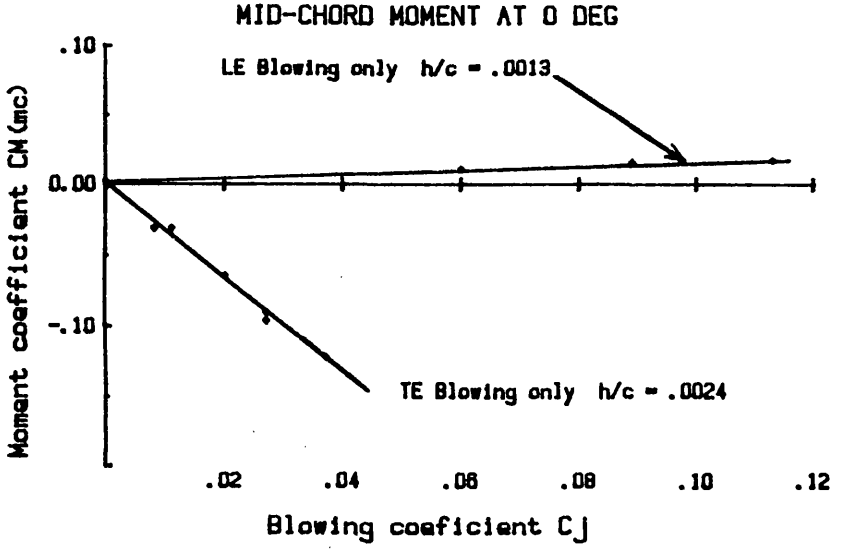

Fig. 3.44: PERFORMANCE OF THE MODEL WITH LE BLOWING AT 0 DEG.

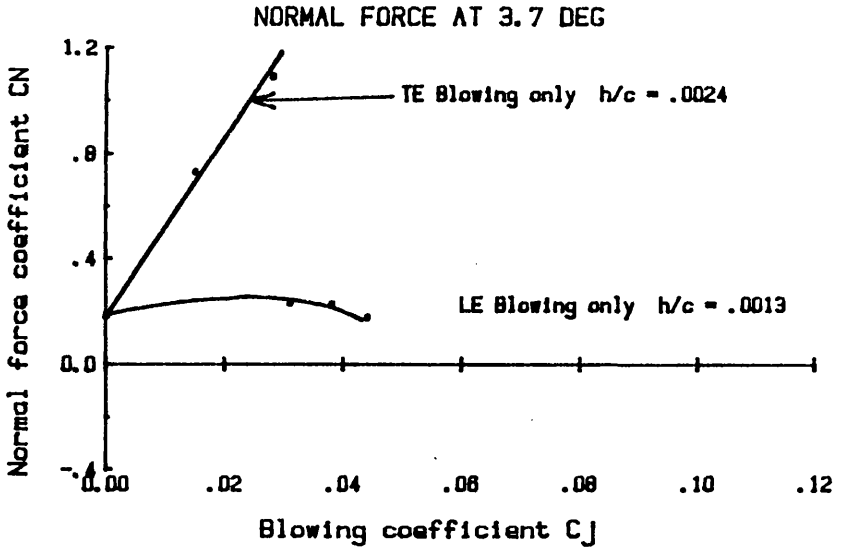

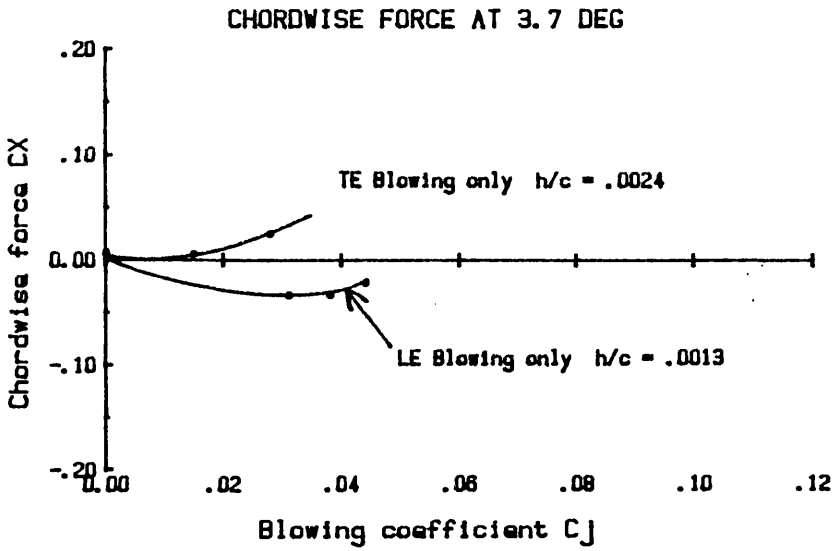

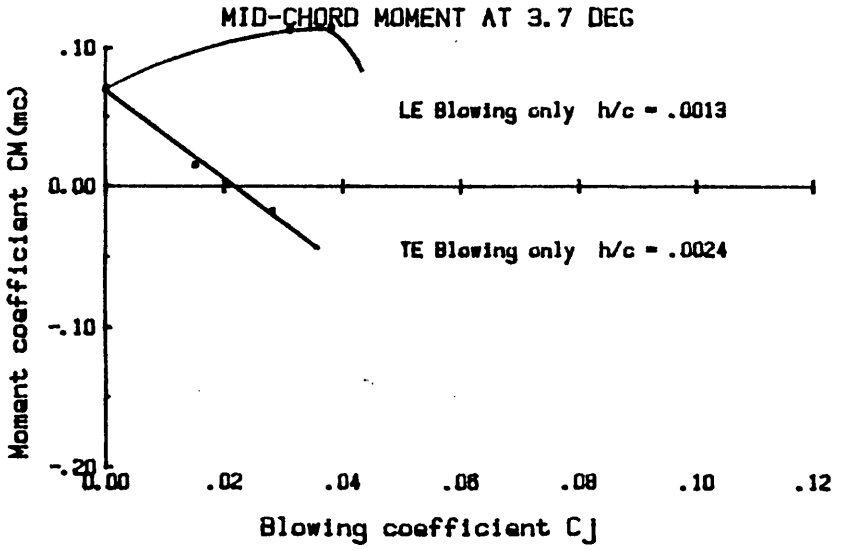

Fig. 3.45: PERFORMANCE OF THE MODEL WITH LE BLOWING AT 3.7 DEG.

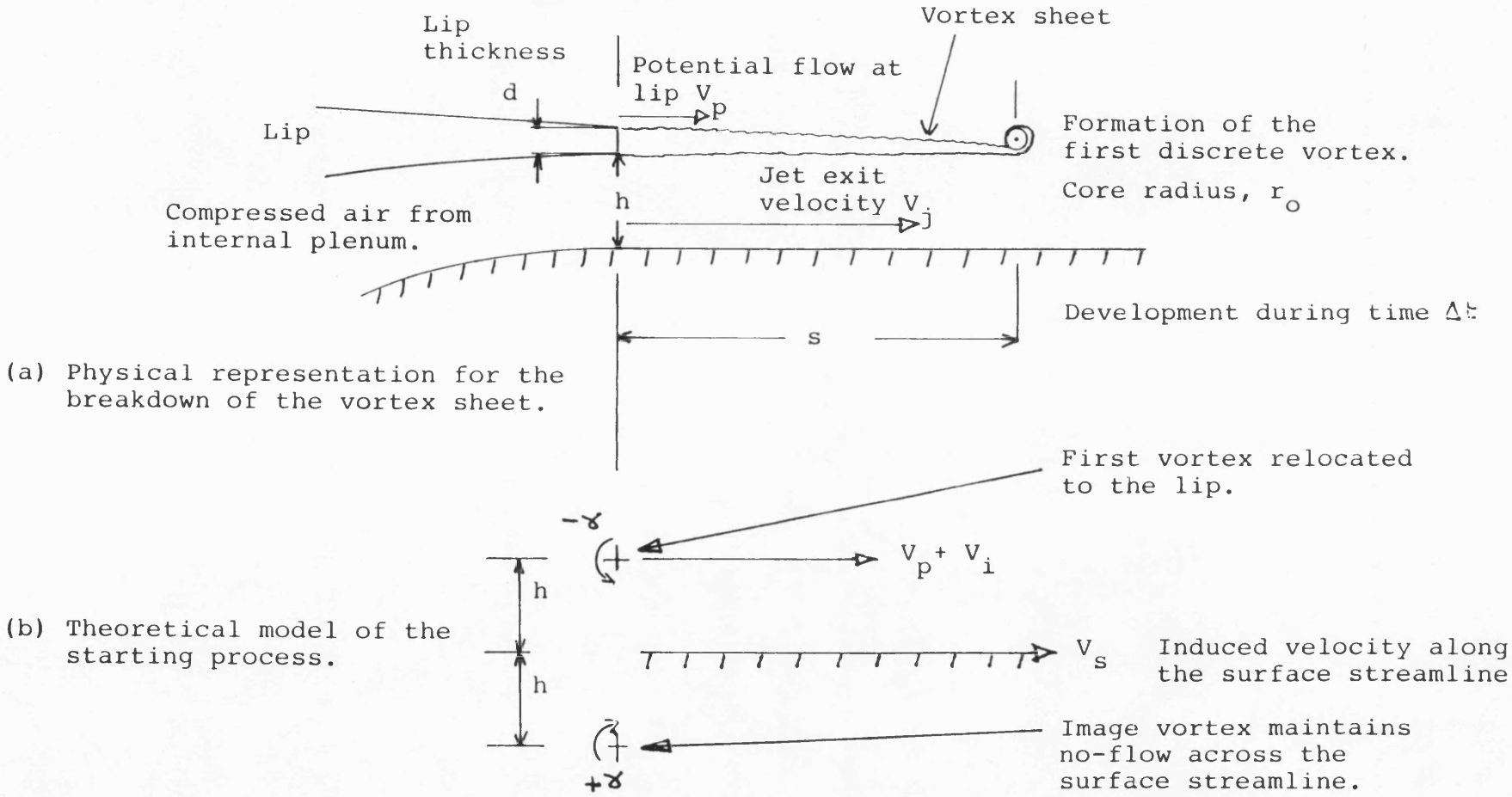

Fig. 4.1: THE STARTING PROCESS FOR THE PROPOSED DISCRETE VORTEX MODEL.

Fig. 4.1

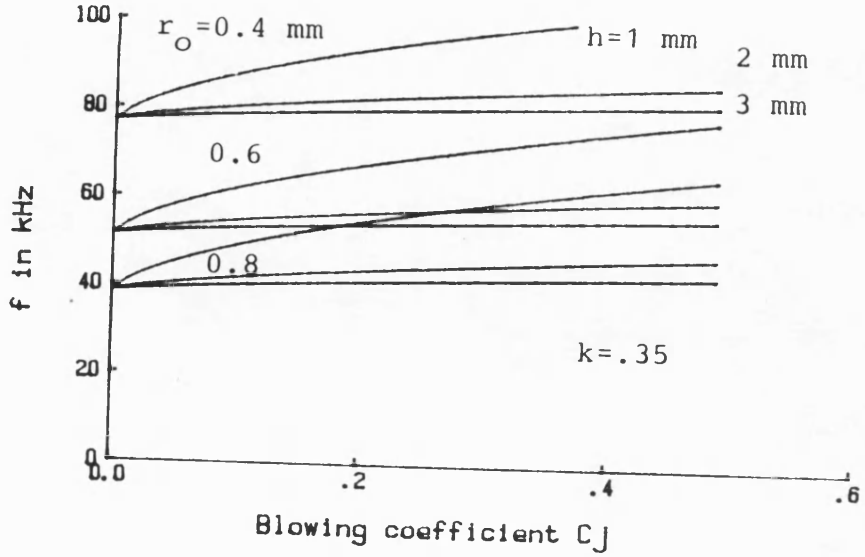

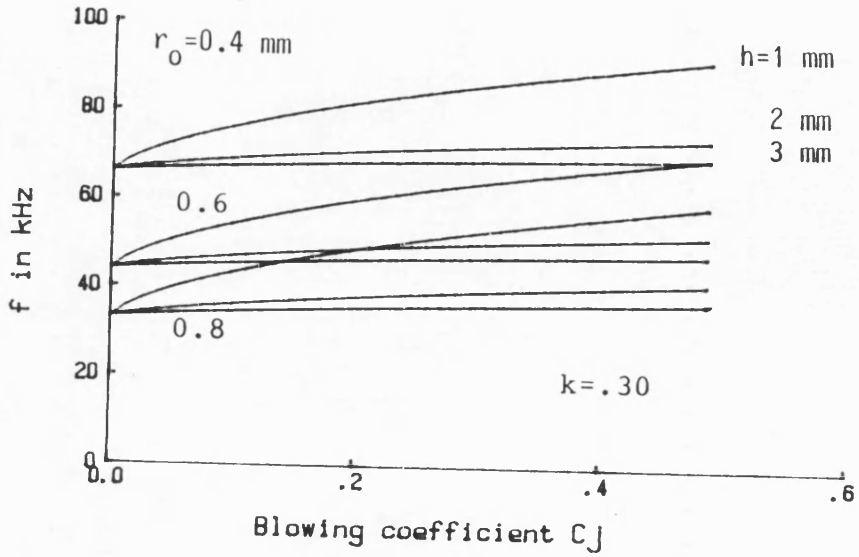

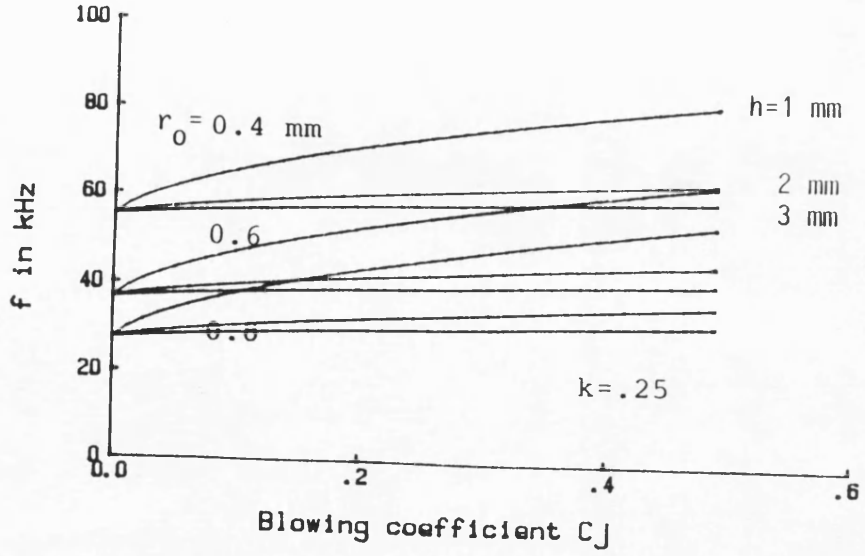

$$f = \frac{kV_p}{r_o} + \frac{V_e}{4\pi h}$$ where

V_p = 88 m/s

r_o = initial core radius

$k = r_o/s$, starting length ratio

h = slot height

Fig. 4.2: VARIATION OF THE VORTEX SHEDDING FREQUENCY WITH BLOWING COEFFICIENT.

Fig. 4.2

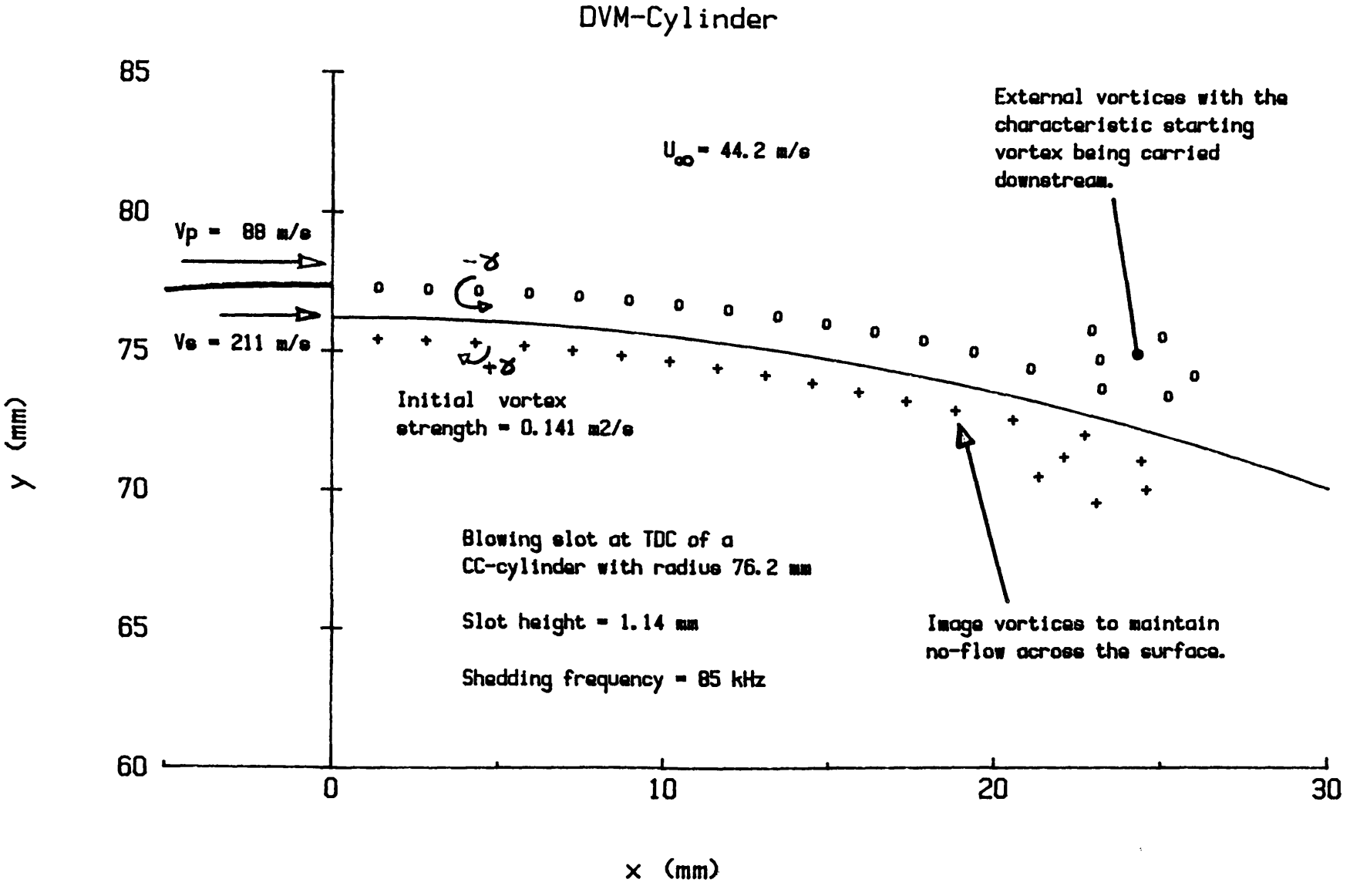

Fig. 4.3: EARLY DEVELOPMENT OF THE VORTICES PREDICTED USING THE THEORETICAL MODEL DVM-CYLINDER.

Fig. 4.3

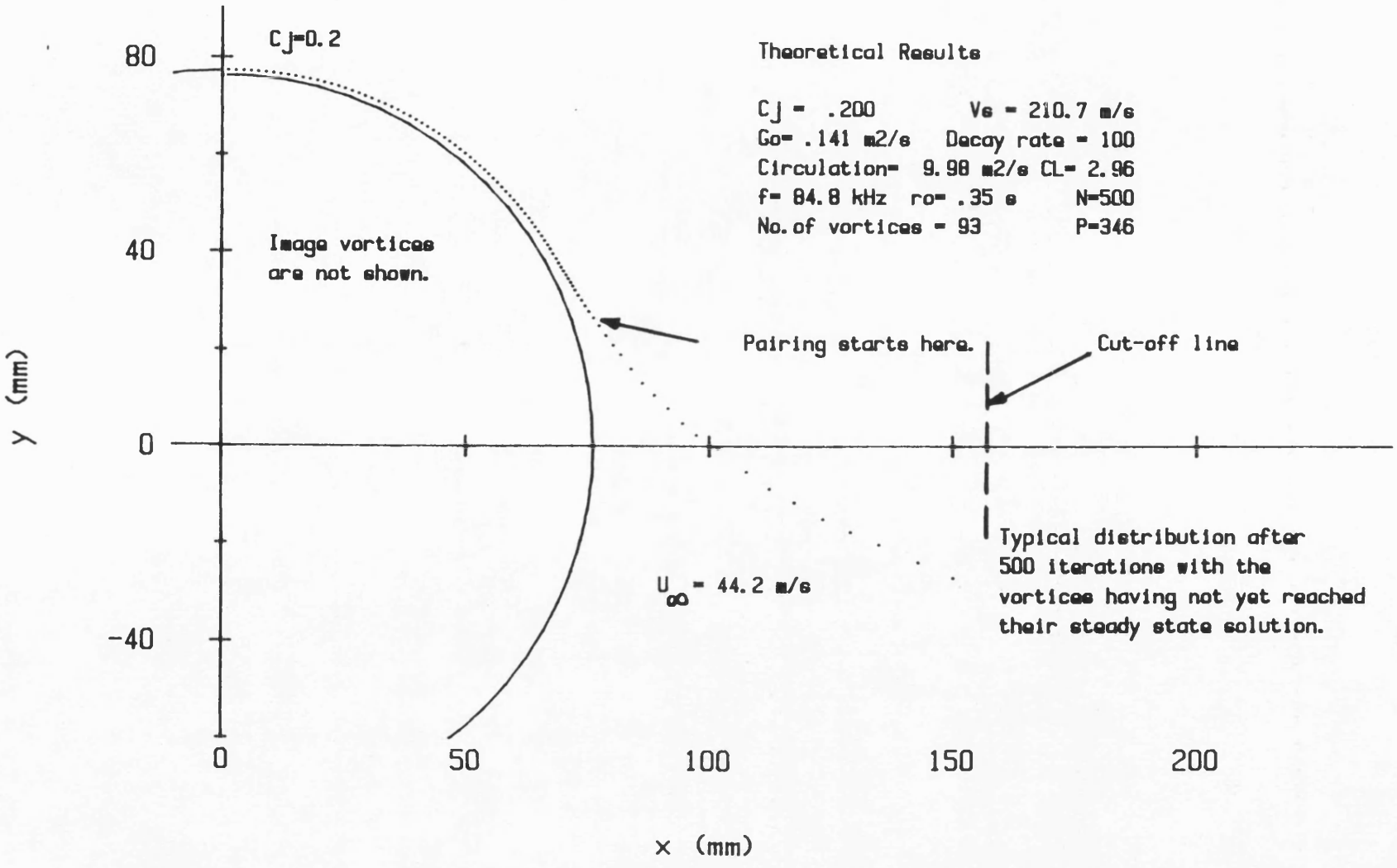

Fig. 4.4: PREDICTED DEVELOPMENT BEFORE A STEADY-STATE SOLUTION USING DVM-CYLINDER.

Fig. 4.4

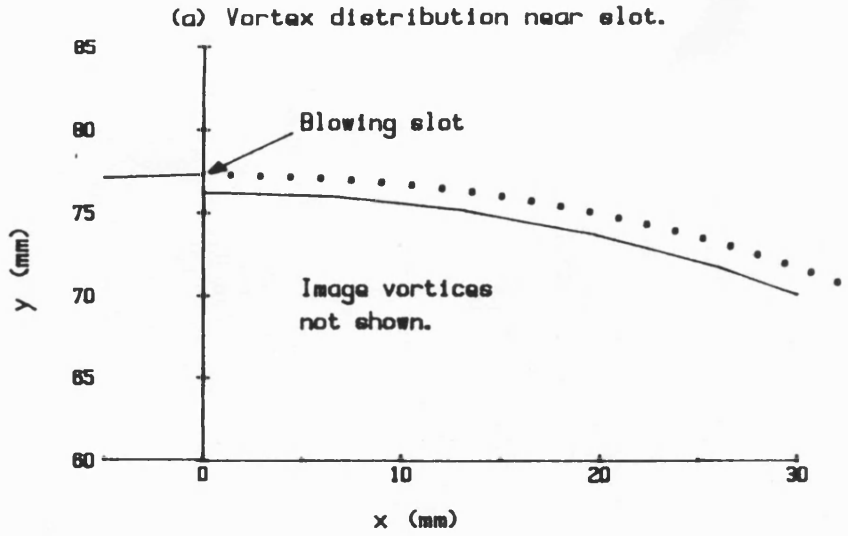

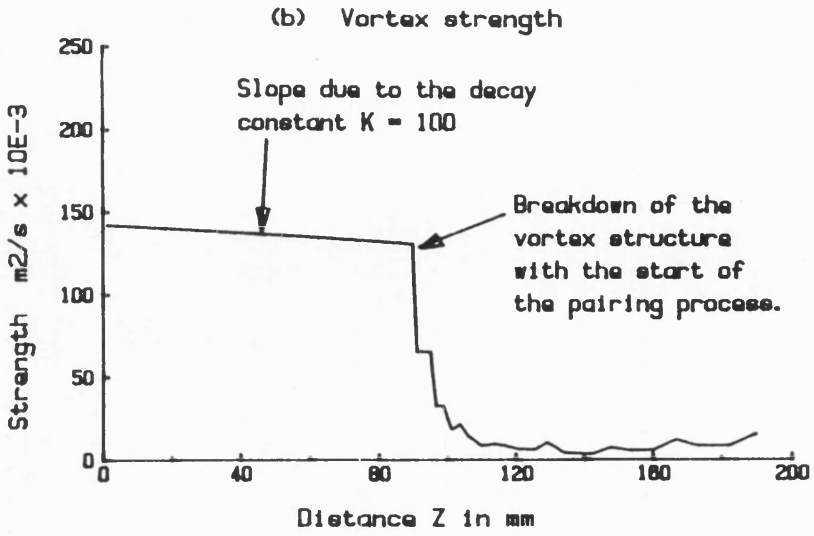

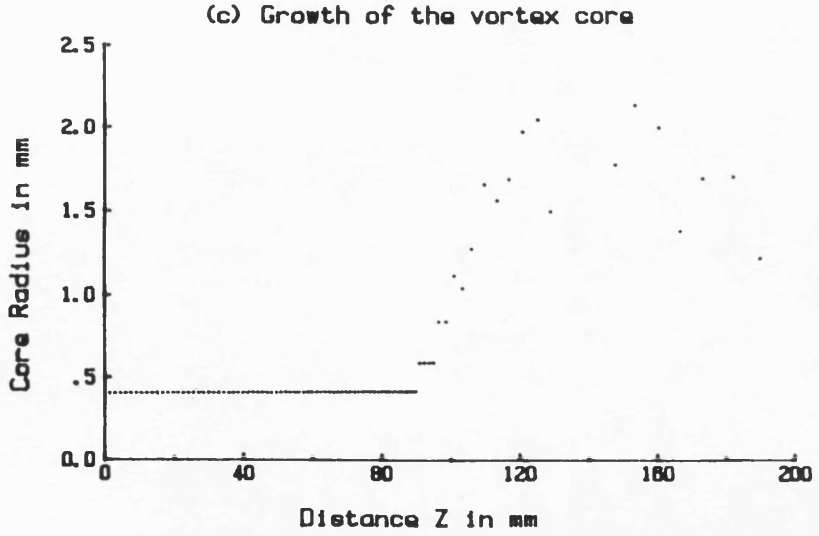

(d) Theoretical Results

****** DVM-CYLINDER 542035 *****

Cj = .200 Vs = 210.7 m/s
Go= .141 m2/s Decay rate = 100
Circulation= 9.98 m2/s CL= 2.96
f= 84.8 kHz ro= .35 s N=500
No. of vortices = 93 P=346

Fig. 4.5: TYPICAL VORTEX DEVELOPMENT USING DVM-CYLINDER WITH PAIRING.

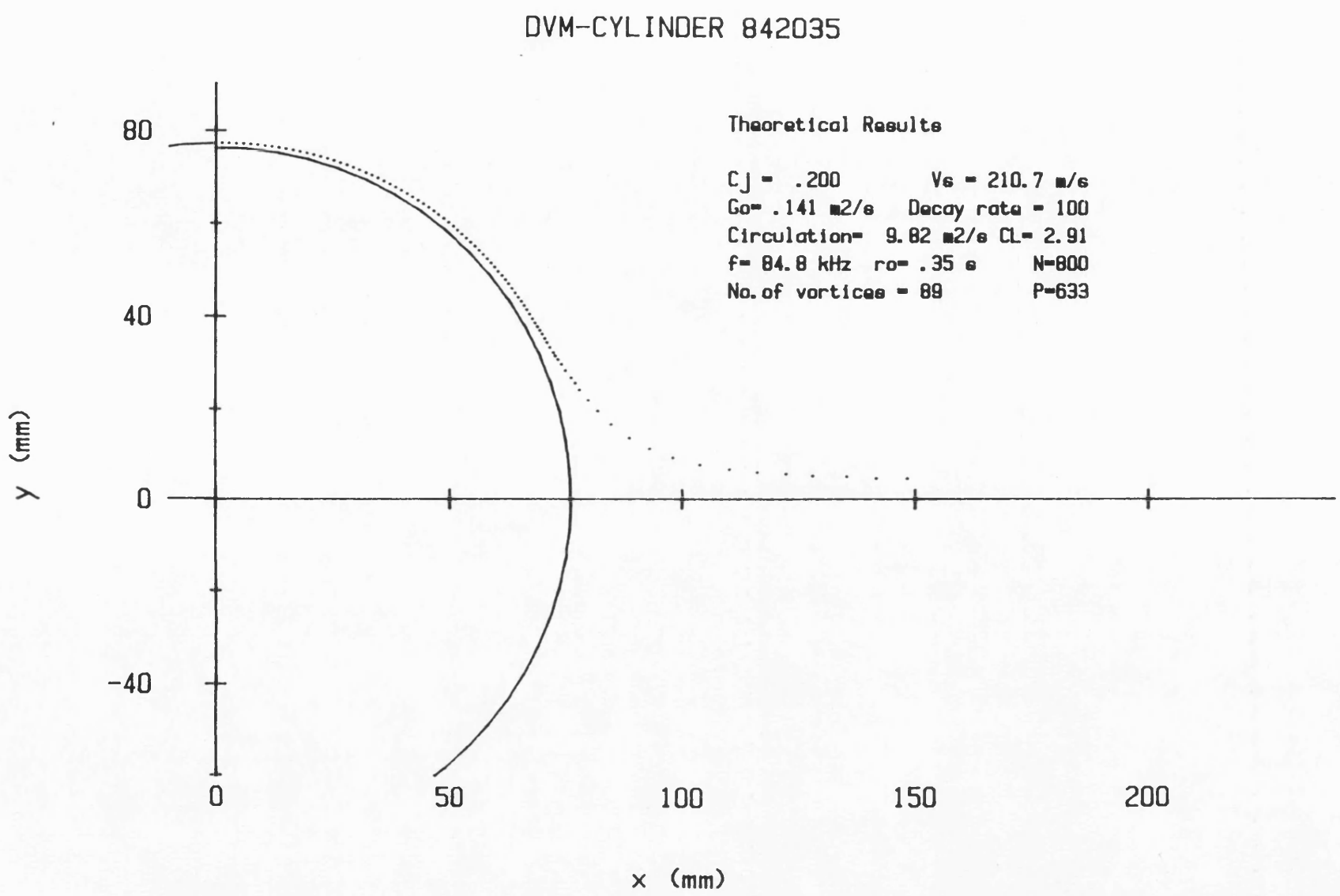

Fig. 4.6: TYPICAL STEADY-STATE VORTEX DISTRIBUTION AFTER 800 ITERATIONS USING DVM-CYLINDER.

Fig. 4.6

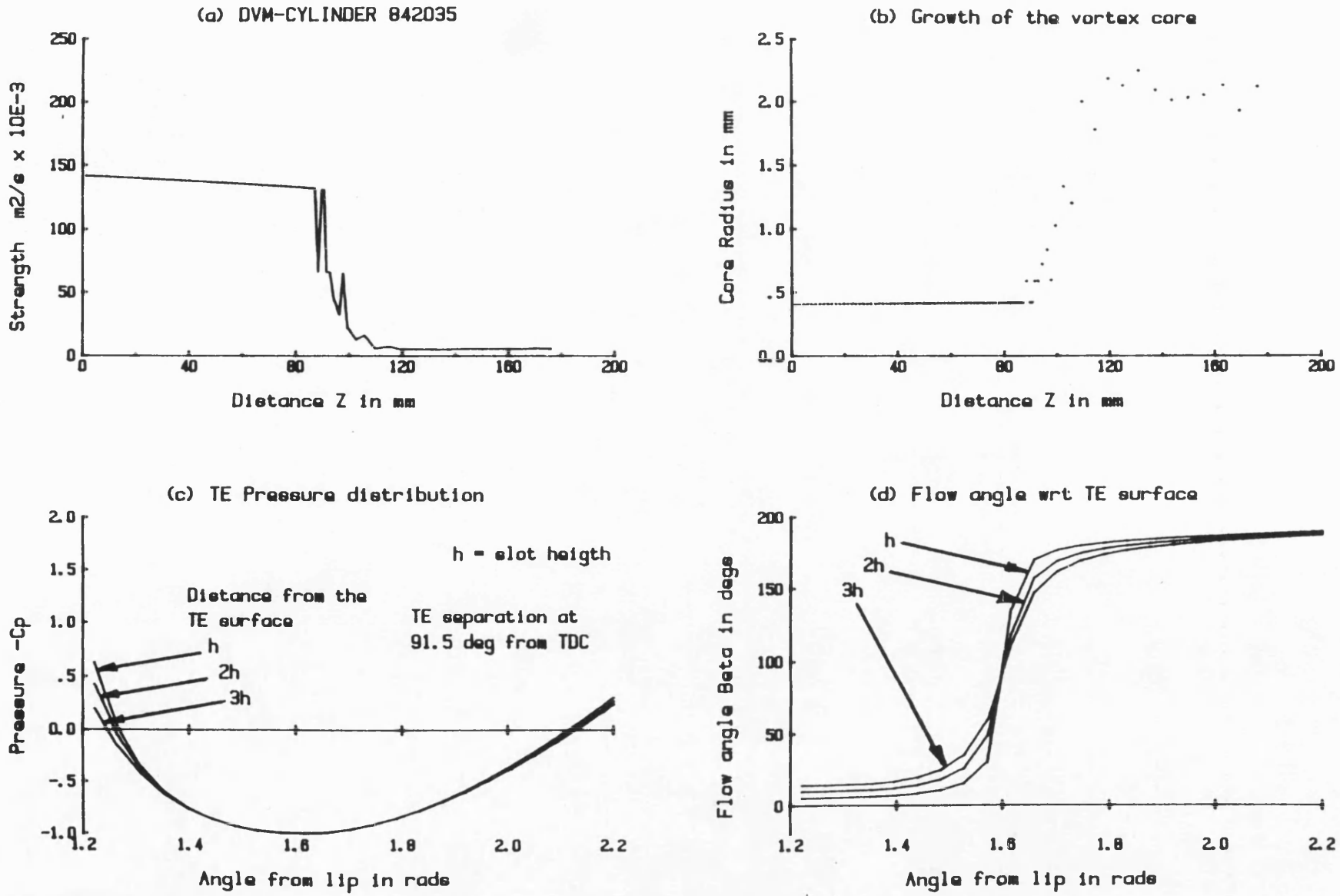

Fig. 4.7: TYPICAL STEADY-STATE SOLUTION USING DVM-CYLINDER WITH CJ=0.2.

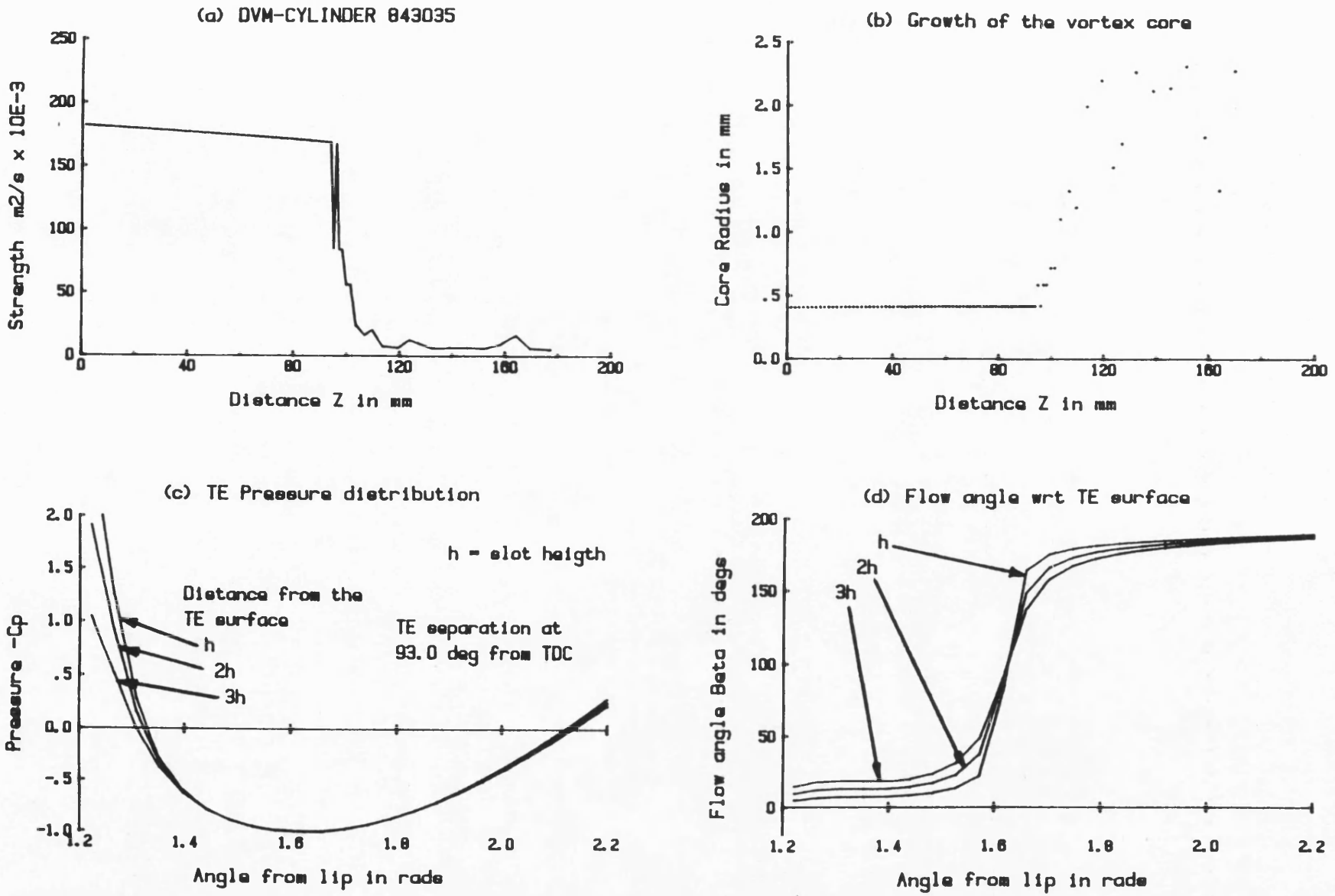

Fig. 4.8: TYPICAL STEADY-STATE SOLUTION USING DVM-CYLINDER WITH CJ=0.3.

Fig. 4.8

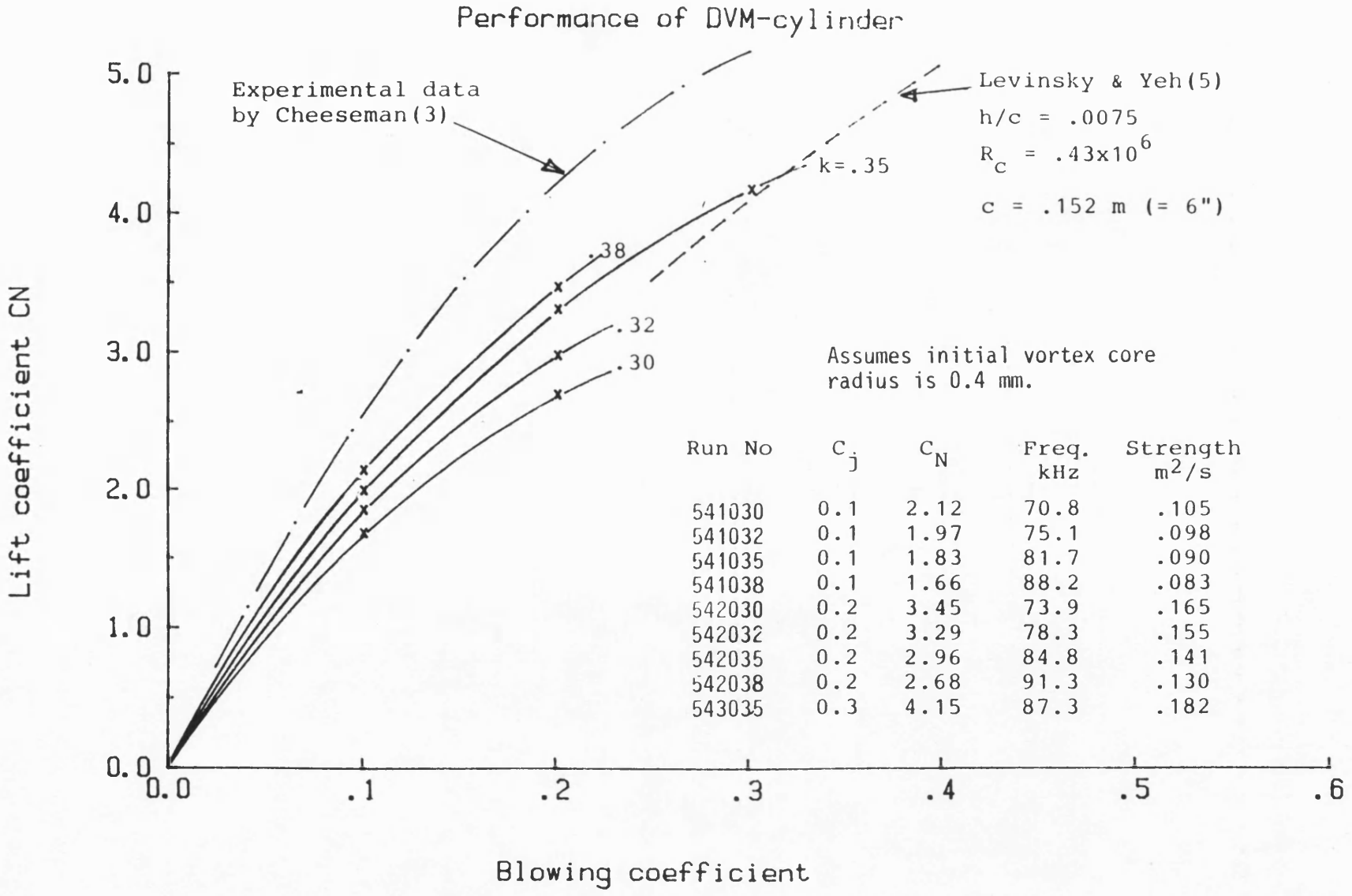

Fig. 4.9: PREDICTED PERFORMANCE AFTER 500 ITERATIONS USING DVM-CYLINDER.

Fig. 4.9

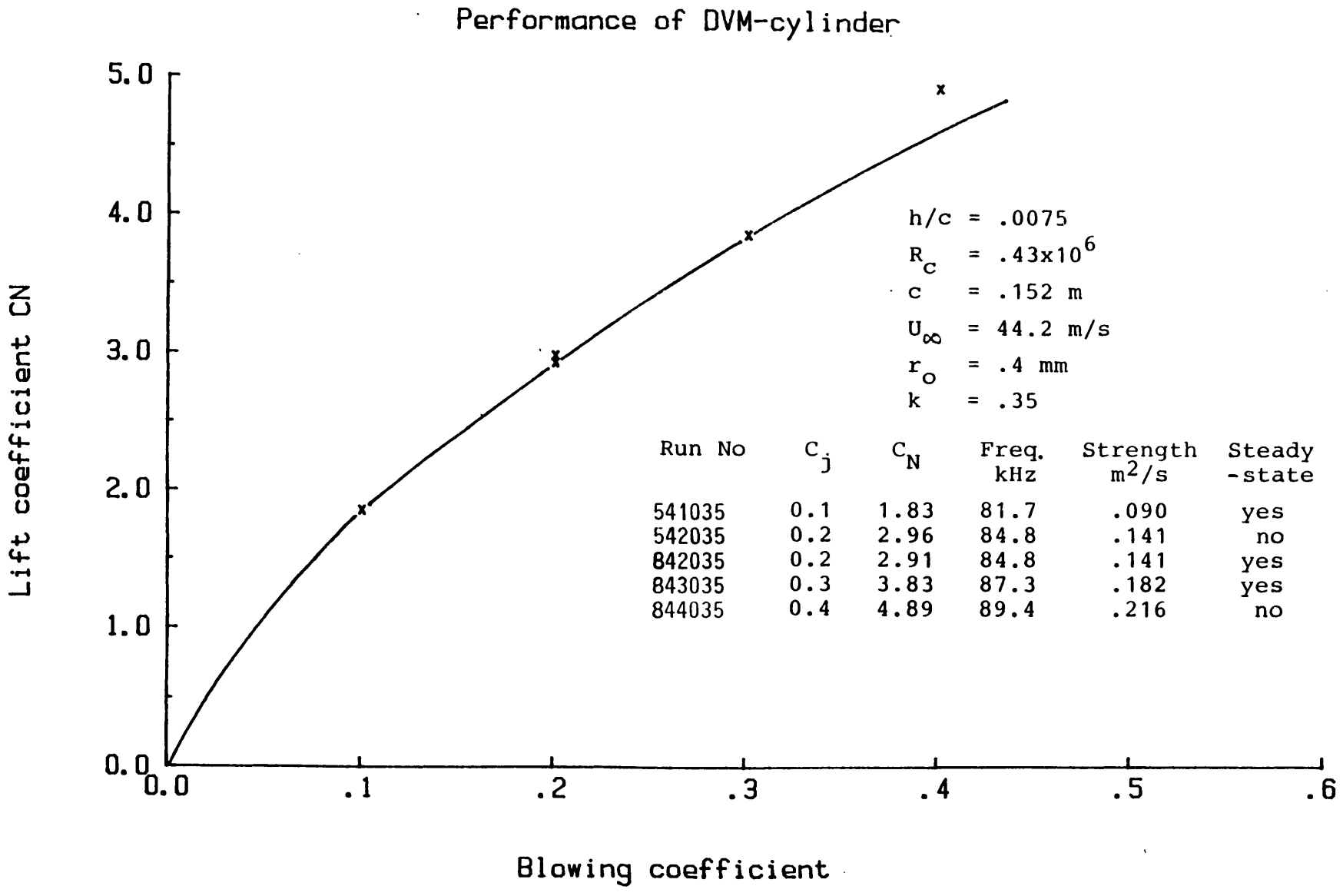

Run No	C_j	C_N	Freq. kHz	Strength m^2/s	Steady -state
541035	0.1	1.83	81.7	.090	yes
542035	0.2	2.96	84.8	.141	no
842035	0.2	2.91	84.8	.141	yes
843035	0.3	3.83	87.3	.182	yes
844035	0.4	4.89	89.4	.216	no

Fig. 4.10: PERFORMANCE OF THE THEORETICAL MODEL DVM-CYLINDER WITH K=0.35.

Fig. 4.10

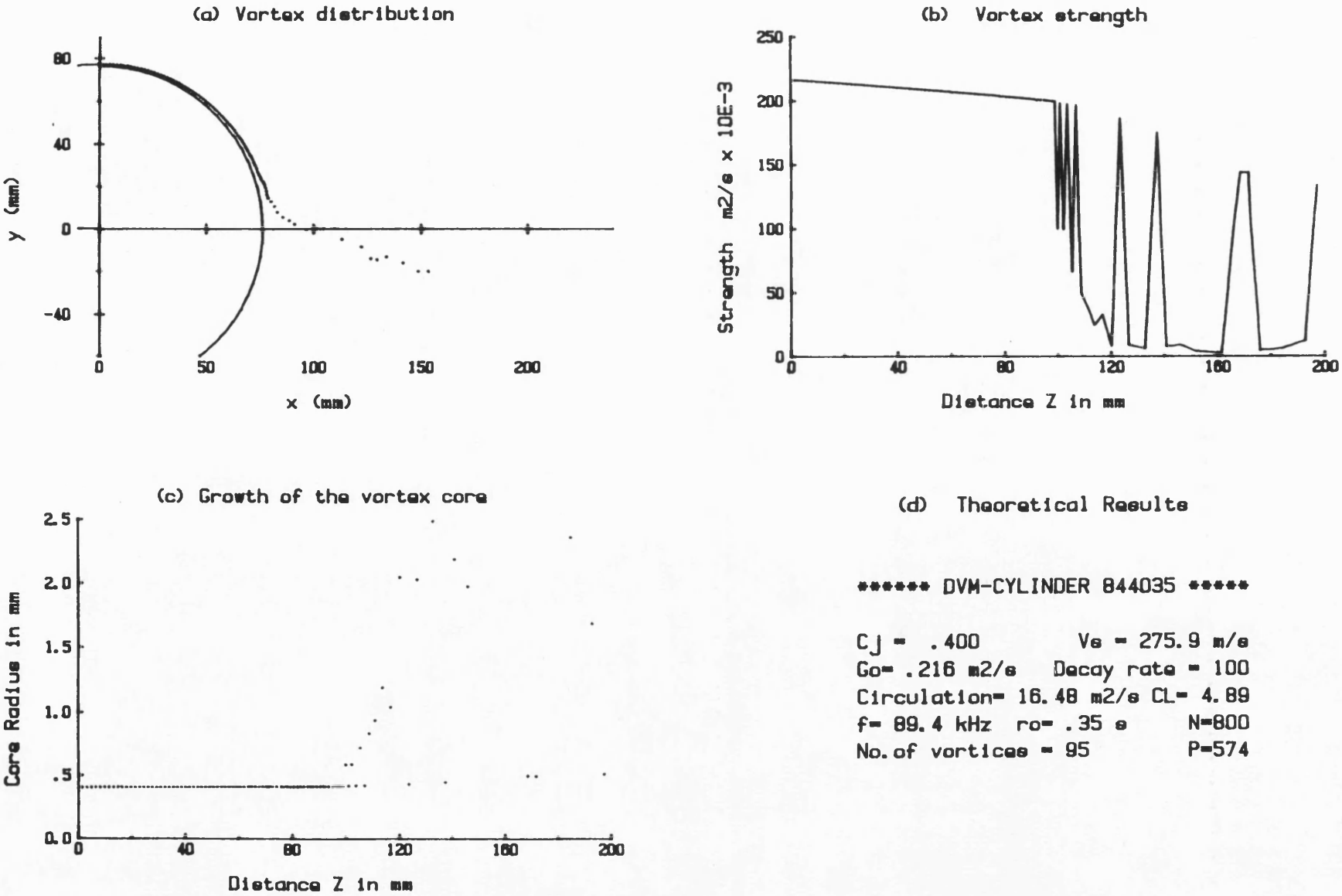

Fig. 4.11: EXAMPLE OF INCOMPLETE VORTEX DEVELOPMENT USING DVM-CYLINDER.

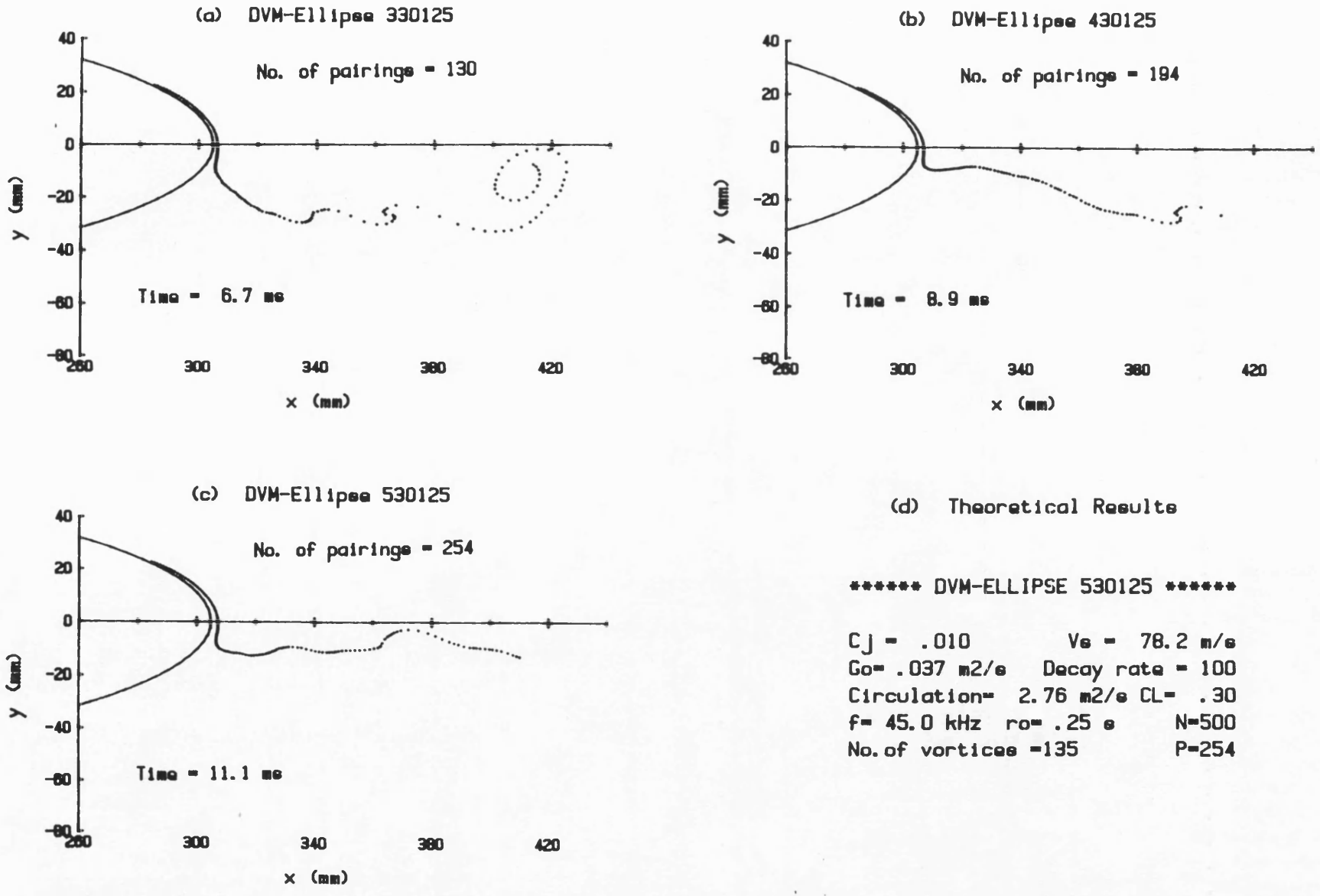

Fig. 4.12: DEVELOPMENT OF THE VORTEX STRUCTURE PREDICTED BY THE THEORETICAL MODEL DVM-ELLIPSE.

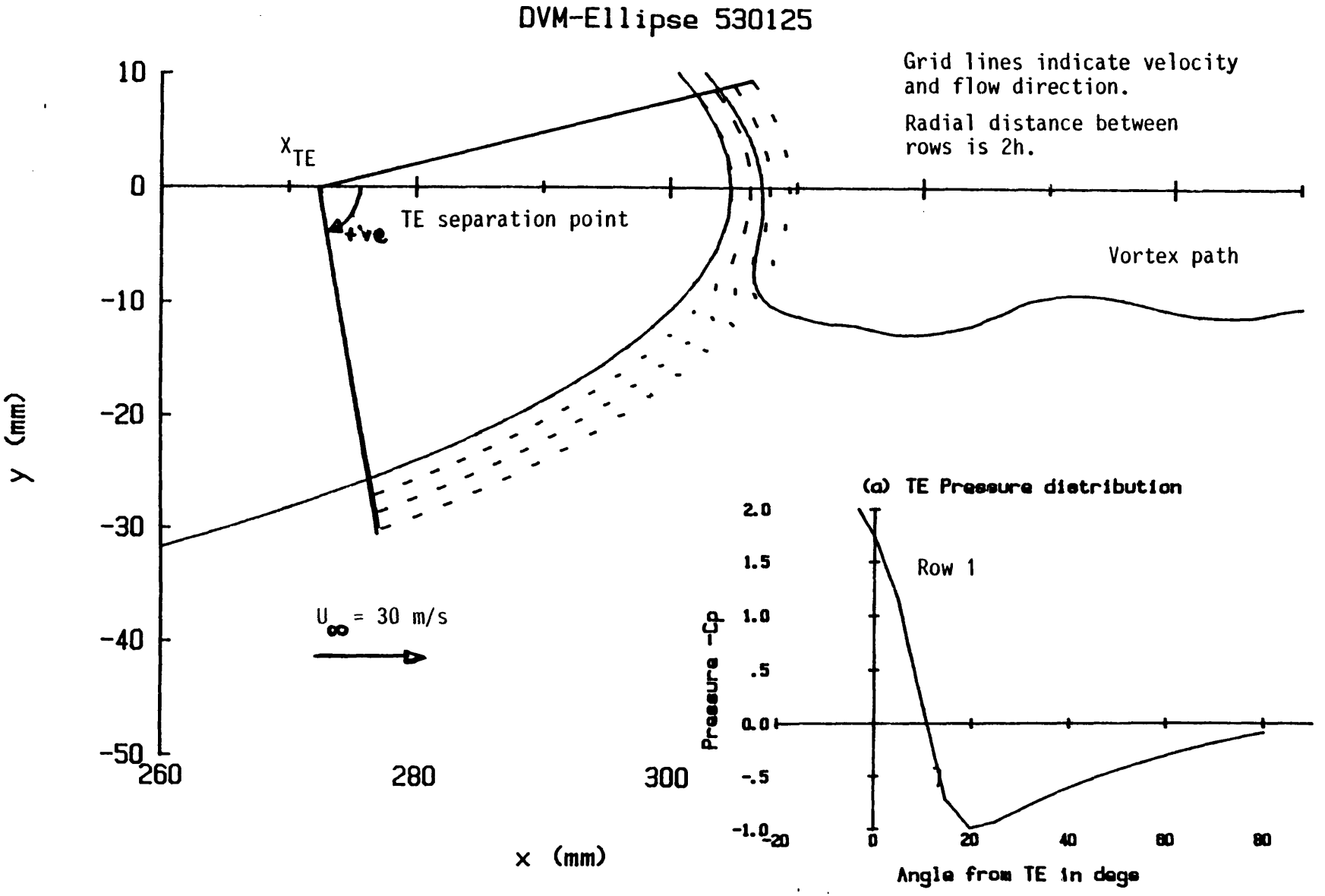

Fig. 4.13: PREDICTED FLOW PATTERN AROUND THE TE OF A 20% ELLIPTIC CCA USING DVM-ELLIPSE.

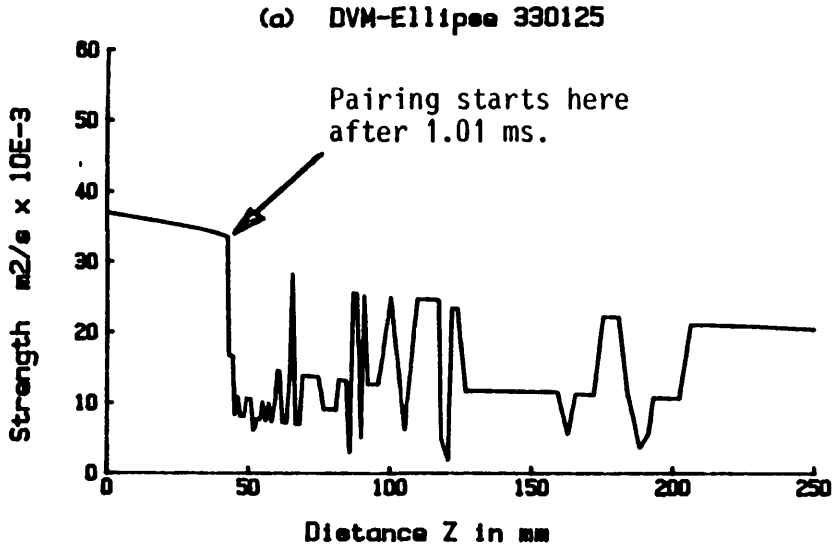

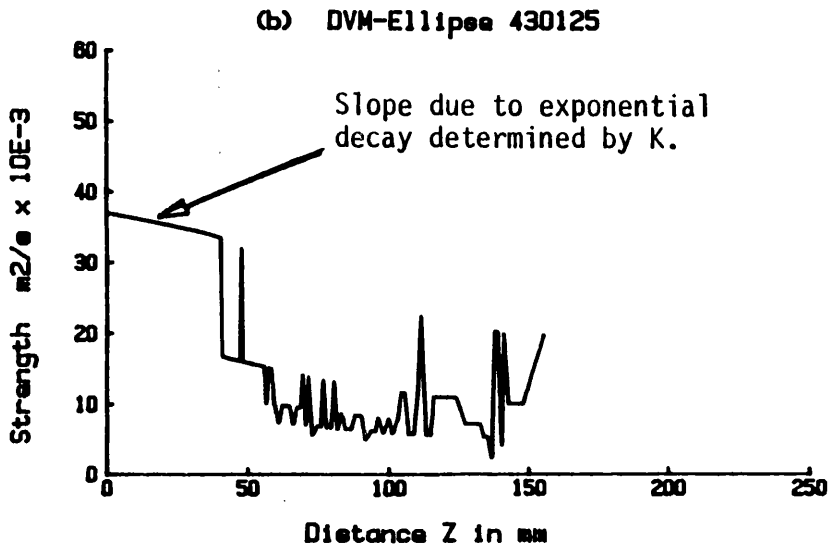

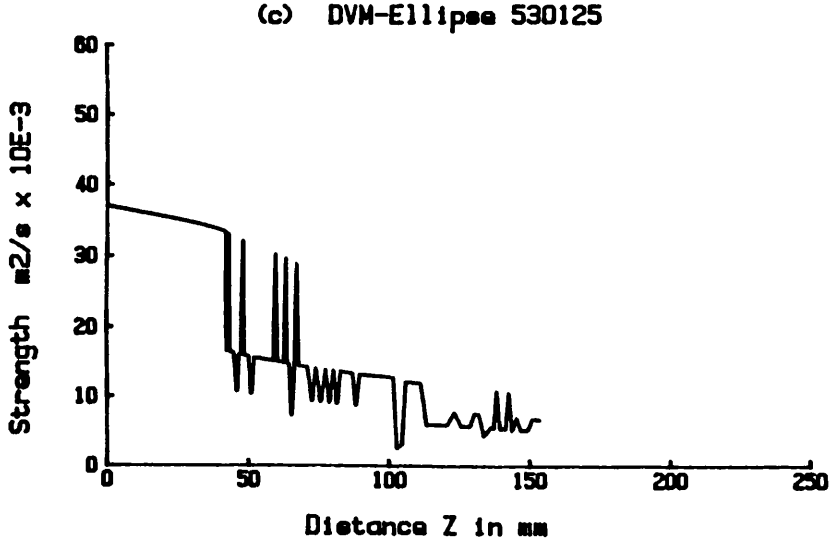

(d) Theoretical Results

****** DVM-ELLIPSE 530125 ******

Cj = .010 Ve = 78.2 m/s
Go= .037 m2/s Decay rate = 100
Circulation= 2.76 m2/s CL= .30
f= 45.0 kHz ro= .25 s N=500
No. of vortices =135 P=254

Fig. 4.14: BREAKDOWN OF THE DISCRETE VORTEX STRUCTURE PREDICTED BY DVM-ELLIPSE.

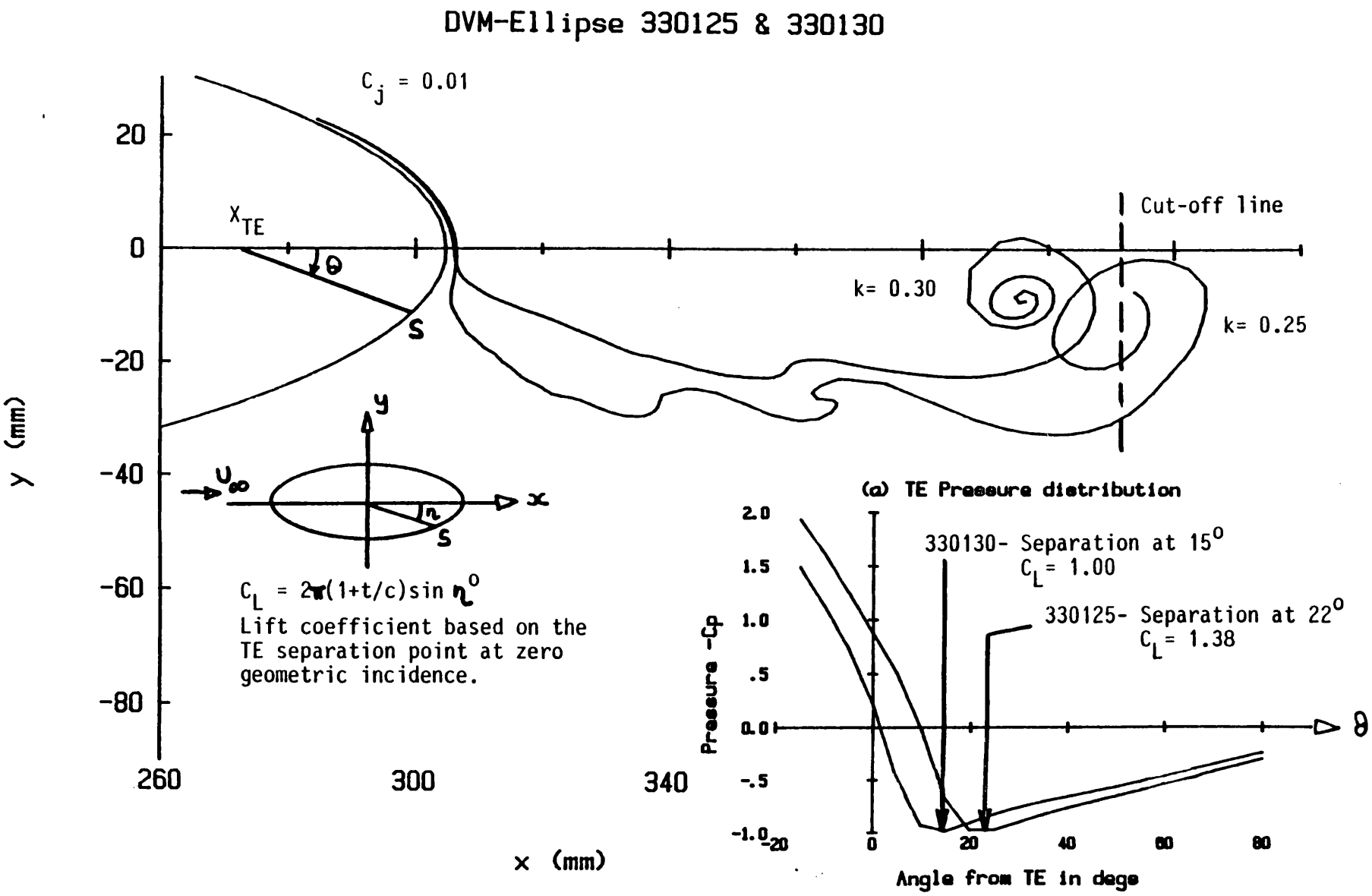

Fig. 4.15: PARTIALLY DEVELOPED FLOW AFTER 300 ITERATIONS WITH K=0.25 AND 0.30 USING DVM-ELLIPSE.

Fig. 4.15

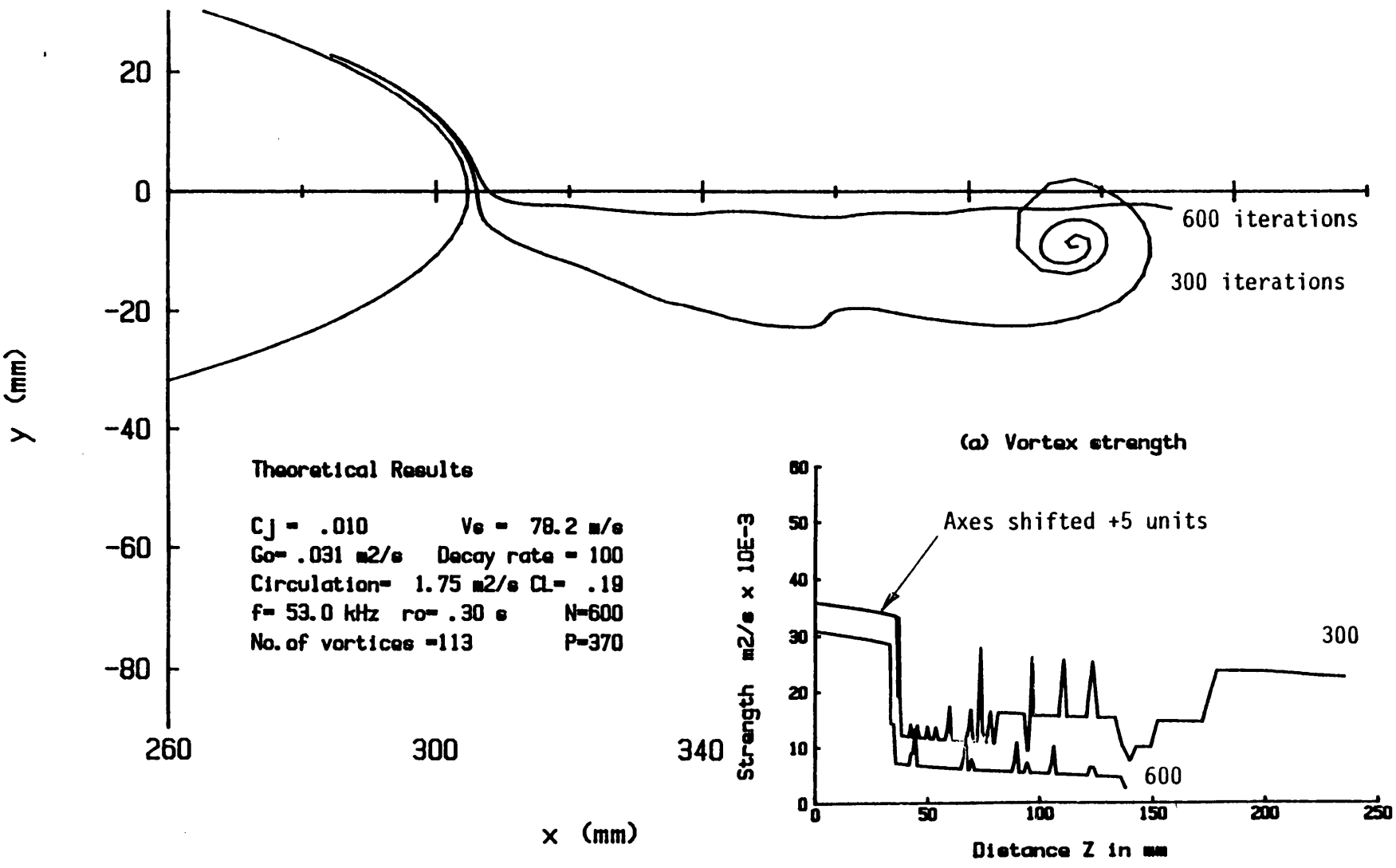

Fig. 4.16: VORTEX STRUCTURE IN THE WAKE PREDICTED BY DVM-ELLIPSE WITH CJ=0.01.

Fig. 4.16

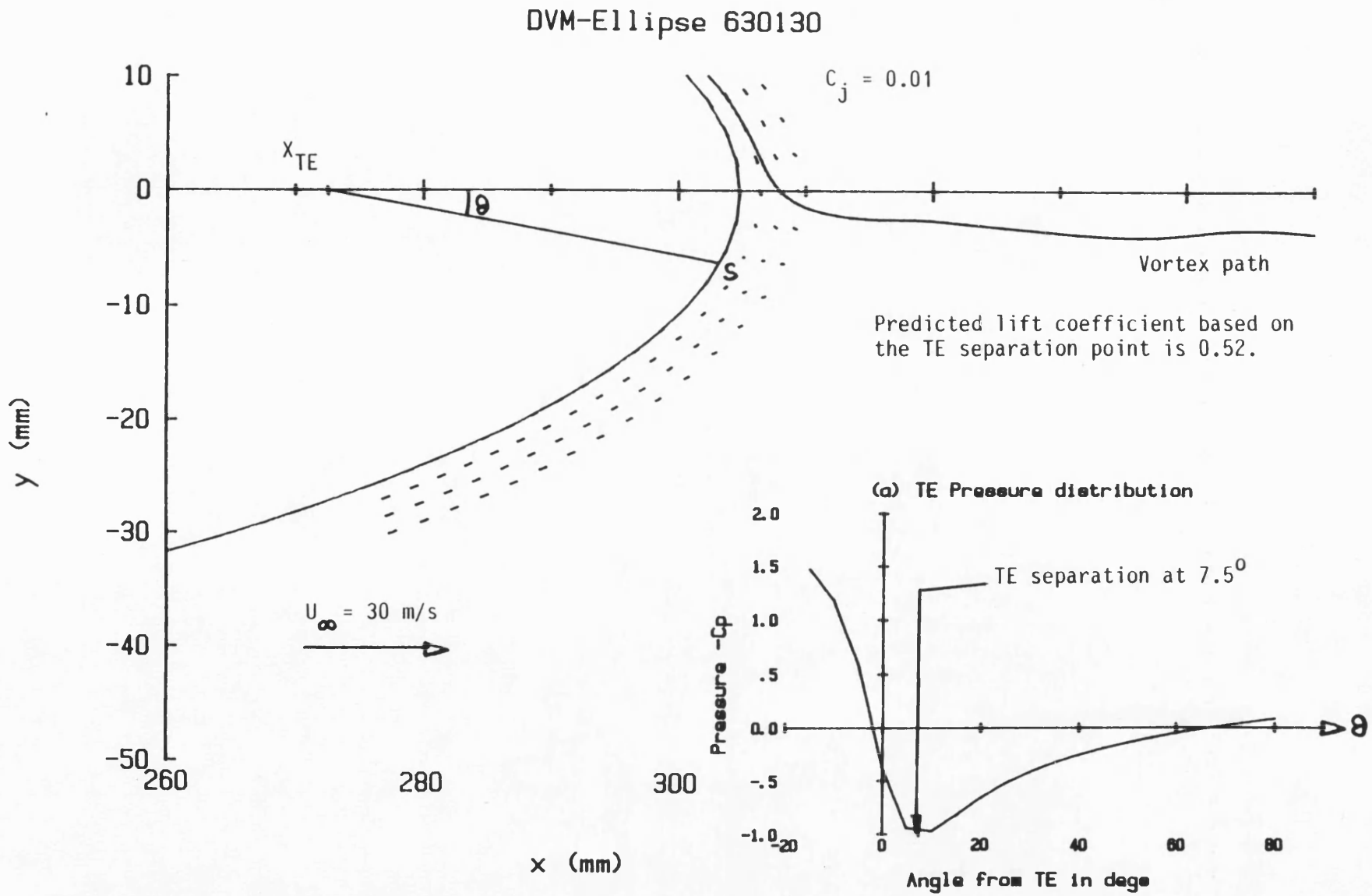

Fig. 4.17: FLOW PATTERN AROUND THE TE PREDICTED BY DVM-ELLIPSE WITH CJ=0.01.

Fig. 4.17

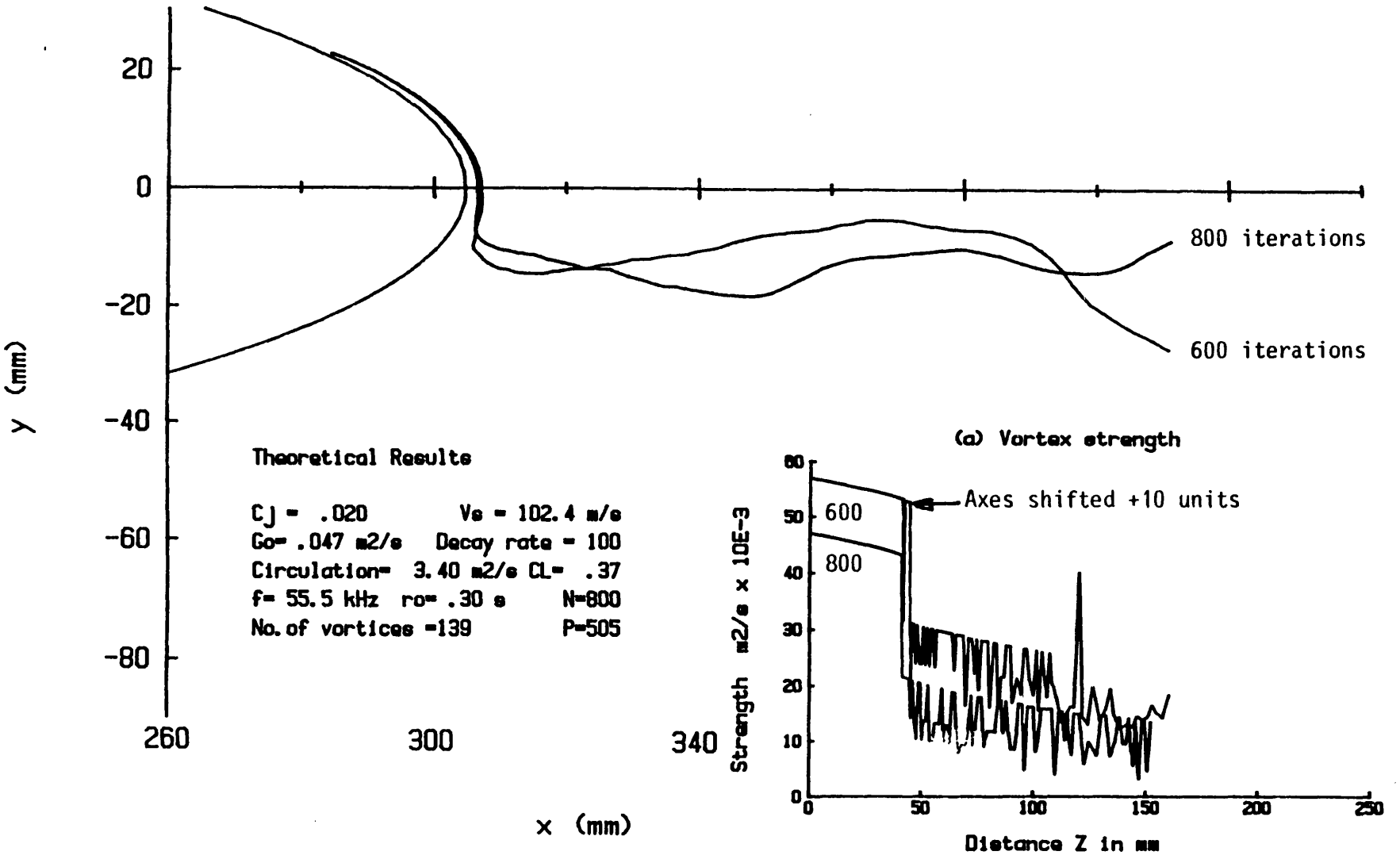

Fig. 4.18: VORTEX DEVELOPMENT AFTER 600 AND 800 ITERATIONS PREDICTED BY DVM-ELLIPSE.

Fig. 4.18

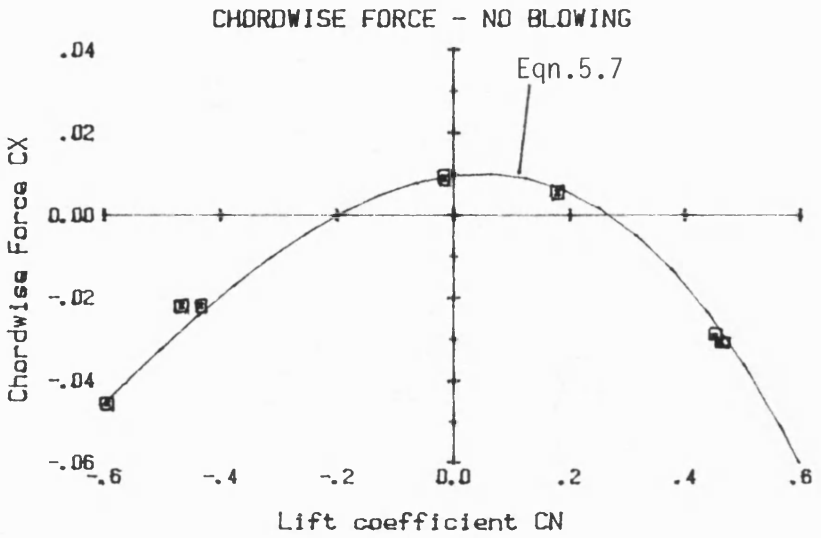

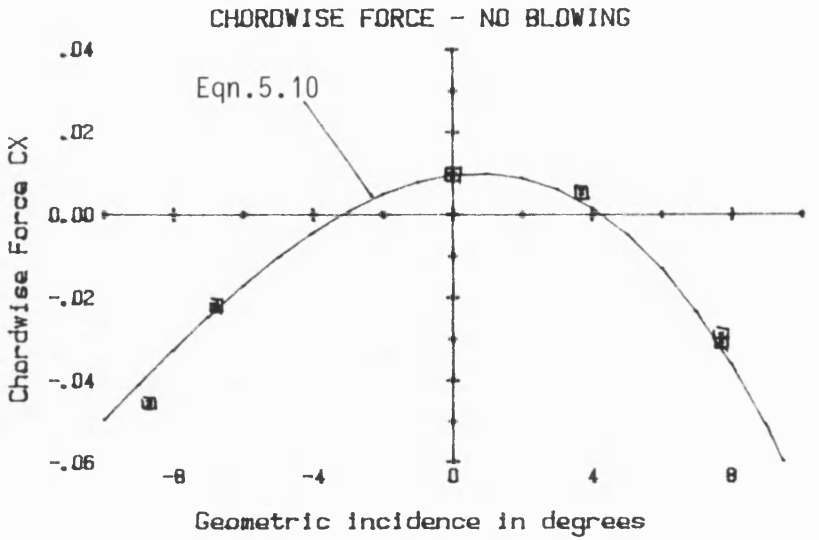

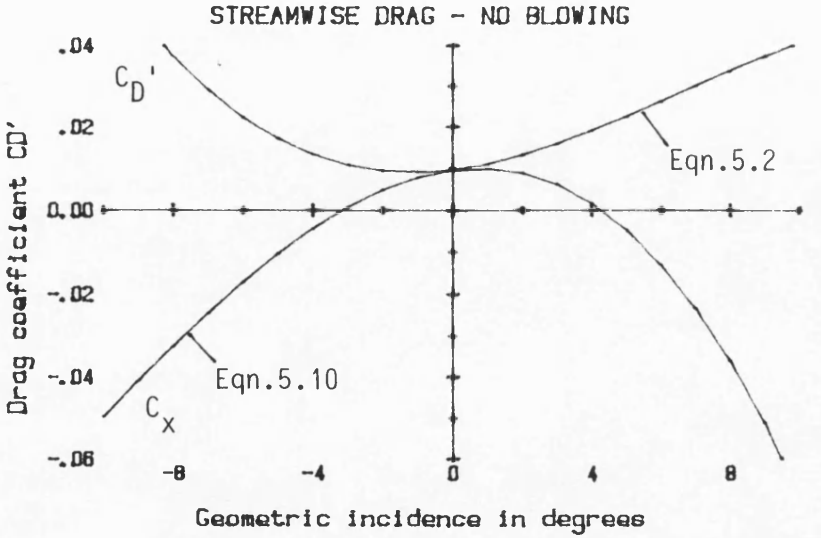

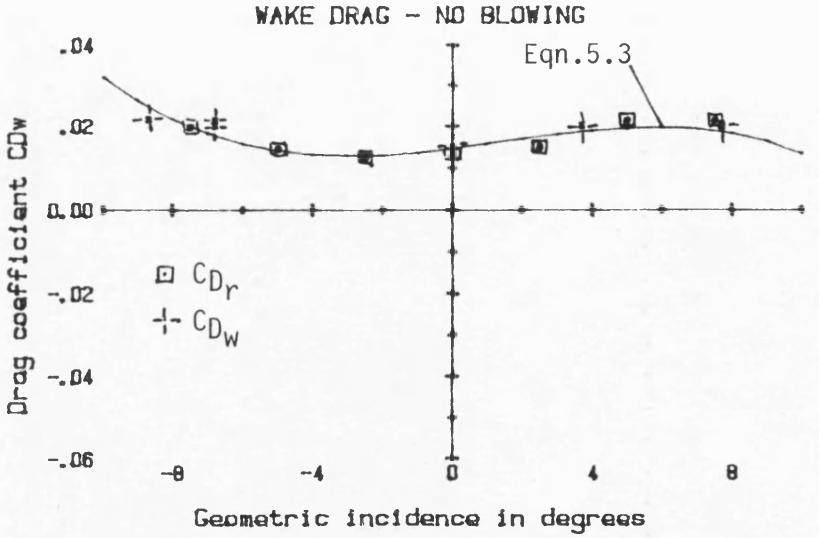

Fig. 5.1: THE DRAG TERMS USED TO DESCRIBE THE WAKE DRAG COEFFICIENT FOR THE UNBLOWN MODEL.

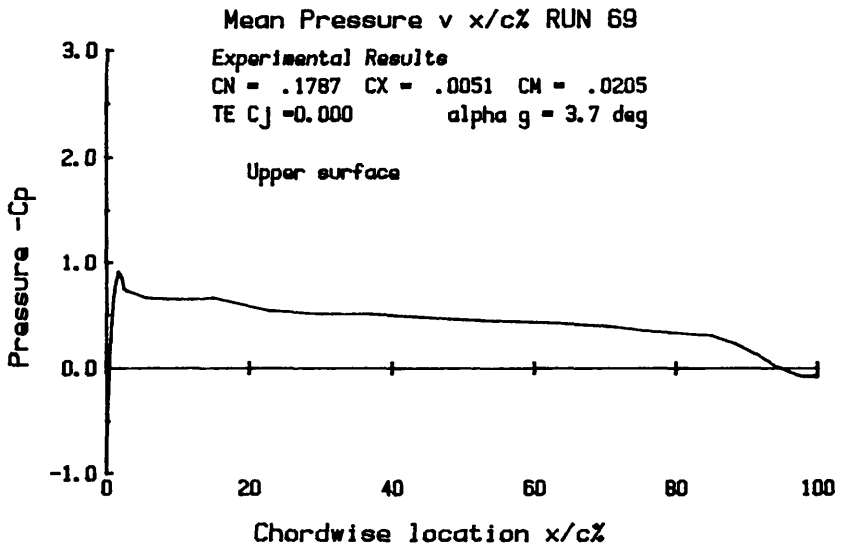

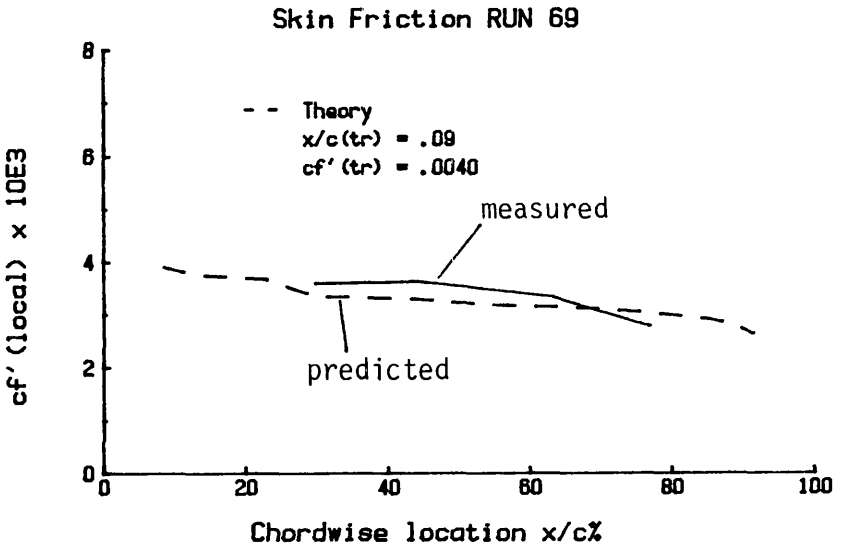

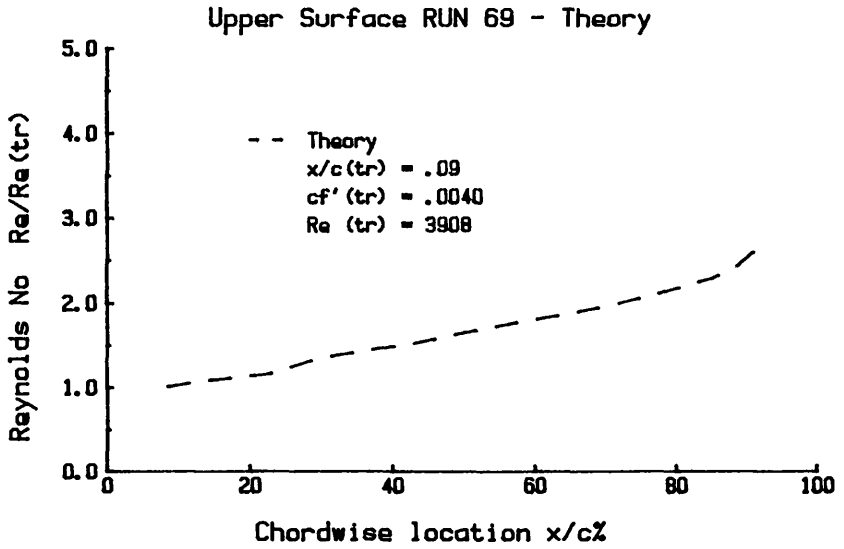

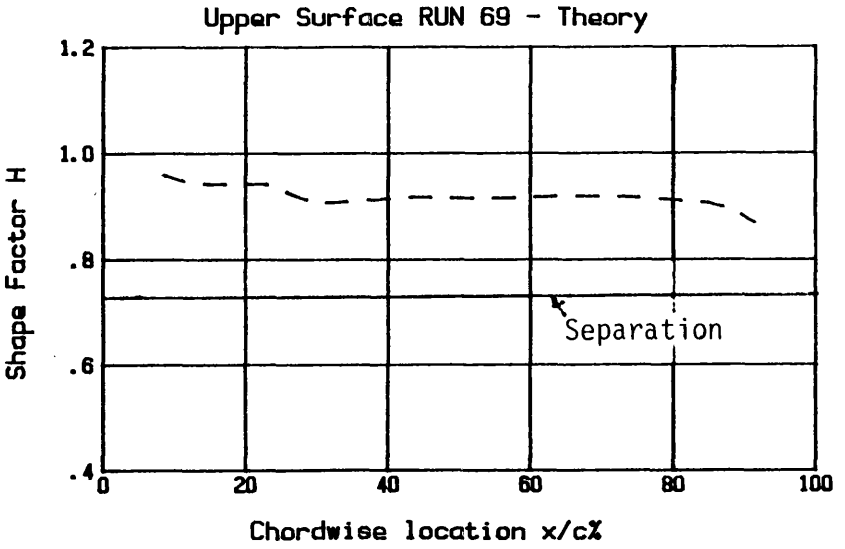

Fig. 5.2: TYPICAL BOUNDARY-LAYER DEVELOPMENT ALONG THE UPPER SURFACE FOR THE MODEL AT +3.7 DEGS.

Fig. 5.2

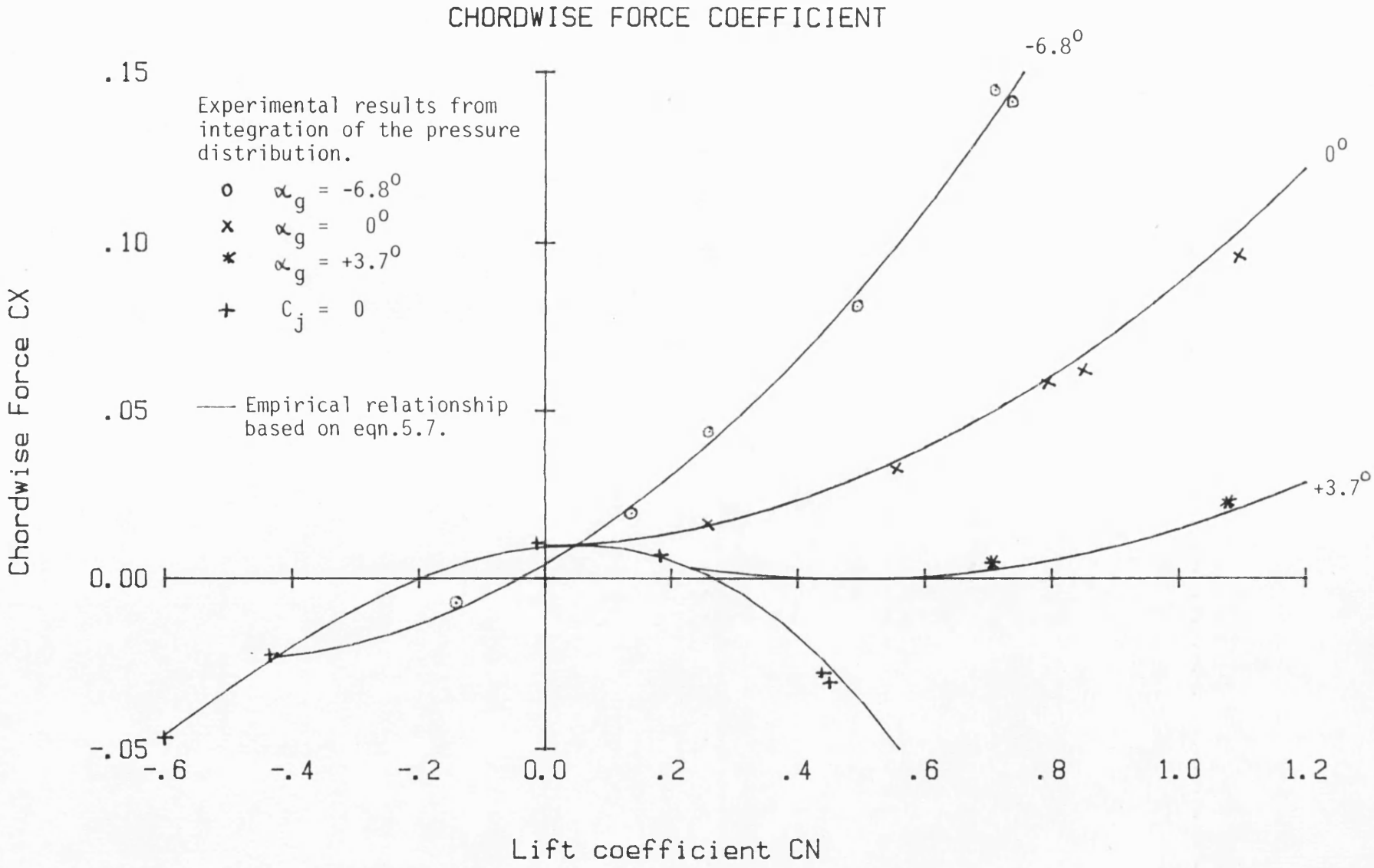

Fig.5.3: CHORDWISE FORCE AGAINST LIFT WITH VARIATION OF GEOMETRIC INCIDENCE AND TE BLOWING.

Fig.5.3

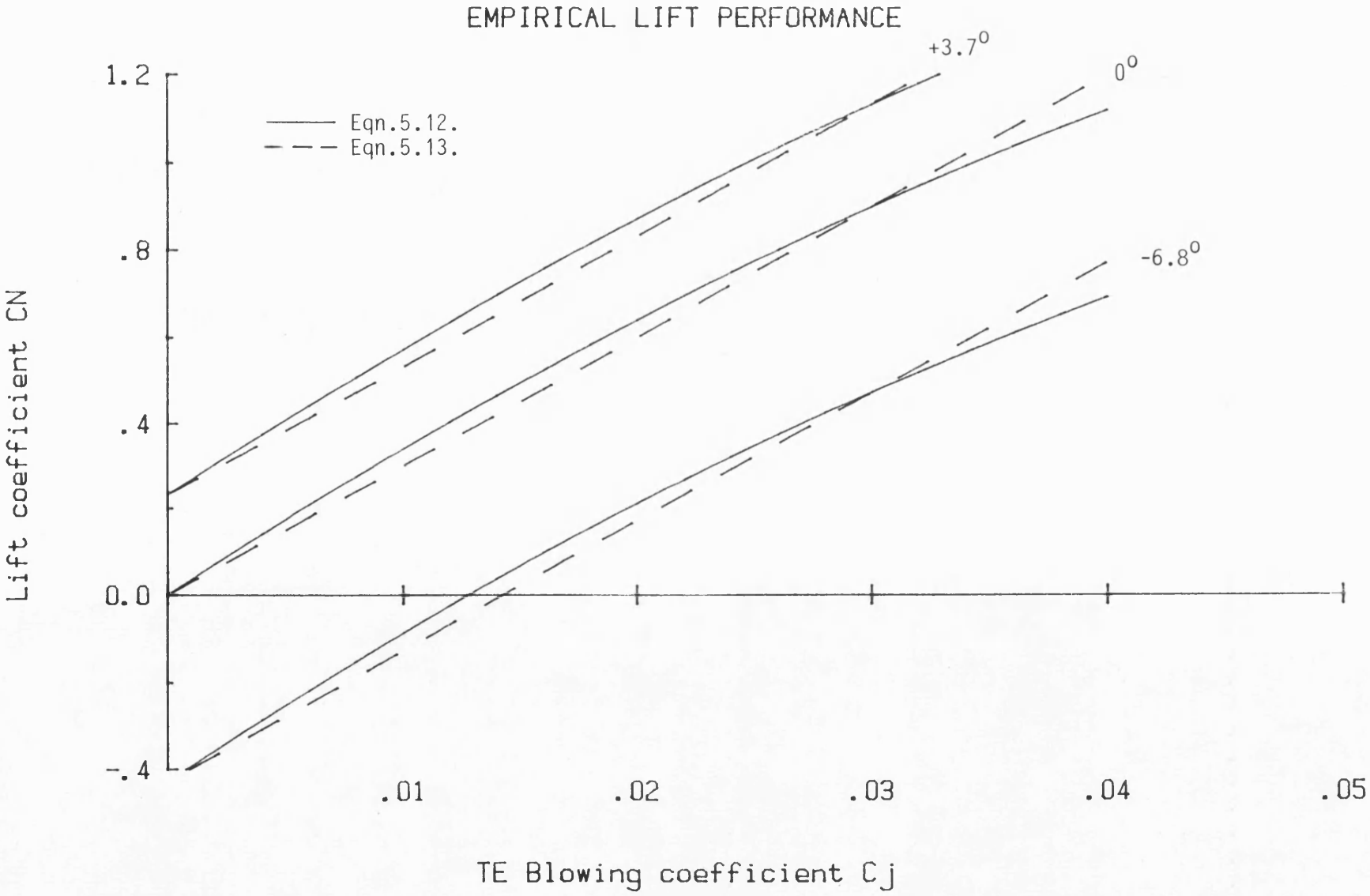

Fig.5.4: EMPIRICAL RELATIONSHIP BETWEEN LIFT AND TE BLOWING WITH VARIATION OF GEOMETRIC INCIDENCE.

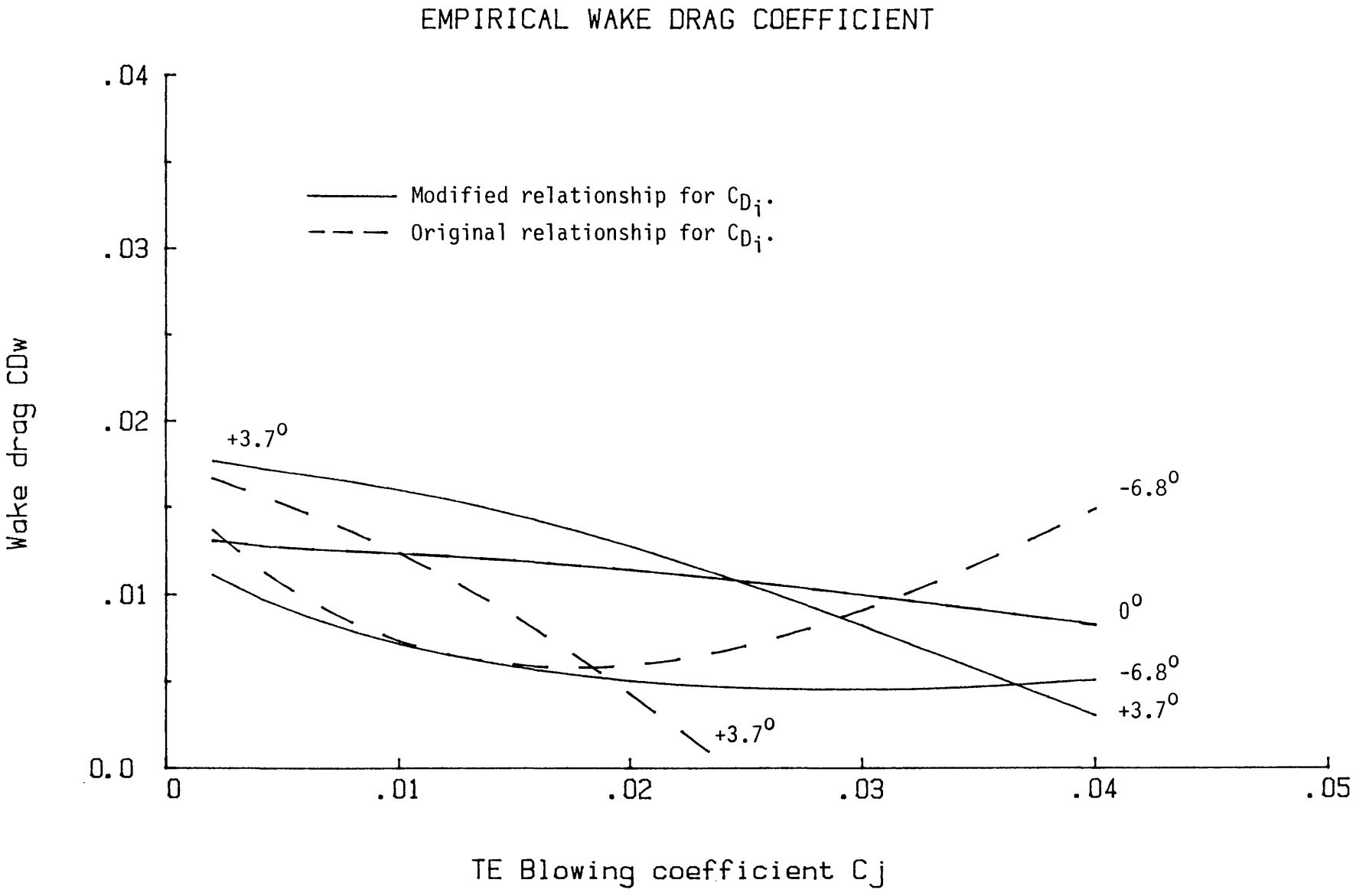

Fig.5.5: WAKE DRAG COEFFICIENT USING A MODIFIED INDUCED DRAG RELATIONSHIP.

Fig.5.5

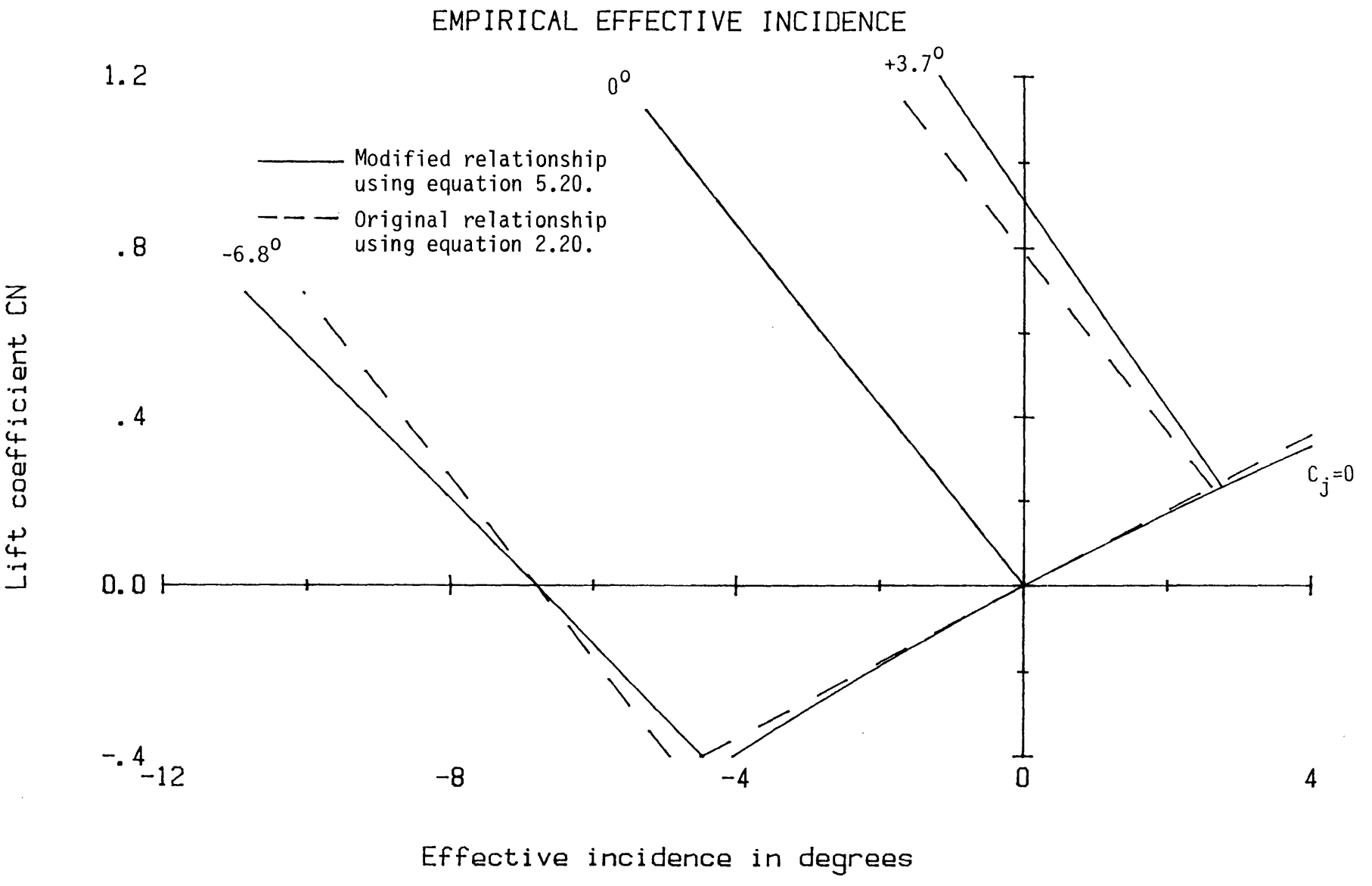

Fig. 5.6: MODIFIED RELATIONSHIP FOR EFFECTIVE INCIDENCE.

Fig.5.6

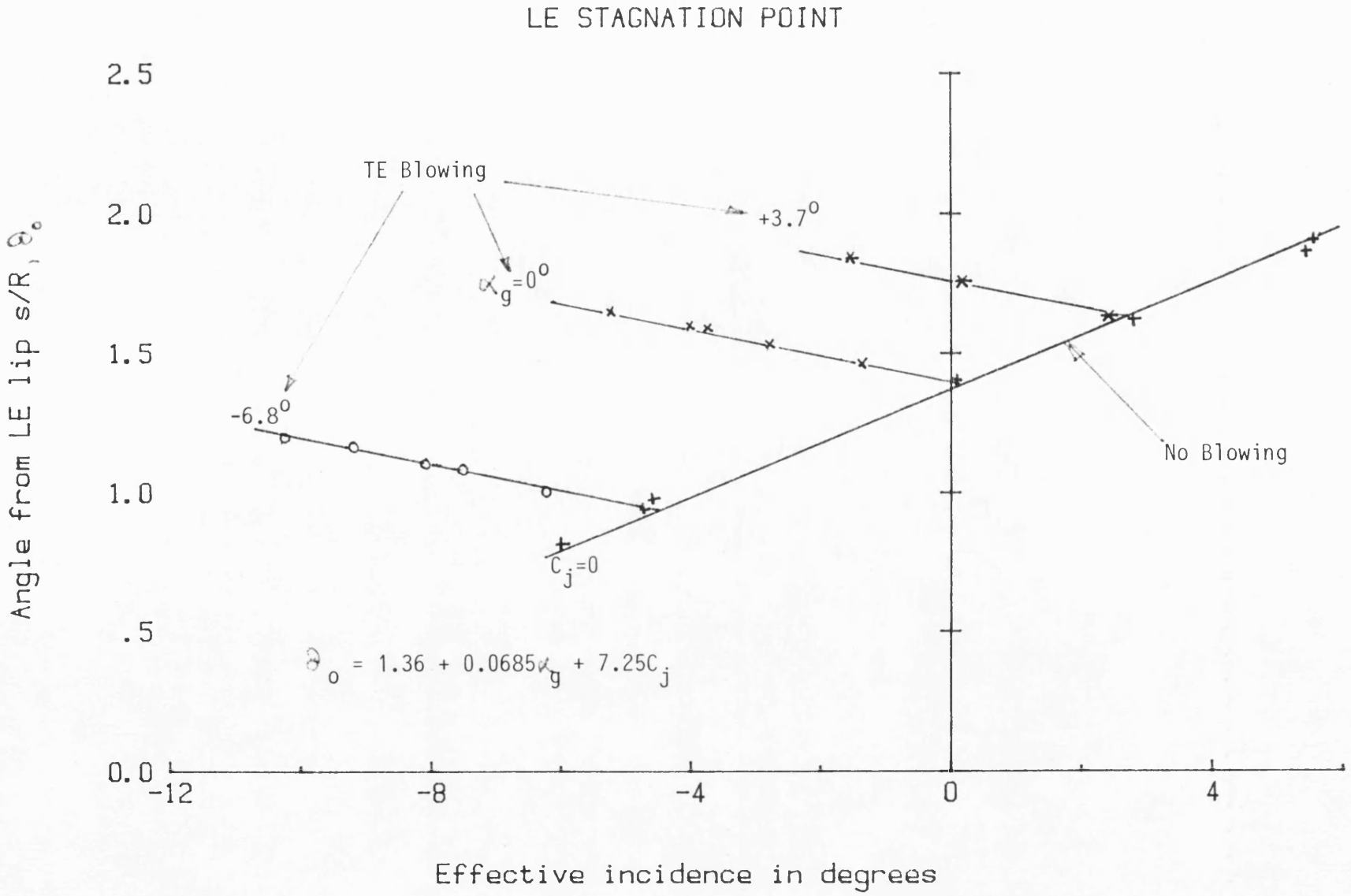

Fig.5.7: MOVEMENT OF THE LE STAGNATION POINT.

Fig.5.7

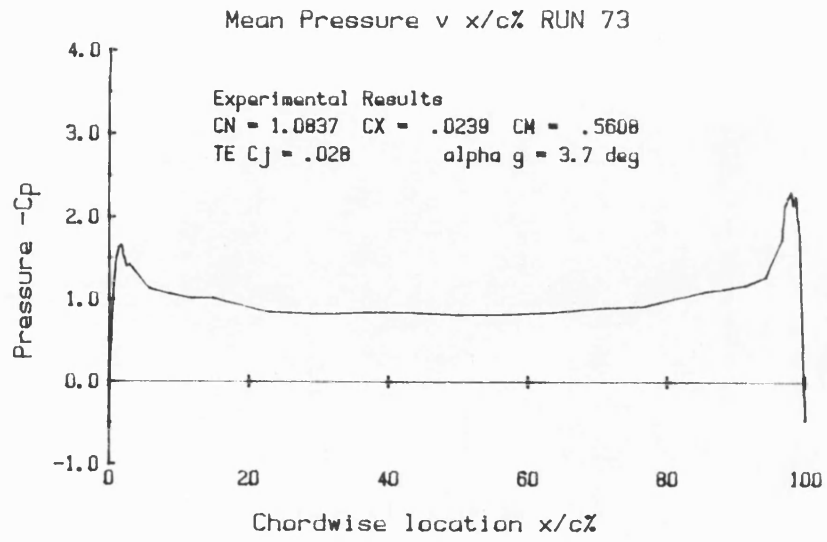

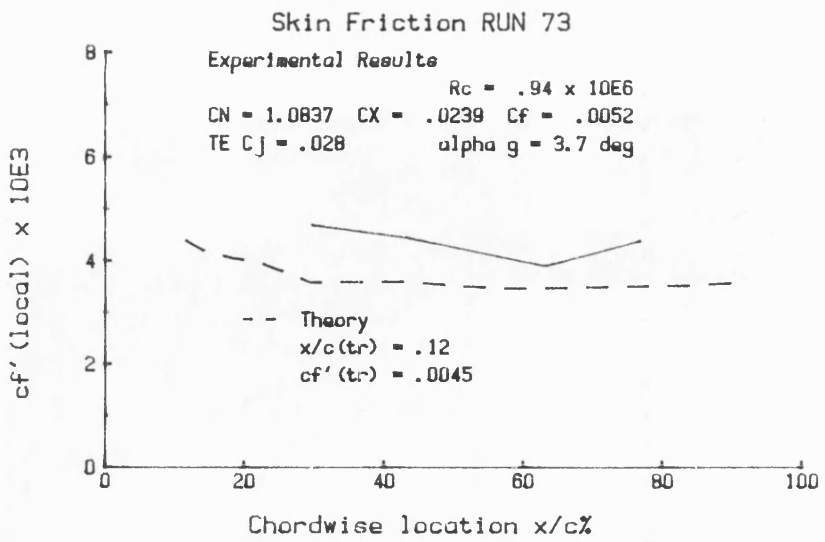

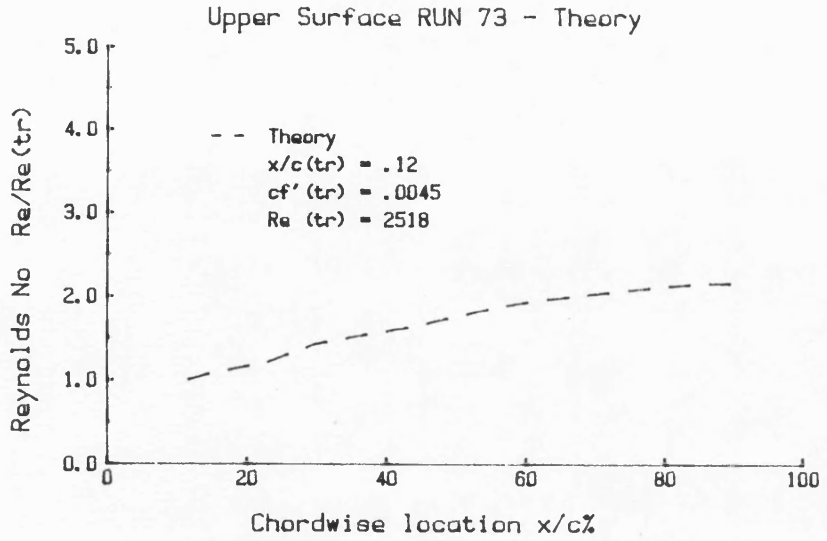

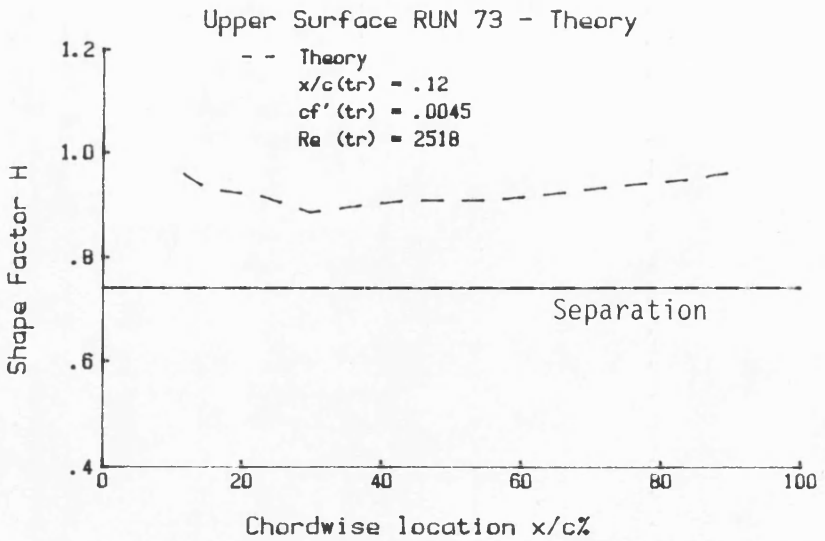

Fig. 5.8: THE UPPER SURFACE BOUNDARY-LAYER FOR RUN-73.

(a) Original flow near the junction between the TE tube and the bottom endplate.

View looking onto the lower surface with free-stream flow moving from left to right.

(b) Modified flow following the addition of endplate blowing slot.

Fig. 5.9: FLOW VISUALIZATION OF THE LOWER SURFACE SHOWING THE IMPROVEMENT WITH ENDPLATE BLOWING.

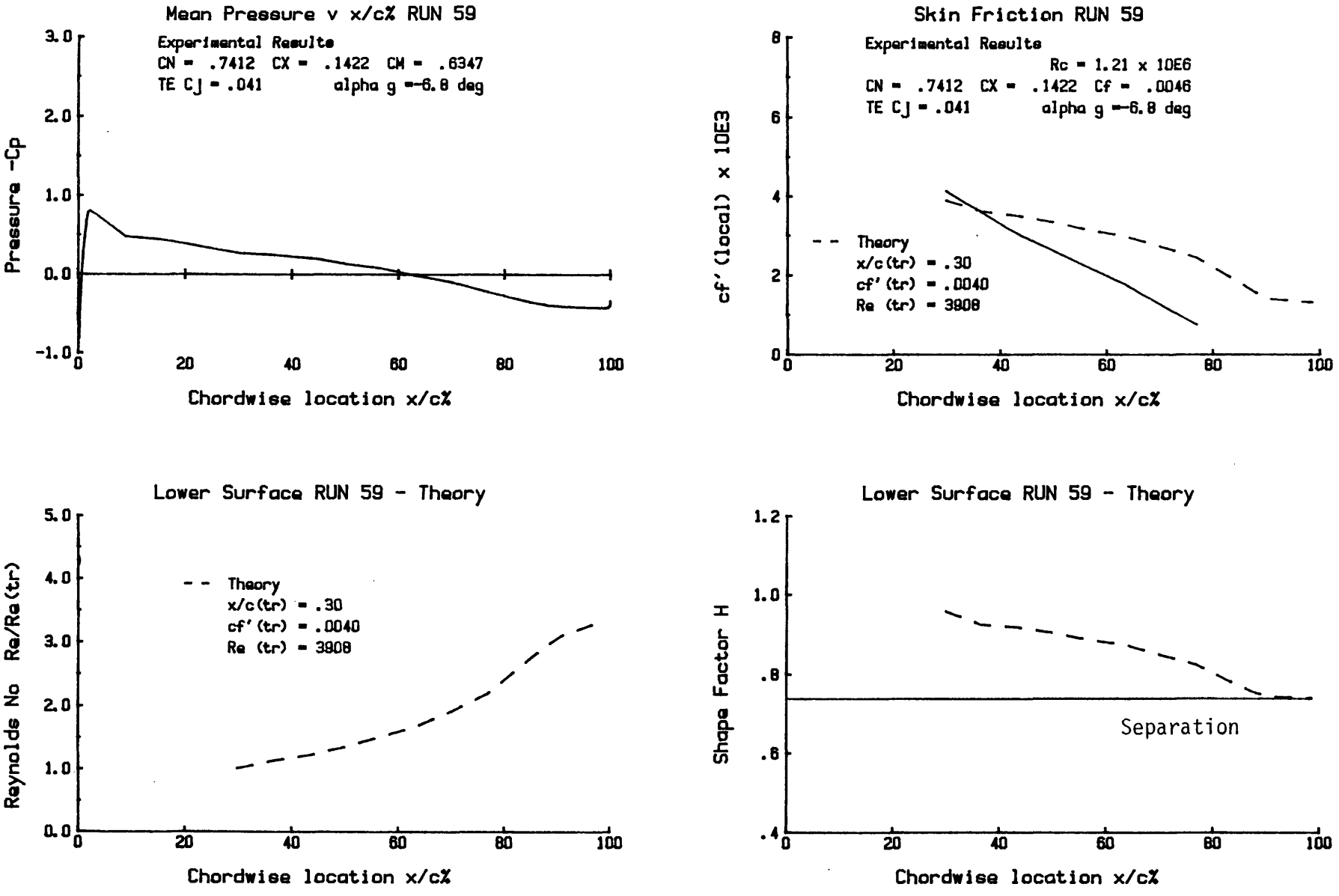

Fig. 5.10: PREDICTED LOWER SURFACE BOUNDARY-LAYER DEVELOPMENT FOR RUN-59.

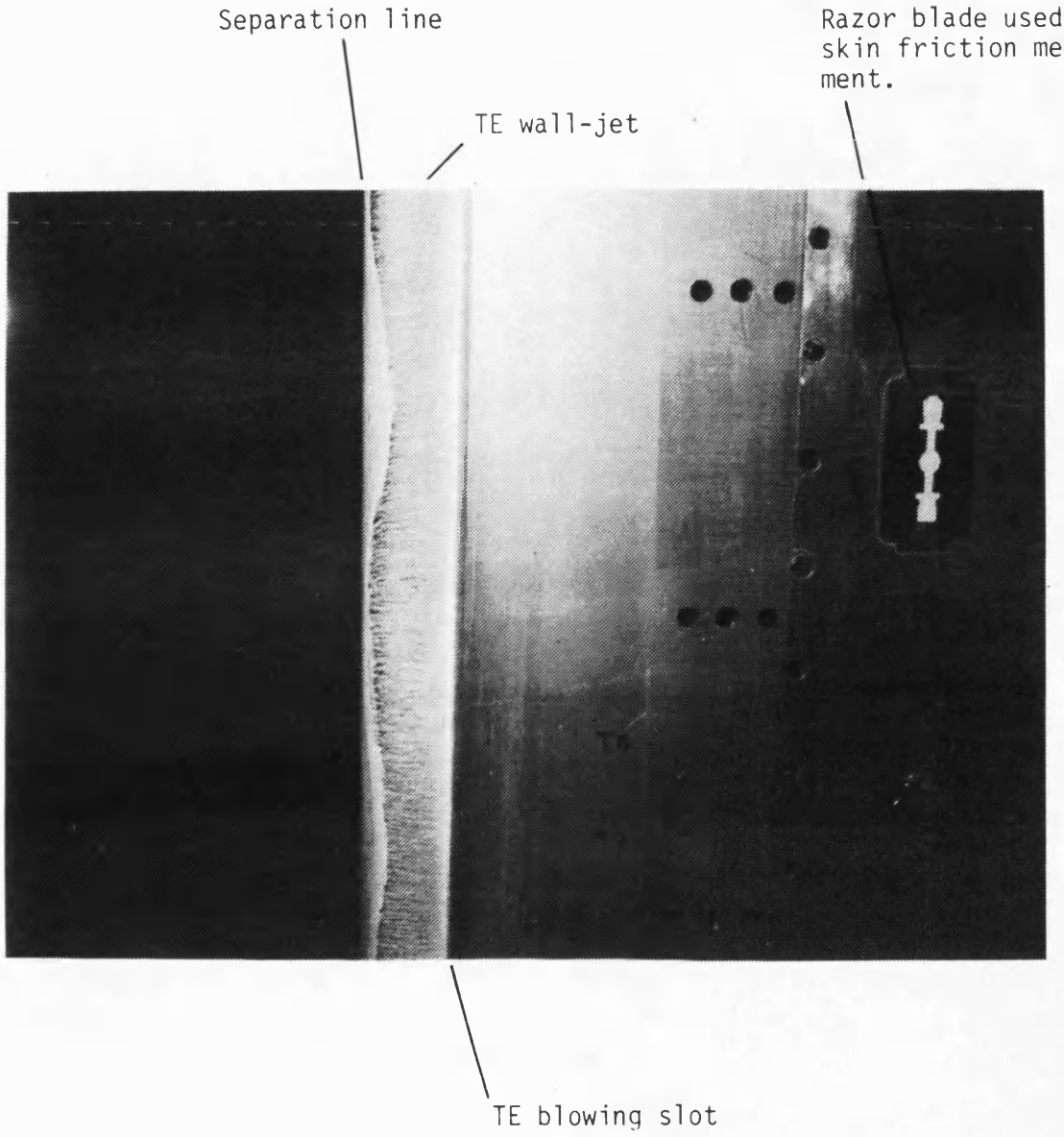

View looking onto the upper surface with free-stream flow moving from right to left.

Fig. 5.11: FLOW VISUALIZATION OF THE TE WALL-JET EMERGING FROM THE TE BLOWING SLOT.

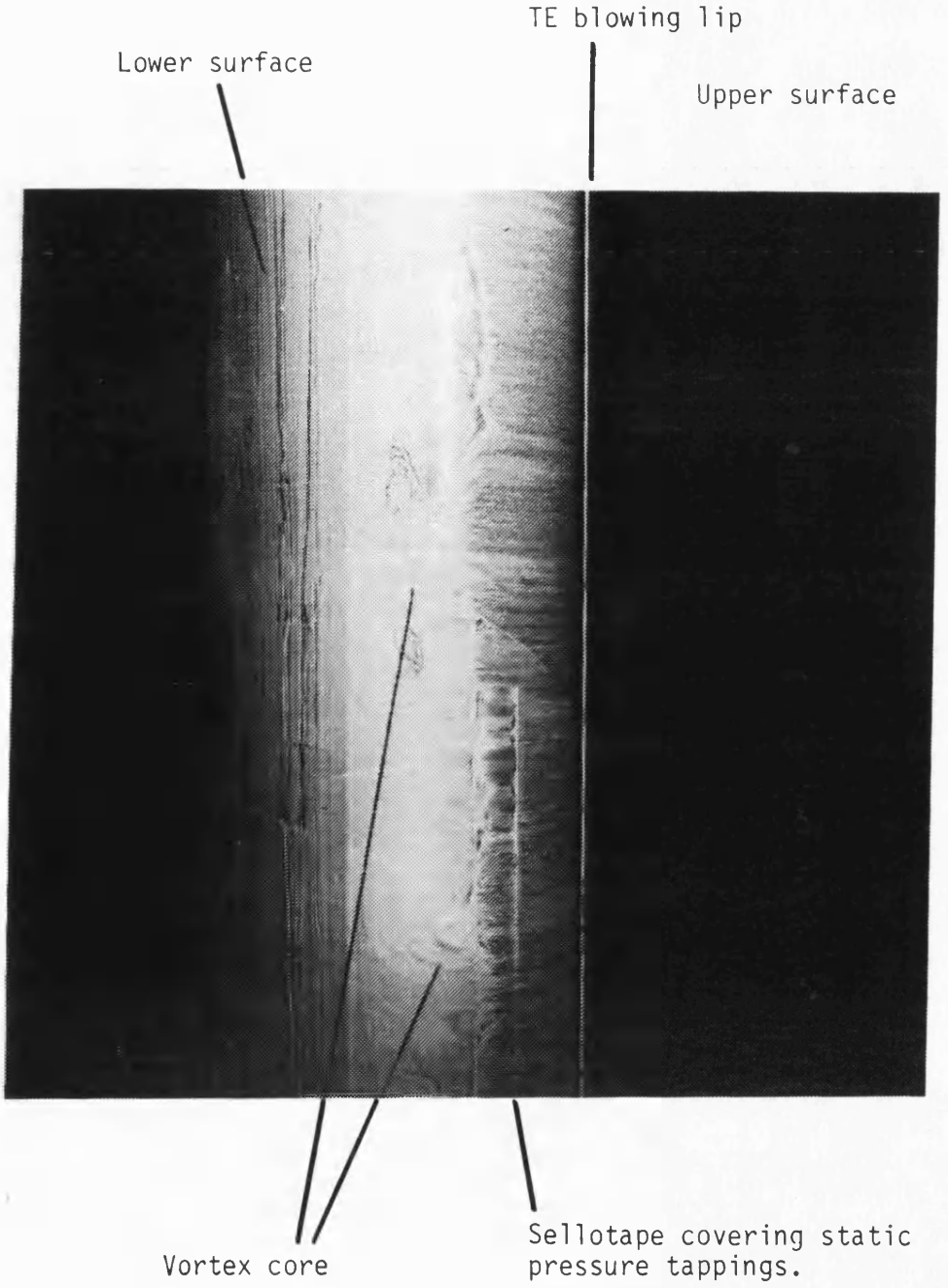

View looking upstream.

Fig. 5. 12: FLOW VISUALIZATION SHOWING TWO STREAMWISE VORTICES EMANATING FROM THE TE SURFACE.

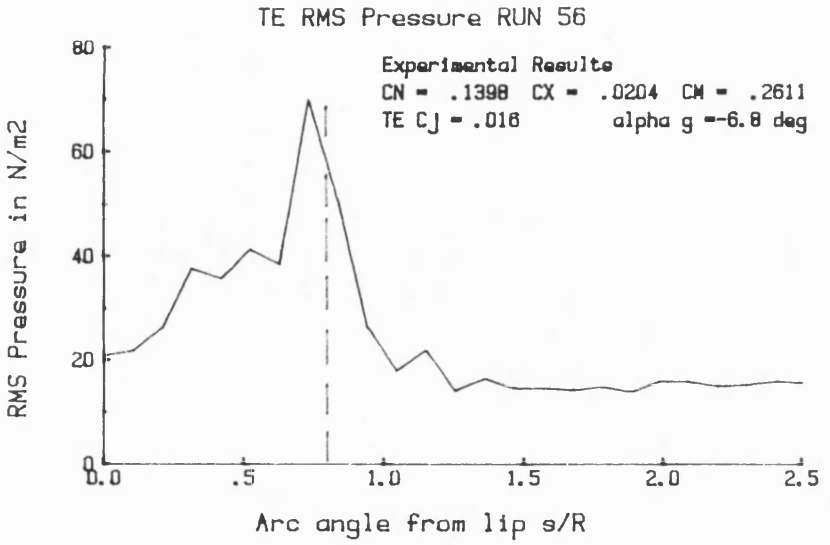

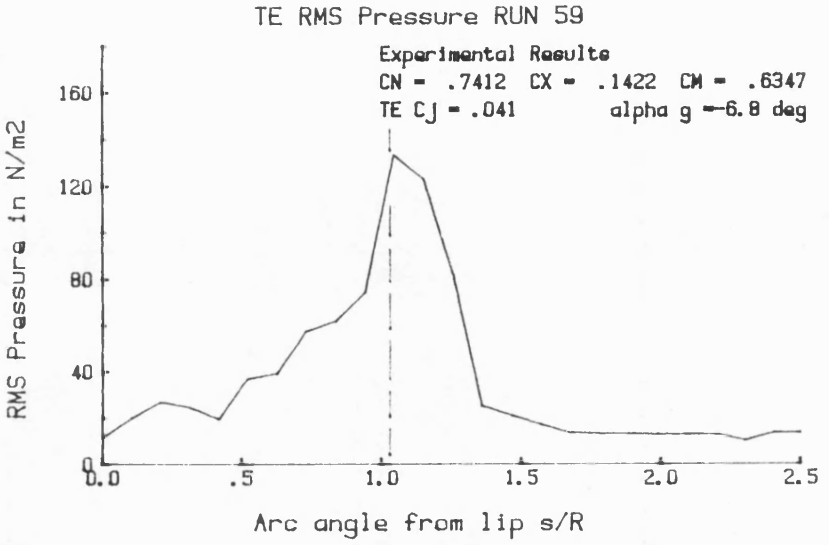

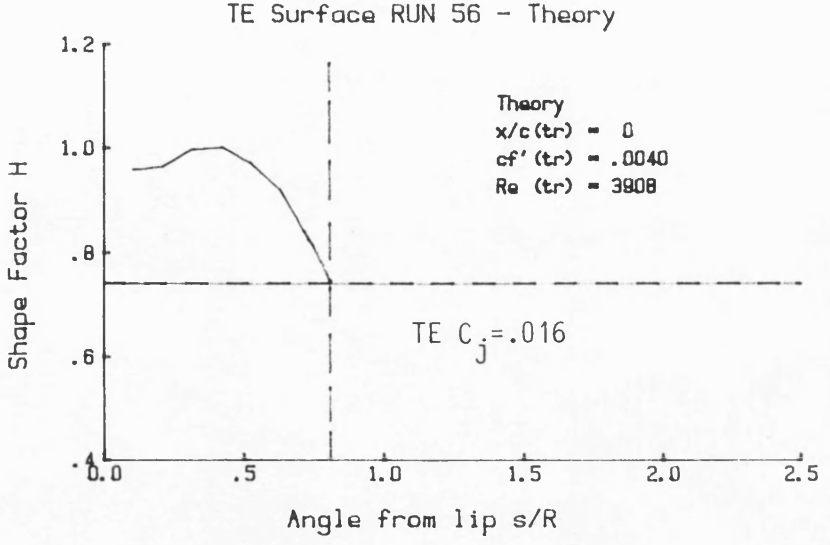

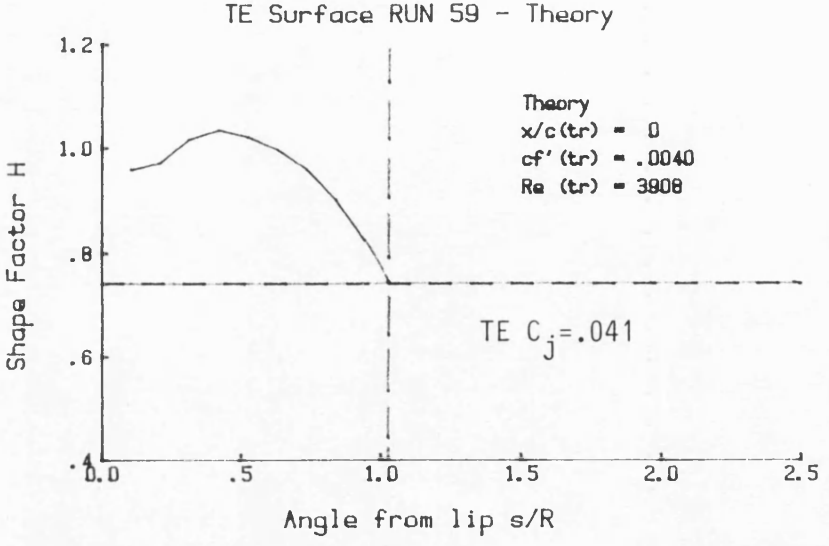

Fig. 5.13: COMPARISON BETWEEN MEASURED AND PREDICTED TE SEPARATION POINTS FOR RUN-56 AND RUN-59.

Fig. 5.13

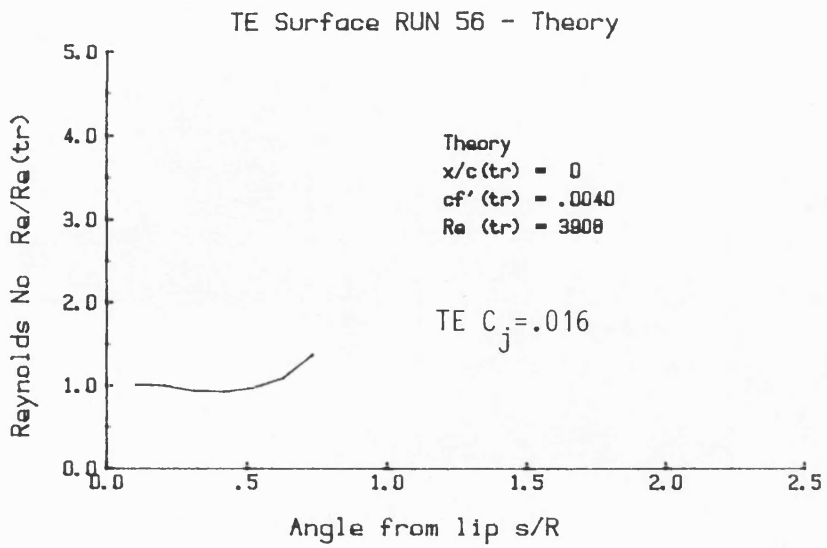

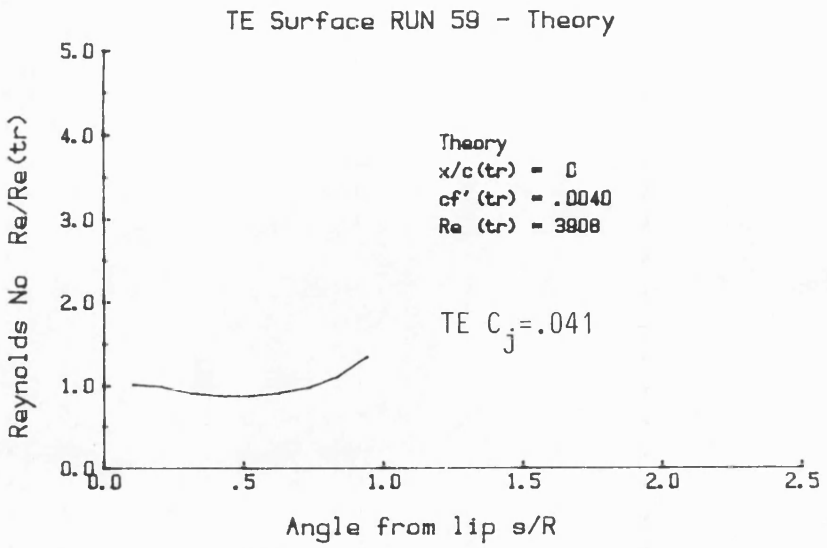

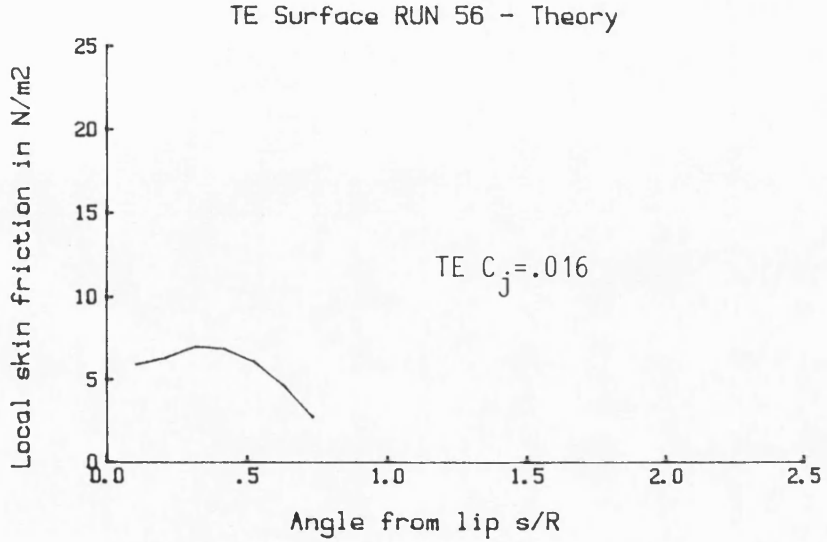

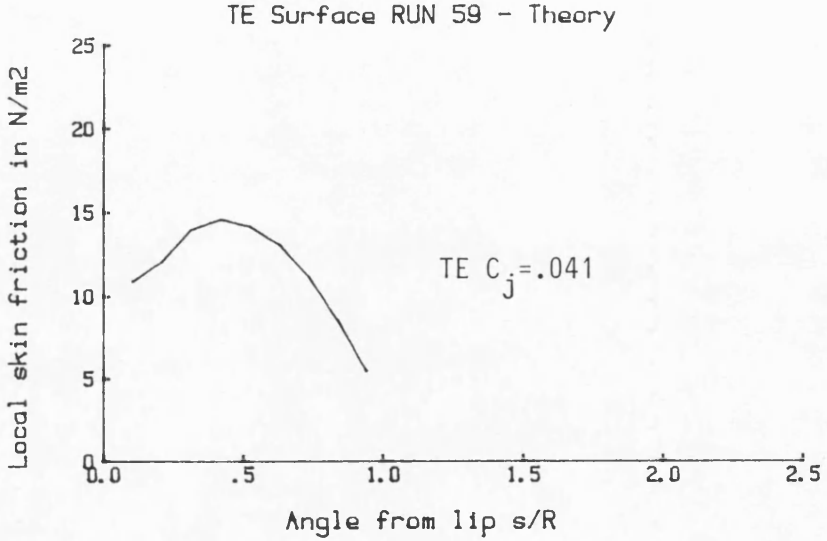

Fig. 5.14: TE BOUNDARY-LAYER DEVELOPMENT PREDICTED FOR RUN-56 AND RUN-59.

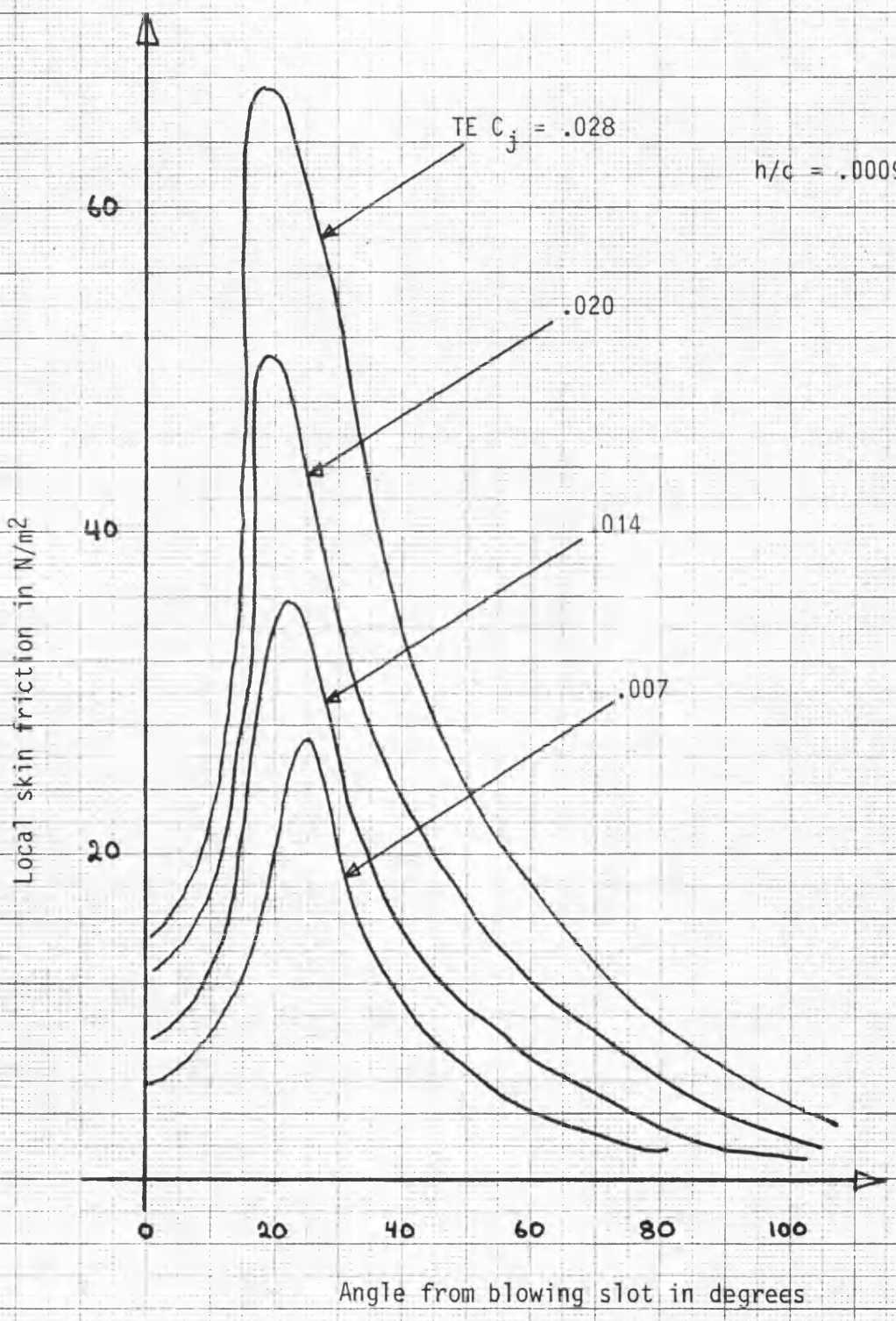

Fig. 5. 15: LOCAL SKIN FRICTION AROUND THE TE AS MEASURED BY WARSOP AND MARRERO SANTO (44).

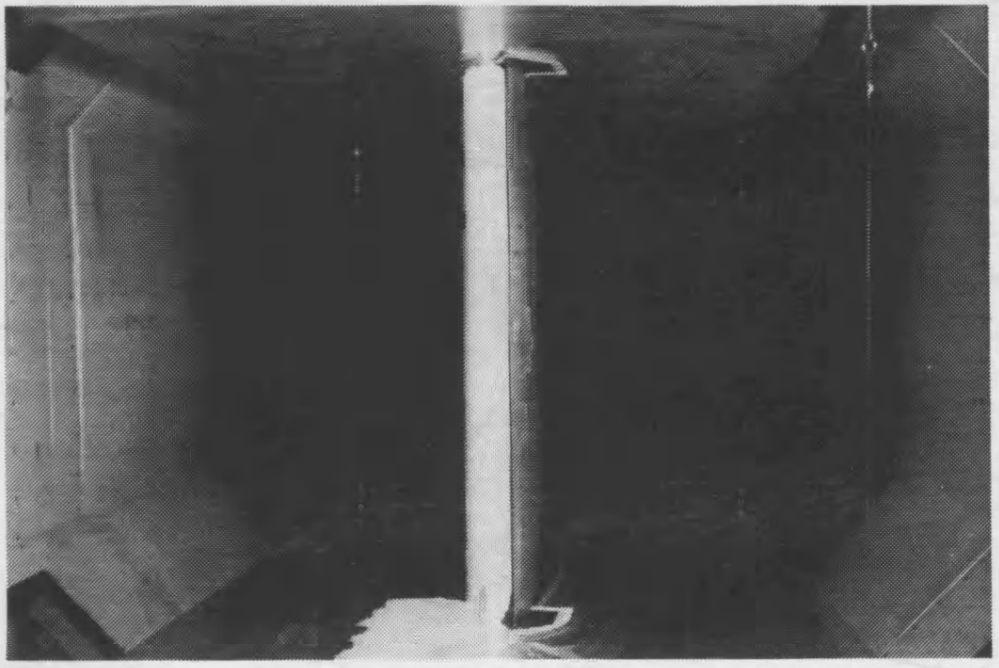

(a) View looking upstream.

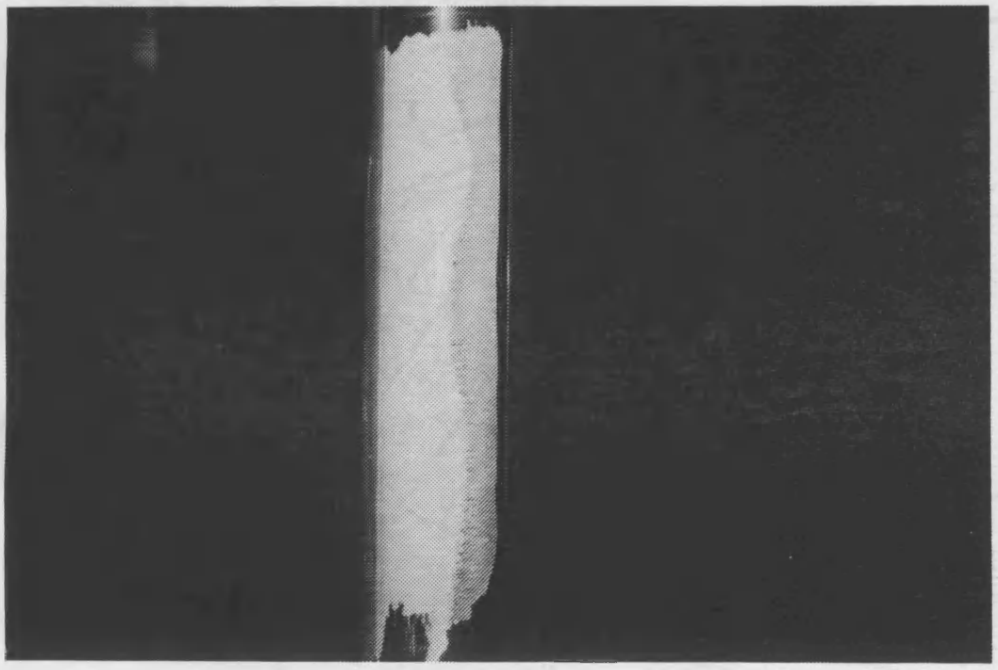

(b) View looking onto the mid-span section of the TE tube.

Fig. 5. 16: FLOW VISUALIZATION SHOWING SPANWISE DISTRIBUTION OF THE TE SEPARATION LINE.

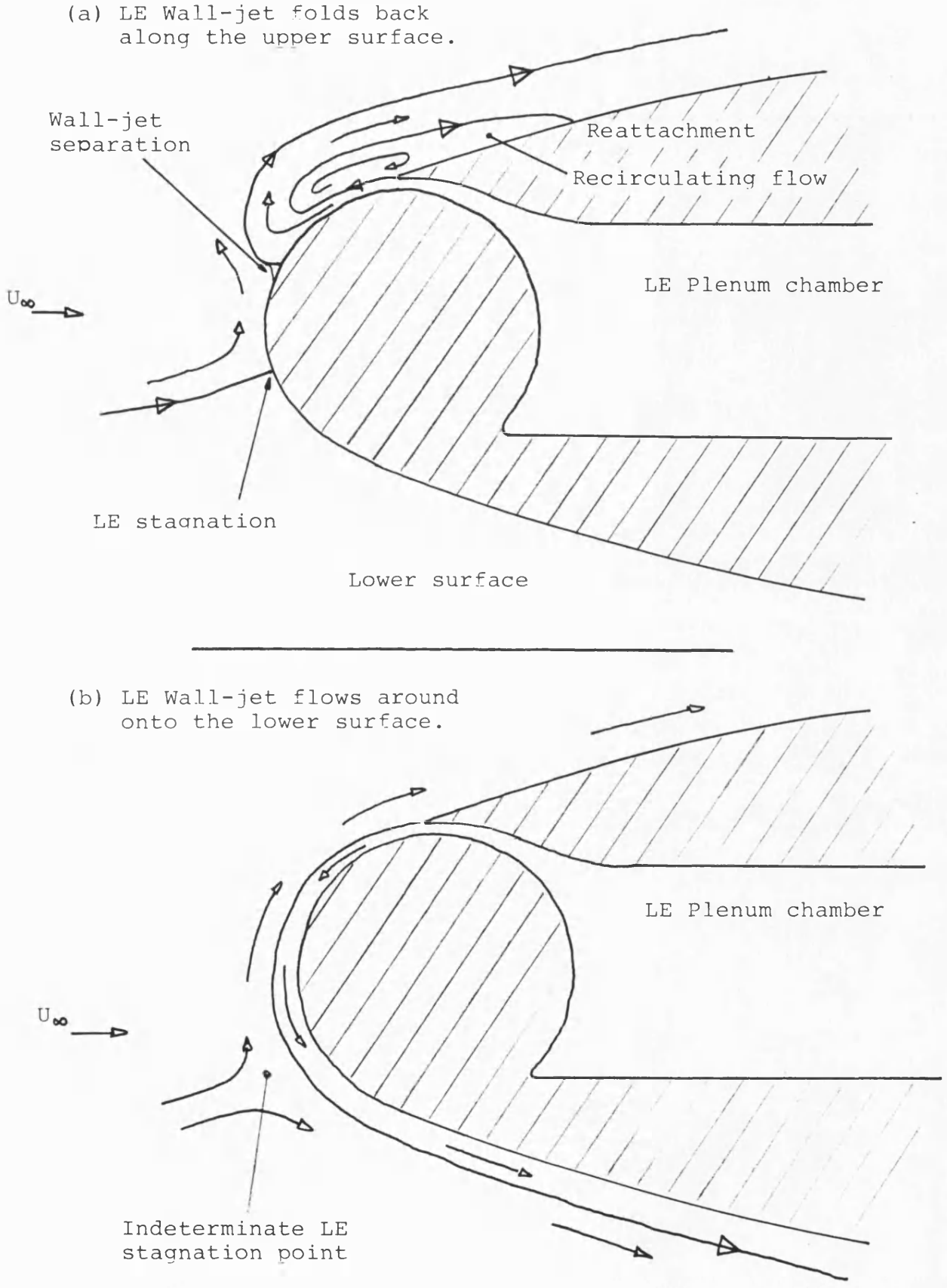

Fig. 5. 17: SKETCH OF TWO POSSIBLE TYPES OF LE WALL-JET FLOW.